

Université de Liège  
Faculté des Sciences

Modeling of the auroral thermal structure  
and morphology of Jupiter

Modélisation de la structure thermique et de  
la morphologie aurorales de Jupiter

Dissertation présentée par

**Denis Grodent**

en vue de l'obtention  
du grade de Docteur en Sciences

**2000**

# Avant-propos — Foreword

*"Un coq disait à ses poules en leur montrant un œuf d'autruche :  
je ne vous propose pas un modèle, je veux simplement  
vous montrer ce qui se fait ailleurs". Anonyme*

Il y a quelque chose de merveilleux dans la rédaction d'une thèse, surtout à l'heure de la conclusion. On prend enfin le temps de rassembler ses idées, d'avoir une vision globale du problème et, petit à petit, tout devient plus clair, on a l'impression d'avoir construit un mécanisme dans lequel tous les engrenages se mettent enfin à tourner de concert.

Un jour, une personne rencontrée à l'étranger m'a dit qu'elle m'enviait de travailler sur Jupiter, que la noblesse qui se dégage de cette planète géante devait me procurer une certaine fierté. Je commence seulement à réaliser ce que cette personne voulait dire; ce qui n'était pour moi qu'une "étoile ratée" s'est rapidement révélé, au travers des images fantastiques prise par le Télescope Spatial Hubble (HST), un objet grandiose. Les dimensions gigantesques, oserais-je dire olympiques, de Jupiter et l'amplitude des phénomènes qui s'y déroulent ne peuvent que forcer l'émerveillement, voire le respect.

Je dois confesser être un fanatique de films de science-fiction. J'ai d'ailleurs été rassuré de voir que je partageais cette passion avec de très sérieux collègues... Les voyages dans l'espace (pas toujours très pacifiques au cinéma) m'ont toujours fait rêver. En travaillant sur les images de Jupiter prises par HST j'ai pu, en quelque sorte, faire mon propre voyage dans le système solaire. Ce fut aussi un voyage initiatique puisqu'au fil de ces années j'ai appris mon métier de chercheur, avec tout ce que cela implique au niveau scientifique, mais aussi au niveau humain. J'ai eu l'occasion d'effectuer une série de voyages à l'étranger (pour des congrès ou des séjours de travail) et d'y rencontrer un grand nombre de personnes, scientifiques ou non et souvent de sympathiser avec elles. Cela m'a permis de découvrir d'autres cultures, d'autres paysages et surtout, cela m'a montré ce qui se fait ailleurs ...

Je tiens à exprimer ma reconnaissance au Professeur Jean-Claude Gérard qui, en m'accueillant dans son laboratoire, m'a fourni les moyens de mener à bien cette étude. Durant ces années, j'ai bénéficié de ses compétences scientifiques et de sa patience. Je ne peux négliger la convivialité dont il a fait preuve, surtout lors des congrès et des conférences à l'étranger.

I am deeply indebted to Dr. J.H. Waite, Jr. and to Dr. G.R. Gladstone who welcomed me at the Southwest Research Institute (San Antonio). Their guidance was invaluable in the stage of development of two of the major models presented in this work. I thank them for their patience (being aware of their extremely high workload) and for making my stays at SwRI an enjoyable and fruitful scientific and human experience.

Vincent Dols m'a appris énormément sur les aurores de Jupiter, ainsi que sur les aspects pratiques de l'étude des images et des spectres obtenus par HST. Je le remercie d'avoir pris le temps de m'expliquer les choses à fond. Je tiens à dire qu'il a été pour moi plus qu'un simple collaborateur, presque un grand frère.

J'ai bénéficié des conseils scientifiques et techniques de Bernard Nemry, Benoît Hubert et Guy Munhoven. Je les remercie de m'avoir donné un peu de leur temps. Jacques Gustin a récemment remplacé V. Dols (qui est parti tenté l'aventure dans le Grand Nord) aux commandes du générateur de spectres. Je le remercie pour sa collaboration et pour l'ambiance qu'il met dans notre bureau.

Un grand merci aussi aux autres collègues du LPAP : Yves, Daniel, Angela, Pierre, Dominique, Anne, Louis, Christine, Nadine, Bernard, Frédéric, Geoffrey, Gilles. Sans oublier la ribambelle d'informaticiens qui se sont succédés au LPAP : Thierry, Claude, Olivier... Par leur bonne humeur, ils ont, à leur manière, contribué à rendre ce long travail techniquement et humainement possible.

Je remercie mon épouse Catherine de m'avoir donné deux merveilleux enfants, Elise et Clément, qui ont grandi en même temps que ce travail. Durant ces dernières semaines leur affection et leur soutien ont été primordiaux. J'espère qu'ils ne m'en voudront pas de les avoir un peu délaissés.

Enfin, mes remerciements vont à toute ma famille qui m'a toujours soutenu pendant toutes ces années d'études.

Ce travail a été financé par le programme PRODEX (S.S.T.C.) et par un contrat d'assistant de la Communauté Française (Université de Liège).

à mon père,  
je crois qu'il aurait été fier.

## Résumé

L'introduction générale de ce travail présente les caractéristiques principales de la planète Jupiter ainsi qu'une description plus détaillée de sa magnétosphère. Cette dernière comprend un rappel sur les mouvements de base d'une particule chargée dans un champ magnétique. On y décrit le champ magnétique interplanétaire et sa reconnexion avec la magnétosphère d'une planète. Les notions de champs de corotation et de convection magnétosphériques sont utilisées pour différencier la Terre et Jupiter. Parmi ces différences, on met en évidence l'interaction de Jupiter avec le satellite Io qui pourvoit au plasma magnétosphérique. Ces notions permettent de discuter l'origine possible des particules qui provoquent les aurores terrestres et, par analogie, les aurores joviennes. On y montre que les particules aurorales sont liées à la présence de courants et de champs alignés le long des lignes du champ magnétique. Les caractéristiques principales du Télescope Spatial Hubble et des instruments WFPC2 et GHRS, dont nous utilisons les observations, sont brièvement décrites à la fin de cette introduction.

Dans la première partie, nous décrivons un modèle morphologique qui simule des vues des arcs auroraux et des émissions diffuses ultraviolettes. Des cas géométriques simples sont décrits pour illustrer l'effet de l'altitude, de la hauteur d'échelle et de la longitude du méridien central sur une morphologie aurorale idéalisée, vue depuis la Terre. En guise d'application du modèle de simulation, quatre images obtenues avec la caméra WFPC2 à bord du Télescope Spatial Hubble sont utilisées pour déterminer les caractéristiques des structures aurorales qui y apparaissent. Une distribution moyenne déduite de la superposition de 10 images, du même groupe d'observations, est construite pour illustrer la dichotomie fréquemment observée entre une structure en forme d'arc mince, apparaissant dans le secteur du matin et une structure diffuse contenant des arcs multiples dans le secteur de l'après-midi. La position de ces structures est exprimée et contrainte dans un référentiel lié au modèle de champ magnétique GSFC-O6.

Nous décrivons ensuite l'application du modèle au rapport de couleur UV lointain. Cette quantité représente le rapport entre l'intensité dans une bande spectrale UV non-absorbée et une bande spectrale UV absorbée par le méthane. Les résultats obtenus par

le simulateur, à partir de géométries déduites d'images HST, sont comparés aux observations du spectrographe IUE. Nous tentons de reproduire les observations IUE en imposant une variation longitudinale intrinsèque de la colonne de méthane située au dessus du niveau de l'émission aurorale.

La deuxième partie est consacrée au modèle de dégradation de l'énergie des électrons auroraux dans l'atmosphère Jovienne et au couplage de celui-ci avec un modèle de conduction thermique. La section théorique comprend une introduction sur l'atmosphère de Jupiter dans laquelle nous décrivons le découpage de l'atmosphère en régions, selon un critère dynamique puis, selon un critère thermique. Nous rappelons les notions d'équilibre hydrostatique et nous l'utilisons pour obtenir une relation entre la pression et l'altitude. Nous décrivons le modèle de transport électronique de Banks et Nagy ainsi que la méthode de résolution numérique que nous lui avons appliquée. Le jeu de sections efficaces de perte d'énergie est entièrement décrit ainsi que le traitement numérique de la perte d'énergie par les électrons auroraux.

Le calcul du profil vertical de température est obtenu à partir de la résolution de l'équation de conduction thermique dont nous décrivons la résolution numérique. Parmi les sources de chaleur nous considérons, entre autre, la dissociation de  $H_2$ , le chauffage dû aux collisions avec les électrons thermiques et le chauffage chimique. D'autres sources, comme la dissipation des ondes de gravité, sont prises en compte de manière indirecte. Les puits de chaleur sont représentés par le refroidissement radiatif infrarouge de  $H_3^+$ ,  $CH_4$  et  $C_2H_2$ . Pour ceux-ci, nous discutons la correction de l'écart à l'équilibre thermodynamique local. Pour calculer la réponse de la structure atmosphérique à la précipitation aurorale, le code de dégradation résout itérativement l'équation de diffusion des constituants majoritaires. Nous discutons des profils verticaux des coefficients de diffusion turbulente et moléculaire ainsi que de leur interaction. Une méthode estimant la densité de  $H_3^+$  dans l'ionosphère, en fonction de l'activité aurorale, est décrite ainsi que son rôle thermostatique dans la thermosphère.

L'équation de conduction de la chaleur, l'équation de diffusion et le système d'équations du transport électronique sont intimement liés. La résolution simultanée de ces équations requiert un processus itératif pour lequel nous décrivons une stratégie limitant la vitesse de convergence.

Dans la section portant sur les applications du code de dégradation nous analysons les

effets de la précipitation d'électrons caractérisés par différentes distributions d'énergie sur l'équilibre thermique de la thermosphère.

Pour contraindre les paramètres de ces distributions, nous utilisons les valeurs de différentes quantités observables, comme l'altitude du pic d'émission UV de H<sub>2</sub>, les émissions IR et UV, le rapport de couleur FUV, ainsi que les températures associées à différentes signatures optiques. Une série de tests de sensibilité sont effectués sur différents paramètres, comme par exemple, la valeur du coefficient de diffusion turbulente à l'homopause.

La troisième et dernière partie décrit le générateur de spectre H<sub>2</sub> UV à haute résolution ainsi que le couplage global des différents modèles.

Nous commençons par une revue des notions de spectroscopie de H<sub>2</sub> dans l'ultraviolet lointain qui sont utilisées dans le générateur de spectre. Ces notions sont appliquées spécifiquement aux bandes de Lyman et de Werner. Pour les bandes de Werner nous considérons, en plus, l'effet de cascade de l'état E,F et nous décrivons la manière dont il a été pris en compte dans le générateur. Les sections suivantes décrivent le couplage du code de dégradation d'énergie avec le générateur de spectre avec, dans un premier temps, un profil de température fixe. Les effets de la distribution d'énergie des électrons auroraux sur les spectres sont illustrés par trois exemples. Les effets de température, via la population des niveaux rotationnels, sont également mis en évidence. Une méthode d'ajustement des spectres théoriques aux spectres observés est appliquée à deux spectres GHRS. Cette méthode permet d'estimer la température de H<sub>2</sub>. Dans le cas des deux spectres GHRS cette température est de l'ordre de 600 K, en désaccord avec la température prédite par le code de dégradation d'énergie qui donne une température moyenne, pondérée par l'émission UV de H<sub>2</sub>, de 200 K. L'utilisation des profils de températures convergés n'apporte aucune solution à cette contradiction.

Le couplage global des trois modèles (dégradation d'énergie, générateur spectral et modèle de morphologie) est étudié dans la dernière section. Ce couplage met en évidence un effet en longueur d'onde et en géométrie d'observation sur la température déduite des observations spectrales. Nous montrons comment ces effets peuvent se combiner avec les profils verticaux de température, de densité et d'émission pour donner une température effective de 600 K, en accord avec les observations.

Pour terminer, nous discutons des perspectives offertes par ce couplage global et

notamment de la possibilité d'effectuer un sondage spectroscopique du profil de température.

# Summary

The general introduction of this work presents the main characteristics of the planet Jupiter and a detailed description of its magnetosphere. The latter reminds the basic motion of a charged particle in a magnetic field. It describes the interplanetary magnetic field and its reconnection with the planetary magnetosphere. The notions of corotating field and magnetospheric convection are used to differentiate the Earth and Jovian magnetospheres. Among these differences the interaction with the satellite Io is stressed out as Io provides most of the magnetospheric plasma material. These notions allow to discuss the potential origin of the particles responsible for the Earth aurorae and, by extension, the Jovian aurorae. It is postulated that the auroral particles are related to the presence of field-aligned currents and fields. The main characteristics of the Hubble Space Telescope and of the WFPC2 and GHRS instruments, which were used for this work, are briefly described at the end of the introduction.

The first part describes a model simulating Earth views of UV auroral arcs and diffuse emissions in the Jovian north polar region. Simple geometric cases are described to illustrate the dependence of the altitude, atmospheric scale height and central meridian longitude of an idealized auroral morphology seen from Earth orbit. As an application of the simulation model, four images obtained with the WFPC2 camera on board the Hubble Space Telescope are used to determine the characteristics of their auroral (discrete and diffuse) structures. A composite average auroral distribution is built by mapping 10 WFPC2 images from the same dataset. It illustrates the dichotomy frequently observed between a narrow single structure confined to the morning sector, and the multiple arc and broad diffuse emission in the afternoon sector. Location of these structures are given and constrained in a reference frame linked to the GSFC-O6 magnetic field model.

This model is then applied to assess the role of the viewing geometry on the auroral far UV color ratio. This value gives the ratio between the intensity measured in an unabsorbed spectral band and the intensity in a methane-absorbed band. The simulated color ratios, obtained from a geometry deduced from images taken with HST, are compared to the color ratio measurements obtained with the IUE spectrograph. We

attempt to reproduce the IUE observations by imposing an intrinsic longitudinal dependence of the column of methane above the level of the auroral emission.

The second part is devoted to the energy degradation model of the auroral electrons in the jovian atmosphere. It then describes the coupling of this model with a thermal conduction model. The theoretical section includes an introduction on the jovian atmosphere and its confinement in regions characterized by different dynamical and thermal regimes. The notion of hydrostatic equilibrium is reminded and used to establish a pressure-altitude relationship. We describe the electron transport model of Banks and Nagy and the numerical resolution method that we applied to it. The set of cross sections used to quantify the energy loss processes is described along with the numerical treatment of the energy "reapportionment" of the auroral electrons.

The vertical thermal profile is calculated from the heat conduction equation. Among the different heat sources we consider  $\text{H}_2$  dissociation, thermal electron heating, and chemical heating. Other sources, such as the breaking gravity waves, are indirectly accounted for. The heat sinks account for the IR radiative cooling from  $\text{H}_3^+$ ,  $\text{CH}_4$  and  $\text{C}_2\text{H}_2$ . A correction regarding the departure from local thermodynamic equilibrium is applied for these species.

In order to calculate the response of the atmospheric structure to the auroral precipitation, the model iteratively solves the diffusion equation for the major constituents. The vertical profiles of the eddy and molecular diffusion coefficients and their connection are addressed. The adopted method for the approximation of the  $\text{H}_3^+$  density in the ionosphere as a function of the auroral activity is presented. The thermostatic role of  $\text{H}_3^+$  in the thermosphere is then discussed.

The heat conduction equation, the diffusion equation and the electron transport equations are tightly coupled. The resolution of this set of equations therefore requires an iterative approach for which we describe a strategy meant to limit the convergence speed.

The energy degradation model is then applied with different energy distributions to assess the importance of the energy spectrum of the incident electrons for the thermal balance of Jupiter's auroral thermosphere. The values of observable quantities such as the altitude of the  $\text{H}_2$  emission peak, the IR and UV emissions, the FUV color ratio and

temperatures associated with various optical signatures are used to constrain the parameters of these energy distributions. A series of sensitivity tests are carried out to analyse the role of critical parameters such as the value of the eddy diffusion coefficient at the homopause.

The third part describes the H<sub>2</sub> UV high-resolution spectral generator and the global coupling of the different models.

We begin with an overview of H<sub>2</sub> far-UV spectroscopy notions that are used in the spectral generator, especially regarding the Lyman and Werner band systems. For the Werner bands, the cascade effect from the E,F state is considered. The coupling of the energy degradation model with the spectral generator is described. In a first stage an unconverged thermal profile is adopted. Three examples are used to illustrate the effect of the electron energy distribution on the spectra. The temperature effect is also highlighted. The H<sub>2</sub> temperature is determined from two GHRS spectra. It gives a best fit temperature of 600 K, in disagreement with the temperature predicted by the energy degradation model. The latter predicts an average temperature, weighted by the H<sub>2</sub> UV emission profile, of the order of 200 K. It is shown that the use of converged thermal profiles, obtained with the heat conduction equation, does not remove the contradiction. The coupling of the three models (energy degradation, spectral generator, and morphology) is performed in the last section. This coupling reveals a wavelength and a viewing geometry effect on the temperature deduced from the observed spectra. It is shown how these effects impinge on the thermal, density and emission vertical profiles to produce an effective H<sub>2</sub> temperature of 600 K in agreement with the temperature deduced from the observed spectra.

We finally discuss a possible application of the coupled models that would allow a spectroscopic probing of the jovian thermal profile.

# Table of contents

## Introduction

I The Planet Jupiter.....	1
I.1 Coordinate systems.....	4
II The planetary magnetosphere.....	8
II.1 Introduction.....	8
II.1.1 Background.....	8
II.1.1.1 Gyromotion.....	9
II.1.1.2 Particle drifts.....	10
II.1.1.3 Magnetic mirroring.....	12
II.2 Magnetospheric morphology.....	14
II.2.1 The interplanetary magnetic field.....	17
II.2.2 Magnetic Reconnection.....	18
II.2.3 Magnetospheric electric fields and convection.....	20
II.2.3.1 The corotation field.....	20
II.2.3.2 Magnetospheric convection field.....	22
II.2.4 The Earth magnetosphere.....	23
II.2.5 The Jovian magnetosphere.....	25
II.2.5.1 Thermal plasma characteristics.....	28
II.2.5.2 The Io plasma torus.....	29
II.2.5.3 The Io-plasma interaction.....	30
II.2.5.4 The plasma sheet.....	31
II.2.5.5 Energetic particle population.....	32
II.2.6 Jovian magnetospheric models (VIP4, GSFC-O6).....	34
II.2.6.1 The VIP4 model.....	34
II.2.6.2 The GSFC-O6 model.....	35
II.3 Origin of the auroral particles.....	36
II.3.1 Introduction.....	36
II.3.2 Diffuse and discrete auroræ on Earth.....	37
II.3.3 Magnetic field-aligned potential drops.....	38
II.3.4 Pitch angle scattering.....	39
II.3.4.1 wave-particle interaction.....	40
II.3.4.2 The "windshield wiper" effect.....	40
II.3.5 The Jovian auroral field-aligned currents.....	41
II.3.6 Evidence of solar wind driven auroras on Jupiter.....	42
III The Hubble Space Telescope.....	44
III.1 The Wide Field and Planetary Camera 2 (WFPC2).....	46
III.2 The Goddard High Resolution Spectrograph (GHRS).....	48

## Part 1

IV Simulation of the Morphology of the Jovian UV North Aurora Observed with the Hubble Space Telescope.....	50
IV.1 Introduction.....	52
IV.2 The auroral simulation model .....	54
IV.2.1 Model description .....	54
IV.2.2 Limb brightening estimate.....	59
IV.3 Simulation of simple test cases.....	62
IV.4 Auroral image simulations.....	64

IV.4.1 The WFPC2 dataset .....	64
IV.4.2 Simulation of observed images.....	65
IV.4.2.1 Image 0503.....	68
IV.4.2.2 Image 0E01.....	72
IV.4.2.3 Image 1701.....	73
IV.4.2.4 Image 1502.....	76
IV.5 The statistical equatorial boundary oval .....	79
IV.6 Discussion and conclusion.....	82
V The longitudinal variation of the color ratio of the Jovian ultraviolet aurora : a geometric effect ?.....	85
V.1 Introduction.....	86
V.2 The geometric simulation model.....	88
V.3 Comparison with observations.....	90
V.4 Discussion.....	95

## Part 2

VI Theory.....	96
VI.1 Introduction.....	96
VI.2 The Jovian atmosphere.....	100
VI.2.1 Atmospheric regions.....	100
VI.2.1.1 Dynamical regime criterion.....	100
VI.2.1.1.1 The homosphere.....	100
VI.2.1.1.2 The heterosphere.....	102
VI.2.1.1.3 The exosphere.....	102
VI.2.1.2 Temperature profile.....	103
VI.2.1.2.1 The troposphere.....	104
VI.2.1.2.2 The lower and upper stratosphere.....	104
VI.2.1.2.3 The thermosphere.....	104
VI.2.2 The hydrostatic equilibrium.....	105
VI.2.2.1 General concepts.....	105
VI.2.2.2 Pressure-altitude relationship.....	107
VI.3 The electron energy degradation model.....	109
VI.3.1 Introduction.....	109
VI.3.2 Auroral electron transport model.....	109
VI.3.2.1 Numerical resolution of the differential equations system.....	112
VI.3.2.2 Lower boundary conditions.....	115
VI.3.2.3 Average pitch angle.....	116
VI.3.3 Two-point Gauss-Legendre quadrature.....	118
VI.4 Cross-sections.....	120
VI.4.1 Total inelastic cross-section.....	121
VI.4.2 Backscattering.....	126
VI.5 Numerical treatment of the electron energy loss.....	129
VI.5.1 Energy reapportionment.....	129
VI.5.2 Energy reapportionment following inelastic collisons.....	129
VI.5.3 Energy reapportionment following ionizing collisions.....	132
VI.6 Calculation of the neutral temperature profile.....	133
VI.6.1 The heat conduction equation.....	133
VI.6.2 Numerical resolution.....	134
VI.6.3 Boundary conditions.....	135
VI.6.4 Heat sources.....	136

VI.6.4.1 H <sub>2</sub> dissociation.....	136
VI.6.4.2 Thermal electron heating.....	137
VI.6.4.3 Chemical heating.....	138
VI.6.4.4 Unspecified heat sources.....	139
VI.6.4.5 Breaking gravity waves.....	139
VI.6.5 Heat sinks.....	142
VI.6.5.1 Estimation of the radiative cooling.....	142
VI.6.5.2 The local thermodynamic equilibrium (LTE).....	143
VI.6.5.3 H <sub>3</sub> <sup>+</sup> density and radiative cooling.....	144
VI.6.5.4 Collisional deexcitation for hydrocarbons and radiative cooling.....	149
VI.6.5.5 Departure from the optically thin approximation.....	151
VI.7 Response of the atmospheric structure to auroral electron precipitation.....	152
VI.7.1 The initial model atmosphere.....	152
VI.7.2 Effects of electron precipitation.....	152
VI.7.2.1 Diffusion of the neutral species.....	152
VI.7.2.1.1 The diffusion equation.....	154
VI.7.2.1.2 Hydrocarbon species.....	157
VI.7.2.1.3 Boundary conditions.....	158
VI.7.2.1.4 Characteristic times for diffusion.....	158
VI.7.2.2 Molecular and eddy diffusion profiles.....	159
VI.7.2.2.1 The eddy diffusion coefficient.....	159
VI.7.2.2.2 The molecular diffusion coefficient.....	161
VI.7.2.2.3 The thermal diffusion factor.....	162
VI.7.2.2.4 Relationship between molecular and eddy diffusion.....	163
VI.7.3 Chemical reactions.....	166
VI.7.3.1 Atomic hydrogen chemistry.....	166
VI.7.3.2 Hydrocarbon photochemistry.....	166
VI.7.3.3 The H <sub>3</sub> <sup>+</sup> density profile.....	167
VI.8 Iteration process.....	170
VI.8.1 Convergence strategy.....	172
VII Model application.....	174
VII.1 Abstract.....	174
VII.2 Energy distribution of auroral electrons.....	176
VII.2.1 H <sub>2</sub> <sup>+</sup> and H <sup>+</sup> production rate profiles.....	178
VII.2.2 Heating and cooling profiles.....	181
VII.3 Observational constraints.....	185
VII.3.1 Thermal profile.....	185
VII.3.2 UV emission.....	187
VII.3.3 Color ratio and CH <sub>4</sub> column density.....	190
VII.3.4 IR emission.....	191
VII.4 Model results.....	194
VII.4.1 Energy distribution.....	194
VII.4.1.1 Effect of a soft electron component : double Maxwellian energy distribution (case B).....	194
VII.4.1.2 Kappa energy distribution (case C).....	197
VII.4.1.3 Effect of the auroral precipitation on the atmospheric composition .....	198
VII.4.2 Thermostatic role of H <sub>3</sub> <sup>+</sup> .....	199
VII.4.3 Sensitivity study.....	201
VII.4.3.1 Sensitivity to the altitude of the emission peak (case D).....	201
VII.4.3.2 Sensitivity to the altitude of the homopause (cases E and F).....	205

VII.4.3.3 Sensitivity to the $H_3^+$ quenching rate coefficient (case G).....	207
VII.4.3.4 Sensitivity to the stratospheric temperature profile (case H).....	208
VII.5 Conclusion.....	211

### Part 3

VIII The spectral generator.....	214
VIII.1 $H_2$ far ultraviolet spectroscopy.....	214
VIII.1.1 Conventions.....	216
VIII.1.1.1 X,.....	216
VIII.1.1.2 $2S+1$ .....	217
VIII.1.1.3 (+,-).....	217
VIII.1.1.4 (g,u).....	218
VIII.1.1.5 Other symmetry properties.....	218
VIII.1.2 $\Lambda$ -type doubling.....	220
VIII.1.3 Selection rules for electronic transitions.....	220
VIII.1.4 General selection rules.....	221
VIII.1.5 Influence of the nuclear spin.....	222
VIII.1.6 Emission intensity.....	223
VIII.1.6.1 Population of the ground level.....	224
VIII.1.6.2 vibrational levels.....	224
VIII.1.6.3 Rotational levels.....	225
VIII.1.7 Transition wave number.....	226
VIII.2 Application to the Lyman and Werner band spectra of $H_2$ .....	227
VIII.2.1 The B state.....	227
VIII.2.1.1 E,F Cascade.....	230
VIII.2.2 The C state.....	234
VIII.2.3 Continuum emission.....	237
VIII.2.4 Self absorption.....	239
VIII.3 Coupling of the two-stream model with the spectral generator.....	240
VIII.3.1 Introduction.....	240
VIII.3.2 Vertical distribution.....	242
VIII.3.3 Model validation and sensitivity.....	246
VIII.3.4 Echelle $H_2$ spectroscopy.....	256
VIII.4 Use of converged temperature profiles.....	259
IX Coupling of the three models.....	262
IX.1 Introduction.....	262
IX.2 Modified morphology model.....	263
IX.3 Methane absorption.....	263
IX.4 Viewing geometry effect.....	264
IX.4.1 Application to case B.....	264
IX.4.2 Line of sight pointing inside the planetary disk.....	264
IX.4.3 Line of sight pointing above the limb.....	270
IX.5 Application to cases D and H.....	276
IX.6 Perspectives : spectroscopic probing of the thermal profile.....	280
IX.6.1 Simple example.....	280
IX.6.2 Further improvement.....	281
IX.7 Conclusion.....	283
References.....	284
Appendix -A. Effect of the geometry of observation on the average temperature.....	294
-B. Papers	

# Introduction

## I The Planet Jupiter

Jupiter's system is very complex, yet many of its processes resemble processes that exist on Earth, magnified by the enormity and extremity of Jupiter. In studying Jupiter, we can learn more about atmospheric effects and interactions that are observed on Earth, such as interactions between the magnetosphere and the atmosphere.



**Figure 1** : WFPC2 (HST) near ultraviolet image showing Jupiter's moon Io passing above the turbulent clouds of the giant planet.

Jupiter is the largest of the nine planets of our solar system, more than 10 times the diameter of the Earth and more than 300 times its mass. In fact, the mass of Jupiter is almost 2.5 times that of all the other planets combined. (A comparison of the bulk

and orbital parameters of Jupiter and Earth is given in tables 1 and 2.) Being composed largely of the light elements hydrogen and helium, its mean density is 4 times smaller than the Earth's mean density. The pull of gravity on Jupiter at the top of the clouds at the equator is 2.4 times as great as gravity's pull at the surface of Earth at the equator. The bulk of Jupiter rotates in 9h55.5m, although the period determined by watching cloud features differs by up to five minutes due to intrinsic cloud motions.

The visible "surface" of Jupiter is a deck of clouds of ammonia crystals, the tops of which occur at a level where the pressure is about half that at Earth's surface. The bulk of the atmosphere is made up of 89 % molecular hydrogen ( $H_2$ ) and 11 % helium (He). There are small amounts of gaseous ammonia ( $NH_3$ ), methane ( $CH_4$ ), water ( $H_2O$ ), ethane ( $C_2H_6$ ), acetylene ( $C_2H_2$ ), carbon monoxide (CO), hydrogen cyanide (HCN), and even more exotic compounds such as phosphine ( $PH_3$ ) and germane ( $GeH_4$ ). At levels below the deck of ammonia clouds there are believed to be ammonium hydro-sulfide ( $NH_4SH$ ) clouds and water crystal ( $H_2O$ ) clouds, followed by clouds of liquid water. The cause of the colors of the visible clouds is not yet known. "Contamination" by various polymers of sulfur ( $S_3$ ,  $S_4$ ,  $S_5$ , and  $S_8$ ), which are yellow, red, and brown, has been suggested as a possible cause of the riot of color, but in fact sulfur has not yet been detected spectroscopically, and there are many other candidates as the source of the coloring.

The meteorology of Jupiter is very complex and not well understood. Even in small telescopes, a series of parallel light bands called zones and darker bands called belts is quite obvious. The polar regions of the planet are dark. Also present are light and dark ovals, the most famous of these being "the Great Red Spot". The great red spot is larger than Earth, and although its color has brightened and faded, the spot has persisted for at least 169 years, the earliest definite drawing of it being Schwabe's of Sept. 5, 1831. It is thought that the brighter zones (in the visible wavelengths) are cloud-covered regions of upward moving atmosphere, while the belts are the regions of descending gases, the circulation driven by interior heat. The spots are thought to be large-scale vortices, much larger and far more permanent than any terrestrial weather system.

The interior of Jupiter is totally unlike that of the Earth. Earth has a solid crust "floating" on a denser mantle that is fluid on top and solid beneath, underlain by a fluid outer core that extends out to about half of Earth's radius and a solid inner core of about 1220 km radius. The core is probably 75 % iron, with the remainder nickel, perhaps silicon, and many different metals in small amounts. Jupiter on the other hand may well be fluid throughout, although it could have a "small" solid core (up to 15 times the mass of Earth) of heavier elements such as iron and silicon extending out to perhaps 15 % of its radius. The bulk of Jupiter is fluid hydrogen in two forms or phases, liquid molecular hydrogen on top and liquid metallic hydrogen below; the latter phase exists where the pressure is high enough, about  $3-4 \times 10^6$  atmospheres. There could be a small layer of liquid helium below the hydrogen, separated out gravitationally, and there is clearly some helium mixed in with the hydrogen. The hydrogen is convecting heat from the interior, and that heat is easily detected by infrared measurements, since Jupiter radiates twice as much heat as it receives from the Sun. The heat is generated largely by gravitational contraction and perhaps by gravitational separation of helium and other heavier elements from hydrogen, in other words, by the conversion of gravitational potential energy to thermal energy. The moving metallic hydrogen in the interior is believed to be the source of Jupiter's strong magnetic field.

Jupiter's magnetic field is much stronger than that of the Earth. It is tipped about  $10^\circ$  to Jupiter's axis of rotation, similar to Earth's, but it is also offset from the center of Jupiter by about 10000 km. The magnetosphere of charged particles which it affects extends from 3.5 to  $7 \times 10^6$  km in the direction toward the Sun, depending upon solar wind conditions, and at least 10 times as far in the anti-Sun direction. The plasma trapped in this rotating, wobbling magnetosphere emits radio frequency radiation measurable from Earth at wavelengths from less than 1 m to as much as 30 km. These trapped charged particles make the inner portions of Jupiter's magnetosphere a very harsh radiation environment.

When the *Voyager I* spacecraft passed through Jupiter's realm in 1979, it spotted nine active volcanoes on Io, the innermost of the four Galilean satellites of Jupiter, spewing sulfur and sulfur dioxide gases and solids as high as 300 km above the surface

at velocities up to  $1 \text{ km s}^{-1}$ . Most of the material emitted falls back onto the surface, but a small part of it escapes the satellite. In space this material is rapidly dissociated and ionized. Once it becomes charged, the material is trapped by Jupiter's magnetic field and forms a torus along Io's orbit. Accompanying the volcanic sulfur and oxygen are many sodium ions (and perhaps some of the sulfur and oxygen as well) that have been sputtered from Io by high energy electrons in Jupiter's magnetosphere. The torus also contains protons and electrons which can be precipitated in the Jovian atmosphere and give rise to auroræ as will be discussed later.

## I.1 Coordinate systems

The standard coordinate system usually used to represent Jupiter's longitudes is a left-handed system known as System III, formulated for astronomical use, in which longitude (called West-longitude) is measured against the direction of rotation. This rotating coordinate system is defined by the mean rotational period of decametric radio sources in Jupiter's atmosphere. Figure 2 is a view from above the north pole of the Jovian coordinate system. The standard astronomical definition of the eastern and western sides of Jupiter as seen from the Earth are indicated by an E and W, respectively. The prime meridian rotates counterclockwise at a constant rate  $\Omega_J$ . Longitude is measured clockwise from this prime meridian. The System III sub-Earth longitude is called the Central Meridian Longitude (CML). This illustration also shows the longitude of some feature (an auroral emission, for example) marked X.

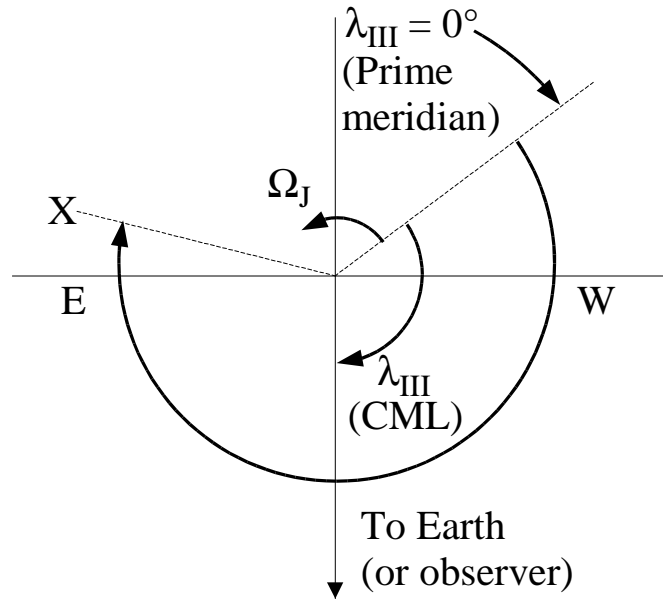


**Figure 2** :Jovian coordinate convention

Two systems are used to designate the Jovian latitude of a point on the surface (or anywhere in space). They are the **jovigraphic latitude** system and the **jovicentric latitude** system (illustrated in figure 3). They are related by a simple formula accounting for the planet's equatorial (a) and polar (b) radii :

$$\tan \Phi' = \left(\frac{b}{a}\right)^2 \tan \Phi$$

where  $\Phi'$  is the jovicentric latitude and  $\Phi$  is the jovigraphic latitude (similar to the geodetic latitude). In the present work, we adopt the jovicentric latitude system.

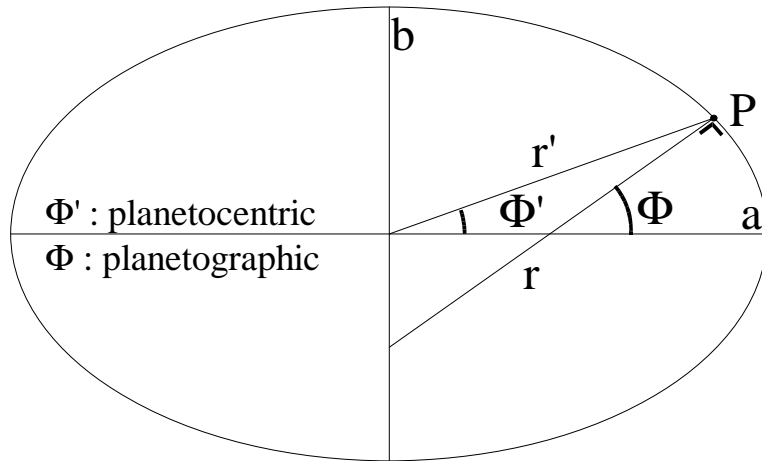


**Figure 3** : Planetocentric ( $\Phi'$ ) and planetographic ( $\Phi$ ) latitudes of a point  $P$  at the surface of an ellipsoidal planet.  $a$  and  $b$  are the equatorial and polar radii.  $r$  is normal to the ellipse at  $P$ .

	Jupiter	Earth	Ratio(Jupiter/Earth)
Mass ( $10^{24}$ kg)	1898.6	5.9736	317.83
Volume ( $10^{10}$ km <sup>3</sup> )	43128	108.321	1321.33
Radius (1 bar level) (km)			
Equatorial	71,492	6,378	11.21
Polar	66,854	6,356	10.52
Volumetric mean radius (km)	69,911	6,371	10.97
Ellipticity	0.0649	0.0034	19.09
Mean density (kg/m <sup>3</sup> )	1,326	5,520	0.240
Gravity (eq., 1 bar) (m/s <sup>2</sup> )	23.13	9.78	2.364
Escape velocity (km/s)	59.5	11.19	5.32
GM ( $\times 10^6$ km <sup>3</sup> /s <sup>2</sup> )	126.686	0.3986	317.8
Bond albedo	0.70	0.385	1.82
Visual geometric albedo	0.52	0.367	1.42
Visual magnitude V(1,0)	-9.40	-3.86	-
Solar irradiance (W/m <sup>2</sup> )	51.	1370.	0.037
Black-body temperature (K)	90.6	247.3	0.366
Moment of inertia (I/MR <sup>2</sup> )	0.254	0.3308	0.768

**Table 1** : Comparison of the bulk parameters of Jupiter and Earth.

	Jupiter	Earth	Ratio(Jupiter/Earth)
Semimajor axis ( $10^6$ km)	778.3	149.6	5.203
Sidereal orbit period (days)	4,332.589	365.256	11.862
Tropical orbit period (days)	4,330.595	365.242	11.857
Perihelion ( $10^6$ km)	740.6	147.1	5.035
Aphelion ( $10^6$ km)	816.0	152.1	5.365
Synodic period (days)	398.88	-	-
Mean orbital velocity (km/s)	13.07	29.79	0.439
Orbit inclination (deg)	1.305	0.00	-
Orbit eccentricity	0.04845	0.0167	2.901
Sidereal rotation period (hours)	9.9250	23.9345	0.415
Obliquity to orbit (deg)	3.12	23.45	0.133

**Table 2** : Comparison of the orbital parameters of Jupiter and Earth.

# II The planetary magnetosphere

## II.1 Introduction

As its name suggests, a planet's magnetosphere is the region of space magnetically controlled by the planet's magnetic field. The *Voyager* tour of the outer solar system has confirmed that, like Earth, all four giant planets (Jupiter, Saturn, Uranus, and Neptune) have extensive magnetospheres due to their strong magnetic fields, generated by convective motions in an electrically-conducting region in the planet's interior. The magnetosphere of Jupiter is a large structure dominated by strong planetary magnetic fields that contain thermal plasma. There are processes that accelerate the thermal plasma to produce populations of energetic particles trapped in radiation belts around the planet. Significant interactions occur between the plasma and satellites that are embedded in the magnetosphere. The magnetosphere produces different types of plasma waves, radio emissions, and aurorae.

This chapter is largely inspired by Fran Bagenal's review of the giant planet magnetospheres (Bagenal, 1992), the reader is referred to this paper for additional references on the different topics that will be discussed in the following sections. Specific information on the Jovian magnetosphere can be found in the book edited by J.A. Dessler (1983) collecting published papers discussing particular aspects of the physics of the Jovian magnetosphere. Useful information can also be found in David Stern's review of the large scale electric fields in the Earth's magnetosphere (Stern, 1977). Most of the figures appearing in this chapter were taken from T. Tascione (1994).

### II.1.1 Background

Before going into the very complex domain of planetary magnetospheres it is useful to remember some basic processes describing the motion of a charged particle in a magnetic field. These relations stand for the basic motions of electrons and ions in the magnetosphere :

- **gyromotion** around a magnetic field line,
- **bounce** motion between mirror points, and
- **drift** due to the configuration of the magnetic field or to the presence of an external force (for example an electric field).

### II.1.1.1 Gyromotion

We consider the motion of a positively charged particle moving in the plane of this page. If there is also a magnetic field present which is directed down into this page, it can be seen by use of the right-hand rule that the positive charge will circle counterclockwise, and an electron would circle clockwise.

The force acting on a charged particle  $q$  moving through a magnetic field  $\mathbf{B}$  (although  $\mathbf{B}$  is properly the magnetic induction, we use the more common term "magnetic field" in referring to it) at a velocity  $\mathbf{v}$  is called the Lorentz force and is written as  $\mathbf{F} = q \mathbf{v} \times \mathbf{B}$ . The particle path about  $\mathbf{B}$  is a circle in that the centripetal force is equal to the Lorentz force, and

$$\frac{-mv^2}{r} \hat{r} = q \mathbf{v} \times \mathbf{B}$$

where  $r$  is the radius of gyration,  $m$  is the charged particle mass, and  $\hat{r}$  is the unit vector in the radial direction. If the particle motion is at right angle to the magnetic field, one gets

$$\frac{mv^2}{r} = q v B$$

solving for  $r$  yields the radius of gyration (gyroradius or cyclotron radius) which is denoted as  $r_c$  as follows :

$$r_c = \frac{m v}{q B}$$

In the most general case, the charged particle velocity can be decomposed into a

component perpendicular to the magnetic field  $v_{\perp}$ , giving rise to the gyration motion, and into a component parallel to  $\mathbf{B}$ ,  $v_{\parallel}$ , which is therefore unaffected by the Lorentz force. The resulting particle motion is depicted in figure 4, it is an helix guided by a magnetic field line and characterized by the pitch angle  $\alpha$ , which is the angle between the magnetic line of force and the direction of the charged particle motion. The pitch angle is related to the velocity of the particle by  $v_{\perp} = v \sin \alpha$

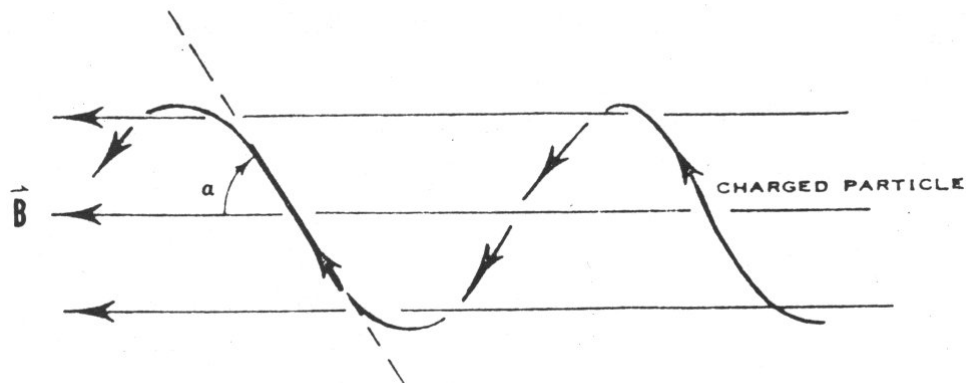


**Figure 4** : Pitch angle  $\alpha$ , the angle between the magnetic field line of force and the direction of the charged particle motion.

### II.1.1.2 Particle drifts

The relations from the previous section hold in a uniform magnetic field. However, if there was an external force, or if the magnetic field was not uniform, the charged particles would not follow perfectly circular paths. The particles would drift through the magnetic field in addition to performing the basic circular motion that has been discussed. If, for example, we assume that an electric field,  $\mathbf{E}$ , lies in the plane of the page, directed toward the bottom of the page, this produces a force  $\mathbf{F} = q \mathbf{E}$  whose direction is charge dependent. In general, the particle drift velocity is given by

$$\mathbf{v}_{\text{drift}} = \frac{\mathbf{F} \times \mathbf{B}}{qB^2}$$

considering the electric force, the drift velocity becomes

$$\mathbf{v}_E = \frac{q \mathbf{E} \times \mathbf{B}}{qB^2} = \frac{\mathbf{E} \times \mathbf{B}}{B^2}$$

and the resulting  $\mathbf{E} \times \mathbf{B}$  drift is charge independent. Therefore, electrons and protons drift in the same direction and velocity, as illustrated in figure 5.

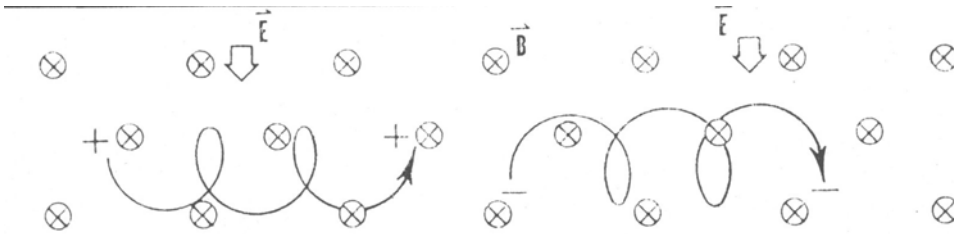


**Figure 5** : Cross B field drift due to an external electric field ( $\mathbf{E} \times \mathbf{B}$  drift). The positive and negative charged particles drift in the same direction and no net current is produced

We now assume that the magnetic field is uniform except for some small variations which give the total field some curvature in a particular direction (as is the case for a dipolar planetary field). As the gyrating particles move along a curved field line, some external force must act on the particle to make it turn and follow the field line geometry. If there are no external electric field, this force must be provided by the magnetic field. As the charged particles follow B, then a force of

$$\mathbf{F} = m \frac{v_{\parallel}^2}{R} \hat{\mathbf{R}}$$

is needed to turn the particle where  $v_{\parallel}$  is the particle velocity parallel to B and R is the radius of curvature (not gyroradius) of the magnetic field line. Therefore, we find

$$\mathbf{v}_c = \frac{mv_{\parallel}^2 \hat{\mathbf{R}} \times \mathbf{B}}{q R^2 B^2}$$

where the explicit appearance of q indicates that positive and negative particles will undergo curvature drift in opposite directions, and then produce a net electric current.

If one assumes a non-uniform magnetic field, with the greatest field strength nearest the bottom of the page, and applies an analysis similar to the above, the external force can be written as

$$\mathbf{F} = \frac{-m v_{\perp}^2}{2} \frac{\nabla \mathbf{B}}{B}$$

therefore, the so-called gradient drift becomes

$$\mathbf{v}_{\text{grad}} = \frac{-m v_{\perp}^2}{2q} \frac{\mathbf{B} \times \nabla \mathbf{B}}{B^3}$$

and since this drift velocity is charge dependent, electrons will drift in a direction while positive particles will drift in the opposite direction, resulting in a net electric current.

In the case of a charged particle following a planetary magnetic field line, the curvature and gradient drifts will combine to give rise to a so called "**ring current**".

### II.1.1.3 Magnetic mirroring

It was suggested above that the motion of a charged particle in the direction of  $\mathbf{B}$  is unaffected by the magnetic field. However, this conclusion does not hold in the cases of converging and diverging magnetic fields.

In figure 6, for example, a cross section is shown of a proton path in a diverging magnetic field. The proton is shown performing the basic cyclotron motion such that it is entering the page near the top of the figure, and leaving the page near the bottom. As shown, the force acting at right angles to the  $\mathbf{B}$  vector does not lie in the plane of circular motion of the charged particle. Instead, the force vectors form a cone whose apex is in the direction of decreasing magnetic field strength. Thus there is a net displacement force in the direction of weaker field strength. This same result holds true for an electron in a converging field. This means that a charged particle spiraling in a magnetic field will experience a force along the field lines, in the direction of weaker field strength. When the magnitude and duration of the force are sufficient to actually

cause the charged particle to reverse direction of motion along the line of magnetic force, the effect is known as **magnetic mirroring** and the location of the particle's path reversal is known as the **mirror point** for that particle.

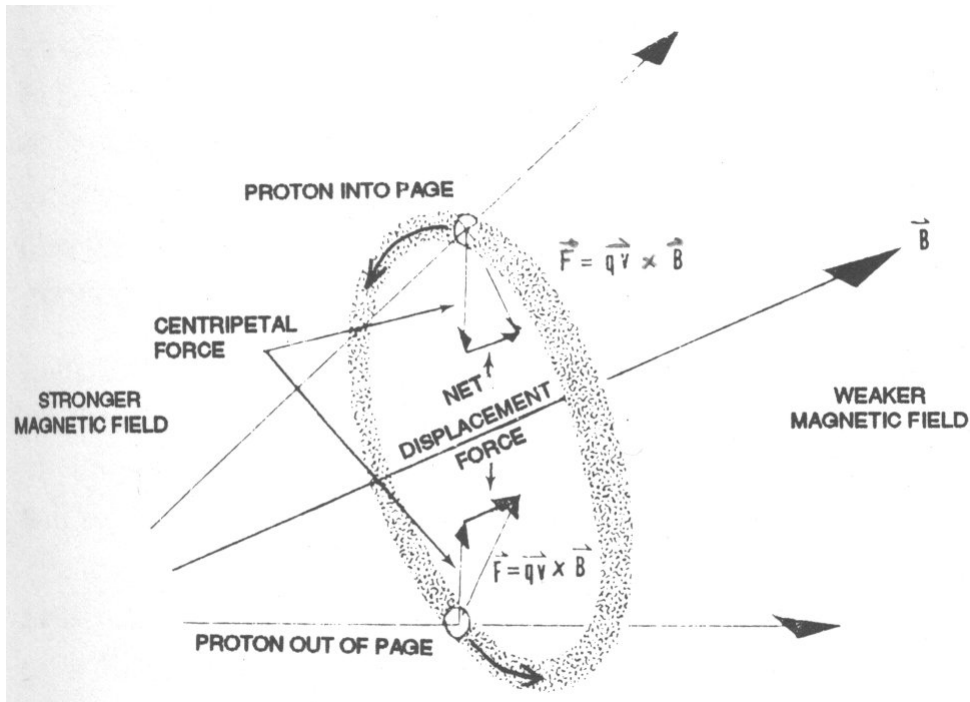


**Figure 6** : Forces acting on a gyrating proton in a diverging magnetic field.

This means that a charged particle spiraling in a magnetic field will experience a force along the field lines, in the direction of weaker field strength. When the magnitude and duration of the force are sufficient to actually cause the charged particle to reverse direction of motion along the line of magnetic force, the effect is known as **magnetic mirroring** and the location of the particle path reversal is known as the **mirror point** for that particle.

It can be shown from the first adiabatic invariant, which states that the magnetic moment of a particle remains constant during one gyro-orbit even though  $B$  may be changing slowly, that

$$\sin^2 \alpha = \frac{B}{B_m}$$

where  $B_m$  is the magnetic field strength at the mirror point.

This relation means that the pitch angle of the particle  $\alpha$  varies with the magnetic field

strength along a field line so as to conserve  $\sin^2 \alpha / B$ . The pitch angle of most particles reaches  $90^\circ$  before the particles reach the top of the atmosphere. Such particles bounce back and forth along magnetic field lines between the points where  $\alpha = 90^\circ$  and are trapped in the planetary magnetic field. Particles with sufficiently small pitch angles reach the top of the atmosphere before  $\alpha$  reaches  $90^\circ$ . Such particles are said to be in the loss cone, and they are absorbed into the atmosphere by collisions.

In summary, charged particles can be trapped in a planetary magnetic field. Their basic motion is circular (gyro-motion), with a superimposed longitudinal drift around the planet ( $\mathbf{E} \times \mathbf{B}$  drift), and a latitudinal reflection (or "bounce") between mirror points at high latitudes as illustrated in figure 7 for the Earth.

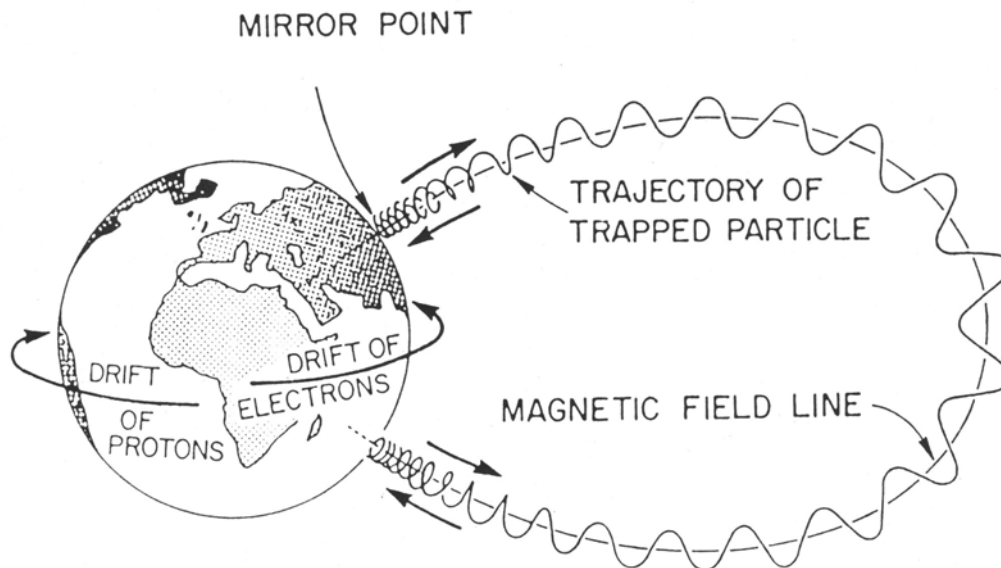


**Figure 7** : Basic motion of a charged particle in the Earth magnetic field.

## II.2 Magnetospheric morphology

The term **magnetosphere** was coined by Gold (1959) to describe the region of space wherein the principal forces on a plasma are electrodynamic in nature and are a result of the planet's magnetic field. Planetary magnetospheres are embedded in the solar wind, which is the outward expansion of the solar corona. At Earth's orbit and

beyond, the solar wind has an average speed of about  $400 \text{ km s}^{-1}$ . The density of particles (mainly electrons and protons) is observed to decrease, from values of about 3 to  $10 \text{ cm}^{-3}$  at the Earth, as the inverse square of the distance from the Sun, consistent with a steady radial expansion of the solar gas into a spherical volume. The solar wind speed, while varying between about 300 and  $700 \text{ km s}^{-1}$ , always greatly exceeds the speed of waves characteristic of a low density, magnetized, and completely ionized gas (**Alfvén waves**). Thus a shock is formed upstream of an obstacle, such as a planetary magnetosphere that is imposed on the super-Alfvénic solar wind flow. A planetary **bow shock** can be described in fluid terms as a discontinuity in bulk parameters of the solar wind plasma. As the flow of solar plasma traverses the shock it is decelerated and heated so that the flow can be deflected around the magnetosphere.

To first approximation, the magnetic field of a planet deflects the plasma flow around it, carving out a cavity in the solar wind. The layer of deflected solar wind behind the bow shock is called the **magnetosheath** and the boundary between the magnetosphere and the solar wind plasma is called the **magnetopause**. The magnetopause is a current layer resulting from the kinetic interaction between the solar wind and the planetary magnetic field. This current shields a large portion of the interplanetary magnetic field from the region interior to the magnetopause. As a result, the magnetopause is a sharp boundary that separates the interplanetary medium from a region of space which is dominated by the planetary magnetic field : the magnetosphere. The solar wind generally pulls out part of the planetary magnetic field into a long cylindrical magnetotail, extending far downstream behind the planet.

Table 3 shows a comparison between the Jovian and Earth magnetic fields. While the net magnetic moment of Jupiter is many times greater than that of the Earth, its large radius result in a surface magnetic field on the order of a Gauss. None of the planetary magnetic fields are purely dipolar but the dipole (first order) approximation gives an indication of the strength ( $B_0$ ) and orientation of the field. Jupiter has a magnetic field like that of the Earth, where the magnetic axis is roughly aligned with the rotation axis and has only moderate deviation from a dipole.

	Earth	Jupiter
Radius (km)	6373	71398
Spin period (hours)	24	9.9
Magnetic moment / $M_{\text{Earth}}$	20000	600
Surface magnetic field (Gauss)		
dipole equator, $B_0$	0.31	4.28
minimum	0.24	3.2
maximum	0.68	14.3
Dipole tilt and sense	+11.3°	-9.6°
Distance (A.U.)	1	5.2
Solar wind density ( $\text{cm}^{-3}$ )	10	0.4
$R_{\text{Corotating Plasma}}$	8 $R_E$	30 $R_J$
Size of magnetosphere	11 $R_E$	50-100 $R_J$

**Table 3** : Comparison of Earth and Jupiter magnetic fields.  
( $M_{\text{Earth}} = 7.906 \times 10^{25} \text{ Gauss cm}^3$ )

While the size of a planetary magnetosphere depends on the strength of the planet's magnetic field, the configuration and internal dynamics depend on the field orientation (illustrated in figure 8) which is described by two angles: the tilt of the magnetic field with respect to the spin axis of the planet and the angle between this spin axis and the solar wind direction which is generally within a few degrees of radially outward from the Sun. Since the direction of the spin axis with respect to the solar wind direction only varies over a planetary year (many Earth years for the outer planets) and the planet's magnetic field is assumed to vary only on geological time scales, these two angles are constant for the purposes of describing the magnetospheric configuration at a particular epoch. Earth and Jupiter have both small dipole tilts and small obliquities. This means that the orientation of the magnetic field with respect to the solar wind does not vary appreciably over a planetary rotation period and that seasonal effects are small. Thus Earth and Jupiter have symmetric and quasi-stationary magnetospheres exhibiting only a small wobble due to their  $10^\circ$  dipole tilts.

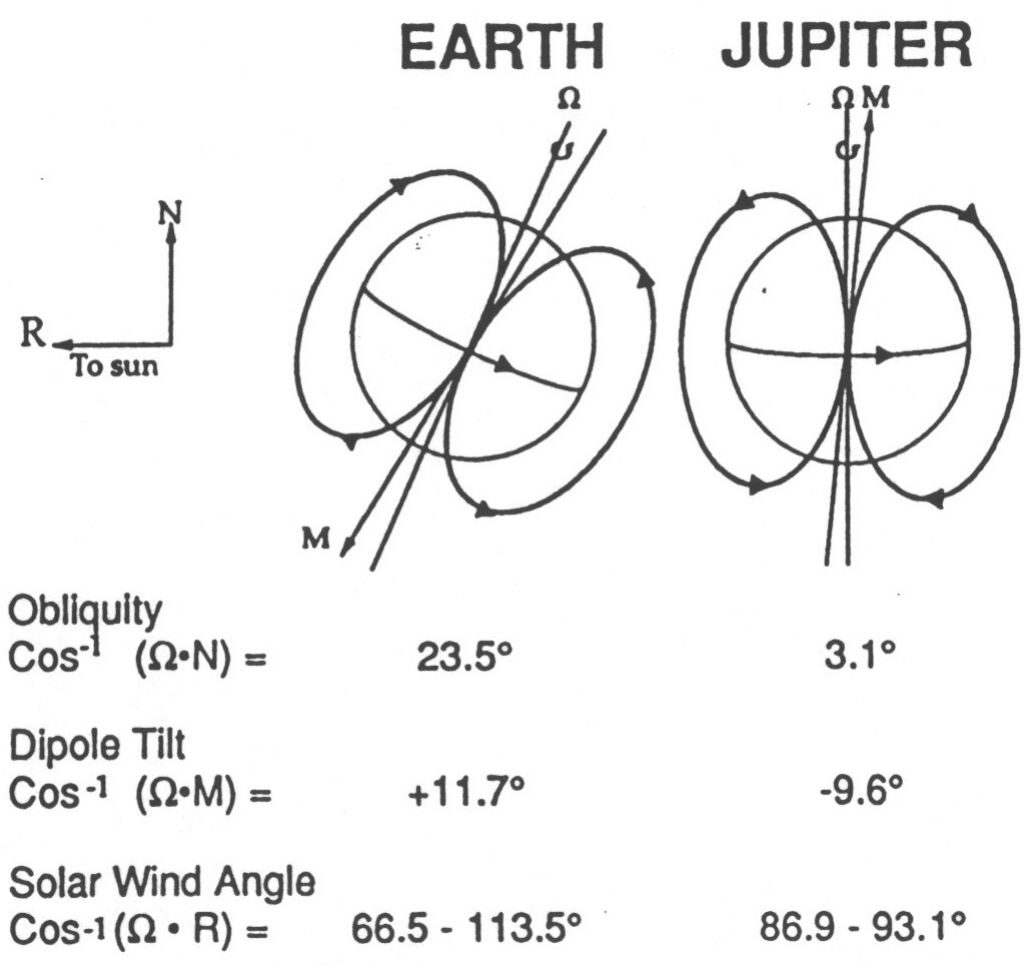
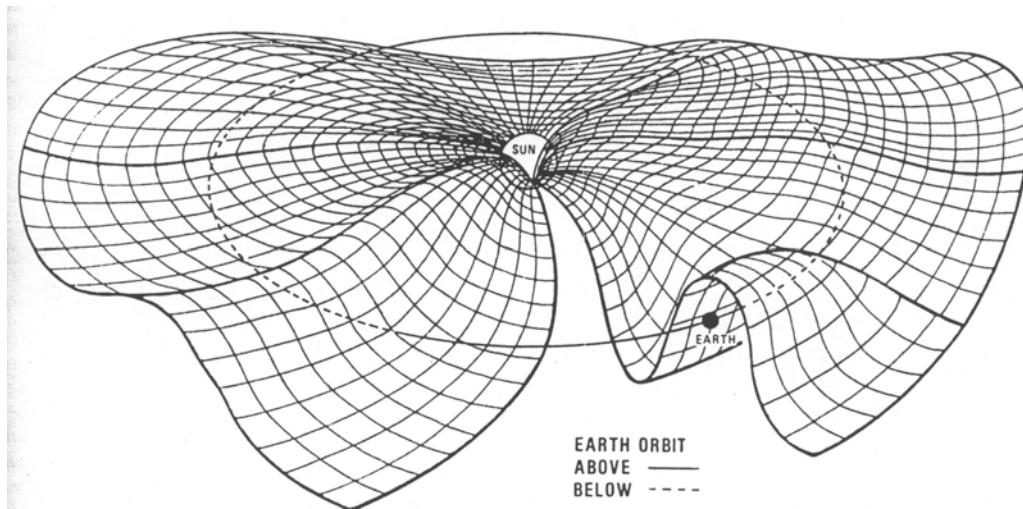


Figure 8 : Orientations of Earth and Jupiter and their magnetic fields.

### II.2.1 The interplanetary magnetic field

The expanding solar wind drags also the solar magnetic field outward, forming what is called the **interplanetary magnetic field (IMF)**. The region of space in which this solar magnetic field is dominant is called the heliosphere. Although the solar wind moves out almost radially from the Sun, the rotation of the Sun gives the magnetic field a spiral form (garden hose effect). At the orbit of the Earth the angle between the field lines and the radial direction is about 45 degrees. Furthermore, sectors (typically four) with alternating inward and outward directed magnetic fields can be identified. These sectors are well illustrated by the wavy structure of the heliomagnetic current sheet due

to current sheet's inclination (figure 9) to the rotational equator of the Sun.



**Figure 9** : Wavy structure of the heliomagnetic current sheet due to current sheet inclination to the rotational equator of the Sun.

## II.2.2 Magnetic Reconnection

In a plasma, **magnetic reconnection** (or merging) is the process by which plasma particles riding along two different field lines can be made to share the same field line. The basic idea behind reconnection is that two (partly) antiparallel magnetic field lines can, when meeting, merge together and produce two topologically totally different field lines. For instance, following reconnection, solar wind particles on an interplanetary field line, and magnetospheric ones on a field line attached to Earth, may find themselves sharing the same "open" field line, which has one end anchored on Earth and the other extending to distant space.

Reconnection is thought to be the main link in the solar wind - magnetospheric coupling process. It is the main process that transports mass, momentum and energy from the solar wind into the magnetosphere, and it drives the large scale magnetospheric convection (figure 10).

Magnetic reconnection can occur when plasma flows through a neutral point or a neutral line at which the intensity of the magnetic field is zero and its direction is not defined. It is an important concept in the theories of energy transfer from the solar wind to the

magnetosphere and of energy release in substorms.

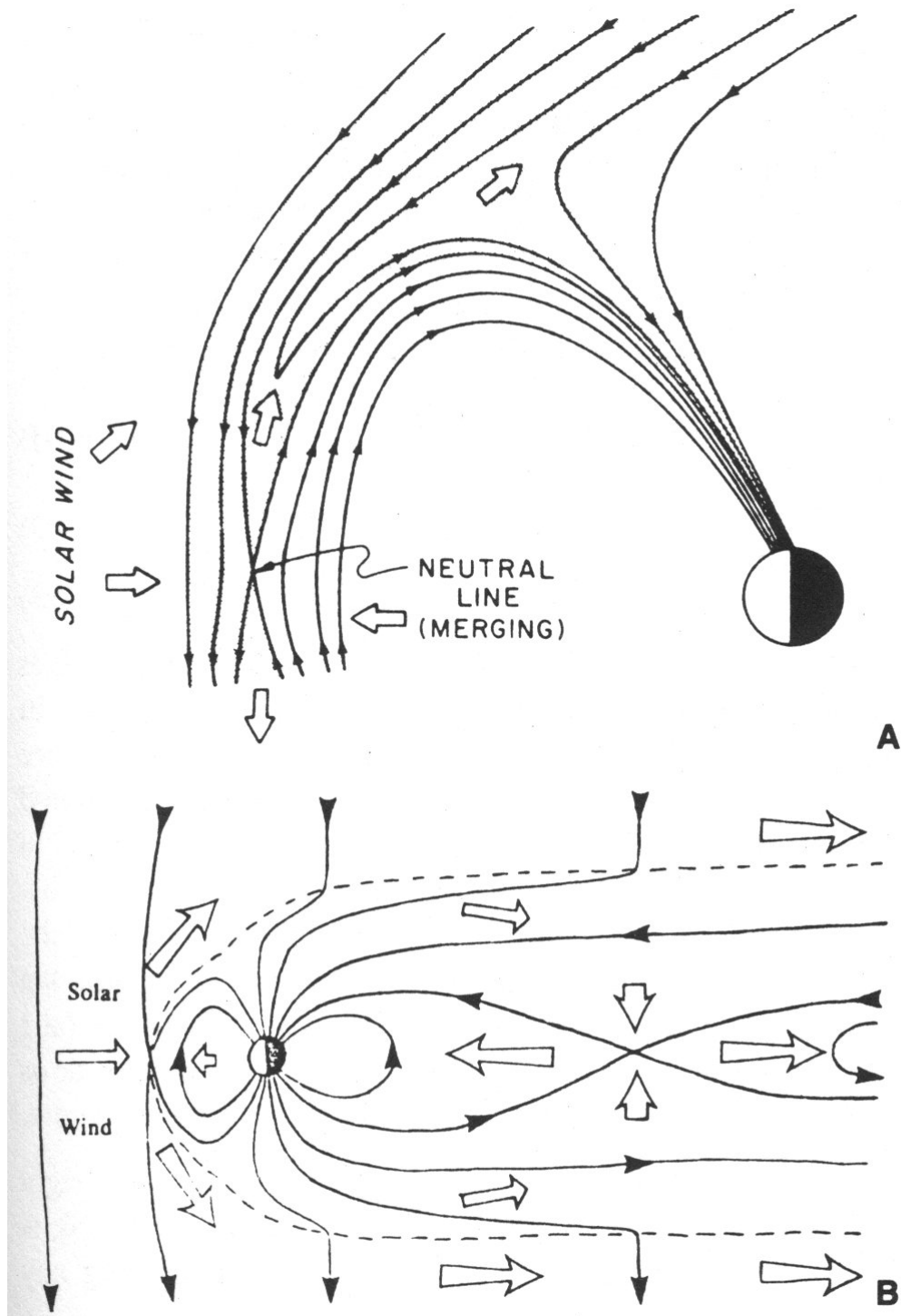


**Figure 10** : (A) Magnetic field topology in the merging region of an open magnetosphere. Large arrows indicate plasma flow direction and arrows on field lines show field line direction. (B) The dashed line represents the magnetopause boundary. The large arrows show the convection system set up inside the magnetosphere by magnetic reconnection.

## II.2.3 Magnetospheric electric fields and convection

The magnetospheric configuration is generally well described by magnetohydrodynamics (MHD) in which the magnetic field can be considered to be frozen into the plasma flow (i.e. the solar magnetic field is carried along within the plasma virtually unchanged) with an infinite conductivity.

There are two main sources of magnetospheric electric fields. The first one is the solar wind related, dawn-to-dusk directed convection field, and the other is the corotation electric field related to the rotation of the planet about its spin axis. The low energy particles move primarily under the  $\mathbf{E} \times \mathbf{B}$  drift, and are less affected by the gradient and curvature drifts which depend only on magnetic field. The energetic particles, following the magnetic drifts more readily, are also affected by the convection field.

### II.2.3.1 The corotation field

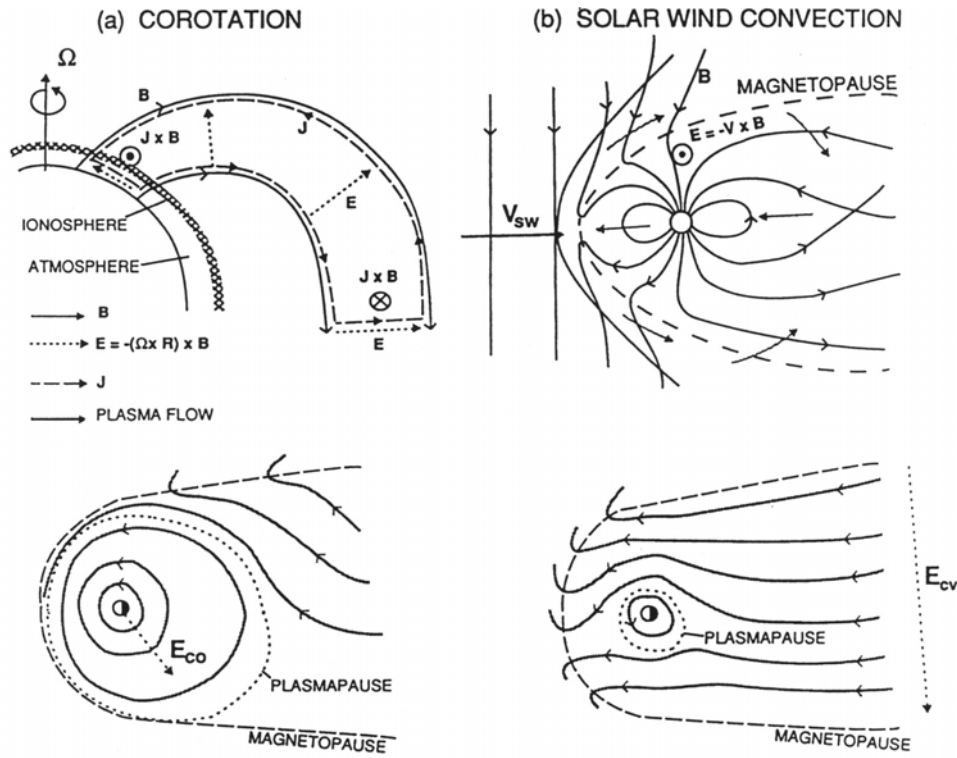


**Figure 11** : Large scale magnetospheric circulation driven by corotation (a) and the solar wind (b). Magnetic field lines (Upper right) are continuous dark arrows, the directions of plasma flow are shown with short arrows. The lower diagrams (views in the equatorial plane) show the plasma flow with continuous arrows.

It may be helpful to think of plasma in the magnetosphere as mass that is coupled by means of magnetic field lines to a giant flywheel (the planet) with the ionosphere acting as the clutch. For magnetospheric plasma to rotate with the planet, the upper region of the neutral atmosphere must corotate with the planet and must be closely coupled to the ionosphere by collisions. The rotation of Jupiter provides the dominant source of energy for the magnetosphere, particularly as much of the ionized material originates from the vicinity of Io and its torus. Newly created ions have to be accelerated (ion pick-up) to rotate with the magnetosphere by the imposition of torques which originate from the planetary ionosphere. The mechanism which will tap the rotational energy source is a field-aligned current system such as depicted in the left side of figure 11.

The electrical conductivity of the ionosphere  $\sigma^i$  is large so that in a corotating ionosphere (with velocity  $\mathbf{v}^i$ ) any horizontal currents (perpendicular to the local magnetic field) are given by Ohm's law,  $\mathbf{J}_{\perp}^i = \sigma_{\perp}^i (\mathbf{E}^i + \mathbf{v}^i \times \mathbf{B})$ . This ionospheric

(Pedersen) current is driven by friction between ions and neutrals. The transverse current flowing in the equatorial magnetosphere and closing the current loop transfers the angular momentum absorbed in the ionosphere to the magnetospheric plasma.

Just above the ionosphere, the conductivity perpendicular to the magnetic field in the (collision-free) magnetosphere,  $\sigma_{\perp}^i$ , is essentially zero. Moreover, the magnetospheric electric field  $\mathbf{E}^m$  in the corotating region is  $\mathbf{E}^m = -\mathbf{v}^m \times \mathbf{B}$  where  $\mathbf{v}^m$  is the magnetospheric plasma velocity. (For the corotating plasmasphere, the plasma is stationary in its local frame of reference and therefore  $\mathbf{E} = 0$ . However, to an observer on the planet, the plasmasphere plasma is kept in balance by an electric field which has to balance the Lorentz force or  $\mathbf{E}^m + \mathbf{v}^m \times \mathbf{B} = \mathbf{0}$ ).

Because plasma particles are far more mobile in the direction of the local magnetic field, the parallel conductivity  $\sigma_{\parallel}^i$  is large and the field lines can be considered to be equipotentials ( $\mathbf{E} \cdot \mathbf{B} = 0$ ). Thus the electric field in the magnetosphere can be mapped into the ionosphere (figure 11). There may exist conditions under which this approximation does not hold, such fields ( $E_{\parallel} \neq 0$ ) are obviously of great interest since they are capable of accelerating charged particles directly. Because the ionosphere is relatively thin, the electric field  $\mathbf{E}^m$  just above the ionosphere is the same as  $\mathbf{E}^i$  so that we can write  $\mathbf{J}_{\perp}^i = \sigma_{\perp}^i (\mathbf{v}^i - \mathbf{v}^m) \times \mathbf{B}$ . The condition for corotation of the magnetospheric plasma is that the ratio  $J^i / \sigma^i$  be sufficiently small so that

$\mathbf{v}^m = \mathbf{v}^i = \boldsymbol{\Omega} \times \mathbf{r}$  where  $\boldsymbol{\Omega}$  is the angular frequency of corotation and  $\mathbf{r}$  is the radial distance. For a dipolar magnetic field that is aligned with the rotation axis  $B = B_0 / r^3$  and the corotational electric field (in the equatorial plane) is therefore radial with magnitude  $E_{co} = \boldsymbol{\Omega} B_0 / r^2$ .

Large ionospheric conductivities facilitate corotation. The large  $\sigma_{\parallel}^m$  also means that any currents in the magnetosphere that result from mechanical stresses on the plasma are directly coupled by **field-aligned currents** (Birkeland currents) to the ionosphere. Thus corotation breaks down when mechanical stresses on the magnetospheric plasma drive ionospheric currents that are sufficiently large for the ratio  $J^i / \sigma^i$  to become significant.

### II.2.3.2 Magnetospheric convection field

We now consider how the momentum of the solar wind may be harnessed by processes occurring near the magnetopause where the external solar magnetic field interconnects with the planetary magnetic field. Figure 11 (right) shows that at the poles the planetary magnetic field lines are open to the solar wind. The solar wind drives a plasma flow across the polar caps and the field lines from the polar region move in the direction of the solar wind flow, being pulled by the solar wind over the poles and back into the extended magnetotail. Conservation of flux requires that field lines are further cut and reconnected in the tail.

The MHD condition of the field being frozen to the flow can be written as  $\mathbf{E} + \mathbf{v} \times \mathbf{B} = \mathbf{0}$  (for an observer on the planet), which allows the convection electric field (the electric field associated to the solar wind) to be written as  $\mathbf{E}_{cv} = -\eta \mathbf{v}_{sw} \times \mathbf{B}_0 / R_m^3$  (where  $\eta$  is the efficiency of the reconnection process in harnessing the solar wind momentum, 0.1 for the Earth, and where we have assumed a simple dipole field  $\mathbf{B} = \mathbf{B}_0 / r^3$ ). In simple magnetospheric models  $E_{cv}$  is assumed constant throughout the magnetosphere. The corresponding circulation is given by the  $\mathbf{E} \times \mathbf{B}$  drift,  $\mathbf{v}_{cv} = \eta \mathbf{v}_{sw} (r/R_m)^3$  where  $R_m$  is the magnetopause distance. After being carried tailward at high latitudes, the plasma drifts towards the equatorial plane and eventually returns in a sunward flow to the dayside magnetopause.

Comparison of the corresponding electric fields indicates whether the magnetospheric circulation is driven primarily by the solar wind or by the planetary rotation. Since  $E_{co}$  is proportional to  $r^{-2}$  and  $E_{cv}$  proportional to  $r^{-3}$ , corotation is expected to dominate within a short distance from the planet while the solar wind driven convection dominates outside a critical distance  $R_c$ . It can be shown that magnetospheres of rapidly rotating planets with strong magnetic fields (such as Jupiter's) are dominated by rotation while the solar wind controls the plasma flow in smaller magnetospheres of slowly rotating planets (such as the Earth's).

## II.2.4 The Earth magnetosphere

The following section is a brief description of the Earth's magnetosphere (figure 12) for the purpose of comparison with the Jovian magnetosphere. The Earth

has a region close to the planet where the plasma corotates with the planet. The magnetic field lines remain closed, and large densities of plasma can accumulate over time. This is the **plasmasphere**. At a distance of about  $4 R_E$  there is a sharp boundary, the **plasmopause**, where the plasma density drops abruptly (from  $\sim 100 \text{ cm}^{-3}$  to  $\sim 1 \text{ cm}^{-3}$ ) and outside of which the solar-wind-driven circulation is sunward at the equator and antisunward at high latitudes. This means that a large proportion of the Earth's magnetosphere is strongly influenced by the solar wind and will respond to changes in solar wind conditions. In particular, the dayside reconnection rate and the convection electric field vary with the orientation of the interplanetary magnetic field, with maximum reconnection occurring when the planetary and solar magnetic fields are oppositely-directed. Reconnection is not always the dominant mechanism. Under some interplanetary conditions, the convection electric field is thought to result from a purely viscous interactions (which must involve collision-free, micro-scale processes and is poorly understood) between the solar wind and the magnetospheric plasma. For a given solar wind condition, however, the reconnection on the dayside magnetopause appears to be quasi-steady. In contrast, the kinetic energy of the solar wind that is stored in the tension of stretched magnetic field lines in the tail is episodically violently released in what are known as magnetospheric substorms. Oppositely-directed magnetic field lines are believed to reconnect in the center of the magnetotail and the plasma in the reconnected flux tubes is accelerated away from the reconnection point ( $10\text{-}15 R_E$ ).

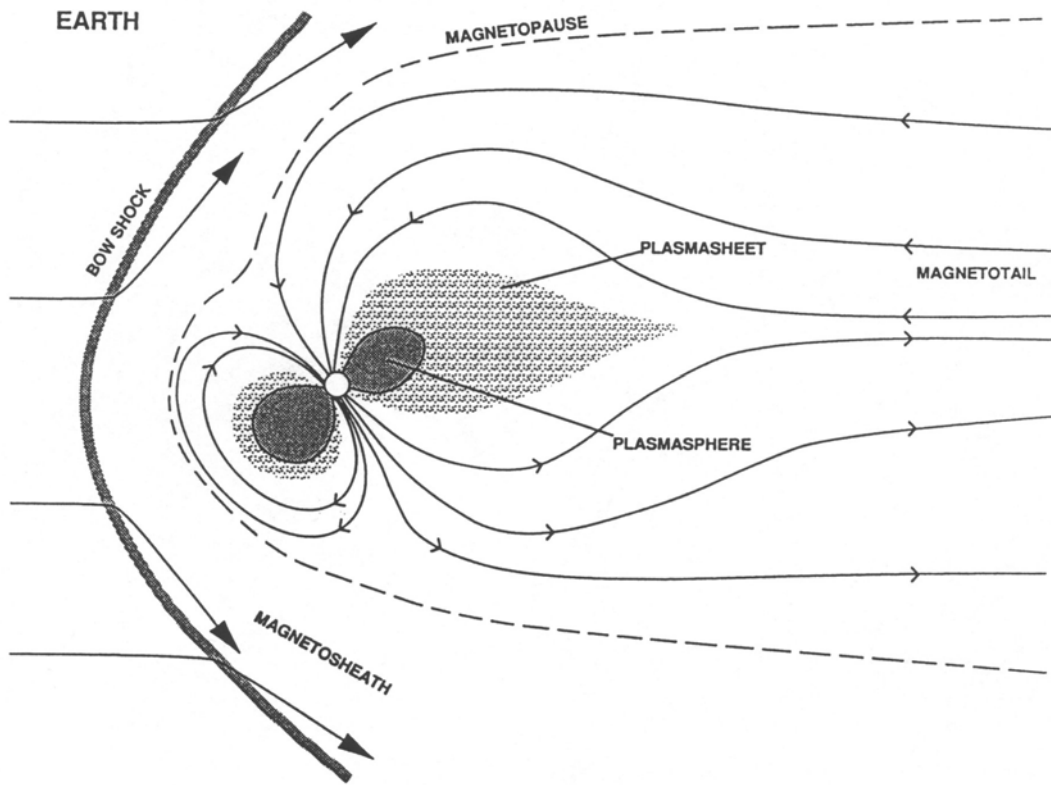


**Figure 12** : The magnetosphere of the Earth.

## II.2.5 The Jovian magnetosphere

Jupiter is a huge object about 1000 times the volume of the Sun with a tail that extends at least 6 AU in the antisunward direction, beyond the orbit of Saturn. If the Jovian magnetosphere were visible from Earth its angular size would be twice that of the Sun even though it is at least four times farther away.

It has become customary to describe the Jovian magnetosphere in terms of three principal regions. The **inner magnetosphere** is the region where the magnetic field generated by currents flowing in the interior of the planet dominates, and contributions from current systems external to the planet are not significant. This region extends from the planetary surface to a distance of approximately  $6 R_J$  (Jovian radii), the orbit of Io. Outside of this region, the effects of an azimuthal current sheet in the equatorial plane produce a significant perturbation, leading to the stretching of the magnetic field lines in the radial direction. The region in which the equatorial current flows is denoted as the **middle magnetosphere**, and extends from  $\sim 6 R_J$  to approximately  $30\text{-}50 R_J$  where the local-time asymmetry due to the magnetopause and tail current systems become important. Inside this region the Jovian internal field is adequately represented as a tilted dipole field, and the magnetic field of the magnetopause and tail currents is small. In the **outer magnetosphere**, the cylindrical symmetry prevalent in the inner regions disappears due to the effects of the solar wind interaction with the magnetosphere. We thus have to differentiate between a "sunward side" outermagnetosphere and a "magnetospheric tail" extending away from the planet in the antisolar direction. The field has a large southward component and exhibits large temporal and/or spatial variations in magnitude and direction in response to changes in solar wind pressure. This region extends from the magnetopause boundary to approximately  $30\text{-}50 R_J$ , and includes the extensive Jovian magnetic tail.

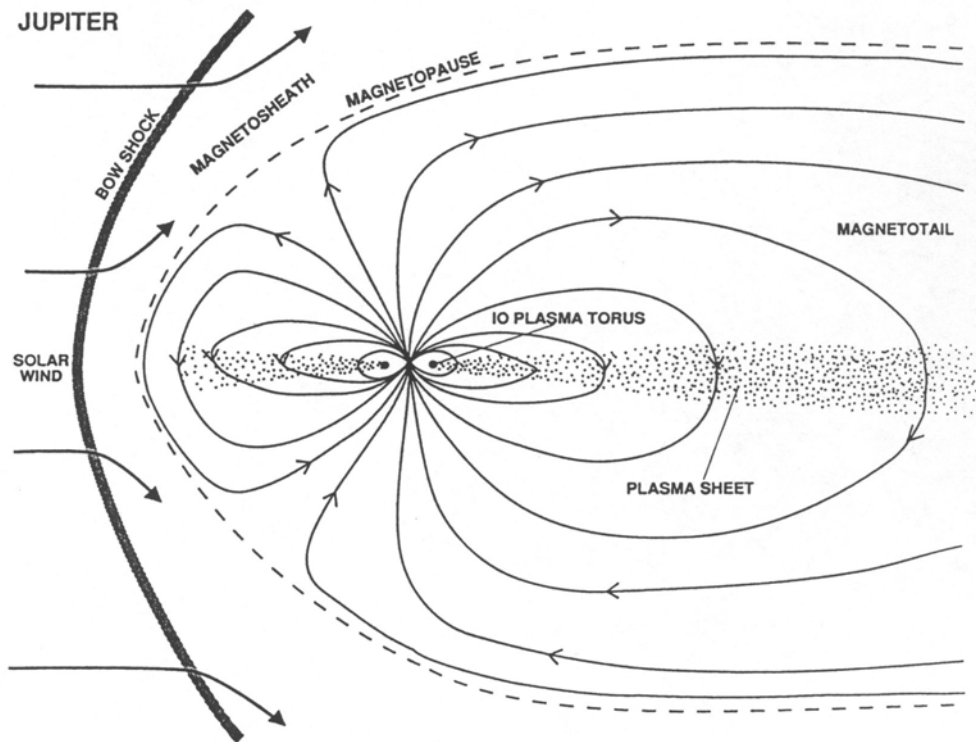


**Figure 13** : The magnetosphere of Jupiter.

The *Voyager* Plasma Science instruments confirmed that the bulk motion of the plasma in the magnetosphere of Jupiter is largely azimuthal but measured significant deviations from rigid rotation. The magnetosphere of Jupiter is sketched in figure 13, the plasma flow was measured to be within 1 % of rigid corotation in the inner region at  $5 R_J$ . At larger distances, the *Voyager* observations confirmed that the angular momentum required to accelerate plasma to higher azimuthal velocities in order to maintain corotation with the planet generates an increasing strain on the frictional coupling between the Jovian ionosphere and neutral atmosphere and the flow lags behind corotation. McNutt *et al.* (1979) reported departure from corotation occurring from about  $12 R_J$  outwards with the azimuthal flow tending towards a constant speed of about  $200 \text{ km s}^{-1}$  beyond  $20 R_J$ . The large plasma source near Jupiter's satellite Io and the subsequent outward transport of this material are the source of the mechanical stresses in the magnetosphere causing departure from corotation.

In order to estimate the plasma flow in the magnetotail, Vasyliunas (1983) proposed a planetary wind model (figure 14) in which at some distance from the planet the kinetic energy of the rotational flow becomes greater than the energy of the magnetic field, i.e.

when the corotational speed equals the local Alfvén speed. The flow then “breaks” and reconnects the magnetic field. Material is then disconnected from Jupiter and flung down the tail.

In the afternoon sector, the corotational flow is expected to approximately match the magnetosheath flow in both magnitude and direction. Therefore, little interaction is expected between the interior and exterior flows across the magnetopause (though to date no spacecraft have crossed the afternoon magnetopause and actually measured the flow). In the morning sector, the corotation flow is oppositely directed to the solar wind plasma just outside the magnetopause. Strong shears in plasma flow lead to instabilities and probably to localized acceleration processes.

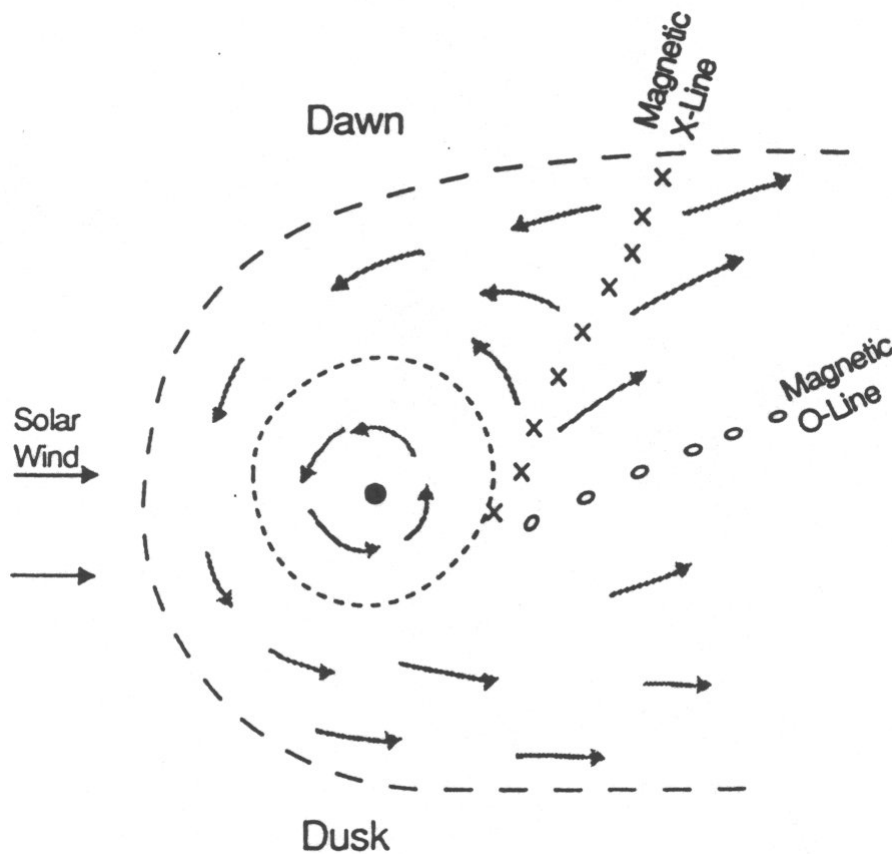


**Figure 14** : Model for the configuration of the magnetotail of a rotation-dominated magnetosphere such as Jupiter.

### II.2.5.1 Thermal plasma characteristics

It is rather misleading to describe a magnetosphere as an empty cavity from which the solar wind is excluded. Magnetospheres contain considerable amounts of plasma which have “leaked in” from various sources (table 4). First, the magnetopause is not entirely “plasma-tight.” Solar wind plasma enters through the polar cusp and, whenever the interplanetary magnetic field has a component antiparallel to the planetary field at the magnetopause, magnetic reconnection is likely to occur and solar wind plasma will leak into the magnetosphere. Secondly, although ionospheric plasma is generally cold and gravitationally bound to the planet, a small fraction has sufficient energy to escape up magnetic field lines and flow into the magnetosphere. Thirdly, the interaction of magnetospheric plasma with any natural satellites that are embedded in the magnetosphere can generate significant quantities of plasma.

	Earth	Jupiter
Maximum density (cm <sup>-3</sup> )	1 - 4000	> 3000
Primary sources	O <sup>+</sup> , H <sup>+</sup> (ionosphere)	O <sup>n+</sup> , S <sup>n+</sup> (Io)
Secondary sources	H <sup>+</sup> (solar wind)	H <sup>+</sup> (ionosphere)
Source strength (ions/s)	2x10 <sup>26</sup>	>10 <sup>28</sup>
(kg/s)	5	700

**Table 4** : Plasma characteristics of the Earth and the Jovian magnetospheres.

At the same time, the planetary magnetosphere supports a variety of plasma waves which have various energy sources and cover a wide range of frequencies. Interactions between these waves and particle populations are thought to be responsible for thermalizing the bulk of the plasma as well as accelerating or scattering particles at higher energies.

In 1979 the *Voyager I* spacecraft confirmed that Io is the major source of plasma in the Jovian magnetosphere. Io’s volcanoes are believed to be responsible for a tenuous ( $\sim 10^{-9}$  bar) atmosphere mostly composed of SO<sub>2</sub>, either via direct venting or sublimation of volcanic frosts deposited on the surface. The atmosphere is probably patchy and is expected to vary with Io’s volcanic activity. Io orbits well inside Jupiter’s magnetosphere, embedded in the corotating magnetospheric plasma and high fluxes of energetic particles which collide with atmospheric constituents, heat Io’s upper

atmosphere, sputter energetic atoms and molecules, resulting in the formation of an extended neutral corona around Io (the **neutral cloud**). Presumably, the main constituents of this sputter-corona are products of SO<sub>2</sub> dissociation.

### II.2.5.2 The Io plasma torus

As the *Voyager* spacecraft approached Jupiter the ultraviolet spectrometer detected powerful emission ( $3-6 \times 10^{12}$  Watts) from sulfur and oxygen ions in a toroidal region encompassing the orbit of Io. When the *Voyager 1* spacecraft flew through the plasma torus, the Plasma Science instrument made local measurements of both the electrons and the various ionic species: O<sup>+</sup>, O<sup>2+</sup>, S<sup>+</sup>, S<sup>2+</sup>, S<sup>3+</sup> and an ion with a mass/charge ratio of 64, which could be SO<sub>2</sub><sup>+</sup> and/or S<sub>2</sub><sup>+</sup>. Observations confirm that the distribution of plasma along magnetic field lines is limited by the strong centrifugal forces which tend to confine the plasma to the region of the field line most distant from Jupiter's spin axis -the centrifugal equator.

Figure 15 shows a model of the Io plasma torus surrounding Jupiter at about 6 R<sub>J</sub>. The figure also shows the Jovian rotational axis vector and the tilted magnetic axis. This tilt is responsible for a wobbling motion of the plasma torus.

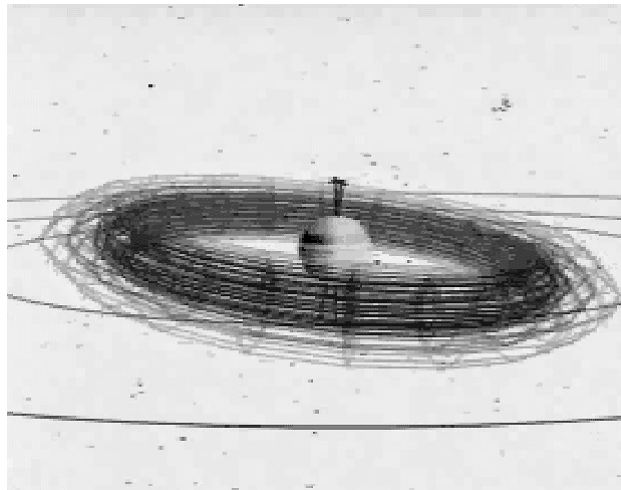


**Figure 15** : Model of the corotating Io plasma torus.

### II.2.5.3 The Io-plasma interaction

Io's motion in the planetary magnetic field might cause the satellite to act as a

**unipolar inductor.** The interaction model is represented in figure 16. The strong electrodynamic interaction with the corotating Jovian magnetosphere and Io leads to field-aligned currents connecting Io with the Jovian ionosphere. The corotational electric field developed by the relative motion between Io and the magnetic field lines swept past the satellite induces a potential difference of approximately 500 kV between the outer and inner faces of this satellite. This potential causes currents to flow from Io towards the Jovian ionosphere, both northward and southward, along the outer portion of the magnetic flux tube linking the satellite to the ionosphere. Return currents flow along the inner portions of the flux tube towards Io. In this simple model, the circuit is closed through the Jovian and Ionian ionospheres.

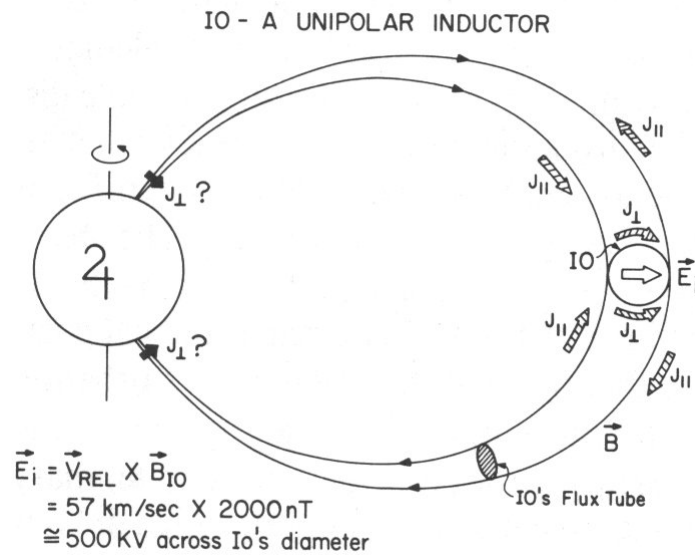


**Figure 16** : Io as a unipolar inductor.

It has been suggested that large field-aligned currents connecting the satellite to the planet are carried by large amplitude Alfvén waves that propagate along the magnetic field to the ionosphere of Jupiter where they form localized auroral UV and IR emissions, the so called Io flux tube footprint (IFT) emission. The feature is observed to move across Jupiter's disc in quasi-concert with Io's orbital motion , tracing out a path around each magnetic poles. The perturbations of the magnetic field and plasma flow that were measured in the vicinity of Io when *Voyager I* passed beneath the satellite confirmed the theoretical expectations of a strong interaction between Io and the magnetospheric plasma as further analysis indicated that an Alfvénic disturbance was

radiated by Io, carrying a  $10^6$  A field-aligned current towards the ionosphere of Jupiter.

#### II.2.5.4 The plasma sheet

While the high plasma densities ( $>1000 \text{ cm}^{-3}$ ) are confined to a toroidal region within 1  $R_J$ , of Io's orbit, the iogenic material extends out to at least 40  $R_J$ , forming a thin ( $< 5 R_J$  thick) sheet of warm (10's of eV) plasma with densities decreasing to a few per  $\text{cm}^3$  by 20  $R_J$  and dominated by sulfur and oxygen ions. This is the **magnetodisc**, where the centrifugal forces on the corotating plasma stretch out the magnetic field at the equator. In addition to the warm iogenic plasma there is a hot ( $\sim 30 \text{ keV}$ ) thermal plasma (with Maxwellian distributions) in the middle magnetosphere, beyond 10  $R_J$ . This hot plasma has an energy density greater than the local magnetic field and inflates the magnetosphere, making it flatter at the poles and more compressible than a vacuum dipole magnetosphere. The magnetodisc is characterized by a strong ring current known as the **azimuthal current sheet**. Once the plasmas are injected in the vicinity of Io, they start to drift around in azimuth by means of the combined effects of magnetic gradient and field curvature drifts, and the corotational electric drift. The energy dependent magnetic gradient drift of the electrons has a direction that opposes the more rapid electric corotational field, while for ions, the gradient drift augments the corotational drift. This axisymmetric current is flowing in the vicinity of the magnetic equatorial plane. The ring current is an essential feature of the Jovian magnetosphere. In the middle magnetosphere the magnetic field is dominated by the external current sheet. The electromagnetic force associated with current is balancing a combination of centrifugal and hot plasma pressure forces.

The current flowing in the Earth plasma sheet is different from the Jovian current sheet in that the Earth plasma sheet current (also referred as the **cross-tail current**) is entirely driven by magnetospheric convection. It has already been seen that this convection gives rise to a convection electric field oriented from dawn to dusk. The resulting cross-tail current flows across the plasma sheet from dawn to dusk.

### II.2.5.5 Energetic particle population

All magnetospheres have substantial populations of particles with energies well above the thermal population, at keV-MeV energies. These particles are largely trapped by the strong planetary magnetic field in long-lived radiation belts.

Energetic particles were possibly "captured" from the external medium, since the interplanetary medium includes energetic particles of solar and galactic origins. For giant planets, observed high fluxes are hard to explain without additional internal sources. Compositional evidence also implies that some fraction of the thermal plasma is accelerated to high energies, either by tapping the rotational energy of the planet, in the case of Jupiter, or by processes in the distorted magnetic field in the tail, in the case of Earth.

Schematically, in the case of Jupiter, the low energy plasma from the various sources (solar wind, high latitude planetary ionosphere, Io and its torus), primarily consisting of electrons, protons and heavy sulfur and oxygen ions diffuses outwards under the effects of centrifugal and plasma pressure gradients, toward the magnetotail where they are accelerated to MeV energies or more. The resulting energetic particles diffuse inwards again under instabilities driven by pressure gradient until they approach Io and its high density torus (see figure 17). In the vicinity of this region most species disappear from the magnetosphere. The loss mechanisms are not well understood. There is a general agreement that most loss occur towards the atmosphere along magnetic field lines by wave-particle interaction (pitch angle scattering) where they can excite auroral emission and deposit large amounts of energy.

Particle drifts occurring in a nonuniform magnetic field lead to ions and electrons drifting in opposite directions around the planet, producing an azimuthal electric ring current (the magnetodisc of Jupiter). If the energy density of the energetic particle populations is comparable to the magnetic field energy (remember that the ring current drift velocity is proportional to  $mv_{\parallel}^2$ ), then the ring current produces a magnetic field that significantly perturbs the planetary magnetic field. This is the case for Jupiter, where the high particle pressures inflate and stretch out the magnetic field and generate a strong ring current in the magnetodisc.

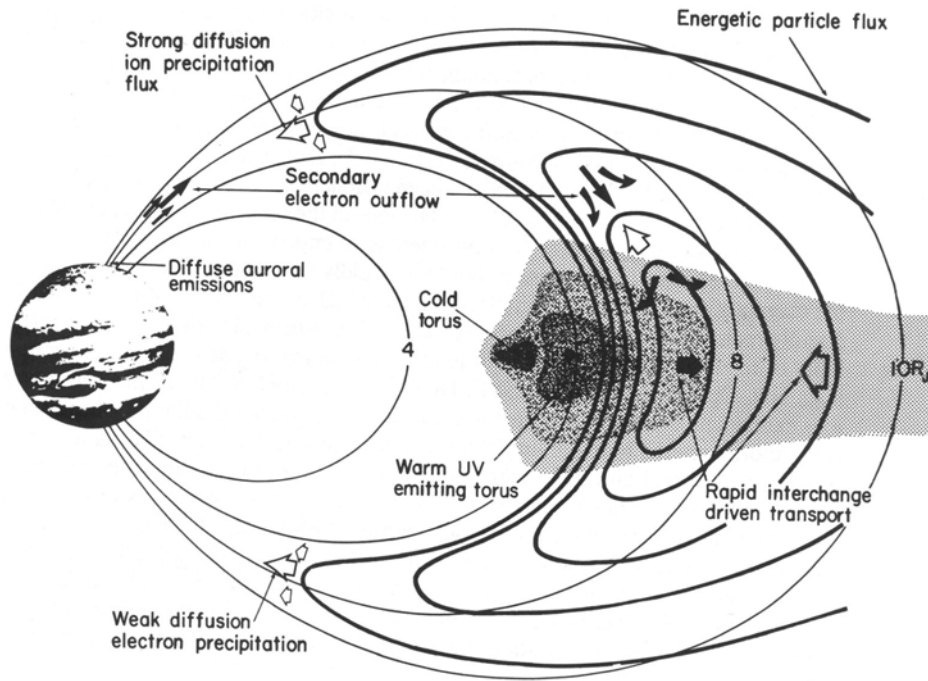


**Figure 17** : A schematic view of physical processes associated with the Io plasma torus.

## II.2.6 Jovian magnetospheric models (VIP4, GSFC-O6)

The details of a planet's magnetic field are determined by fitting magnetometer data obtained along spacecraft trajectories with a spherical harmonic expansion model of the magnetic field.

### II.2.6.1 The VIP4 model

Connerney et al. (1998) obtained a spherical harmonic model of the planetary magnetic field of Jupiter from *in-situ* magnetic field measurements and remote observations of the position of the foot of the Io flux tube in Jupiter's ionosphere. As already discussed, the Io flux tube (IFT) footprint locates the ionospheric footprint of field lines traced from Io's orbital radial distance in the equator plane ( $5.9 R_J$ ). The IFT footprint is a valuable constraint on magnetic field models, providing "ground truth" information in a region close to the planet and thus far no sampled by spacecraft. The magnetic field is represented by a spherical harmonic expansion of degree and order 4

for the planetary ("internal") field and explicit model of the magnetodisc for the field ("external") due to the distributed currents. The observed path of the IFT footprint serves as a fiducial marker; it provides an unambiguous reference on Jupiter's surface through which magnetic field lines with an equatorial crossing distance of 5.9  $R_J$  must pass.

Connerney *et al.* (1998) assume that a spherical harmonic expansion to degree and order 3 or 4 is sufficient to represent the internally generated planetary magnetic field over the radial distance spanned by the observations. The resulting magnetic field model is referred to as the "VIP4 model". The name recognizes the use of *Voyager*, Io footprint, and *Pioneer* observations (VIP) and the maximum degree and order (four) of the fit. The major advantage of the VIP4 magnetic field model relative to previous models is the use of the IFT footprint constraint. As a consequence, this model very accurately locates satellite magnetic footprints. Figure 18 shows the path of the Io footprint obtained with the VIP4 model. The ionospheric footprints of the Jovian satellites Europa (9.4  $R_J$ ), and Ganymede (15  $R_J$ ), and the footprint of the equatorial region at 30  $R_J$  (for the VIP4 and GSFC-O6 models), which has proven to be consistent with the size of the observed auroral oval, are also plotted in figure 18.

### II.2.6.2 The GSFC-O6 model

A previous spherical harmonic expansion of the planetary field to degree and order 6 (Connerney, 1992) was similarly combined with an explicit model of the magnetodisc to represent the field due to magnetodisc currents. The resulting Goddard Space Flight Center O6 (GSFC-O6) model was constrained with magnetospheric observations from *Pioneer 11* and *Voyager 1* but did not account for the location of the observed auroral emissions. The footprint of the equatorial region at 30  $R_J$  (for the VIP4 and GSFC-O6 models) is shown in figure 18.

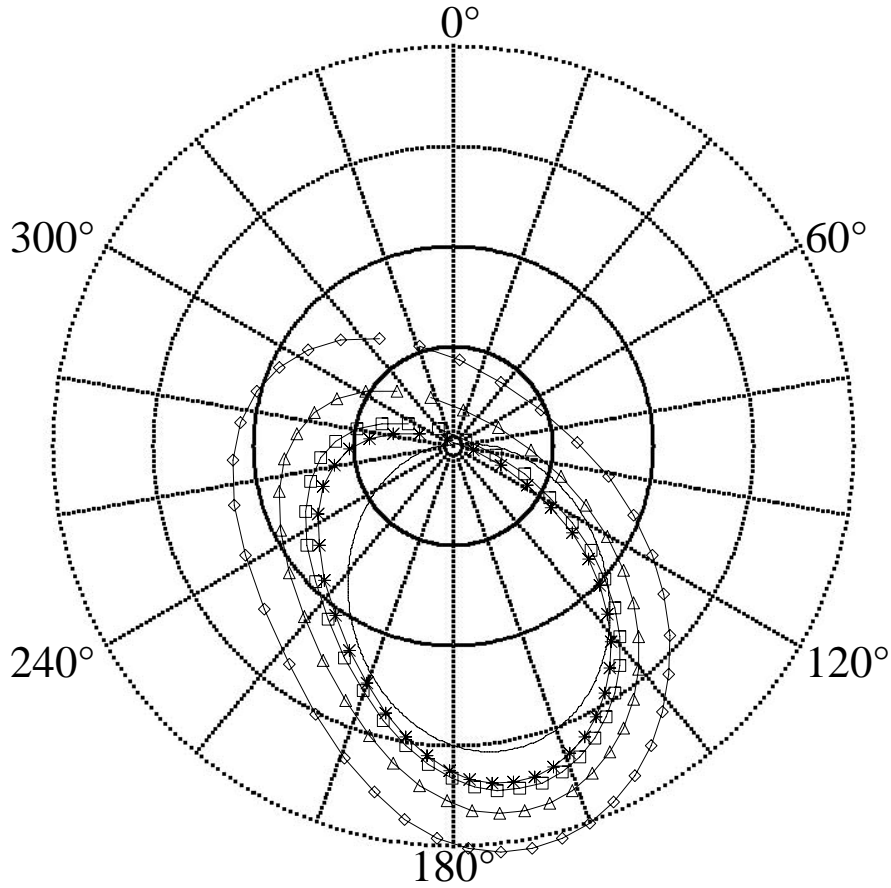


**Figure 18** :Footprints obtained with the VIP4 model in the northern hemisphere. \* : 30  $R_J$  (VIP4),  $\square$  : 15  $R_J$  (Ganymede),  $\triangle$  : 9.4  $R_J$  (Europa),  $\diamond$  : 5.9  $R_J$  (Io), continuous line : 30  $R_J$  (GSFC-O6).

## II.3 Origin of the auroral particles

### II.3.1 Introduction

High magnetic latitude auroræ have now been observed on all the solar system planets with an intrinsic magnetic field: Mercury, the Earth, Jupiter, Saturn, Uranus and Neptune. In each case, the auroral emissions are related to precipitation of energetic particles from the magnetosphere and/or from the solar wind. However the details of the auroral mechanisms are very poorly understood, with the exception of the Earth, for which there has been extensive studies, both of the auroral atmosphere and of the plasma population on the corresponding magnetic field lines. Particle precipitation (and auroræ) of various origins have been identified on Earth, representative of the dynamics of different regions of the magnetosphere. The two major processes are:

1. the diffuse auroral precipitation of energetic particles outside the plasmapause by wave-particle interaction and pitch-angle diffusion along magnetic field lines, producing a closed oval of moderate diffuse auroral emission and brightening with magnetic activity,
2. the impulsive precipitation of particles accelerated along field lines by parallel potential drops, leading to intense discrete auroral arcs during solar-wind driven "substorms".

Additional particle precipitation is observed at very high latitudes which results from mechanisms in the outer magnetosphere, and even from direct entry of solar wind particles in the cusps.

Similar mechanisms can in principle be expected in all magnetospheres. Nevertheless, different convection/corotation regimes, solar wind/magnetosphere coupling and plasma sources, result in different energetic particles dynamic, and are expected to favor differently one or the other of the precipitation processes at the various planets. In addition to Earth-like mechanisms, the abundance of hot plasma, the fast planetary rotation of Jupiter, and even the resulting stretched magnetosphere, might also give rise to instabilities, ultimately generating field-aligned currents and parallel particle acceleration in the middle magnetosphere.

### II.3.2 Diffuse and discrete auroræ on Earth

The presence of diffuse and discrete auroral structures in the Jovian atmosphere might be explained by analogy with the theories developed for the corresponding structures appearing in the Earth aurora (figure 19).

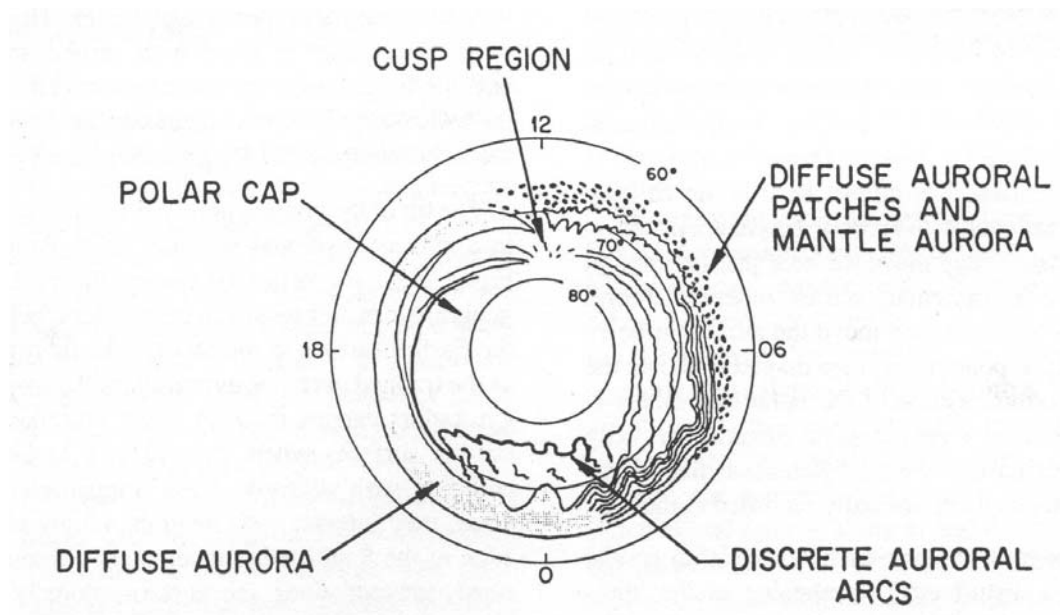


**Figure 19** : Principal phenomenological features in the high-latitude auroral zone during geomagnetic substorm.

As already mentioned the two major structures appearing in the Earth aurora are:

1. the **diffuse auroræ** which are formed by the precipitation into the atmosphere of geomagnetically trapped particles that are not accelerated by field-aligned electric fields. Diffuse auroræ tend to be broader in latitudinal extend and less spatially structured than discrete auroral arcs. Diffuse auroræ are found on the equatorward part of auroral oval, which is in the region of the so-called central plasma sheet precipitation most likely mapping to inner plasma sheet, where magnetic field is almost dipolar. The precipitating particles are drifting around Earth, electrons to the east and protons to the west. The strongest diffuse auroræ are found on the post-midnight sector, which indicates that they are produced mainly by electrons.
2. the **discrete auroræ** formed by the precipitation of electrons that have been accelerated by field-alligned electric fields. Such auroræ tend to be narrow in latitudinal extend (approximately one to tens of kilometers), but they can extend large distances in longitude around the Earth. They are located on the poleward edge of the auroral oval, in the region of the so-called boundary plasma sheet precipitation mapping to plasma sheet and its boundary layer.

### II.3.3 Magnetic field-aligned potential drops

Observation by low-altitude polar satellites of "inverted V" electron precipitation events suggests that electric fields parallel to the magnetic field lines (field-aligned fields or field-aligned potential drops) may occasionally exist on closed field lines in the Earth magnetosphere. In such an event (figure 20), as the spacecraft crosses high auroral latitudes, a band of electron precipitation is observed in which the mean energy rises from  $\sim 100$  to  $\sim 10^4$  eV and then decreases again, forming a spectrogram resembling an inverted letter V. This is often explained by a field-aligned configuration of electric equipotentials.

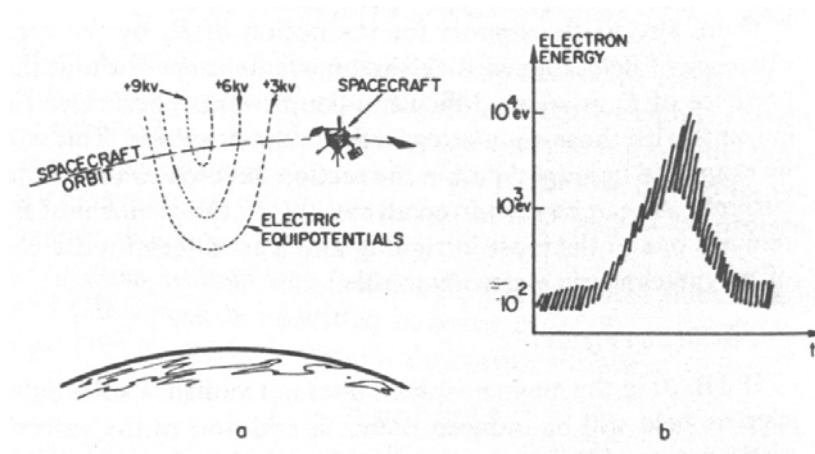


**Figure 20** : Schematic view of the electron spectrum observed during an inverted V event and its interpretation in terms of  $E_{\parallel}$ .

In the simplified discussion of magnetosphere-ionosphere coupling, we treated magnetic field-lines as perfect conductors ( $E_{\parallel}=0$ ). However significant potential drops are observed along auroral zone magnetic field lines. These potential drops usually occur in regions of strong upward field-aligned current. Downward field-aligned current can be carried relatively easily by upward flow of ionospheric electrons, which are available in great numbers and are easy for electric fields to move. However, upward field-aligned current requires either an upward flow of ionospheric ions, which is somewhat difficult because of their relatively large mass, or a downward flow of electrons from the plasma sheet, which can be difficult if the electrodynamically required current exceeds what can be supplied by electrons in the loss cone. Indeed the electrons that are not in the loss cone bounce back and forth between their mirror points, leading to a zero net current. Only the electrons that are "absorbed" by the atmosphere

,i.e. the loss cone electrons, can contribute an electric current.

If the field line has difficulty carrying the required amount of upward current, an electric field is created upward along the field line. The most dramatic effect of these potential drops is acceleration of downcoming plasma-sheet electrons to energies above those characteristic of normal plasmashet. These electrons are responsible for most bright auroral forms.

According to Lyons (1992) these potential drops could be directly linked to the magnetospheric convection field. The mapping of the magnetospheric electric field to the ionosphere gives an electric field reversal in the auroral zones lying near the ionospheric mapping of the open-closed field line boundary. This electric field reversal drives ionospheric currents, which leads to magnetic field-aligned currents. A field-aligned potential difference of 1-10 keV is required to maintain ionospheric current continuity, and it accelerates electrons downward, toward the atmosphere. The accelerated electrons impinge upon the atmosphere leading to discrete auroral arcs.

### II.3.4 Pitch angle scattering

It has already been mentioned that only particles within the loss cone can contribute to a field-aligned current, and that auroral emission results from the collisions of these particles with the atmosphere. The loss cone is very small along auroral magnetic field lines, so that only a small fraction of the magnetospheric electrons can contribute to the field-aligned current. However, a field-aligned potential difference that accelerates particles toward the atmosphere causes the particle  $v_{\parallel}$  to increase, which causes their pitch angle to become more field-aligned. This increases the number of particles in the loss cone and is called **pitch angle scattering**.

#### II.3.4.1 wave-particle interaction

Angular scattering can result from interactions with electromagnetic waves. An example of which is gyro (or cyclotron) resonance: radiation belt particle spiraling around a magnetic line of force will gyrate at a rate determined by the magnetic field strength, mass, and charge of the particle. An electromagnetic wave (with electric and magnetic vectors) also propagating along that field line will rotate according to its wave frequency. When both the sense of rotation and the rotation frequency match for both

wave and particle, the particle will be subject to an essentially constant "wave" field for the duration of the encounter. The particle can exchange energy with the wave through the electrical interaction and/or deflection can occur through the magnetic interaction. When the particle-wave interaction is primarily occurring via the magnetic wave vector the result is primarily angular scattering; this is the pure pitch angle scattering limit. Since the loss cone particles are lost from the radiation belts upon entering the atmosphere it is clear that interaction between energetic particles and plasma waves can significantly affect the energy of the trapped particle population and the angular distribution. When the strong diffusion limit is reached, the scattering mechanism is faster than the loss mechanism and the particle pitch angle distribution essentially remains isotropic.

#### II.3.4.2 The "windshield wiper" effect

In an asymmetric magnetosphere, pitch angle scattering gives rise to the so called "windshield wiper" effect. In this process, magnetically trapped charged particles are pitch angle scattered such that their mirror point is above the atmosphere at one magnetic longitude, but below it at another. If the rate of pitch angle scattering is less than the time required for the particles to circle the magnetosphere via  $\nabla\mathbf{B}$  drift, then the particle will drift into a region where it precipitates, and will be lost. If this mechanism takes place in the Jovian aurora, it would point to a particle source dominated by westward drifting electrons (20-30 eV) or by low energy (1 MeV) ions lagging behind the corotation velocity in the Io torus. The latter of these sources implies the existence of a secondary enhancement in the vicinity of  $0^\circ$  longitude due to eastward high energy ( $\geq 2 - 3$  MeV) ion infall. No indication of this secondary enhancement was observed by *Voyager*.

The concept of windshield wiper effect was tested by Prangé and Elkamsi (1991) who modeled the longitudinal distribution of auroral emission produced by particles azimuthally drifting in the Jovian magnetic field from a longitudinally uniform source. They predicted the possibility of a maximum in the flux precipitated in the north aurora due to electrons near  $\lambda_{\text{III}} = 180^\circ$ , close to where we observe the western limit of the discrete structures and a maximum due to ions near  $\lambda_{\text{III}} = 250^\circ$ . Prangé and Elkamsi (1991) also predicted that at high latitudes, the electron precipitation by pitch angle

diffusion should occur preferentially in the southern hemisphere, due to the relative longitudinal variation of the surface magnetic field strengths. In any case, this mechanism would only generate unstructured emission such as the diffuse aurora underlying the brighter structures but would not account for the discrete arcs observed at  $\lambda_{\text{III}} \geq 180^\circ$ .

In contrast, the narrow structure of the auroral arc observed with HST and the presence of very localized impulsive bright spots are more reminiscent of discrete auroral emissions triggered by field-aligned potential drops as in Earth's auroræ.

### II.3.5 The Jovian auroral field-aligned currents

The primary source of field-aligned currents at Earth is the solar wind-magnetosphere interaction. High-latitude current systems result in the imposition of solar-wind-induced magnetospheric circulation on the ionosphere. In the case of Jupiter, the much higher rotation speeds than those observed at Earth mean that the primary source of field-aligned currents is likely to be in the torques associated with the (partial) imposition of corotation on the magnetospheric plasma. Departures from corotation on any magnetic shell or set of shells will result in sheets of field-aligned currents being set up which may be quite localized in the local meridian direction transverse to the field, but which would vary little in the azimuthal direction. The resulting magnetic signature consists of gradients in the azimuthal component of the field (i.e. in the direction of rotation) across the ambient field direction in the meridian. Such current signatures were detected in the outer Jovian magnetosphere during the *Ulysses* flyby of Jupiter in 1992 beyond  $\sim 15 R_J$  and near the magnetopause. In particular, the *Ulysses* magnetometer observed changes of magnetic field associated with sheets of field-aligned currents near 15 and 20  $R_J$  in the dusk sector (Dougherty *et al.*, 1993). When mapped down along magnetic field lines, these currents were shown to close along the high latitude auroral arc in the Lyman  $\alpha$  images (Prangé *et al.*, 1994). They were also shown to originate from the boundary between open and closed field lines (50-60  $R_J$  in the equatorial plane).

## II.3.6 Evidence of solar wind driven auroras on Jupiter

HST WFPC2 images have demonstrated that the main auroral oval rotates with the magnetic field, implying that the main aurora maps to the corotating current sheet and is driven energetically by Jupiter's rotation and plasma processes inside Jupiter's magnetosphere. It is not known how the solar wind acts to modulate this energy release in the form of auroral emission. Recent STIS time-tag images have shown that rapid variations in Jupiter's aurora occur in the polar caps, where dramatic flaring on timescales of 1-10 s is commonly observed. These transient brightenings map to the dusk flank of the Jovian magnetotail near the magnetopause boundary (Waite *et al.*, 1999). The rapid variability of the STIS data suggests that reconnection events triggered by the passage of the solar wind and its embedded interplanetary magnetic field are the source of the auroral brightenings. However, this suggestion cannot be verified owing to the lack of solar wind data near Jupiter. By contrast, all other emissions (including the main oval and satellite footprint emissions) vary more slowly, on timescales of minutes to hours. One example is the "equatorward surge" of part of the oval as it moves from local morning to afternoon (Clarke *et al.*, 1996; Ballester *et al.*, 1996). The motion appears consistent with the dynamics of Jupiter's corotating magnetospheric plasma, which is compressed during local morning and expands in local evening. This may be related to the common appearance of the polar cap emissions, which tend to fill in the dusk side of the polar cap but not the dawn side. Occasional "dawn storms" emissions are observed along the main oval near local dawn which can brighten rapidly (Gérard *et al.*, 1994; Clarke *et al.*, 1998). These emissions remain fixed above magnetic local dawn, while the rest of the main oval emissions rotate with the planet. Their origin is not understood but their location fixed above local dawn requires a solar wind influence on Jupiter's magnetosphere.

The overall variability of Jupiter's aurora is very complex, resulting from the combined influence of internal, rotationally-driven magnetospheric processes and external, solar wind-interaction driven processes. While the former dominate magnetospheric dynamics and energetics, there is an increasing evidence that the solar wind has a substantial influence on auroral processes.

### III The Hubble Space Telescope

The Hubble Space Telescope (HST) is an observatory first dreamt of in the 1940s, designed and built in the 1970s and 80s, and operational only in the 1990s. It is the first and flagship mission of NASA's Great Observatories program. HST is a 2.4 m, f/24 Ritchey-Chretien telescope capable of performing observations in the visible, near-ultraviolet, and near-infrared (1150 Å to 1 mm). HST was launched on 25 April 1990 and placed into a low-earth orbit by the space shuttle, it is designed to be modular so that on subsequent shuttle missions it can be recovered, have faulty or obsolete parts replaced with new and/or improved instruments, and be re-released. HST is roughly cylindrical in shape, 13.1 m end-to-end and 4.3m in diameter at its widest point. It is in a 600 km high orbit and completes one navigation of the Earth every 96 minutes (see the orbital parameters in table 5).

Semimajor axis	6,971 km
Altitude	600 km
Rate of descent	0.4 km/year
Inclination	28.5°
Nodal period	96.4 minutes
Orbital precession time	56.0 days

**Table 5** : HST's orbital parameters (as in March 1996)

HST uses an elaborate scheme for attitude control to improve the stability of the spacecraft during observations. Maneuvering is performed by four of six gyros, or reaction wheels. Pointing can be maintained in this mode (coarse track) or the Fine Guidance Sensors (FGSs) can be used to lock onto guide stars (fine lock) to reduce the spacecraft drift and increase the pointing accuracy.

Power to the two on-board computers and the scientific instruments is provided by two 2.4 x 12.1 m solar panels. The power generated by the arrays is also used to charge six nickel-hydrogen batteries which provides power to the spacecraft during the roughly 25 minutes per orbit in which HST is within the Earth's shadow. The solar arrays are turned (and the spacecraft rolls its optical axis) so that they face the incident sunlight.

Communications with the satellite are maintained with the Tracking and Data Relay Satellites (TDRS) via HST's two high-gain antennas. Observations taken during the time when neither TDRS is visible from the spacecraft are recorded on tape recorder and dumped during periods of visibility. The spacecraft also supported real-time interactions with the ground system during times of TDRS visibility, enabling observers to make small offsets in the spacecraft pointing to perform their observations.

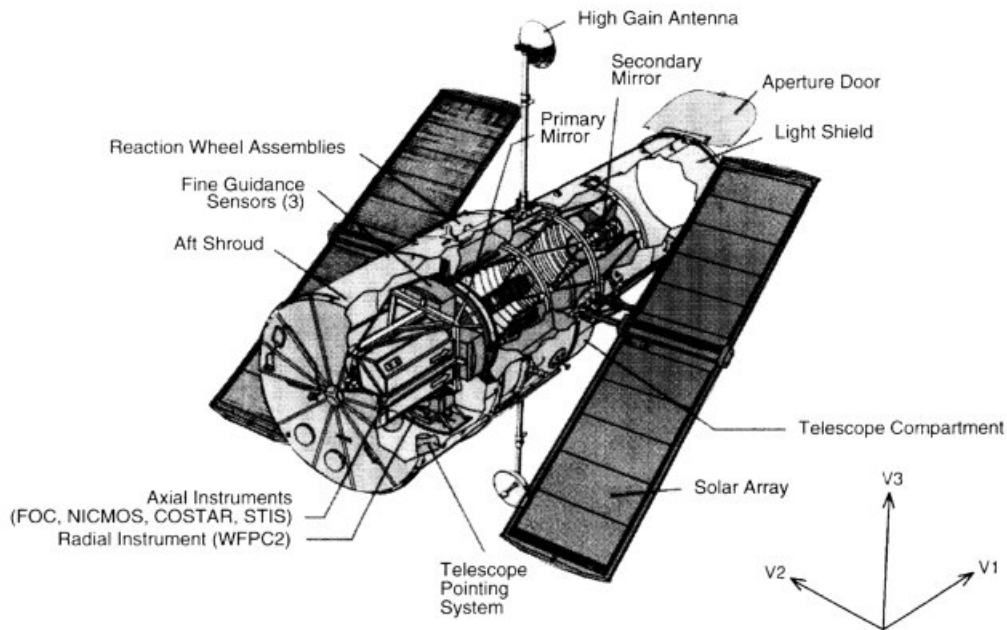


**Figure 21** : The Hubble Space Telescope

The mission was troubled soon after launch by the discovery that the primary mirror was spherically aberrated. In addition, problems with the solar panels flexing as the spacecraft passed from the Earth's shadow into sunlight caused difficulties with the pointing stability. Steps were taken to correct these problems, including replacement of the solar panels, replacement of the Wide Field and Planetary Camera with a second-generation version with built-in corrective optics, and replacement of the High-Speed Photometer with COSTAR (Corrective Optics Space Telescope Axial Replacement) to correct the aberration for the remaining instruments.

As shown in figure 21, HST's scientific instruments are mounted in bays behind the primary mirror. The Wide Field Planetary Camera 2 occupies one of the radial bays, with an attached 45 degree pickoff mirror that allows it to receive the on-axis beam.

Three scientific instruments (Faint Object Camera, Near Infrared Camera and Multi-Object Spectrometer, and Space Telescope Imaging Spectrograph) are mounted in the axial bays (figure 23) and receive images several arcminutes off-axis. During the servicing mission in December 1993, the astronauts installed COSTAR in the fourth axial bay (in place of the High Speed Photometer).

Because the primary mirror has about one-half wave of spherical aberration, the Optical Telescope Assembly did not achieve its design performance until after the December 1993 servicing mission. Table 6 gives a summary of the optical performance now being achieved.

Aperture	2.4 m
Wavelength coverage	1100 Å to 2.6 μm
Focal ratio (without COSTAR)	f/24
Plate scale (on axis without COSTAR)	3.58 arsec/mm
FWHM of WFPC2 images (at 6328 Å)	0.053 arcsec
WFPC2 encircled energy within 0.1" radius (at 6328 Å)	55-65%

**Table 6** : HST Optical Characteristics and Performance

### III.1 The Wide Field and Planetary Camera 2 (WFPC2)

The Wide Field and Planetary Camera 2 (WFPC2) is a two-dimensional imaging device covering a wavelength range from Lyman- $\alpha$  to about 1 μm. It is HST's only axis instrument and was built as a replacement for the first Wide Field and Planetary Camera (WF/PC). It includes built-in correction for the spherical aberration of the HST optical telescope assembly and was installed in HST during the first servicing mission in December 1993. The scientific objective of the WFPC2 is to provide photometrically and geometrically accurate images of astronomical objects over a relatively wide field-of-view, with high angular resolution across a broad range of wavelengths. The WFPC2 has three "wide-field" charge-coupled devices (CCDs), and one high-resolution (or "planetary") CCD. Each CCD covers 800 x 800 pixels and is sensitive from 1200 to 11,000 Å. All four CCDs are exposed simultaneously, with the target of interest being placed as desired within the field-of-view.

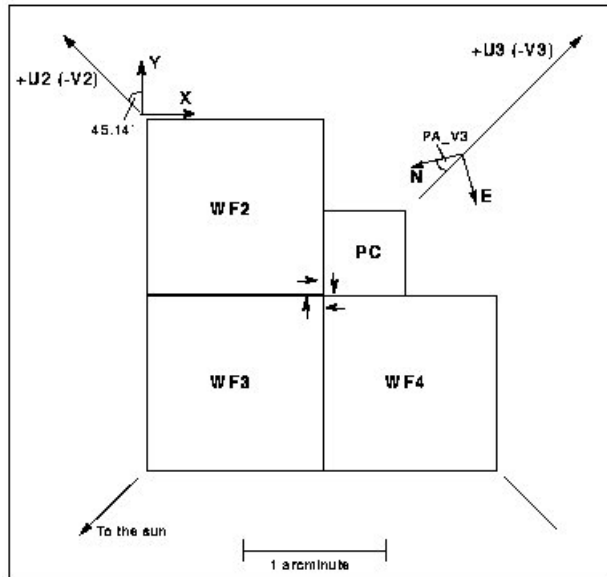


**Figure 22** : WFPC2 field-of-view projected on the sky.

The three Wide Field Camera (WF1, WF2, WF3) CCDs are arranged in an "L"-shaped field-of-view (figures 22 and 23) whose long side projects to 2.5', with a projected pixel size of 0.10". The optics of three of the four cameras are essentially identical and produce a final focal ratio of f/12.9, each CCD covers a 77"x77" field-of-view. The Planetary Camera (PC) CCD has a field-of-view of 35" x 35", a projected pixel size of 0.0455", and a focal ratio of f/28.3. A total of 48 spectral elements and polarizers are contained in an assembly of 12 filter wheels which may be inserted into the optical path.

The Wide Field Camera configuration provides the largest field-of-view available on HST, but undersamples the cores of stellar images; the Planetary Camera configuration samples the images better, over its smaller field-of-view.

The Planetary Camera provides a field of view sufficient to obtain full disk images of all planets except for Jupiter (about a quarter of the disk is imaged in the camera). However, even with this high resolution camera, the pixels undersample the point spread function of the telescope and camera optics by a factor of two at 5800 Å. The WF pixels are over a factor of two larger, and thus undersample the image by a factor of four at visual wavelengths.

A unique capability of the WFPC2 is that it provides a sustained, high resolution, wide field imaging capability in the vacuum ultraviolet. Broad passband far-UV filters, including a solar-blind Wood's filter (1200-1900Å), are included. Photometry at wavelengths short of 3000Å is improved through the control of internal molecular contamination sources and the ability to put the CCDs through warm-up decontamination cycles without loss of prior calibrations.

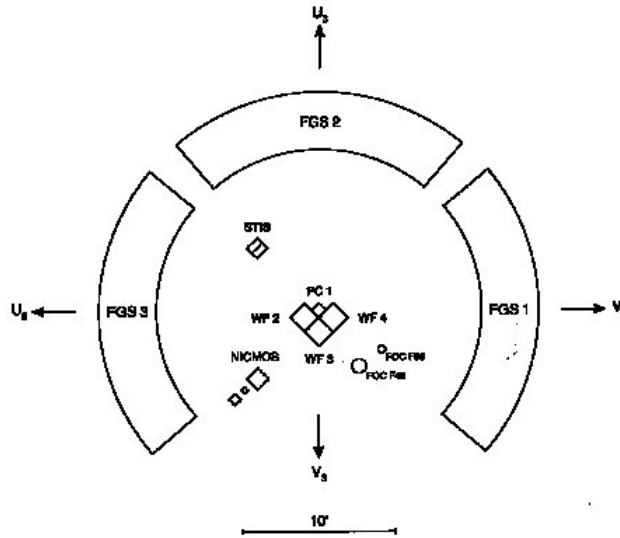


**Figure 23** : Effective aperture locations for the instruments available after the 1997 servicing mission. STIS now replaces GHRS.

## III.2 The Goddard High Resolution Spectrograph (GHRS)

The Goddard High Resolution Spectrograph (GHRS) was one of the first-generation science instruments aboard HST. It was removed from HST during the second servicing mission in February 1997, and replaced by the current Space Telescope Imaging Spectrograph (STIS) (a catastrophic failure occurred one week before the second servicing mission, resulting in the complete shutdown of the GHRS). The

GHR spectrograph was designed to provide a variety of spectral resolutions, high photometric precision, and excellent sensitivity in the wavelength range 1100 to 3200 Å. The GHR was a modified Czerny-Turner spectrograph with two science apertures (large: LSA, and small: SSA), two photon counting detectors (D1 and D2), several dispersers, and camera mirrors. There were also a wavelength calibration lamp, flatfield lamps, and mirrors to acquire and center objects in the observing apertures.

The GHR was installed as one of the axial scientific instruments (figure 23), with the entrance aperture adjacent to FGS 2 and FGS 3. With the installation of COSTAR, the entrance apertures were at the former position of the High Speed Photometer. The GHR had two science apertures, designated Large Science Aperture (LSA or 2.0) and Small Science Aperture (SSA or 0.25). The 2.0 and 0.25 designations were the pre-COSTAR size of the apertures in arcseconds. The post-COSTAR size of the LSA was 1.74 arcsec square and the SSA was 0.22 arcsec square. The separation of the two apertures was approximately 3.7 arcsec on the sky and 1.05 mm on the slit plate.

The dispersers were mounted on a rotating carousel, together with several plane mirrors used for acquisition. The first-order gratings were designated as G140L, G140M, G160M, G200M, and G270M, where "G" indicates a grating, the number indicates the blaze wavelength (in nm), and the "L" or "M" suffix denotes a "low" or "medium" resolution grating, respectively. The carousel also had an echelle grating. The higher orders were designated as mode Ech-A, and they were imaged onto D1 by the cross-disperser CD1. The lower orders are designated as mode Ech-B, and they are directed to D2 by CD2. Detector D1 was solar-blind, that is only far-ultraviolet photons (1060 to 1800 Å) could be detected. Use of the various gratings or mirrors in concert with the camera mirrors produced one of three kinds of image at the camera focus: 1) an image of the entrance aperture, which may be mapped to find and center the object of interest; 2) a single-order spectrum; or 3) a cross-dispersed, two-dimensional echelle spectrum.

# Part 1

## IV Simulation of the Morphology of the Jovian UV North Aurora Observed with the Hubble Space Telescope

This chapter is a transcription of a paper written by D. Grodent, G.R. Gladstone, J.-C. Gérard, V. Dols and J.H. Waite and published in *Icarus* **128**, 306-321 (1997)

### Abstract

A model simulating Earth views of UV auroral arcs and diffuse emissions in the Jovian north polar region is described. It assumes a Chapman profile of vertical brightness distribution and various horizontal structures. Simple geometric cases are described to illustrate the dependence of the altitude, atmospheric scale height and central meridian planetary longitude (CML) of an idealized auroral morphology seen from Earth orbit. The numerical simulation makes it possible to assess the importance of limb brightening and the contribution from high altitude auroral emission located behind the planetary limb. As an application of the simulation model, four images obtained with the Wide Field and Planetary Camera 2 (WFPC2) on board the Hubble Space Telescope are used to determine the characteristics of their auroral (discrete and diffuse) structures. The apparent brightness distribution along the arcs may only be reproduced if intrinsic longitudinal (or local time) variations are introduced, in addition to the path length effects of the viewing geometry. A composite average auroral distribution is built by mapping 10 WFPC2 images from the same dataset. It illustrates the dichotomy frequently observed between a narrow single structure arc at System III longitudes larger than  $180^\circ$  (or morning sector) and the multiple arc and broad diffuse

emission at longitudes less than  $180^\circ$  (or afternoon sector). It is shown that the equatorial auroral emission boundary is located between the  $6 R_J$  and the  $30 R_J$  magnetic field line footprints of the Goddard Space flight Center (GSFC)  $O_6$  model.

## IV.1 Introduction

The ultraviolet Jovian aurora was first observed with the ultraviolet spectrometer (UVS) on board the Voyager 1 and 2 spacecraft (Sandel *et al.*, 1979; Broadfoot *et al.*, 1979). It is characterized by strong emissions of the 121.6 nm Lyman- $\alpha$  line of atomic hydrogen and H<sub>2</sub> Lyman and Werner bands. A crude description of the morphology of the auroral emission was obtained by North-South scans of the UVS slit across the planetary disk (Broadfoot *et al.*, 1981; Herbert *et al.*, 1987). Analysis of these data concluded that the equatorward boundary of the auroral emission is defined by the footprint of the Io torus magnetic field lines into the Jovian atmosphere. The existence of emission at a higher L-values was considered compatible with the observations. No indication of a local time intensity variation could be deduced from the pre- and post-encounter sequences of both spacecraft (Herbert *et al.*, 1987). By contrast, a strong longitudinal dependence of the emission rate was observed and explained in terms of the "windshield wiper effect".

The main features of the Voyager view of the Jovian morphology were confirmed with the observations by the International Ultraviolet Explorer (IUE) which has limited imaging within the aperture. Its spectrograph obtained ultraviolet spectra as the planet rotated during the exposures (Clarke *et al.*, 1980; Yung *et al.*, 1982; Livengood *et al.*, 1990). In the northern aurora, a maximum brightness is statistically observed near System III longitudes  $\lambda_{\text{III}} = 180^\circ$ . This conclusion rests on assumptions concerning the morphology of the emission which was represented by a simple arc with a defined analytical longitudinal dependence (Livengood *et al.*, 1992).

A new era opened when high resolution ultraviolet images became available with the Faint Object Camera (FOC) on board the Hubble Space Telescope (HST) (Dols *et al.*, 1992; Caldwell *et al.*, 1992). These images showed that the auroral emissions do not exactly follow the footprint of a constant L-shell as represented by the GSFC-O<sub>6</sub> model, whose accuracy is on the order of 5 to 10° (Connerney, 1992). Observations at 153 nm (Gérard *et al.*, 1993, 1994a,b) showed the presence of a narrow discrete arc close to the 30 R<sub>J</sub> oval for System III longitudes exceeding  $\sim 180^\circ$ . In contrast, a

broader diffuse emission region is generally observed at  $\lambda_{\text{III}} < 180^\circ$ . It was not possible, however, to discriminate between a pattern fixed in longitude from a local time dependent morphology. FOC images at shorter wavelengths (Grodent *et al.*, 1996) indicated that the equatorward auroral boundary is nearly coincident with the 6 R<sub>J</sub> - O<sub>6</sub> GSFC auroral oval.

Recently, Jovian auroral images have also been obtained with the second Wide Field-Planetary Camera (WFPC2) (Clarke *et al.*, 1995, 1996 ; Ballester *et al.*, 1996). This camera has an increased ultraviolet sensitivity as its Woods filters transmit a much broader portion of the auroral UV emission. The WFPC2 images limiting sensitivity is estimated on the order of 10 kiloRayleighs (kR) of total H<sub>2</sub> emission (~ 15 kR when the F130LP blocker is used), to be compared with the > 100 kR threshold of the FOC. As a consequence, additional weaker structures are seen in the WFPC2 images but they require a detailed analysis to untangle real brightness variations from purely geometrical effects, such as limb brightening of structured emitting regions seen from Earth orbit. In particular, the WFPC2 images show an apparently closed auroral oval, possibly due to emission originating from behind the limb or diffuse emission inside the polar cap. This goal may only be reached by using a numerical auroral simulation model.

We first describe the main components and the parameters of the simulation code. A few selected test cases are then presented and analyzed to describe some of the characteristics of the apparent brightness variations due to geometric effects. Four sample individual WFPC2 ultraviolet images of the north Jovian aurora are modelled using the simulation code. These simulations are used to determine simple discrete or diffuse structures able to match auroral UV observations from Earth orbit. Finally, a set of 10 WFPC2 ultraviolet images is used to determine a statistical equatorial boundary of the emission and derive a statistical picture of the morphology of the north Jovian UV aurora. It must be stated that these 10 WFPC2 images are taken from the July 1994 dataset, during the period of collision of comet Shoemaker-Levy 9 fragments with Jupiter. Even though the polar northern aurora looked fainter than usual, there is no evidence to date that the auroral morphology was biased by the impacts (Clarke *et al.*, 1995, 1996). Accordingly, the polar auroral morphology deduced from these images may be considered as typical.

## IV.2 The auroral simulation model

### IV.2.1 Model description

The purpose of these simulations is to visualize an auroral-like emission distribution on the planet as would be seen from Earth orbit for various possible geometries. It uses simplified emission structures which, by geometrical effect, are able to reproduce the main features of the observed auroral emission distribution.

The viewing geometry is defined by the sub-Earth planetocentric latitude, the sub-Earth System III longitude and the geometrical elements of the planet (polar and equatorial radii). The main task of the simulation code is to perform a coordinate system transformation from a general rectangular cartesian coordinate system  $(x,y,z)$  to one or more local coordinate systems  $(\alpha_i, \beta_i, Z)$  in which auroral characteristics are more easily described.

Once the viewing geometry parameters have been set, a two-dimensional model image of the jovian disk seen from Earth orbit is generated. The northern auroral emission zone is enclosed in a rectangle 90,000 km wide and 18,000 km high (23.9"x4.8" for Jupiter, 5.2 AU from Earth), approximately centered on the jovicentric north pole ( the exact location of the center depends on the sub-Earth latitude and the polar radius). This rectangle is mapped with a 100 by 100 km<sup>2</sup> (0.027"x0.027") grid along the x and y directions. For every point  $(x,y)$  of the rectangle, a line of sight (LOS) is defined along the z direction (normal to the x,y plane) and divided into 100 km segments.

The auroral emission is therefore described on a 3-dimensional cartesian grid where one point represents the emission from a 100x100x100 km<sup>3</sup> cube in the Jovian atmosphere. It should be noted that the alignment of the lines of sight is an approximation which is valid for observers far from the planet (e.g. at Earth). Each local coordinate system (indexed by the subscript i) is based on a reference oval on the jovian surface (figure 24) defined as the 1 bar pressure level.

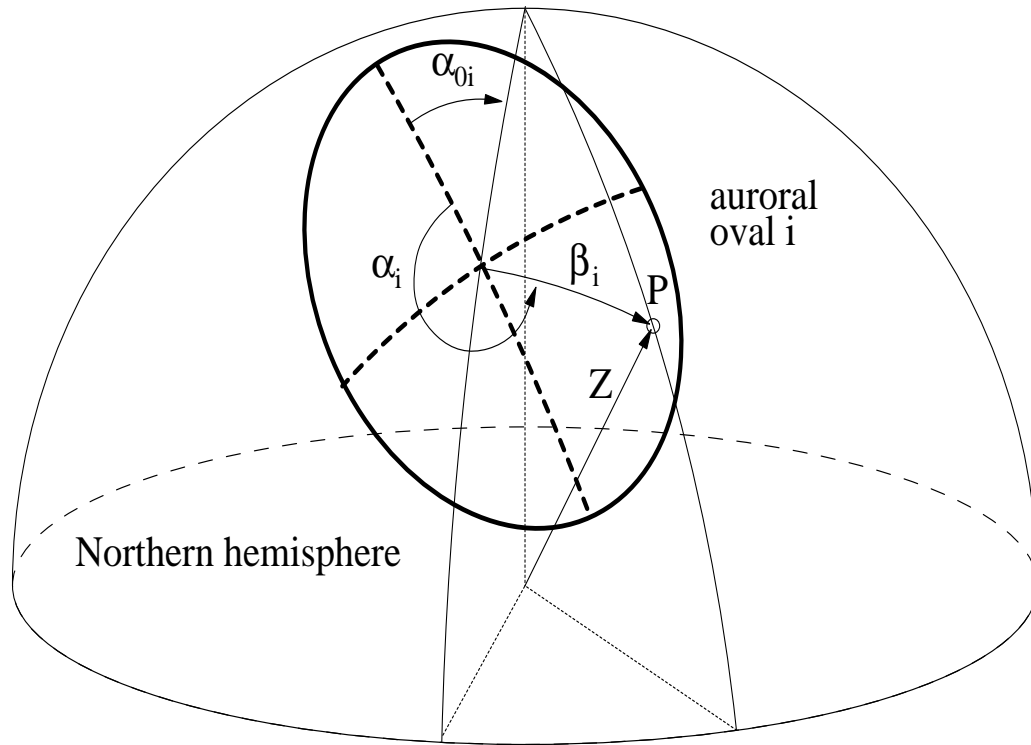


**Figure 24** : Schematic representation of the local coordinates  $\alpha_i$ ,  $\beta_i$  and Z localizing a point P on the surface in the reference oval i. The orientation parameter of the oval ( $\alpha_{0i}$ ) is also shown.

An auroral oval is characterized by 5 parameters that define its center, size, and orientation :

- the oval center is located on the jovian surface by its longitude and planetocentric latitude
- the size is defined by its semi-major and semi-minor axes. They are expressed as spherical distances on the surface.
- the orientation is given by the angle ( $\alpha_{0i}$ ) between the semi-major axis and the longitude meridian intercepting the center of the oval.

In these local coordinate sets, a position is defined by :

- $\alpha_i$  : the surface angle between the semi-major axis and the intersection of the LOS

point and the jovian surface

- $\beta_i$  : the length of the great circle distance between the center of the oval and the projected point
- $Z$  : the altitude of the point, which is measured from the surface along the radial vector connecting the center of the planet to the position  $(\alpha_i, \beta_i)$ .

The auroral emission is reproduced by the combination of auroral structures defined in the coordinate systems of these reference ovals (different structures may be defined from the same oval). Two kinds of auroral brightness distribution structures are used : arcs and diffuse zones. In the following simulations, we refer to these arcs as ARC1, ARC2, ARC3, and to the diffuse zones as GLOW1, GLOW2 and GLOW3. The arcs follow the description of the oval from which they are defined. The brightness distribution across the arc (the thickness of the arc) can be a boxcar function or a Gaussian function of the great circle distance  $\beta_i$ . In both cases, the function is centered on the oval and the width is controlled by a single parameter.

The length and the position of an arc along the oval are controlled by two System III longitudes, (one for the beginning, one for the end) which are converted in local coordinates :  $\alpha_{i,start}$  and  $\alpha_{i,end}$ . An optional modulation of the auroral brightness along the arc may be imposed by a sine to the 4<sup>th</sup> power. This function is applied between two System III longitudes converted in local coordinates  $\alpha'_{i,start}$  and  $\alpha'_{i,end}$ . A filled zone is a region inside the oval which has a uniform horizontal brightness distribution. It can either fill the inside of a whole oval or be limited by two System III longitudes converted in local coordinates. In the latter case, the filled region is defined by the center of the oval and the two local angles  $\alpha''_{i,start}$  and  $\alpha''_{i,end}$ .

We assume that the  $H_2$  auroral vertical emission rate distribution  $V(Z)$  can be approximated by a Chapman profile applied to an isothermal exponential atmosphere :

$$V(Z) = \frac{4\pi I_{thin}}{H} \exp\left(\frac{-(Z-Z_0)}{H}\right) \exp\left[\exp\left(\frac{-(Z-Z_0)}{H}\right)\right]$$

where  $Z$  is the altitude (km) defined in the local coordinate system,

$Z_0$  is the peak altitude (km) of the Chapman profile

H is the H<sub>2</sub> atmospheric scale height.

I<sub>thin</sub> is the vertically observed surface brightness for an optically thin atmosphere,  
it is expressed in units of 10<sup>6</sup> photons cm<sup>-2</sup> s<sup>-1</sup> ster<sup>-1</sup>

Integrating the previous equation along altitude gives the normalization relation :

$$\int_0^{\infty} V(Z) dZ = 4\pi I_{\text{thin}} 10^6$$

where  $4\pi I_{\text{thin}}$  is the brightness expressed in Rayleighs.

The auroral structures are easily parameterized in the i<sup>th</sup> local coordinate system.  
The arcs are formulated by the combination of :

Length of the arc L( $\alpha_i$ )

$$L(\alpha_i) = \begin{cases} 1, & \text{if } \alpha_{i,\text{start}} < \alpha_i < \alpha_{i,\text{end}} \\ 0, & \text{else.} \end{cases}$$

Gaussian width G( $\beta_i$ )

$$G(\beta_i) = \exp\left(-\left(\frac{\beta_i - \beta_{0i}}{\beta_{wi}}\right)^2\right)$$

where  $\beta_{0i}$  is the great circle distance of the boundary of the i<sup>th</sup> oval

$\beta_{wi}$  is the e-folding half width of the brightness distribution in the direction  
perpendicular to the length of the arc

Boxcar width R( $\beta_i$ )

$$R(\beta_i) = \begin{cases} 1, & \text{if } \left(\beta_{0i} - \frac{\beta_{wi}}{2}\right) < \beta_i < \left(\beta_{0i} + \frac{\beta_{wi}}{2}\right) \\ 0, & \text{else.} \end{cases}$$

where  $\beta_{wi}$  is the width of the brightness distribution in the direction perpendicular to the length of the arc.

Enhancement function  $E(\alpha_i)$  (intensification zone)

$$E(\alpha_i) = \left\{ \begin{array}{l} 1 + 2 \sin^4 \left( \frac{\pi(\alpha_i - \alpha'_{i,end})}{(\alpha'_{i,end} - \alpha'_{i,start})} \right), \text{ if } \alpha'_{i,start} < \alpha_i < \alpha'_{i,end} \\ 1, \text{ else.} \end{array} \right\}$$

with these notations, any arc segment brightness distribution may be written as

$$S_i(\alpha_i, \beta_i, Z) = V(Z) L(\alpha_i) \left\{ \begin{array}{l} G(\beta_i) \\ R(\beta_i) \end{array} \right\} [E(\alpha_i)]$$

where the braces allow selection of either a Gaussian or a boxcar shape and the brackets indicate that the enhancement is optional.

Similarly, the filled zones can be formulated with a single function  $F(\alpha_i, \beta_i)$

$$F(\alpha_i, \beta_i) = \left\{ \begin{array}{l} 1, \text{ if } \alpha''_{i,start} < \alpha_i < \alpha''_{i,end} \wedge \beta_i \leq \beta_{i0} \\ 0, \text{ else.} \end{array} \right\}$$

This diffuse zone is called GLOW2. If it fills the entire polar cap ( $\alpha''_{i,start} = \alpha''_{i,end}$ ) then it is called GLOW1. As will be illustrated in the image simulations, it is useful to define a modulation of the poleward boundary of a diffuse zone. This modulation gives rise to a moon quarter shape diffuse zone (GLOW3). It is imposed by a relation of the form :

$$K(\alpha_i, \beta_i) = \left\{ \begin{array}{l} 1, \text{ if } \beta_i > \sqrt{\sin \left( \frac{\pi(\alpha_i - \alpha'''_{i,end})}{(\alpha'''_{i,end} - \alpha'''_{i,start})} \right) \circ \text{constant}} \\ \text{and } \alpha'''_{i,end} < \alpha_i < \alpha'''_{i,end} \\ 0, \text{ else.} \end{array} \right\}$$

Therefore a filled zone brightness distribution is given by :

$$S_i(\alpha_i, \beta_i, Z) = V(Z) F(\alpha_i, \beta_i) [K(\alpha_i, \beta_i)]$$

the brackets indicate that the poleward boundary is optional. Accordingly, the auroral volume emission rate associated with any (x,y,z) point can be written as

$$A(x,y,z) = \sum_i s_i S_i(\alpha_i(x,y,z), \beta_i(x,y,z), Z(x,y,z))$$

where  $s_i$  is a weighting factor controlling the contribution of the different auroral structures at the point considered. The integration along a line of sight (z direction) gives the simulated auroral brightness at the (x,y) position of the jovian disk image as seen from Earth orbit. This integration is numerically achieved by a step summation along the z axis :

$$Br(x,y) = \sum_z A(x,y,z) \Delta z,$$

where  $\Delta z$  is the length element along the line of sight.

## IV.2.2 Limb brightening estimate

Observations of auroral emission on Earth as well on Jupiter indicate that limb brightening is an important factor which affects the apparent brightness of both discrete and diffuse emissions. It is therefore of prime importance to estimate the expected brightness limb enhancement, using an analytical approach applied to a simple case. This evaluation is also useful as a comparison to the results of the more sophisticated model described previously.

The expected ratio of the limb to CML brightness at  $70^\circ$  of latitude for an aurora uniformly covering the surface of a spherical planet can be estimated from the Chapman function (which should not be confused with the Chapman profile used in the previous section). This function gives the ratio of the slant column emission rate to the vertical column emission rate line. Since the latter integral is given, in any case, by the normalization relation (equ. 2), the limb brightening factor is given by the ratio of the

Chapman function at the limb  $\text{Ch}(\text{limb})$  to the Chapman function calculated at the CML for a latitude of  $70^\circ$   $\text{Ch}(\text{CML}, 70^\circ)$ . At the CML for a latitude of  $70^\circ$ , the plane parallel approximation may still be used with sufficient accuracy and the Chapman function may be approximated by the secant of the latitude angle :

$$\text{Ch}(\text{CML}, 70^\circ) \simeq \sec(70^\circ) = 2.9$$

At the limb, the Chapman function can be simplified by the variable transformation

$$z = Z_0 / \tan \chi$$

where  $z$  is the integration variable along the line of sight

$Z_0$  is the altitude of the peak of the Chapman profile

$\chi$  is the angle between the radial vector from the center of the planet to a given point ( $z$ ) along the line of sight and the direction to the observer.

Since the maximum of emission is reached near the maximum of the Chapman profile, the Chapman function is estimated at the limb  $+Z_0$  by

$$\text{Ch}(\text{limb}, Z_0) = \int_0^\pi \exp(\Gamma) \exp(-\exp(\Gamma)) \frac{d\chi}{\sin^2 \chi}$$

with

$$\Gamma = \frac{-Z_0}{H} \left[ \frac{1}{\sin \chi} - 1 \right]$$

Case	CML ( $\lambda_{\text{III}}^\circ$ )	Peak altitude (km)	Scale Height (km)
1	180	400	100
2	120	400	100
3	240	400	100
4	180	400	400
5	180	1000	100
6	180	400	100
7	180	400	100

**Table 7** : Main characteristics of the simulated test cases.

The peak altitude refers to the altitude of the maximum of the Chapman profile measured from the 1 bar level.

Case 7 is the sum of cases 1 and 6.

Varying  $\lambda$  from 0 to  $\pi$  accounts for the emission originating from behind the limb as well as in front. For a scale height H of 100 km corresponding to a temperature  $T \simeq 600$  K prevailing at the altitude of the auroral peak (Trafton *et al.*, 1994, Liu and Dalgarno, 1996), and a spherical planet of radius 66,850 km, numerical integration gives:

$$\text{Ch}(\text{limb}+Z_0)=33.5$$

The maximum expected limb brightening (the aurora is not really uniform over the planet) is therefore :

$$\frac{\text{Ch}(\text{limb}+Z_0)}{\text{Ch}(\text{CML},70^\circ)} = \frac{33.5}{2.9} \simeq 11.5$$

This value will be compared to that obtained in the image simulations.

### IV.3 Simulation of simple test cases

In order to assess the influence of the geometrical features of the auroral morphology on the limb brightening effect, we have simulated a simple realistic northern jovian auroral oval in seven different configurations. In each case, the sub-Earth latitude is  $3^\circ$  S and the polar and equatorial radii are 66,854 km and 71,492 km, respectively. The parameters of the oval used in this section correspond to the fit of the equatorial auroral boundary that will be discussed in the statistical equatorial boundary oval section. The arc has a  $1^\circ$  wide boxcar shape along the local coordinate  $\beta_i$ . The other parameters (CML, peak altitude of the Chapman profile and scale height) are listed in table 7.

In **test case 1**, (figure 25.1) the peak altitude of the Chapman profile is set to 400 km and the scale height is 100 km. With these realistic values and a CML of  $180^\circ$ , the maxima of limb brightening appear close to the dawn and dusk limbs, well inside the planetary disk. Indeed, only a fraction of the auroral emission originating from behind the planet exceeds the critical altitude to stand above the planetary limb. The brightness ratio between the Earth facing section of the oval at the CML and the maximum brightness is on the order of 5.

**Test cases 2 and 3** (figure 25.2 and 25.3) present the same oval as in case 1 with different CMLs ( $120^\circ$  and  $240^\circ$ , respectively). The maxima still appear near the ansae of the oval. Two features are readily observed :

1. the oval appears as an incomplete structure. The section of the oval around midnight is obscured by the planetary disk. This is because the emission from behind the planet is not located high enough for the considered viewing geometry (in particular the planet's tilt angle from the observer) and the parameters of the oval.
2. the overall shapes of these two cases are very different : with its larger CML, case 3 shows a longer Earth facing section of the oval. This is due to the orientation of the major-axis of the oval. Had this axis been aligned along a meridian, cases 2 and 3 would have produced two symmetrical images.

**Test case 4** (figure 25.4) is the same as case 1 with an emission scale height increased from 100 km to 400 km. The oval appears thicker at all latitudes and longitudes. At higher latitudes, and especially at the limb, the emission extends to higher altitudes. The decrease in brightness apparent in the maximum limb brightening regions, is due to the normalization of the Chapman profile which spreads the emission brightness over a longer distance, with a weaker peak brightness.

**Test case 5** (figure 25.5) shows the case 1 oval with the emission peak moved from 400 km to 1000 km. This change has a negligible effect on the brightness distribution along the oval and on the maximum value. The main effect occurs at the polar limb where the emission gap between the planetary disk and the basis of the auroral emission arc is increased. The depth in the atmosphere to which an incident beam of electrons with a given energy penetrates mainly depends on the characteristics of the auroral neutral atmosphere. Waite et al. (1983) have derived levels of maximum electron energy deposition for 10 KeV and 1 KeV monokinetic electron beams at 400 km and 700 km, respectively.

**Test case 6** (figure 25.6) shows a uniformly filled polar cap inside the previous oval with the same scale height and peak altitude as case 1. Unlike the previous cases, one observes only one line of maximum limb brightening which is centered near the polar limb. The exact location of the center depends on the orientation of the oval major-axis. The maximum ratio of the polar limb to the CML brightness at  $70^\circ$  of latitude is about 10.5. This value is in good agreement with the ratio 11.5 estimated analytically in the previous section. The small difference stems from the fact that the auroral emission is not covering the whole planetary disk and that we consider here a flattened and tilted planet.

**Test case 7** (figure 25.7) is the sum of cases 1 and 6. It shows how the emission from inside the auroral oval can apparently complete the oval in the night limb region. The effect of this nightside closure by an unstructured emission would even be more pronounced for cases 2 and 3, for which the region where the actual emission arc disappears behind the planetary disk would be replaced by a limb brightened emission, giving the illusion of a complete oval. This effect is noticeable in several HST images, which very frequently exhibit a line of emission along the polar limb.

## IV.4 Auroral image simulations

This work is organized as a global approach of the auroral morphology simulation which consists in determining the most likely simple geometrical structures which are able to simulate the main auroral features observed with the WFPC2 camera. It is clear that with such simple structures, the simulation code cannot reproduce each pixel of the observed image. An inverse method like the one presented by Satoh *et al.* (1996) for the infrared  $H_3^+$  aurora is not applicable here since the signal to noise ratio is too low for most pixels and our dataset is too restricted in longitudinal range. In addition, it is not possible to analyze the available UV images as a unique set of homogeneous observations, since the UV aurora exhibits temporal variations on a time scale of about 10 minutes and more (Gérard *et al.*, , 1993, 1994a; Ballester *et al.*, 1996). We therefore use a direct method to visually adjust the parameters of the simulation for one image at the time.

Ovals are defined with the 5 parameters described in Section 2.1 which we compare with the observed image. The parameters are adjusted until an oval intercepts the central part and/or the brightest pixels of an auroral feature, or the equatorward limit of a diffuse emission zone. The analytical representation of the oval determined this way is not unique as more than one oval may meet the adjustment. In many cases, more than one structure can reproduce the same auroral feature, especially when the signal to noise ratio of the pixels defining a feature is low. In any case, this approach is useful to determine and test the most likely structures able to reproduce the main observed auroral features.

### IV.4.1 The WFPC2 dataset

The images of Jupiter's ultraviolet aurora used in this work have been selected in a dataset of HST observations obtained in July 1994, at the time of the impact of comet Shoemaker-Levy 9 (SL9) with Jupiter (Clarke *et al.*, 1994) and in March 1995. These images consist of exposures with the wide field CCD detector #3 and #4 of the WFPC2 instrument, providing a 800 x 800 pixel format with a pixel size of 0.10" x 0.10" at the center of the CCD. At the distance of Jupiter, a pixel represents a distance of 350 km on

Jupiter projected area in July 1994 and 380 km in March 1995. For CCD #4, the F160BW (1150 to 2100 Å) filter was used to isolate the H<sub>2</sub> Lyman and Werner bands UV emission. For CCD #3 the same bandpass is isolated with the partially rotated filter position F160BN15. In both cases, the filter is crossed with the F130LP blocker to filter out the emissions below ~1230 Å, including the H Lyman- $\alpha$  emission which may introduce morphological differences.

The effects of methane absorption have been neglected as less than 20% of the total H<sub>2</sub> emission transmitted by the filter set is absorbed by CH<sub>4</sub>. Table 8 lists the dates, times, durations, central meridian longitudes and identifications of the 11 images used in this paper. As part of the standard data processing, the images were field flattened after correction of the bias level and dark frames. In these images, Jupiter was targeted to display the northern auroral region near the center of the chip, where the geometric distortion is on the order of a few tenths of a pixel. A correction was applied to remove this geometric distortion and the shift introduced by the MgF<sub>2</sub> field flattener on the CCD detector (Gilmozzi *et al.*, 1995; Holtzman *et al.*, 1995; E. Kinney, pers. Comm. 1995). We used a limb fitting method similar to that described by Clarke *et al.* (1995), its accuracy is better than 2 pixels. The inaccuracy introduced by the WFPC2 (WF) point spread function is on the order of 1 to 2 pixels, resulting in a cumulated positional systematic inaccuracy of 2 to 3 pixels. The traces of the cosmic rays have been removed for presentation. Their intensity has been interpolated from nearby pixels.

#### IV.4.2 Simulation of observed images

In this section, we describe the simulation of four observed auroral images. Three of them belong to the July 1994 dataset while the fourth image is extracted from the recently available set of WFPC2 images obtained in March 1995. This latter image belongs to the set of images recently described by Clarke *et al.* (1996) and was used by these authors to define a reference auroral oval. In each simulation, the smearing effect due to the rotation of the auroral region with the planet during the exposure depends, among other parameters, upon the mean central longitude, the size and the orientation of the auroral structures. Its effect is approximately reproduced by imposing different Gaussian-shaped widths to the arcs of oval, instead of a single boxcar shape. The smoothing effect of the WFPC2 point spread function (PSF) has been reproduced by

convolving the simulated images by a model PSF kernel determined at 2000 Å, accounting for the observed wavefront and the pixel response function (Burrows *et al.*, 1995). Its effect is individually discussed for each simulation. In the following description, the default value for the peak altitude of the Chapman profile (referred in the text as the altitude of the emission) is set to 400 km above the NH<sub>3</sub> clouds top, that is at an altitude nearly coincident with the altitude of the unit tangential optical depth for CH<sub>4</sub> absorption (i.e. The methane homopause). The default value of the scale height is set to 100 km. The various structures (arcs and zones) are represented in figure 27 in an equidistant polar projection. The relative brightness of each structure and its variation along the arc are represented in an overlaid box.

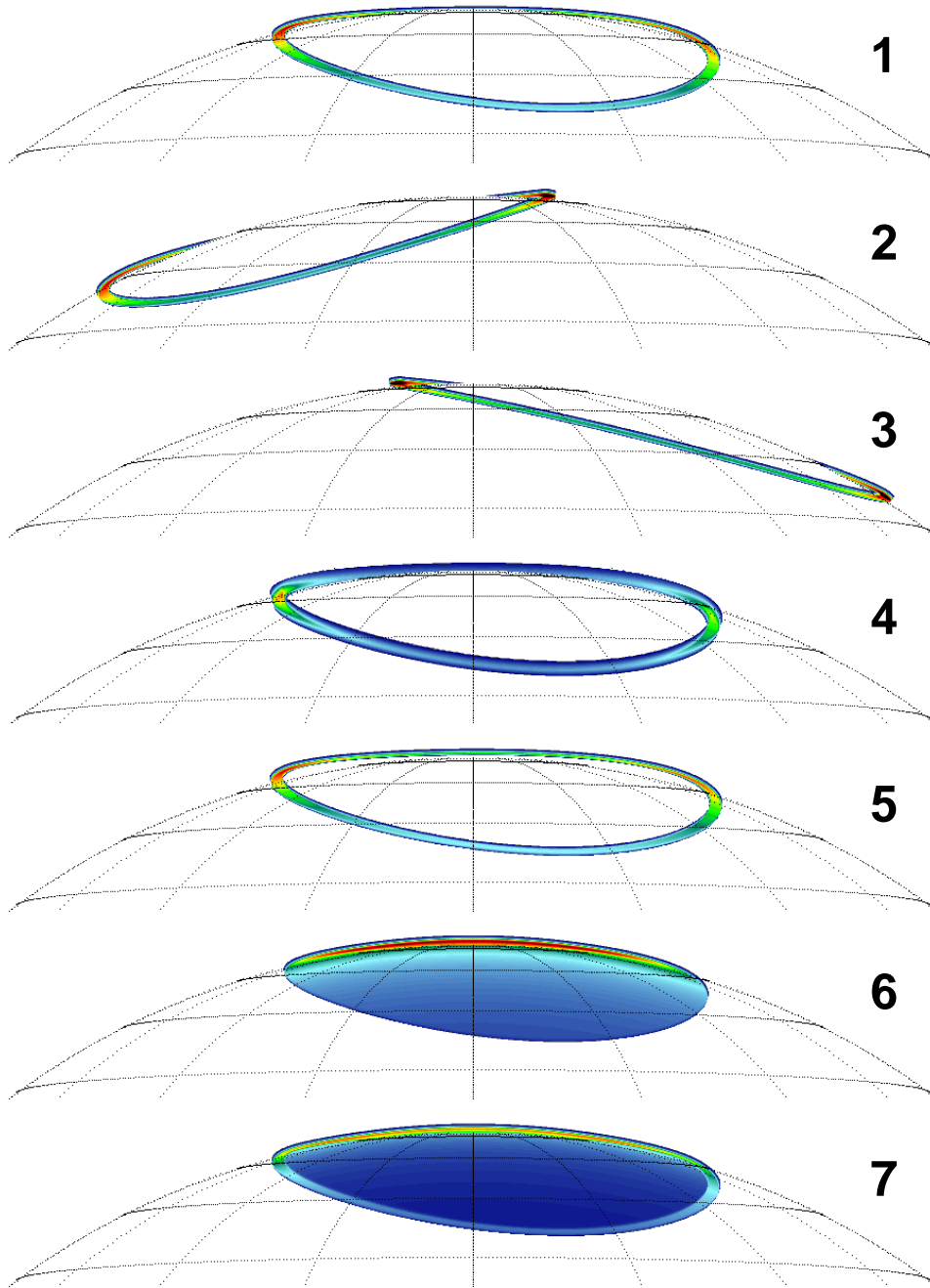


**Figure 25** : Simulation of simple test cases (see table 7). Parallels of planetocentric latitudes are drawn every  $10^\circ$ . Local time longitudes, measured from the CML, increase by  $20^\circ$  increments.

#### IV.4.2.1 Image 0503

This first image, obtained in March 1995 (figure 27.A), shows an apparently simple geometry which comes down to a single auroral oval. Figure 26.A shows a simulation obtained with one single oval. The brightness distribution is uniform along the oval and with a Gaussian-shape across it. The comparison with the observed image (figure 27.A) clearly shows that this simple brightness distribution cannot reproduce the observation. The locations of the morning and evening limbs brightening are different from the observation. In addition, the observation shows that the front section of the oval is brighter than the rear section, that is the opposite of what is expected from the limb brightening effect. Three phenomena could explain this behavior : 1) a brightness weakening of the rear section of the oval, 2) a fraction of the emission arising from the section of the oval near  $0^\circ$  could be occulted by the planetary disk, 3) the limb brightening of a diffuse zone is sufficient to apparently close the limb section of the oval, without the presence of an arc near the limb. This third possibility seems the most likely since a weak glow emission is indeed observed in the polar cap.

The fact that the positions of the maxima at the morning and evening limbs of the simulated image do not correspond to the observed positions and the presence of bright localized zones along the front section of the oval can only be simulated by intrinsic brightness variations along the arc. Figure 26.B illustrates two major effects of the point spread function of the WFPC2 camera on the single oval simulation.

The spread of the thin limb brightened line along the limb conspicuously shows the dilution effect of the PSF. This dilution reduces the maximum brightness value in this region by a factor 2. A less pronounced effect of the PSF is the slight shift equatorward of the position of the brightness maxima at the morning and evening limb. Figure 27.B shows the final simulation of the observed image.

We will now describe and discuss the different structures that we added to and/or removed from the original single oval in order to reproduce the main auroral features of figure 27.A.

ID	date (mm/dd/yy)	UT (hh:mm)	exposure time (s)	mean CML (System III)
<b>0E01</b>	07/17/94	09:06:00	700	193°
0j01	07/17/94	18:56:00	400	186°
0s01	07/18/94	13:55:00	700	158°
0y01	07/19/94	11:07:00	400	205°
1501	07/20/94	14:10:00	400	107°
<b>1502</b>	07/20/94	14:19:00	400	112°
<b>1701</b>	07/20/94	16:12:00	400	180°
1b01	07/21/94	08:09:00	400	39°
1f01	07/21/94	13:01:00	400	215°
1p01	07/22/94	09:54:00	400	253°
<b>0503</b>	03/06/95	20:33:00	600	211°

**Table 8** : Main characteristics of the WFPC2 images used in this work. All the images were acquired in July 1994 with the F160BW + F130LP filter set, excepted 0503 which was taken in March 1995 with the F160BN15 + F130LP filter set. The bold IDs show the 4 images selected for the simulations. The ID names are extracted from the full HST archive file names.

1. In the simulation, the rear section is closed by a diffuse zone uniformly filling the inside of the oval. As already discussed, the presence of an arc in this sector is not required since the limb brightening of the diffuse zone, which we call GLOW1, gives an apparent closing with a pronounced line of maximum brightness above the limb, at an altitude close to the peak of the Chapman profile. The PSF dilutes this bright emission line, but its trace is still visible. Such a trace is not clearly seen on the observed image. This could mean that the diffuse emission GLOW1 is not peaked like a Chapman layer with a well defined maximum altitude, but would spread in altitude according to a distribution flatter than the Chapman profile. Another reason could stem from the large inhomogeneity of the diffuse emission filling the observed oval which appears to include many faint pixels spots rather than a uniformly filled zone.

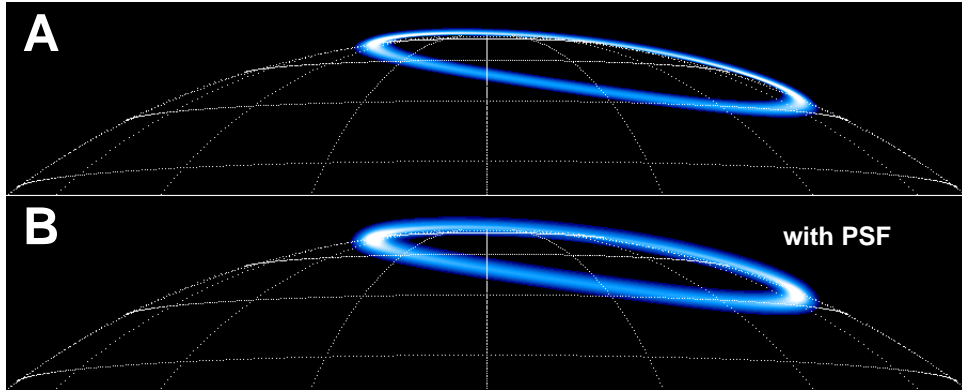


**Figure 26** : (A) Localization of the maxima and (B) effect of the PSF on a single auroral oval defined from image 0503.

2. Another diffuse emission (not simulated) appears at the left side of the bright morning arc. This feature could be reproduced by a faint localized glow region which is revealed by limb brightening. The shape of the diffuse region which produces this emission is hardly determined. In any case, as shown by figure 27.B, it cannot result from the effect of the PSF on the bright morning emission.
3. An arc of oval (ARC3, plotted in red in figure 27.C) defined between  $225^\circ$  and  $250^\circ$  can simulate the morphology of the bright morning feature. However, as already mentioned, the observed maximum brightness of this feature does not coincide with the position of the maximum of the limb brightening which is therefore closer to the limb. A shift of the position of the brightness maximum requires the presence of an intrinsic brightening effect along ARC3. The shift is reproduced by using an intensification zone (defined in the model description section) centered on the position of the observed brightness maximum, that is between  $220^\circ$  and  $250^\circ$ . The relative brightness distribution of ARC3 is represented in red in the overlaid bar-plot of figure 27.C. In this bar-plot, the rectangular base represents the brightness of the arc without intensification and the top Gaussian-like shape represents the effect of the intrinsic intensification with a peak value 3 times the base brightness of ARC3. In the polar plot, the intensification zone is materialized by a black curve inside the arc.
4. Another intensification zone between  $180^\circ$  and  $230^\circ$  has to be used to reproduce

the brightness distribution of ARC2 : the arc of oval defined between  $190^\circ$  and  $225^\circ$  on the same oval than ARC3. It is represented in yellow in figure 27.C. Once more, this intensification is clearly independent of the limb brightening and reveals an intrinsic brightness variation along the arc. Another possible interpretation of the brightness distribution of ARC2 could be a weakening of the brightness at the edges of the arc rather than an intensification around the center of ARC2. Its relative brightness is represented in figure 27.C by the yellow bar and the effect of the intrinsic intensification is represented by plotting a Gaussian-like shape above the bar.

5. The long arc of oval ARC1 defined on the same oval than ARC2 and ARC3 between  $125^\circ$  and  $190^\circ$  (the green arc and the green bar with its intensification in figure 27.C) is a bit more complex. The brightness intensification between  $140^\circ$  and  $195^\circ$  cannot be explained by a limb brightening effect and we use an intrinsic intensification zone to simulate it. By contrast, the brightness of the section of ARC1 between  $125^\circ$  and  $140^\circ$  is solely due to the limb brightening effect. It should be noted that this latter section of ARC1 might as well be reproduced by the limb brightening of a localized accumulation of diffuse emission. However, the continuity of the brightness distribution along the whole bright feature favors the idea of a long arc of oval.
6. The effect of the PSF on the limb brightened section of ARC1 cannot by itself reproduce the small discontinuity in the emission altitude observed at the limb, just above the low longitude end of ARC1. In order to account for this discontinuity, the peak altitude of the Chapman profile of ARC1 was set to 600 km and the scale height was set to 200 km.
7. As for ARC3, the effect of the PSF on ARC1 is not sufficient to reproduce the equatorward diffuse emission below ARC1. A low latitude localized diffuse emission (not simulated here) would therefore be required.

The detailed analysis of this image with the Earth-viewing geometry code indicates that, within individual structures, intrinsic variations are present along the arcs which cannot be ascribed to geometric effects. It is also possible to explain the apparent closing of the oval behind the polar cap by limb brightening of a high altitude weak diffuse emission not observable elsewhere.

#### IV.4.2.2 Image 0E01

This image (figure 27.D) has a mean CML of  $193^\circ$  which is comparable to that of the previous one. Large differences are observed between those two images which are separated by 8 months. This is not surprising since morphological variations with scale times of a few minutes to a few days have been observed (Gérard *et al.*, , 1993, 1994a; Ballester *et al.*, 1996). As in the previous case, the use of one single homogeneous oval cannot simulate the observed features. This simulation (fig. 4.E) requires 3 new structures : one defined by an additional oval and two kinds of limited diffuse zones.

1. The marked inhomogeneity of the diffuse emission filling the auroral cap cannot be readily simulated. However, the composition of three different diffuse zones allows to account for the main brightness variations. We call these three diffuse zones GLOW1, GLOW2 and GLOW3. Their relative brightnesses are represented in blue on the overlaid bar-plot of figure 27.C. The blue bar is subdivided in three smaller bars for GLOW1, GLOW1+GLOW2 and GLOW1+GLOW2+GLOW3, respectively.
  - GLOW1 is the faint diffuse emission uniformly filling the entire auroral polar cap. It may be responsible for the weak apparent closing of the midnight-morning limb region. For clarity, it is not drawn on the polar plot of figure 27.F.
  - GLOW2 is limited to the afternoon region by two longitudes and by the center of the oval fitting its equatorial boundary (blue shaded region in figure 27.F). It reproduces the diffuse emission above the afternoon bright arcs and increases the brightness of the apparent closing of the midnight-evening limb region. It also simulates the low latitude emission observed at longitudes around  $155^\circ$ .
  - GLOW3 has a moon quarter shape (model description section)(blue shaded region in figure 27.F). Its low longitude limit is larger than GLOW2 and its altitude is set to 800 km. The limb brightening of this zone gives rise to a maximum limb emission line at a higher altitude than GLOW2, leading to the observed break of altitude emission compared to the curvature of the model limb. As previously, a flatter altitude distribution or a variation of the altitude of emission should be considered.
2. We define ARC3 as the red arc in figure 27.F. Its brightness is weak (red bar in

bar-plot of figure 27.F) and no intensification had to be used in the simulation. The extension of this arc to longitudes close to  $180^\circ$  reproduces the observed closing of the equatorward Earth facing section of the aurora.

3. The afternoon region of the aurora shows a fork-like bright feature that we attributed to the crossing of two arcs of oval, ARC1 and ARC2, that are defined on different ovals and represented in figure 27.F by the green and yellow arcs and bars, respectively. The equatorward arc, ARC1, bears an intrinsic intensification zone. It is much shorter than its counterpart in the previous simulation as no bright feature appears in the evening region of the aurora. The poleward arc, ARC2, also requires an intensification zone in order to simulate the observed brightness enhancement which is not simulated by the addition of the two arcs in this region. This set of arcs reasonably simulates the observed fork-like feature but it is clear that it is only one of the many possible structures able to match the observation.
4. The low longitude ends of ARC1 and ARC2 are not straightforwardly determined because inhomogeneities observed in the evening diffuse region tend to form a structured emission. This structuring phenomenon is best observed in the next image.

#### IV.4.2.3 Image 1701

With a mean CML close to  $180^\circ$ , much of the auroral region is visible from Earth orbit. This image (figure 27.G) was taken 3 days after the previous one and shows morphological variations, some of which might be attributed to the temporal variability of the Jovian aurora. The most striking difference is the disappearance of the fork-like afternoon bright feature which is replaced by two individual bright structures that we have simulated (figure 27.H) with a 2 distinct arcs.

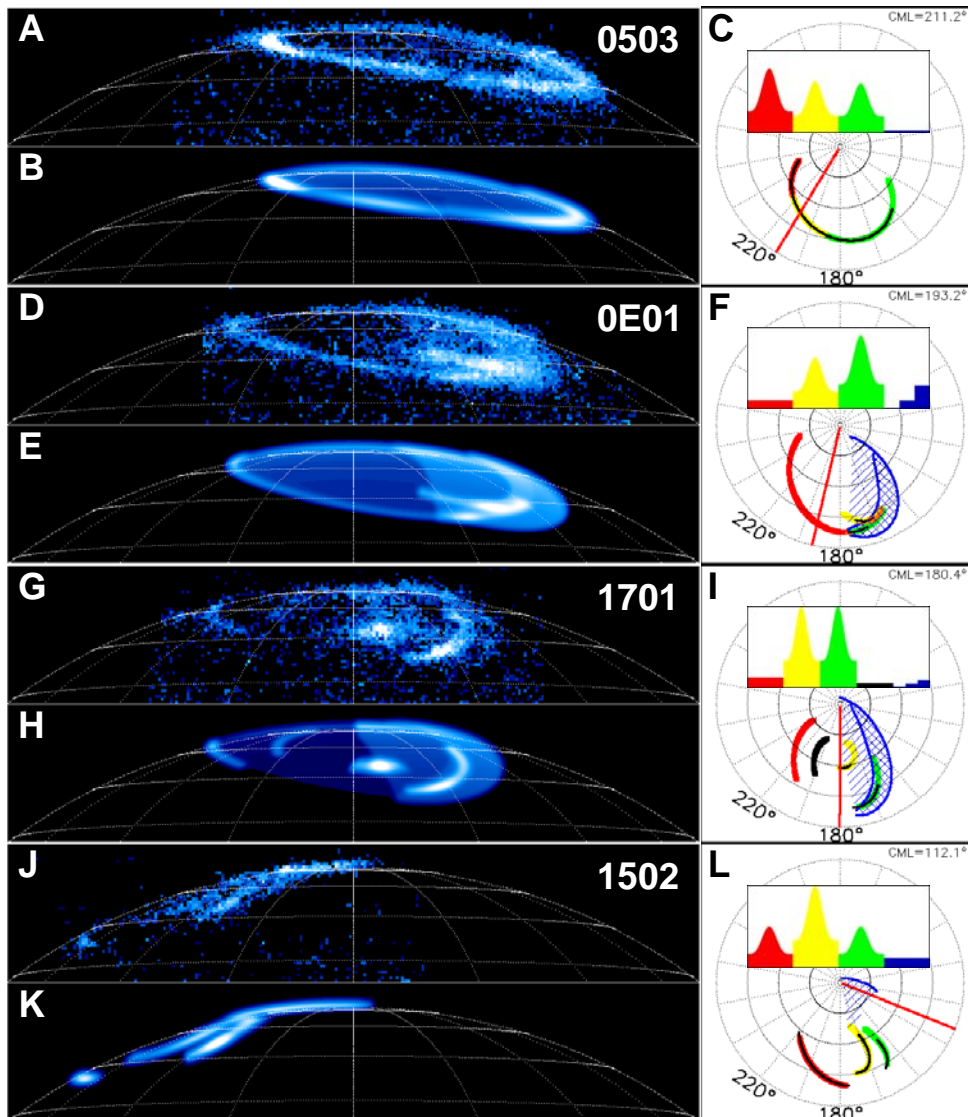


**Figure 27**

Composite representation of the observed images simulations. Upper left corner (A,D,G,J) is the observed image with a grid showing  $10^\circ$  spaced parallels and  $20^\circ$  spaced meridians centered on the CML, bottom left corner (B,E,H,K) is the simulated image with the same grid. Right side (C,F,I,L) is a polar plot representing the simulation parameters. The latitude circles are separated by  $10^\circ$  and the System III longitudes increase in  $20^\circ$  steps clockwise from the ( $\lambda_{\text{III}} = 0^\circ$ ) meridian. The CML is represented as a red meridian line. ARC1 is in green, ARC2 is in yellow, ARC3 is in red and the diffuse zones GLOW2 and GLOW3 are in blue. For simplicity, GLOW1 (filling the entire polar cap) is not drawn. The intensification zones are materialized by black curves inside the arcs. The relative brightnesses attributed to these structures are presented as an overlaid barplot with the same color index. The Gaussian-like shapes above the bars represent the intensification zones. In the case of complex diffuse zones (0E01, 1701) the blue bar is divided in three smaller bars for GLOW1, GLOW1+GLOW2 and GLOW1+GLOW2+GLOW3, respectively. As part of the standard data processing, the WFPC2 images were field flattened after correction of the bias

level and dark frames. Further correction was applied to remove the geometric distortion and the shift introduced by the field flattener on the CCD detector. The traces of the cosmic rays have been removed for presentation. Their intensity has been interpolated from nearby pixels.

1. Similar to the two previous simulations, we define ARC3 as a weak arc of oval, represented by the red arc of figure 27.I. The position of the brightness maximum of this arc seems solely determined by the limb brightening and therefore no intrinsic intensification zone was used in the simulation. As in image 0503, a faint diffuse emission (not simulated) appears at the limb equatorward of ARC3. Here again, this possibly localized faint diffuse emission is revealed by limb brightening and cannot be explained by the effect of the PSF on ARC3.
2. The break of emission at the high longitude end of ARC3 and the presence of a weak diffuse emission inside the morning region favor the suggestion of an apparent closing of the morning-midnight limb region by the limb brightening of a diffuse zone (GLOW1). A faint structured emission feature stands out from GLOW1 around  $200^\circ$  of longitude. It could stem from a fortuitous accumulation of glow or from a weak arc of oval. We simulate this feature with an arc of oval which is represented in figure 27.I as a black arc. At high latitudes, the limb brightening of this feature could contribute to the closing of the limb region.
3. The front morning section of the auroral region is not closed, probably because the emission is too faint to be detected. We define ARC1 as the long equatorward arc of oval represented by the green arc in figure 27.I. The limb brightening cannot explain the intensification needed for the equatorward part of ARC. However, at latitudes larger than  $60^\circ$  it becomes important and can explain the brightening region observed near the end of the arc. The poleward bright feature is simulated by a relatively short arc of oval, ARC2, represented in yellow in figure 27.I. An intensification zone is imposed to reproduce the brightness distribution of this feature. It is surrounded by diffuse emission that we simulate by arbitrarily increasing the width of ARC2.
4. The inhomogeneity of the diffuse emission in the polar cap is still present. We account for it by adding two diffuse emission zones to GLOW1 similar to those used in image 0503 : GLOW2, which is limited by two longitudes and the center of its fitting oval and GLOW3 which has a moon quarter shape and a low longitude limit greater than GLOW2 (blue regions and bars in figure 27.I). The

altitude of emission of GLOW2 is 400 km and the altitude of GLOW3 is set to 800 km. Both diffuse emissions are responsible for the apparent closing of the midnight-evening limb region and for the diffuse emission equatorward of ARC1. In this simulation, one cannot really discriminate the diffuse emission simulated by GLOW2 and GLOW3 from the diffuse emission that surrounds ARC1 and ARC2 and which is not an effect of the PSF.

Oval	Center		semi-major axis	semi-minor axis	orientation
	latitude	longitude			
O <sub>6</sub> 30 R <sub>J</sub>	75.1°	170.7°	15.6°	12.8°	-5.0°
O <sub>6</sub> 6 R <sub>J</sub>	75.9°	175.7°	25.3°	20.3°	-14.5°
0503	75.0 °	177.8°	17.3°	14.4°	-15.°
IR 28 feb 92	77.5°	181.1°	17.7°	14.6°	-5.0°
IR 22 mar 92	77.4°	179.4°	17.3°	14.2°	-5.0°
Boundary oval	74.2°	173.0 °	21.0 °	17.5°	-50.°

**Table 9** : Simulation parameters of several ovals (see section 2.1 for complete description of these parameters). The centers are defined by jovicentric latitudes and System III longitudes. IR 28 Feb 92 and IR 22 Mar 92 are the uniformly bright infrared ovals determined by Satoh *et al.* (1996) (see section 6). The characteristics of the boundary oval are displayed for information, they should not be directly compared with the other parameters.

#### IV.4.2.4 Image 1502

This last image (figure 27.J) is selected because of its different viewing geometry (CML around 112°). For such CMLs, most of the auroral information is concentrated near the morning limb, where the effects of the limb brightening and of the viewing geometry complexify the appearance of the auroral region, and increase the number of structures able to simulate the observed features. In the present case, we show that the aurora, which might look atypical, is in fact made of auroral structures similar to those used in the previous three simulations (figure 27.K).

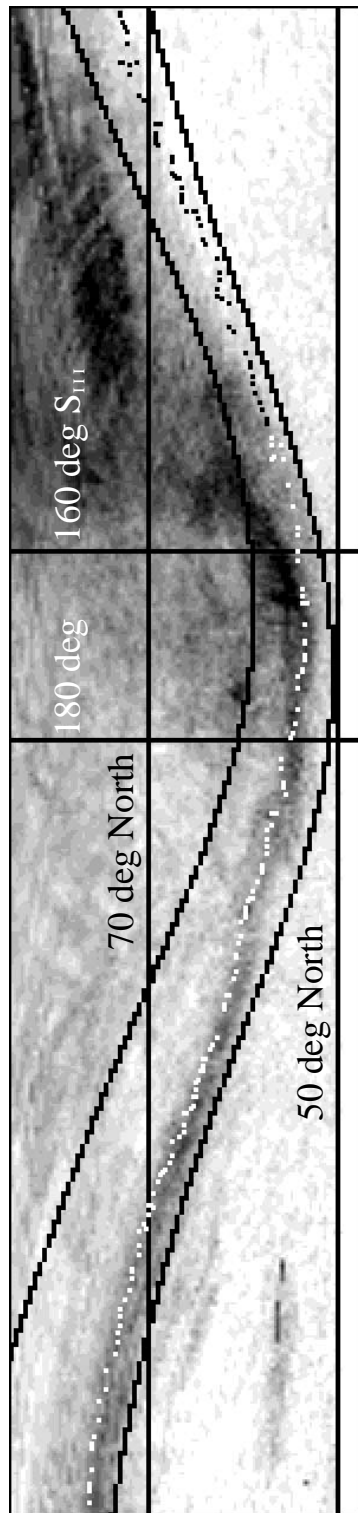


**Figure 28**

Equidistant cylindrical projection of the average map. Two System III longitudes and two joventric latitudes are displayed. The boundary oval is defined by the points. The footprints of the  $6R_J$  (equatorward gray line) and  $30R_J$  (poleward gray line) ovals of the GSFC  $O_6$  model are displayed for comparison.

1. ARC3, the arc located by the red arc of figure 27.L, is so weak that no discrete maximum can be localized. However, ARC3 is not affected by the limb brightening and an intensification zone is applied to shift the brightness distribution away from the limb.

2. There is no clear closing of the half left part of the limb region, nor of the front section at the right of ARC3. ARC1, the equatorward arc of oval plotted as a green arc in figure 27.L, has a higher signal to noise ratio. It simulates the bright feature with an intrinsic intensification zone.
3. A faint feature stands out from the diffuse emission region located between ARC1 and the limb. It is simulated with a weak arc of oval, ARC2 in yellow in figure 27.L. It is clear that according to its location and to the bright diffuse emission surrounding it different emission zones, such as a localized accumulation of glow, are able to simulate that feature.
4. The most striking feature of this image is probably the bright emission appearing at the right part of the limb. The simulations show that a localized diffuse emission zone, GLOW2 (blue zone in figure 27.L), similar to those used in the previous simulations, is able to reproduce the observed limb emission through limb brightening effect. However, inhomogeneities account for the position of the maximum brightness along the limb. Localized diffuse emission at the edge and below ARC1 and between ARC2 and the limb can not be simulated by a uniform diffuse zone such as GLOW2.
5. A very weak diffuse emission, revealed by its limb brightening, is observed equatorward of ARC3. Once more, it is not due to the effect of the PSF on ARC3.

## IV.5 The statistical equatorial boundary oval

One common feature of the images described before and of the other available FOC (Gérard *et al.*, 1993, 1994b) and WFPC2 (Clarke *et al.*, 1996; Ballester *et al.*, 1996) observations is the difference between the structures observed for  $\lambda_{\text{III}} < 180^\circ$  (or afternoon sector) and  $\lambda_{\text{III}} > 180^\circ$  (or morning sector).

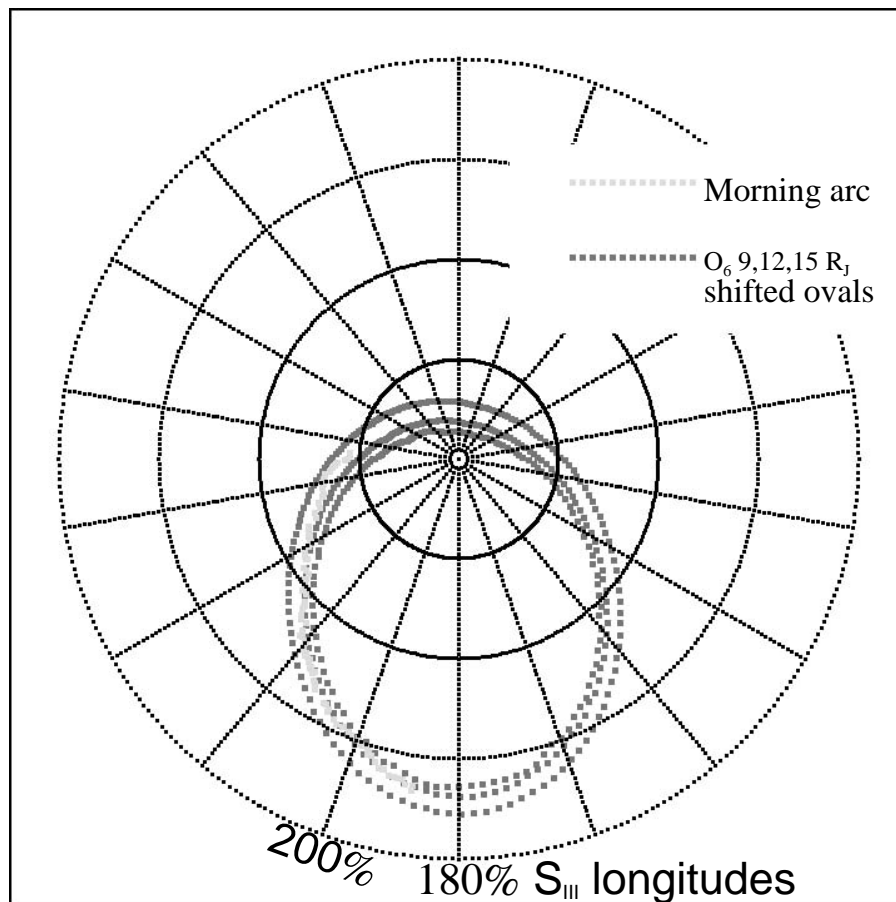


**Figure 29** : Equidistant polar projection of the morning ( $\lambda_{\text{III}} < 180^\circ$ ) section location of the boundary oval shown in figure 28. The latitude circles are separated by  $10^\circ$  and the System III longitudes increase in  $20^\circ$  steps clockwise from the reference meridian ( $\lambda_{\text{III}} = 0^\circ$ ) which is oriented toward the top. The  $180^\circ$  meridian is toward the bottom. The inner, middle and outer dark ovals represent the footprints of the shifted GSFC O<sub>6</sub> 15, 12 and 9 R<sub>J</sub> ovals, respectively.

In addition to the main oval (ARC1 in figure 27) generally observed for  $\lambda_{\text{III}} > 180^\circ$ , patchy and multiple structured emissions are frequently observed for  $\lambda_{\text{III}} < 180^\circ$ . The 10 images from July 17 to 22, 1994 (table 8) were co-added to visualize the statistical distribution of the auroral emission and to determine the equatorward boundary of the north aurora. In order to account for the different sub-Earth longitudes (CML), and for the roll angles of the spacecraft about the optical axis of the telescope, each image was projected on an equidistant cylindrical map. An average map (figure 28) was created where the intensity of each pixel, located by its planetocentric latitude and System III longitude, is the average of the corresponding pixels of the maps that cover this particular position. The equatorial boundary of the auroral emission zone is located on the average map by a series of latitude-longitude points. As apparent from the inspection of individual images, the auroral emission divides into two distinct regions showing different auroral morphologies (Gérard *et al.*, 1993, 1994b; Clarke *et al.*, 1996). The left side region, corresponding to System III longitudes between  $180^\circ$  and  $260^\circ$ , displays a single, long and thin auroral arc that results in the summation of several smaller overlapping arcs. The right side region, corresponding to longitudes between  $100^\circ$  and  $180^\circ$ , is completely filled by auroral emission with brighter features near the equatorial boundary and near the limb. Since the viewing geometry has not been corrected prior to cylindrical projection, it must be noted that these bright features could be attributed to geometrical effects. This region is the result of the accumulation of emission spread between the equatorial boundary and the pole in the individual images. This average map resembles those derived from previous studies of the ultraviolet Jovian auroral morphology made with the FOC (Gérard *et al.*, 1993, 1994b) which indicated a clear dichotomy between the longitude zones on each side of the  $180^\circ$  System III meridian. The equatorward emission boundary can be fit by an oval characterized by the 5 parameters defining a local coordinate set described in the model description section (these parameters have been used for the test cases simulation). For longitudes above  $180^\circ$ , the boundary follows the bright linear arc structure conspicuous in figure 28. At longitudes less than  $180^\circ$ , where no clear arc structure is apparent, it is defined by the equatorial limit of the diffuse emission. The equatorial boundary oval so defined is plotted in figure 28. It is located between the footprints of the magnetic field lines at  $6 R_J$  and  $30 R_J$  in the GSFC  $O_6$  model (Connerney *et al.*, 1992). It should be noted that these  $O_6$  ovals are frequently used as standard references for comparison with

the morphological results presented in the literature. Table 9 lists the simulation parameters defining the centers and sizes of the boundary oval and the 6  $R_J$  and 30  $R_J$  ovals in the GSFC  $O_6$  model. It shows that the latitude of the center of the boundary oval is close to that of both the 6 and 30  $R_J$  ovals. Its size is intermediate between these two ovals but closer to that of the 6  $R_J$  boundary. A gap of  $4^\circ$ - $6^\circ$  of latitude is observed between the foot of the Io flux tube and the oval detected by Clarke *et al.* (1996) with the WFPC2 camera.

Gérard *et al.* (1994b) and more recently Satoh *et al.* (1996), have shown that the best agreement with the observed bright auroral oval in the northern hemisphere is obtained by shifting the center of the  $O_6$  30  $R_J$  oval about  $10^\circ$  parallel to the  $270^\circ$  meridian. Figure 29 shows a polar projection of the equatorial boundary morning section, i.e. the location of the composite thin morning arc. Three theoretical ovals are overplotted and represent the footprints of the shifted ( $11^\circ$  parallel to the  $270^\circ$  meridian) 9, 12 and 15  $R_J$  ovals of the  $O_6$  model (whose accuracy is on the order of 5 to  $10^\circ$ ). It clearly illustrates that the thin morning arc can be bracketted by the shifted 9 and 15  $R_J$  ovals and might be fit by the the shifted 12  $R_J$  oval. This result corroborates those derived by Clarke *et al.* (1996) on the analysis of WFPC2 images taken in March 1995.

## IV.6 Discussion and conclusion

A model simulating Earth view of UV auroral emissions in the jovian north polar region has been developed. This model untangles the real brightness variations from purely geometrical effects, such as limb brightening, of structured and unstructured emitting regions. The application of the model to simple geometric cases shows the characteristics of the apparent brightness variations due to the altitude, the scale height and the CML of idealized auroral structures. It demonstrates how faint diffuse auroral emission inside the polar cap is able to apparently close the auroral oval along the limb. As an application of the model, we have simulated 4 images selected in the WFPC2 dataset. The model does not account for hydrocarbons absorption since its effects have been neglected in these images. Some general features can be derived from the set of simulations :

1. In the first three simulations, the limb brightening of an observed weak diffuse emission zone (GLOW1) may account for the apparent closing of the auroral oval.
2. The arc of oval ARC3 is present in the four simulations. It always appears at the morning limb of the auroral region and therefore could be linked to a phenomenon fixed in local time.
3. The emission in the afternoon region of the last three images is made of inhomogeneous diffuse zones (GLOW2, GLOW3) and of bright arcs (ARC1, ARC2). The emission altitude of this sector spreads between 400 km and 800 km. This could stem from a variation of the energies of the precipitating particles.
4. Longitudinal and/or local time variations along the auroral arcs are present in addition to the apparent brightness variations due to limb brightening effects.

It must be mentioned that the notion of "altitude of emission" is closely connected to the Chapman profile. The change in the altitude of emission between different parts of the aurora to reproduce the observed images is only valid if we consider that the vertical distribution of the brightness follows the Chapman profile everywhere in the auroral region. A composite average auroral structure was built by mapping 10 images obtained with the WFPC2 camera, covering observations taken in July 1994 (table 8). It shows a clear dichotomy between a narrow structure emission at

System III longitudes  $> 180^\circ$  (or morning sector) and broad diffuse emission at longitudes  $< 180^\circ$  (or afternoon sector). This statistical structure defines the UV equatorward boundary which is located between the  $30 R_J$  and  $6 R_J$  ovals of the GSFC  $O_6$  model.

Since most of the auroral observations were made for CMLs close to  $180^\circ$ , it is difficult to discriminate between true longitudinal and local time effects. However, for CMLs around  $180^\circ$ , the morning section appears quite thin in latitude and the auroral arc tends to follow the same distribution as clearly demonstrated by figure 29. It maps equatorial regions bracketed by the  $9 R_J$  and  $15 R_J$   $O_6$  ovals. The afternoon side, by contrast, frequently shows multiple arcs and diffuse emission regions. Some of them extend close to the pole. Such a morphological dichotomy, conspicuous both in single images and in the statistical map, could be attributed to a local time effect which is clearly detected (though not understood) in the X-ray pattern observed with the *ROSAT* High Resolution Imager in July 1994 (Waite *et al.*, 1997)

Our conclusions present both similarities and discrepancies with those reached by Satoh *et al.* (1996) based on their inversion of eight  $H_3^+$  auroral images obtained with the ProtoCAM instrument at the NASA IRTF in 1992. They concluded that, in addition to a slight shift from the nominal positions of  $O_6$  plus current sheet model, a better fit is obtained by adding two anomalies. The main one is a thin arc fixed in System III longitude with a maximum brightness near  $\lambda_{III} = 230^\circ$ . In the northern polar region, it exceeds a second weaker anomaly fixed in local time showing broad and bright emission in the afternoon section. In addition, the infrared (IR) observations indicate the presence of weaker diffuse emissions both poleward and equatorward of the main oval. The IR equatorial boundary extends approximately to the footprint of the Io torus. The dataset used in the present work is heavily weighted by images taken at CML close to  $180^\circ$  and therefore, the auroral structures that we have derived cannot be reliably fixed in longitude nor in local time. Accordingly, the comparison with the IR anomalies is somewhat ambiguous. It should be noted, however, that at CMLs close to  $180^\circ$  ARC3 is similar to the inferred thin morning arc, while ARC1, ARC2 and GLOW2 could be correlated to the infrared bright and broad emission in the afternoon section. Table 9 compares the centers and the sizes of the uniformly bright infrared auroral ovals

determined for images acquired on February 28 and on March 22, 1992 (Satoh *et al.*, 1996).

This work represents a first step in the analysis, with a simulation code, of the geometrical effects of the Jovian UV auroral images observed from Earth orbit. It demonstrates some of the considerable potentialities of the simulation code. In a near future, as more images (HST and other) become available, this code could be used to address different problems. These include the discrimination of local time and System III longitude effects, the longitudinal variation of the color ratio, the analysis of localized effects of the auroral emission such as the lag to corotation (Ballester *et al.*, 1996) or more complex details of the auroral emission structures. Many improvements of the code are possible in order to analyze specific matters. In particular, it could be coupled to an energy deposition model in the frame of a Jovian thermospheric general circulation study.

# V The longitudinal variation of the color ratio of the Jovian ultraviolet aurora : a geometric effect ?

This chapter describes a second application of the morphology model. The text is taken from a paper written by Jean-Claude Gérard, Denis Grodent, Vincent Dols, J. Hunter Waite, Jr. and published in *Geophysical Research Letters*, **25**, 1601-1604, 1998.

## **abstract**

A three-dimensional model is used to assess the role of the viewing geometry on the auroral color ratio. The simulations show that both an auroral arc with a geometry deduced from images obtained with the Hubble Space Telescope (HST) and a uniform polar cap emission produce no modulation or a minimum absorption when the longitude of the Jovian central meridian (CML) is close to  $200^\circ$ . This result is in contrast with the statistical measurements made with the International Ultraviolet Explorer (IUE) spectrograph that the hydrocarbon optical depth above the auroral emission maximizes for CMLs about  $180^\circ$ . In the frame of this simplified model, we examine a possible way to reconcile the model with the IUE data. An intrinsic longitudinal dependence of the column of methane above the level of the auroral emission is introduced in the simulation. It may result from a combination of a vigorous upwelling in sectors of strong and stable precipitation and/or a longitudinal dependence of the characteristic energy of the auroral particles.

## V.1 Introduction

The characteristics of the Jovian auroral ultraviolet emissions bear to some extent the signature of the precipitation processes. In addition to their morphology, they exhibit systematic variations in their spectral distribution. The color ratio

$$C = \frac{I(1550-1620)}{I(1230-1300)}$$

is related to the considerable drop in the CH<sub>4</sub> absorption cross section at wavelengths above 1350 Å (Yung *et al.*, 1982). It leaves the bulk of the longer wavelength H<sub>2</sub> Lyman band emissions unattenuated, while the H Ly- $\alpha$  and H<sub>2</sub> Werner and Lyman band emissions at wavelengths less than 1350 Å are substantially absorbed.

Based on eleven years of IUE spectral observations, Livengood and Moos (1990) and Harris *et al.* (1996) have shown that the brightness and relative intensity of the components of the auroral spectrum exhibit a systematic statistical dependence on the System III central meridian longitude  $\lambda_{\text{CML}}$ .

Recently, Kim *et al.* (1997) determined the absorption by methane using the Goddard High Resolution Spectrometer (GHRS) on board the HST. Their results indicate that the overlying CH<sub>4</sub> column density varies between 1 and 7 x 10<sup>16</sup> cm<sup>-2</sup> and that the highest CH<sub>4</sub> columns tend to be associated with the lowest temperatures derived from the H<sub>2</sub> rotational intensity distribution.

The correlation between the peaks of C and of the emission brightness suggests that the longitudinal maximum in the flux coincides with the highest characteristic energy of the auroral particles (Livengood *et al.*, 1990). An alternative explanation is that the maximum color ratio occurs in the longitude sector with major atmospheric perturbations generating an increased hydrocarbon column density.

A difficulty with the interpretation of the IUE observations stems from the large field of view of its aperture (21.4 x 8.9 arc sec<sup>2</sup>) used for the auroral observations. A considerable fraction of the dayside auroral emission is spatially integrated making it

difficult to untangle real from geometrical effects. The variation of the H<sub>2</sub> color ratio, including the effects of the limb brightening and the variation of the slant path in the IUE aperture was modeled in a simplified way by Livengood *et al.* (1980). However, the auroral morphology was not correctly represented due to the lack of imaging observations. Furthermore, the effect of the IUE point spread function (PSF) (Ballester *et al.*, 1996; Prangé *et al.*, 1997) was not accounted for. The PSF introduces into the measurements contributions at large slant angles from the limb which were not included in previous analyses.

This question can now be addressed with a model simulation integrating the geometrical complexity of a Jovian auroral observation from Earth orbit and data recently obtained with the new generation of imaging instruments. The HST auroral UV images (Gérard *et al.*, 1994; Clarke *et al.*, 1996; Ballester *et al.*, 1996; Grodent *et al.*, 1997) show that the morphology of the aurora is different from that based on the IUE - Voyager paradigm. They show that the discrete aurora is more closely connected with the distant magnetosphere than with the Io plasma torus region.

## V.2 The geometric simulation model

The results presented in this paper are based on the model described by Grodent *et al.* (1997). For the simulations described below, two simple morphological structures are adopted :

1. a continuous oval with a constant peak altitude and a latitudinal Gaussian distribution with an e-folding value of  $1^\circ$ . Its position, orientation and size are fitted to the "reference oval" described by Clarke *et al.* (1996)
2. a uniform auroral glow filling the polar cap inside the oval structure described before. Such a polar cap diffuse aurora appears in some HST images. It provides a second component of the auroral morphology with a distribution of slant view angles different from a simple oval.

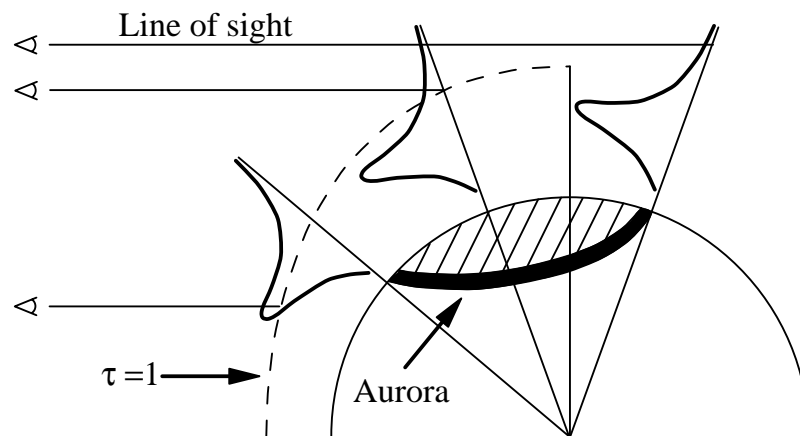


**Figure 30** : Geometry of the model simulations. The vertical distribution of the auroral emission is represented by a Chapman layer (not to scale). The dashed line corresponds to the altitude of the methane unit optical depth for the observer (see text).

The sub-Earth latitude is set to  $3^\circ$  S and the sub-Earth longitude is varied from  $0^\circ$  to  $360^\circ$ . As an approximation (Gladstone and Skinner, 1989), a Chapman profile with a topside scale height arbitrarily fixed at 50 km is used to describe the vertical auroral

emission rate. Previous studies with the simulation model (Grodent *et al.*, 1997) as well as determinations of the small but finite absorption by CH<sub>4</sub> derived from the spectral color ratio (Yung *et al.*, 1982; Gladstone and Skinner, 1989; Livengood *et al.*, 1990) indicate that the auroral emission peak probably lies close to the Jovian homopause. Figure 30 illustrates the model geometry of the simulated IUE observations.

case	emission peak (km)	altitude* (km) of $\tau_{\text{CH}_4} = 1$	CH <sub>4</sub> above emission peak* (cm <sup>-2</sup> )
a	320	313	$2.1 \times 10^{16}$
b	320	422	$1.4 \times 10^{18}$
c	420	313	$1.5 \times 10^{11}$

**Table 10** : Characteristic altitudes and methane column of the three sensitivity tests. (\* for a 60° emission angle)

As a guideline, we adopt the North Equatorial Belt (NEB) atmospheric model described by Gladstone *et al.* (1996). The methane absorption cross section is nearly constant between 1230 and 1300 Å and we use an average value of  $1.8 \times 10^{-17}$  cm<sup>2</sup> (Lee and Chiang, 1983). For an emission angle  $\chi = 60^\circ$ , the unit optical depth  $\tau$  is reached at 313 km above the 1-bar level. It raises to 330 km for an observation at 90°. Consequently, as noted by Skinner *et al.* (1984) and Livengood *et al.* (1990), for an emission layer of fixed altitude and shape, the color ratio  $C$  increases at large slant angles. The effect of the absorption by methane is simulated in good approximation by setting an emission cutoff at the  $\tau = 1$  altitude for the 1230-1300 Å range. For each value of the CML, a pair of images is simulated. The first image has no methane absorption and corresponds to a long wavelength ( $\lambda > 1400$  Å) observation. The second one has no emission contribution below  $\tau = 1$  to represent a short wavelength ( $\lambda < 1300$  Å) image. The color ratio  $C$  is then calculated based on the value of 1.1 for an unattenuated H<sub>2</sub> spectrum derived from the laboratory spectrum for 100 eV electrons on H<sub>2</sub> obtained by (Liu *et al.* (1995).

### V.3 Comparison with observations

A set of simulations was performed to assess the effect of the observing geometry on the color ratio in the case of the two simple morphological patterns described before. The peak of the emission layer is set to 320 km, an altitude close to the  $\tau = 1$  level when the atmosphere is viewed at a slant angle of  $60^\circ$ .

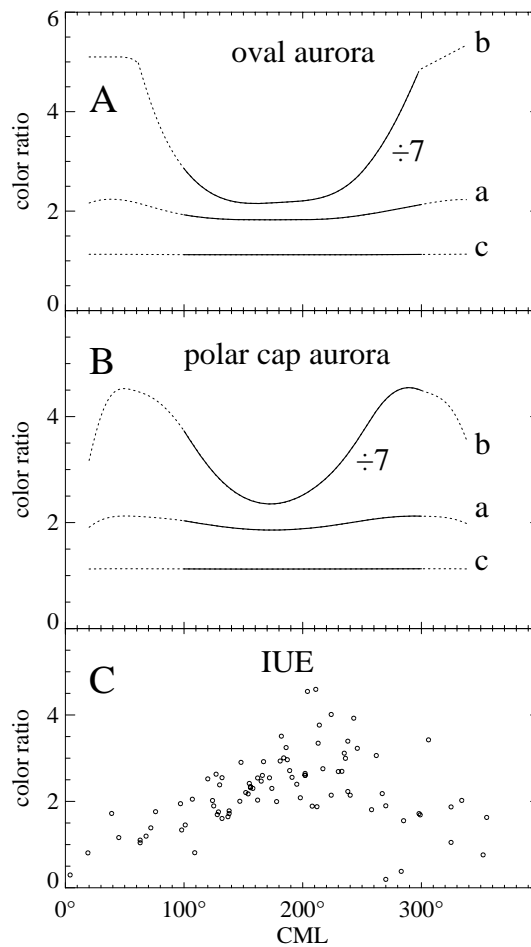


**Figure 31 :**

Simulated central meridian longitude variation of the color ratio  $C$  for three different cases: (a) auroral peak near  $\tau_{\text{CH}_4} = 1$  (see text), (b) fully mixed atmosphere, (c) emission peak 100 km higher than case a. For all three cases, a continuous homogenous oval (A) and a uniform polar cap emission (B) are used to represent the auroral distribution. The color ratio derived from the IUE data (Harris *et al.*, 1996) is also shown (C). The dotted line corresponds to longitudes with poorly defined observational constraints.

The effect of the PSF of the IUE spectrograph is accounted for by convolving the model brightness distribution with a 3.5 arc sec FWHM Gaussian (Ballester *et al.*, 1996; Prangé *et al.*, 1997) and the result is integrated over the projection of the IUE large aperture on the planetary disk. Since the IUE dataset includes observations collected over a 11-year period encompassing various aperture locations and orientations, a nominal statistical pointing centered on  $60^\circ$  and tilted  $15^\circ$  from the planetary spin axis was adopted (Harris *et al.*, 1996). It was subsequently verified that, although the orientation and projected size of the IUE aperture are important to analyze individual data sets, they are not critical to the conclusions of this study.

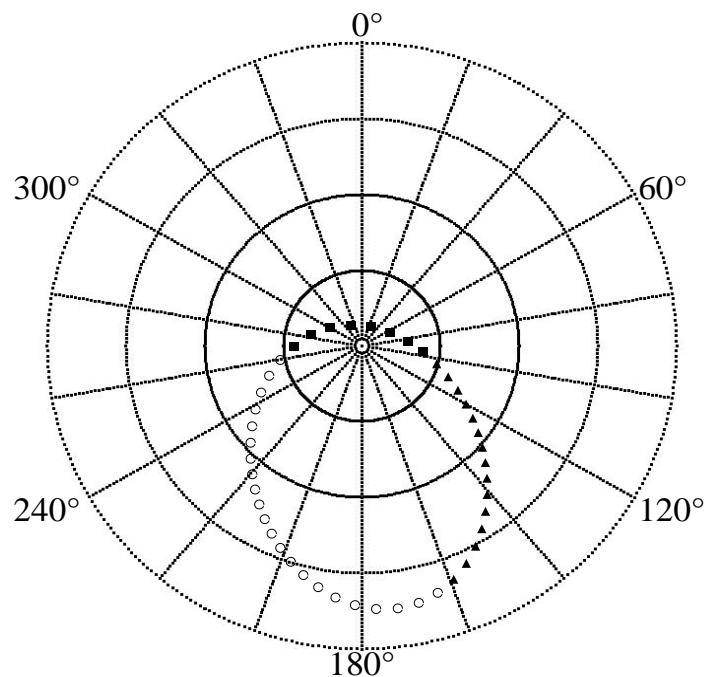


**Figure 32 :**

Polar projection of the reference auroral oval adopted for the simulations. The parallels indicate planetocentric latitudes from the North pole to  $50^\circ$  N by  $10^\circ$  increments. The auroral altitude and  $\text{CH}_4$  vertical distribution vary along the oval;  $\blacktriangle$  : case a ,  $\bigcirc$  : case b,  $\blacksquare$  case c (see Table 10).

Figure 31.A shows the CML variation of the simulated color ratio  $C$  as seen from IUE calculated for the "reference oval" described before and the NEB atmosphere by Gladstone *et al.* (1996) (case a). The comparison indicates that the longitudinal variation of  $C$  due to geometrical factors results in a shallow minimum near  $200^\circ$ , in contrast with the maximum observed near this CML with the IUE. This result is in agreement with the conclusions by Skinner *et al.* (1984) and Livengood *et al.* (1990) that the IUE color ratio

varies in the opposite sense of that required by simple geometric considerations.

The presence of the shallow color ratio seen in figure 31.A (a) above  $\lambda_{\text{CML}} = 200^\circ$  is explained by considering the path length of the auroral emission for Earth orbit observations. The main contribution at this longitude originates from the section of the oval facing the Earth with some contribution from the ansae and from the high altitude emission above the polar limb. The color ratio remains relatively small and varies only moderately along most of the oval. In contrast, the contribution near  $\lambda_{\text{CML}} = 0^\circ$  is due to an edge viewing of the emission near the pole. Larger color ratios are associated with these viewing conditions since, for large zenith angles, much of the optical path penetrates into the absorbing hydrocarbon region.

The deposition of large amounts of heat by auroral particles below the homopause may cause upwelling of  $\text{CH}_4$ -rich gas. In order to simulate vigorous upwelling (case b), a limiting case is considered where the methane mixing ratio is constant throughout the thermosphere at its value below the homopause ( $2.5 \times 10^{-3}$ ). In this "fully mixed" atmosphere, the unit optical depth in the 1230-1300 Å region is reached at 422 km for  $\chi = 60^\circ$ , that is about 100 km higher than in case a. Table 10 lists the altitude of the emission peak and of the  $\tau = 1$  level and the overlying  $\text{CH}_4$  column for an emission angle of  $60^\circ$  in the Gladstone *et al.* (1996) model. As seen in figure 31.A (b), the color ratio simulated in this case is much larger than in case a and the dependence on the CML is much more pronounced.

Finally, case c is simulated for the NEB atmosphere for an emission peak located at 420 km, 100 km above  $\tau = 1$ , corresponding to a softer particle precipitation. In this case, the color ratio remains constant at its unabsorbed value of 1.1. It is expected that these three cases represent an extreme range of methane columns encountered in the Jovian aurora.

The simulated CML dependence of the color ratio for a uniform polar cap emission with the reference oval as an equatorward boundary exhibits a shape similar to the discrete oval case (figure 31.B). The major discrepancy between the observations and the simulations remains for reasonable variations of the planetary tilt, auroral oval width, size and orientation. From these simulations covering two distinct types of auroral

morphology and various peak altitudes with respect to the methane absorption, it may be concluded that geometrical effects cannot account for the observed CML dependence of the color ratio.

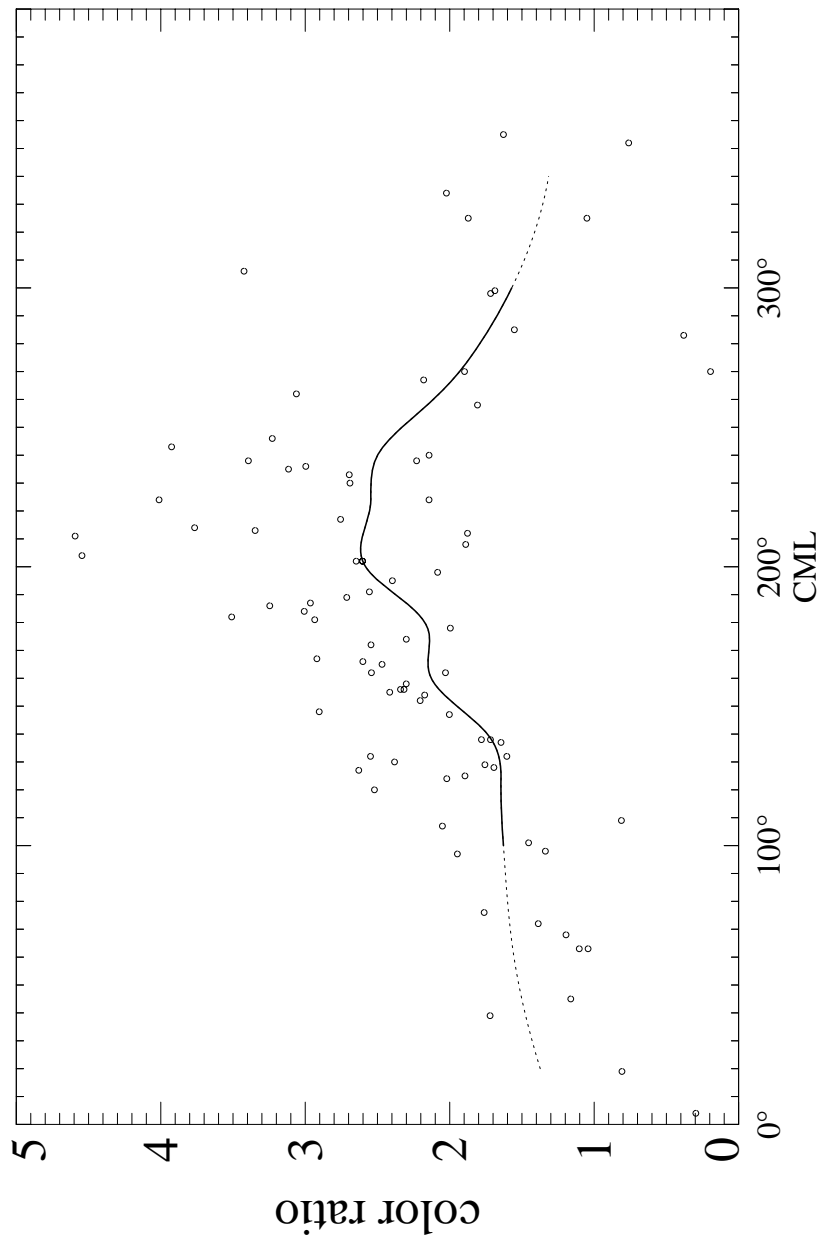


**Figure 33** : CML distribution of the simulated color ratio  $C$  of an aurora with altitude characteristics varying along the oval as illustrated in figure 32 (solid line). The dotted line corresponds to longitudes with poorly defined observational constraints. For comparison, the IUE observations are also shown as circles.

As suggested by Skinner *et al.* (1984) and modeled by Livengood *et al.*(1990), a statistical System III longitudinal dependence ( $\lambda_{\text{III}}$ ) of the column of methane in front of the auroral emission is required to explain the IUE observations. The present state of knowledge of the Jovian magnetospheric and auroral acceleration processes and of the auroral atmospheric composition does not permit a well constrained and unique solution to this problem. We have used the simulation model to verify that, using a prescribed longitude dependence of the methane column overlying the emission peak, an adequate shape of the C ratio CML variation could be obtained.

Figure 32 shows an example of such an hypothetical dependence. The oval is divided into three sectors corresponding to case a in the  $\lambda_{\text{III}}$  100°-160° sector, case b between 160° and 260° and case c from 260° to 100°. The corresponding color ratio variation with the CML as viewed through the IUE aperture is shown in Figure 33. It is seen that a maximum at 200° and a minimum near 0° are now obtained. However, the agreement with the IUE observations deteriorates in the 300°-100° region which was poorly sampled with the IUE and whose visibility from Earth orbit is at best marginal.

## V.4 Discussion

Detailed model simulations show that a morphology with a uniform aurora compatible with recent HST imaging observations leads to a CML dependence of the color ratio in the opposite sense to that of the IUE observations. A longitudinal variation integrated over the IUE aperture resembling the IUE dataset may be obtained if the altitude of the emission varies with respect to the methane absorption level. No independent evidence exists for a longitudinal dependence of the mean energy of the auroral particles. Another possibility is that the CH<sub>4</sub> column varies along the oval, leading to differential absorption as a function of longitude, possibly also reflecting changes with latitude. Upwelling of methane due to the large amount of auroral energy deposited near the homopause may indeed cause redistribution of the CH<sub>4</sub> mixing ratio above the homopause similar to the N<sub>2</sub>/O enrichment observed in the Earth's auroral thermosphere.

A System III dependence of the characteristic auroral energy, flux and/or atmospheric composition properties may be linked to the morphological features observed in the HST ultraviolet images. Examination of the HST images of the north aurora (Gérard *et al.*, 1994; Clarke *et al.*, 1996; Grodent *et al.*, 1997) have led to the conclusion that the aurora at  $\lambda_{\text{III}} > 180^\circ$  is characterized by a narrow and morphologically stable bright oval. In contrast, the aurora is generally diffuse and widespread at  $\lambda_{\text{III}} < 180^\circ$ , with much more variable structures in this sector. Concerning the three-sector oval described in Figure 32, it may be speculated that the sector  $\lambda_{\text{III}} > 180^\circ$  is characterized by an efficient upwelling of CH<sub>4</sub> due to the stability of the morphology in this sector. Alternatively, it may correspond to a region of more energetic precipitation depositing its energy at a lower altitude than the more diffuse aurora in the  $\lambda_{\text{III}} < 180^\circ$  sector.

# Part 2

## Self-consistent model of the jovian auroral thermal structure

### VI Theory

#### VI.1 Introduction

Recent progress in imaging and spectroscopy of the jovian aurora have considerably increased and improved our knowledge of the energetics induced by particle input and its potential effect on the thermospheric thermal structure of the planet. Spectroscopic observations of the UV aurora with the International Ultraviolet Explorer (IUE) satellite (Clarke *et al.*, 1979) and the ultraviolet spectrometer (UVS) onboard the *Voyager* spacecraft (Broadfoot *et al.*, 1979) suggest a total auroral particle input flux on the order of  $10^{13}$ - $10^{14}$  W in each hemisphere, about 3 orders of magnitude stronger than the corresponding value for the Earth's aurora. Such a large energy flux has been confirmed by UV images of the jovian aurora obtained with the Faint Object Camera (FOC) (Gérard *et al.*, 1993, 1994) and the Wide Field Planetary Camera (WFPC2) (Clarke *et al.*, 1998; Morrisey *et al.*, 1997) on board the Hubble Space Telescope (HST). The large amount of energy input into the atmosphere (about 100 times the global extreme ultraviolet (EUV) solar energy input) produces ionization, radiation, and particle heating in the planet's upper atmosphere. Since the energy flux in the auroral regions is so much larger than the solar heating in the thermosphere it is expected that the auroral processes maintain the large exospheric temperature observed at mid- and high-latitudes.

One-dimensional models of the interaction between energetic primary particles and the jovian atmosphere have been developed in the past on the basis of the continuous slow down approximation (Heaps *et al.*, 1973; Gérard and Singh, 1983), the two-stream (Waite *et al.*, 1983) or the multistream approximation (Kim *et al.*, 1992). These studies assumed that most of the energy input is associated with electrons rather than protons or heavy ions. This assumption rests on the lack of evidence for strong proton precipitation in the Lyman- $\alpha$  line profile (Clarke *et al.*, 1994) and the absence of characteristic lines expected for O<sup>+</sup> and S<sup>+</sup> ion precipitation (Trafton *et al.*, 1998). Furthermore, model studies indicate that about 50% of the electron beam energy is ultimately converted into heating of the neutral atmosphere (Gérard and Singh, 1982; Waite *et al.*, 1983, 1997). However, in previous studies, the thermal vertical structure and the atmospheric composition were prescribed, based on data collected by UV occultation in the equatorial regions.

Information on the thermospheric thermal structure has three principal components covering different altitude regions : 1) hydrocarbon infrared measurements at pressures around  $10^{-4}$  to  $10^{-6}$  bar, 2) H<sub>2</sub> rovibrational temperatures derived from ultraviolet spectra in the  $10^{-5}$  to  $10^{-8}$  bar range, and 3) H<sub>3</sub><sup>+</sup> spectra in the  $10^{-6}$  to  $10^{-10}$  bar pressure range. A re-analysis of the temperature structure in the North auroral region was performed by Drossart *et al.* (1993) using the *Voyager-1* infrared interferometer and radiometer spectrometer (IRIS) data. The infrared (IR) excess emission rate by the hydrocarbons was found to be  $\sim 93$  ergs cm<sup>-2</sup> s<sup>-1</sup> by methane and  $\sim 86$  ergs cm<sup>-2</sup> s<sup>-1</sup> by acetylene averaged over an auroral hot spot. Good agreement with the data was obtained by adopting a steep temperature near the homopause reaching lapse rate values of about 2 K/km.

Rovibrational H<sub>2</sub> temperatures have been determined from observations of high resolution (0.3-0.5 Å) UV spectra obtained with the Goddard High Resolution Spectrograph (GHRS) on board HST (Trafton *et al.*, 1994, 1998; Kim *et al.*, 1997; Clarke *et al.*, 1994; Dols *et al.*, 1999). The H<sub>2</sub> temperature reflects the temperature along the line of sight weighted by the auroral volume emission rate. It was found to vary between 300 to 700 K with little correlation to the H<sub>2</sub> emission brightness.

Additional information on the thermospheric auroral temperature is provided by the

analysis of the rovibrational structure of the  $\text{H}_3^+$  fundamental band near  $3.5 \mu\text{m}$  (Trafton *et al.*, 1989; Drossart *et al.*, 1989; Miller *et al.*, 1990; Lam *et al.*, 1990). These measurements indicate that the  $\text{H}_3^+$  temperature, which was shown to be close to the gas kinetic temperature, varies between 700 and 1000 K (in addition a strong anti-correlation was found between the temperature and the  $\text{H}_3^+$  column density). A neutral temperature structure constrained by these three sets of measurements, ranging from 200 K at  $10^{-7}$  bar to 2100 K at  $10^{-14}$  bar, was presented by Trafton *et al.* (1994). However, this profile is empirical and, so far, no attempt was made to link a model of particle energy deposition (and emission) with a consistent calculation of the thermal profile. No *in situ* measurement of Jupiter's auroral atmosphere vertical structure is available. The recent vertical profile derived from the *Galileo* probe (Seiff *et al.*, 1998) concerns a low latitude site. The equilibrium exospheric temperature is controlled by the total particle energy input and the energy spectrum of the primary electrons. The  $\text{H}_3^+$  concentration enhancement generated by the deposition of soft primary particles and secondary electrons acts as an efficient cooling process for the thermosphere by transferring a large fraction of the energy input to the ionosphere and subsequently radiating most of it away into space. Another fraction of the heat input is conducted downward into the hydrocarbon layer where it radiatively cools to space. The relative location of the heat source from auroral energy deposition and the altitude of the homopause will determine, in a complex way, the relative importance of  $\text{H}_3^+$  cooling, direct hydrocarbon radiation to space and downward conduction from the region of heat production to the hydrocarbon layer. The vertical distribution of hydrocarbons may also, in part, be controlled by the amount of heat dissipation below the homopause. Upwelling of hydrocarbon-rich gas due to the release of large amounts of auroral heat has been invoked as a possible source of hydrocarbon enhancement above a region of strong precipitation (Livengood *et al.*, 1990), similar to the  $\text{N}_2/\text{O}$  enhancement observed in the Earth's thermosphere during strong auroral disturbances. Inversely, a large auroral energy input near or below the homopause may cause a local temperature increase, resulting in a thermal expansion of the overlying atmosphere, a change of the altitude of the deposition peak and a resulting perturbation of the hydrocarbon cooling efficiency.

A one-dimensional model has been developed to address the question of the close coupling between auroral heat input, and the atmospheric temperature and composition structure. It couples a two-stream electron transport model of energy deposition with a 1-D thermal conduction model including particle heating and  $\text{CH}_4$ ,  $\text{C}_2\text{H}_2$  and  $\text{H}_3^+$  cooling (Waite *et al.*, 1997). In the absence of *in situ* measurements of the energy distribution of the primary auroral electrons, different distributions are used to investigate the effect on the thermal profile. The values of observable quantities such as the altitude of the  $\text{H}_2$  emission peak, IR and UV emissions and temperatures associated with various optical signatures are used to constrain the parameters of these distributions. Sensitivity tests are performed to evaluate the importance of the energy spectrum of the incident electrons for the thermal balance of Jupiter's auroral thermosphere.

## VI.2 The Jovian atmosphere

### VI.2.1 Atmospheric regions

The atmosphere of Jupiter can be divided into several regions that are defined according to the different dynamical regimes and to the behavior of the temperature profile. The nomenclature defined hereafter will be used throughout the text.

#### VI.2.1.1 Dynamical regime criterion

Like the Earth, the jovian atmosphere can be divided into three main regions (figure 34) characterized by the different dynamical regimes occurring in these atmospheric layers. They are the **homosphere** below ~300 km (measured from the 1 bar pressure level approximately corresponding to the NH<sub>3</sub> cloud deck), the **heterosphere** between ~300 km and ~2000 km, and the **exosphere** above ~2000 km (this latter altitude depends on temperature).

##### VI.2.1.1.1 The homosphere

The homosphere is the atmospheric region where mixing phenomena, such as wind and turbulence are sufficiently fast and important to keep the bulk composition of the major constituents constant in altitude. The major constituents are said to be in **perfect mixing**. As a consequence, the **mixing ratio**  $f_i = n_i / \sum n_i$ , where  $n_i$  is the density number of any constituent, is independent of altitude. The homogeneity of the major constituents disappears at an approximate altitude of 300 km known as the **homopause**. This term is often used to characterize the altitude from which turbulence phenomena are no longer efficient enough to sustain perfect mixing. The homopause is not really set at a well defined altitude but should be considered as a transition zone between homosphere and heterosphere. Numerically speaking, the homopause is defined by the altitude where the eddy diffusion coefficient becomes equal to the molecular diffusion coefficient. Since each constituent has its own molecular diffusion

coefficient, a different homopause should be defined for each species. However, these homopause altitudes are very close to each other and we therefore conveniently use the methane diffusion coefficient to calculate the altitude of the homopause.

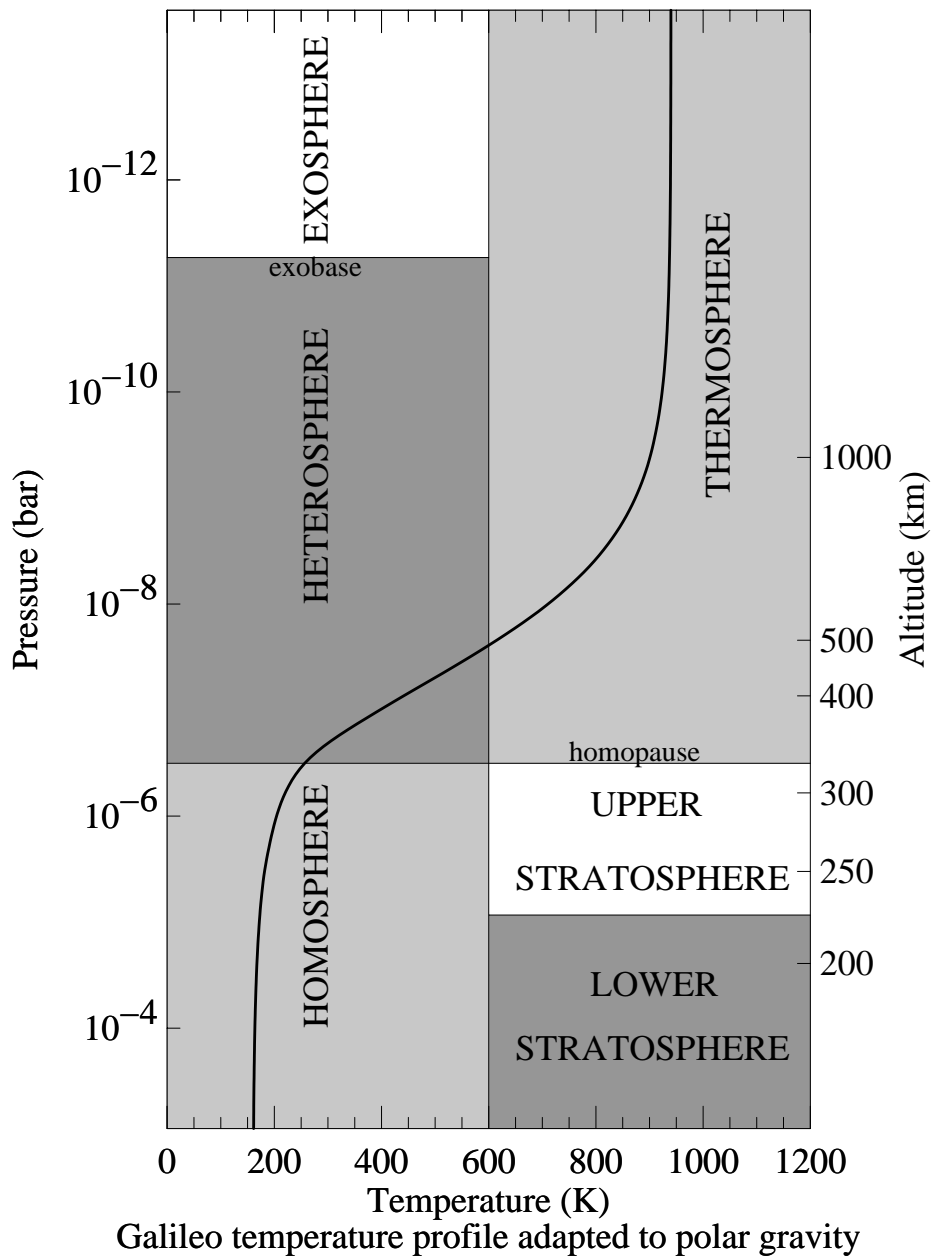


**Figure 34** : The different regions of the jovian atmosphere

#### VI.2.1.1.2 The heterosphere

In the heterosphere, molecular diffusion in the gravity field tends to separate the major constituents according to their own mass (and scale height). Molecular diffusion is also present in the homosphere but is eventually dominated by the mixing processes. Therefore, the dynamic regime in the heterosphere is completely different from the homosphere. Molecular diffusion leads to an altitude variation of the mixing ratio of the major constituents. The lighter species having a larger scale height, their concentration decrease with altitude is less pronounced than for heavier components. This can be illustrated at high altitudes where atomic hydrogen density becomes more important than molecular hydrogen density.

#### VI.2.1.1.3 The exosphere

Above a temperature dependent altitude, collisions between atmospheric particles become so rare that they can be neglected. This altitude is the **heteropause** or **exobase** and corresponds to the level from which atmospheric particles can follow parabolic, elliptic or hyperbolic paths in the gravity field. This altitude may be defined in such a way that a proportion  $\exp(-1)$  of a group of very fast particles moving vertically upwards will experience no collisions as they move out of the atmosphere. For molecules of diameter  $d$ , the probability of no collision being made in a vertical path  $dz$  is given by  $\exp[-\pi d^2 n(z) dz]$  (Houghton, 1977) where  $n(z)$  is the particle density at height  $z$ . For a proportion  $\exp(-1)$  of no collision, it comes

$$\exp[-\pi d^2 n(z) dz] = \exp(-1) ,$$

The probability for no collision in the altitude range  $z = z_{\text{exo}} \rightarrow z = \infty$  is

$$\left\{ \int_{z_{\text{exo}}}^{\infty} -\pi d^2 n(z) dz \right\} = (-1) .$$

Substituting for  $n(z)$  from the hydrostatic equation (see next section for details) :

$$n(z) = n_{\text{exo}} \exp\left(\frac{-(z - z_{\text{exo}})}{H}\right),$$

the condition for the exobase level  $z_{\text{exo}}$  is

$$\int_{z_{\text{exo}}}^{\infty} \pi d^2 n_{\text{exo}} \exp\left[\frac{-(z - z_{\text{exo}})}{H}\right] dz = 1.$$

Considering that  $T$  and  $g$  (the acceleration of gravity) are constant in this altitude range, the scale height  $H$  is constant and the integral of the exponential is exactly equal to  $H$ . The condition finally becomes :

$$n_{\text{exo}} = (\pi d^2 H)^{-1}$$

Since  $[n(z)\pi d^2]^{-1}$  is the mean free path in the horizontal direction at level  $z$ , the exobase may also be defined as the altitude at which the mean free path in the horizontal direction is equal to the scale height  $H$ . For a high altitude auroral region of Jupiter at latitude  $60^\circ$  (the acceleration of gravity  $g = 2622 \text{ cm s}^{-2}$ ), a limiting temperature of 1000 K may be assumed. Considering that  $\text{H}_2$  is still the dominant species, one estimates that the  $\text{H}_2$  density at the exobase  $n_{\text{exo}}$  is on the order of  $3 \times 10^7 \text{ cm}^{-3}$ . In the auroral atmospheric model which is used in this work, this density corresponds to an altitude of  $\sim 1700 \text{ km}$  ( $5.4 \times 10^{-12} \text{ bar}$ ).

### VI.2.1.2 Temperature profile

The atmosphere of Jupiter may also be divided according to the temperature profile. According to Hunten (1976) four regions of the non-auroral atmosphere can be highlighted : the troposphere, the stratosphere, the mesosphere and the thermosphere.

#### VI.2.1.2.1 The troposphere

The **troposphere** (below ~100 km and therefore out of reach of the present model) is rapidly stirred by vertical motions made of some combination of free convection and the vertical components of the large-scale circulation. It is characterized by a negative vertical temperature gradient which leads to temperatures between 100 and 120 K (deduced from *Galileo* probe observations at the equator).

#### VI.2.1.2.2 The lower and upper stratosphere

The **stratosphere** and **mesosphere** are regions of radiative balance : the heat sources are planetary and solar radiation (and auroral precipitation), and the sink is infrared cooling. The stratopause on Earth is located by a temperature peak near 50 km, but for Jupiter this peak is either absent or not very pronounced. The notion of mesosphere appears inappropriate for the jovian atmosphere and is not used here. Instead, we suggest that the region between the tropopause and the homopause be referred to as the stratosphere. So defined, the stratosphere may be divided into 2 sub-regions : the **lower stratosphere**, between the bottom of our model (~100 km) and approximately the level of  $\tau = 1$  methane absorption of the Ly- $\alpha$  line (~225 km), and the **upper stratosphere** between ~225 km and the homopause (~320 km). The upper stratosphere corresponds to the region where the auroral effects are the most important. The lower stratosphere is a cold region largely influenced by the strong hydrocarbon cooling (and the unspecified heating processes). At the bottom of this region the temperature is assumed to be constant (boundary condition for the resolution of the heat conduction equation) and we refer to it as the **tropospheric temperature**.

#### VI.2.1.2.3 The thermosphere

Above the upper stratosphere is the **thermosphere** where temperature increases with altitude until a constant temperature (isothermal regime) is reached referred to as the **thermospheric or exospheric temperature**.

## VI.2.2 The hydrostatic equilibrium

The stratification of the jovian atmosphere is controlled by the law of hydrostatic equilibrium which determines the variation of the gas pressure under the action of the weight of the atmospheric gas.

### VI.2.2.1 General concepts

The general motion equation of a fluid element in an external force field is given by

$$\frac{D\mathbf{V}}{Dt} = \nabla p + \mathbf{F}_{\text{ext}}$$

where  $\mathbf{V}$  is the macroscopic group velocity vector of the fluid element resulting from external macroscopic forces  $\mathbf{F}_{\text{ext}}$  and pressure gradient and

$$\frac{D}{Dt} = \frac{\partial}{\partial t} + \mathbf{v} \cdot \nabla \quad \text{is the Eulerian derivative.}$$

In the conditions of hydrostatic equilibrium  $\frac{D\mathbf{V}}{Dt} = 0$  and we can write

$$\nabla p = -\mathbf{F}_{\text{ext}}$$

Limiting ourselves to vertical motions in an atmosphere controlled by gravitational forces, this equality becomes the **hydrostatic equation**

$$\frac{dp}{dz} = -\rho g$$

in which  $p$  denotes the atmospheric pressure,  $\rho$  the atmospheric density, and  $g$  is the acceleration of gravity at height  $z$ .

The hydrostatic equation tells us that in the conditions of hydrostatic equilibrium the vertical atmospheric pressure gradient is balanced by gravitational force at all altitudes.

To a first approximation the atmospheric density is governed by this equation. This means that other transport processes, such as convection or diffusion, play a negligible role compared to pressure gradient and weight and can be considered as low order corrective terms.

For an ideal gas, the pressure  $p$  is related to the neutral gas temperature by

$$p = nkT$$

where  $n$  is the number density and  $k$  is the Boltzmann's constant.

With  $\rho = nm$  ( $m$  being the mean molecular mass), the hydrostatic equation can be written in the following form :

$$\frac{dp}{p} = \frac{dn}{n} + \frac{dT}{T} = \frac{d\rho}{\rho} + \frac{dT}{T} - \frac{dm}{m} = \frac{-dz}{kT/mg}$$

This differential equation introduces the **atmospheric scale height** parameter  $H(z)$

$$H(z) = \frac{kT(z)}{m(z)g(z)}$$

with this parameter, the hydrostatic equation can now be written as

$$\frac{dp}{p} = -\frac{dz}{H}$$

which has the formal solution

$$p = p_0 \exp\left(-\int_{z_0}^z \frac{dz'}{H}\right)$$

where  $z_0$  is a reference altitude at which pressure  $p_0 = p(z_0)$  is known.

The atmospheric scale height can therefore be viewed as the vertical length required to decrease the atmospheric pressure by a factor  $e$ .

The perfect gas law can be applied to this equation to derive the relation giving the numerical density ( $n$ ) as a function of altitude (density profile) :

$$n = n_0 \frac{T_0}{T(z)} \exp\left(-\int_{z_0}^z \frac{dz'}{H}\right)$$

where  $T_0 = T(z_0)$  and  $n_0 = n(z_0)$ .

If both  $T$  and  $g$  are constant, the scale height  $H$  is constant and the equations can be analytically integrated and give :

$$\frac{n}{n_0} = \frac{p}{p_0} = \exp\left[\frac{-(z-z_0)}{H_0}\right]$$

$$\text{where : } H_0 = \frac{kT_0}{m g_0}$$

giving rise to an exponential variation of pressure and number density above the reference level  $z_0$ .

### VI.2.2.2 Pressure-altitude relationship

All the equations developed in this model are calculated with the altitude variable ( $z$ ). However for some practical reasons that we shall discuss, it is more convenient to express the different outputs of the code according to a pressure grid. The pressure grid which we consider is characterized by a linear variation of the base-10-logarithm of the pressure. This allows to tighten the atmospheric layer steps in the region of maximum energy deposition and, conversely, to expand them in the upper thermosphere where little interaction is expected. Another important reason for using a pressure grid is that pressure is an absolute variable, while the altitude is a relative variable which has to be defined according to a reference level. The reference is set to the generally admitted 1 bar pressure level (corresponding to the  $\text{NH}_3$  cloud deck),

however other references have been used in the literature (like the 1  $\mu$ bar or the .2  $\mu$ bar levels).

The hydrostatic law can be numerically integrated to provide a relation between pressure and altitude

$$\int_{z_0}^z dz' = - \int_{p_0}^p \frac{H(p')}{p'} dp'$$

if the integrals are evaluated over sufficiently small intervals, the scale height can be considered as constant and can be taken out of the integral. Therefore :

$$z \simeq z_0 - \bar{H} \ln \left( \frac{p}{p_0} \right) \quad \text{where } \bar{H} \text{ is an average scale height.}$$

This numerically translates in a recurrence formula :

$$z(n+1) = z(n) - \left( \frac{H(n) + H(n+1)}{2} \right) \ln \left( \frac{p(n+1)}{p(n)} \right) \quad \text{for } n=1, \dots, NZ-1$$

and  $z(1) = z_0, \quad p(1) = p_0$  .

## VI.3 The electron energy degradation model

As will be discussed later, the calculation of the thermal structure of the jovian atmosphere requires the knowledge of the heating and cooling rate profiles. As far as the auroral region is concerned, the heating rate is related to the heat released by the interaction of the precipitating auroral electrons with the neutral atmospheric species. Therefore, the calculation of the auroral heating rate is achieved by an energy degradation model which is described below.

### VI.3.1 Introduction

The energy degradation scheme used in the present model is an updated version of the model described by Waite *et al.* (1983). It is based on a two-stream electron transport method for the energetic electron flux in a planetary atmosphere, as described by Nagy and Banks (1970) and Banks and Nagy (1970). A mean pitch angle is assumed for all transported electrons so that their distribution is approximated by an upward and a downward stream of electrons. The two-stream transport code calculates the flow and redistribution of the electron energy as a function of altitude from atomic and molecular processes by means of discrete energy bins. The use of a variable energy bin structure, with small 0.5 eV wide energy bins below 10 eV gradually increasing to 25 keV wide bins near 1 MeV, allows the treatment of complex energetic electron flux distributions spanning energies from 0.5 eV to 1 MeV. Once the electron fluxes are calculated, the rates of ionization, dissociation, heating and emission processes can be determined. Auroral intensities from various spectral features are also calculated.

### VI.3.2 Auroral electron transport model

A simple model of electron transport (Banks and Nagy, Nagy and Banks, 1970) that takes into account both elastic and inelastic collisions between electrons and the neutral and ionized particles of the upper atmosphere is outlined in this section. To treat this problem, it is assumed that the electron flux in the energy range  $(\epsilon, \epsilon + d\epsilon)$  along a

magnetic field line (coordinate  $s$ ) consists of two components; one component  $\Phi^+(\epsilon, s)$  directed upward along the field line (or away from the planet) and the other,  $\Phi^-(\epsilon, s)$  directed downward along the field line (or toward the planet). Electrons are assumed to be created within the atmosphere by ionization or other processes at a rate  $q(\epsilon, s)$  per unit energy and volume, such that  $q/2$  contributes to  $\Phi^+$  and to  $\Phi^-$  (Mariani, 1964).

In traveling along magnetic field lines, it is assumed that the electrons interact with the neutral and charged particles of the atmosphere through elastic collisions of cross section  $\sigma_e(\epsilon)$  and inelastic collisions of cross section  $\sigma_a(\epsilon)$ . An elastic collision can convert a downward moving electron into one moving upward and vice versa; the fraction of electrons that are backscattered by the  $k^{\text{th}}$  atmospheric species in an elastic collision of cross section  $\sigma_e(\epsilon)$  is taken as  $p_e^k(\epsilon)$ . Due to the mass factor involved in the electron-neutral or electron-ion elastic energy transfer rate, it is assumed that elastic collisions do not result in appreciable electron energy degradation.

Inelastic collisions, in contrast, cause cascading between the various electron energy groups, with the electrons absorbed at higher energies reappearing at appropriate lower energies. The fraction of backscattered electrons resulting from an inelastic collision leading to the  $j^{\text{th}}$  excitation level of the  $k^{\text{th}}$  species particle is taken as  $p_{aj}^k(\epsilon_1 \rightarrow \epsilon_2)$

As already mentioned, the electron flux is divided into two angular groups, the upward flux  $\Phi^+$  for which the pitch angle of the electron ( $\vartheta$ ) belongs to the interval  $[0 \leq \vartheta \leq 90^\circ]$  and the downward flux  $\Phi^-$  for which  $[90^\circ \leq \vartheta \leq 180^\circ]$ . The value of the resulting mean pitch angle  $\langle \cos \vartheta \rangle$  is discussed at the end of this section.

Under these conditions and neglecting gravity, thermal electric fields, and the converging nature of the magnetic field, the steady state continuity equations for the upward and downward moving electron fluxes in the range  $(\epsilon, \epsilon+d\epsilon)$  are :

$$\frac{d\Phi^+}{ds} = \frac{-1}{\langle \cos \vartheta \rangle} \sum_k n_k (\sigma_a^k + p_e^k \sigma_e^k) \Phi^+ + \frac{1}{\langle \cos \vartheta \rangle} \sum_k n_k p_e^k \sigma_e^k \Phi^- + \frac{q}{2} + \frac{q^+}{\langle \cos \vartheta \rangle}$$

$$-\frac{d\Phi^-}{ds} = \frac{-1}{\langle \cos \vartheta \rangle} \sum_k n_k (\sigma_a^k + p_e^k \sigma_e^k) \Phi^- + \frac{1}{\langle \cos \vartheta \rangle} \sum_k n_k p_e^k \sigma_e^k \Phi^+ + \frac{q}{2} + \frac{q^-}{\langle \cos \vartheta \rangle}$$

where :

$$q^{\pm}(\varepsilon, s) = \sum_k n_k(s) \sum_{i(E > \varepsilon)} \left\{ p_{ai}^k(E) \sigma_{ai}^k(E \rightarrow \varepsilon) \Phi^{\mp}(E, s) + [1 - p_{ai}^k(E)] \sigma_{ai}^k(E \rightarrow \varepsilon) \Phi^{\pm}(E, s) \right\}$$

and

$s$ , distance along a magnetic field line (positive outward)

$\Phi^+(\varepsilon, s)$ , electron flux outward along  $s$

$\Phi^-(\varepsilon, s)$ , electron flux inward along  $s$

$n^k(s)$ ,  $k^{\text{th}}$  species number density

$p_e^k(\varepsilon)$ , electron backscatter probability for elastic collisions with  $k^{\text{th}}$  species

$q(\varepsilon, s)$ , photoelectron production rate in the range  $(\varepsilon, \varepsilon + d\varepsilon)$  due to direct ionization process

$q^{\pm}$ , electron production in the range  $(\varepsilon, \varepsilon + d\varepsilon)$  due to cascading for higher energy electrons undergoing inelastic collisions

$p_{ai}^k$ , electron backscatter probability for collision with the  $k^{\text{th}}$  species resulting in the  $i^{\text{th}}$  inelastic process

$\sigma_{ai}^k$ , inelastic cross section for the  $i^{\text{th}}$  excitation of the  $k^{\text{th}}$  particle species.

By letting

$$T_1 = \frac{1}{\langle \cos \vartheta \rangle} \sum_k n_k p_e^k \sigma_e^k$$

$$T_2 = \frac{-1}{\langle \cos \vartheta \rangle} \sum_k n_k (\sigma_a^k + p_e^k \sigma_e^k)$$

$$p^{\pm} = \frac{q}{2} + \frac{q^{\pm}}{\langle \cos \vartheta \rangle}$$

and assuming that the two streams of electrons are perpendicular to the plane of the atmosphere (in the plane parallel approximation),  $ds \approx dz$  and we can write the system of

coupled differential equations :

$$\frac{d\Phi^+}{dz} = -T_2\Phi^+ + T_1\Phi^- + p^+ \quad 1)$$

$$-\frac{d\Phi^-}{dz} = -T_2\Phi^- + T_1\Phi^+ + p^- \quad 2)$$

From this system of equations, the roles of  $T_1$  and  $T_2$  are readily understood.  $T_2$  is the loss term which controls the electrons leaving a stream as a result of inelastic collision or elastic collision followed by backscattering.  $T_1$  is the backscattering (production) term which controls the electron flux leaving the opposite stream to integrate the actual ones;  $p^+$  and  $p^-$  are the electron production terms injecting the electrons that loose their energy as a result of an inelastic collision, and the secondary electrons produced by ionization.

### VI.3.2.1 Numerical resolution of the differential equations system

It is possible to turn this sets of two coupled differential equations of the first order into one single 2<sup>nd</sup> order differential equation. Indeed, from 2)  $\Phi^+$  can be written in terms of  $\Phi^-$ . The derivative of this new relation is equal to 1). From this equality one derives the 2<sup>nd</sup> order differential equation

$$\frac{d^2\Phi^-}{dz^2} + \alpha \frac{d\Phi^-}{dz} + \beta\Phi^- + \gamma = 0$$

with

$$\alpha = T_1 \frac{d}{dz} \left( \frac{1}{T_1} \right)$$

$$\beta = T_1^2 - T_2^2 - T_1 \frac{d}{dz} \left( \frac{T_2}{T_1} \right)$$

$$\gamma = T_1 p^+ + T_2 p^- + \frac{dp^-}{dz} - \frac{p^-}{T_1} \frac{dT_1}{dz}$$

Discretization of the derivatives over NZ altitude points gives the following relation, by temporarily removing the minus exponent of the downward flux :

$$\Phi_j'' + \alpha_j \Phi_j' + \beta_j \Phi_j + \gamma_j = 0 \quad 2 \leq j \leq \text{NZ}-1$$

with the two Dirichlet boundary conditions:

$$\Phi_1 \text{ and } \Phi_{\text{NZ}} \text{ fixed.}$$

Expanding  $\Phi_{j+1}$  and  $\Phi_{j-1}$  in Taylor series limited to 2<sup>nd</sup> order, two relations are obtained :

$$\Phi_{j+1} = \Phi_j + p_j \Phi_j' + \frac{p_j^2}{2} \Phi_j'' + O(p^3)$$

$$\Phi_{j-1} = \Phi_j + q_j \Phi_j' + \frac{q_j^2}{2} \Phi_j'' + O(q^3)$$

with  $p_j = z_{j+1} - z_j$  ( $z_j$  are the NZ altitude points)

$$q_j = z_{j-1} - z_j$$

which allows to eliminate  $\Phi_j''$  in order to write  $\Phi_j'$  as a function of  $\Phi_j$  alone,

then to eliminate  $\Phi_j'$  to write  $\Phi_j''$  as a function of  $\Phi_j$  alone.

Replacing  $\Phi_j''$  and  $\Phi_j'$  in the discrete form of the 2<sup>nd</sup> order differential equation, one gets :

$$a_j \Phi_{j+1} + b_j \Phi_j + c_j \Phi_{j-1} + d_j = 0$$

with 
$$a_j = \left[ \frac{q_j \alpha_j - 2}{p_j (q_j - p_j)} \right]$$

$$b_j = \left[ \frac{2 - (q_j + p_j) \alpha_j}{p_j q_j} + \beta_j \right]$$

$$c_j = \left[ \frac{2 - p_j \alpha_j}{q_j (q_j - p_j)} \right] \quad \text{and} \quad d_j = \gamma_j$$

A linear system can therefore be formed with the NZ-2 individual equations :



So far, we have obtained a method allowing complete determination of the downward electron flux  $\Phi_j^-$  along the NZ points, with the two Dirichlet boundary conditions fixing the values of  $\Phi_1^-$  and  $\Phi_{NZ-1}^-$ . The upward electron flux can be calculated from the downward flux. Indeed, from equation 1), one gets the relation :

$$\Phi^+ = R_1 - \frac{1}{T_2} \frac{d\Phi^+}{dz} \quad \text{with} \quad R_1 = \left( \frac{T_1}{2} \Phi^- + \frac{p^+}{T_2} \right)$$

First order development of the derivative leads to a recurrence relation between  $\Phi_j^+$  and  $\Phi_{j+1}^+$

$$\Phi_j^+ = R_1 + \frac{(\Phi_{j-1}^+ - R_1)}{1 + T_2(z_j - z_{j-1})} \quad \text{for } j \geq 2$$

and we can apply the lower boundary condition  $\Phi_1^+ = \Phi_1^-$  (which must be close to 0)

### VI.3.2.2 Lower boundary conditions

We have described a numerical method solving the coupled differential equation system 1) and 2) which requires two Dirichlet boundary conditions. It is however possible to apply the method to a Neumann lower boundary condition. Indeed, if  $\Phi_1^-$

equals  $\Phi_2^-$  then  $\frac{d\Phi^-}{dz} = 0$  at the bottom of the atmosphere. Consequently  $\frac{d^2\Phi^-}{dz^2} = 0$

and the second order numerical differential equation locally becomes:  $\beta\Phi^- + \gamma = 0$

that is  $\Phi_1^- = \frac{-\gamma_2}{\beta_2}$  which is the required Dirichlet boundary condition.

This method allows to choose between a Dirichlet or a Neumann lower boundary condition by simply commenting out one line in the FORTRAN program.

### VI.3.2.3 Average pitch angle

We have not given yet a numerical value to the average cosine of the electron pitch angle  $\langle \cos\theta \rangle$ . In the remaining of the text we write  $\mu = \cos\theta$  where  $\theta$  is the electron pitch angle. In the two-stream approximation, the upward flux is usually defined as  $\Phi^+ = \Phi(\mu)$  for  $0 < \mu < 1$  and the downward flux is defined as  $\Phi^- = \Phi(\mu)$  for  $-1 < \mu < 0$  and

$$\int_{-1}^1 d\mu = \int_{-1}^0 d\mu + \int_0^1 d\mu$$

If the electron pitch angle distribution is isotropic,  $\langle \cos\theta \rangle = 1/2$  for both streams. A more general approach can be invoked to derive a more appropriate value for  $\langle \cos\theta \rangle$  in better agreement with the numerical resolution method of the integrals.

Strickland *et al.* (1976) derived a general equation (from the Boltzmann transport equation) describing the behavior of an incident electron beam along a magnetic field line. It can be written as follows :

$$\mu \frac{d\Phi}{dz} = \sum_l n_l \sigma_l \Phi + \sum_l n_l \sigma_l \int_{E'>E}^{\infty} \int_{-1}^{+1} R_l(E, E', \mu, \mu') \Phi(\mu') dE' d\mu'$$

where  $n_l$  is the  $l^{\text{th}}$  species number density

$\sigma_l$  is the total scattering cross section for collision with the  $l^{\text{th}}$  species

$R_l$  is the redistribution function in energy and direction, it is related to cross sections by

$$R(\mu', \mu, E', E) = \sum_j^{\text{all processes}} \frac{\sigma_j(\mu', \mu, E', E)}{\sigma(E)}$$

The integral over  $d\mu$  can be numerically approached by summation using Gauss's numerical quadrature formula. In Gauss's formula the interval  $(-1, +1)$  is divided according to the zeros ( $\mu_j$ ) of the Legendre polynomial  $P_m(\mu)$  and the integral of a

function  $f(\mu)$  over the interval  $(-1,+1)$  is expressed as a sum in the form

$$\int_{-1}^{+1} f(\mu) d\mu \approx \sum_{j=1}^m a_j f(\mu_j)$$

where the weights  $a_j$  (also referred as the Christoffel's numbers) are given by

$$a_j = \frac{1}{P'_m(\mu_j)} \int_{-1}^{+1} \frac{P_m(\mu_j)}{\mu - \mu_j} d\mu.$$

The Rodrigues formula gives

$$P_m(\mu) = \frac{1}{2^m m!} \frac{d^m}{d\mu^m} (\mu^2 - 1)^m$$

In the two-stream approximation  $m=2$  and the two zeros of  $P_2(\mu)=0$  are  $\mu^\pm = \pm \frac{1}{\sqrt{3}}$

where the + and - indices refer to the upward and downward fluxes, respectively. The associated Christoffel's numbers are  $a^\pm = \pm 1$ .

Dividing the electron flux into 2 streams in the directions  $\mu^+$  and  $\mu^-$ , we can replace the general electron transport equation by the 2 linear equations similar to those of Banks and Nagy, but where

$$\langle \cos \vartheta \rangle = \frac{1}{\sqrt{3}}.$$

The reason Gauss's formula is superior to other formulae for quadratures in the interval  $(-1,+1)$  is that for a given  $m$  it evaluates the integral exactly for all polynomials of degree less than  $2m$  and not merely those of degree less than  $m$ ; in other words, Gauss's formula is almost twice as accurate as a formula using only  $m$  values of the function in the interval would be expected to be.

From these considerations,  $\langle \cos \vartheta \rangle = \frac{1}{\sqrt{3}}$  appears to be a value in a better agreement with the general multistream approach and is therefore adopted in this work.

### VI.3.3 Two-point Gauss-Legendre quadrature

We already introduced the concept of Gaussian quadrature in the two-stream approximation (previous section) in order to estimate the average cosine of the pitch angle distribution ( $\langle \cos\theta \rangle$ ).

The Gauss-Legendre quadrature approximates the integral

$$\int_{-1}^{+1} f(x) dx \simeq \sum_{k=1}^N w_{N,k} f(N,k)$$

by sampling  $f(x)$  at the  $n$  unequally spaced abscissas  $x_{N,1}, x_{N,2}, \dots, x_{N,N}$ , where the corresponding weights are  $w_{N,1}, w_{N,2}, \dots, w_{N,N}$ . We have seen that the abscissas and weights are obtained from the Legendre Polynomials using the Rodrigues formula.

For the **2-point Gauss-Legendre** rule,  $N=2$  and we have :

$$w_1 = 1.0 ;$$

$$w_2 = 1.0 ;$$

$$x_1 = \frac{-1}{\sqrt{3}} ;$$

$$x_2 = \frac{1}{\sqrt{3}} ;$$

$$\text{and} \quad \int_{-1}^{+1} f(x) dx \simeq f(x_1) + f(x_2) .$$

To approximate the integral  $\int_a^b f(t) dt$  we use the **shifted Gauss-Legendre rule for [a,b]**.

Introducing the change of variable  $t = \frac{a+b}{2} + \frac{a-b}{2}x$  and  $dt = \frac{b-a}{2} dx$ , and

$$\text{letting} \quad g(x) = f \left[ \frac{a+b}{2} + \frac{a-b}{2}x \right] ,$$

we can apply the previous Gauss-Legendre rule for the integral  $\frac{b-a}{2} \int_{-1}^{+1} g(x) dx$

This method is used throughout when numerical approximation of an integral is required.

## VI.4 Cross-sections

While traveling along magnetic field lines, the electrons undergo elastic and inelastic collisions with the major neutral constituents of the jovian atmosphere  $\text{H}_2$ , H, and He. The elastic electron impact cross section is taken from Moiseiwitsch (1962) for He and from Callaway (1993) for H. The  $\text{H}_2$  elastic cross section, the elastic backscatter probability and the inelastic  $\text{H}_2$  backscatter probability are derived from Shyn and Sharp (1980, 1981). Most of the inelastic electron impact cross sections are computed with the analytical formulation described by Garvey *et al.* (1977). The

$\text{B}^1 \Sigma_u^+$  state, hereafter noted B (upper level of the  $\text{H}_2$  Lyman band system) and the  $\text{C}^1 \Pi_u$  state, hereafter noted C (upper level of the  $\text{H}_2$  Werner band system) are taken from Liu *et al.* (1998). The  $\text{B}'^1 \Sigma_u^+$ ,  $\text{B}''^1 \Sigma_u^+$ ,  $\text{D}^1 \Pi_u$ ,  $\text{D}'^1 \Pi_u$   $\text{H}_2$  Rydberg states (hereafter noted B', B'', D, D', respectively) and the  $\text{E,F} \Sigma_g^+$  (E,F) excitation rates are computed with the analytical representation of Shemansky *et al.* (1987). The  $\text{a}^3 \Sigma_g^+$  triplet state (a3) of  $\text{H}_2$  cross section is compatible with Ajello *et al.* (1993) and Khakoo *et al.* (1994) and the  $\text{b}^3 \Sigma_u^+$  state (b3) excitation cross section is comparable with the measurements of Rescigno *et al.* (1993). The  $\text{c}^3 \Pi_g$  (c3) excitation cross section is compatible with Khakoo *et al.* (1986). According to Cravens *et al.* (1975) little error is introduced by assuming that it completely decays to the b3 level and then dissociates.

The Lyman- $\alpha$  emission resulting from electron impact is produced by two mechanisms. The dominant mechanism is dissociative excitation of  $\text{H}_2$ . The cross section for this process is taken from Ajello *et al.* (1995). The other mechanism is direct excitation of H, with the cross section from James *et al.* (1997). The Lyman- $\beta$  emission cross section from dissociative excitation of  $\text{H}_2$  is from Ajello *et al.* (1996).

The differential ionization cross sections are computed following the formulation of Green and Sawada (1972), Jackman *et al.* (1977) and the relativistic formulation of Garvey *et al.* (1977). They are adjusted to match the total ionization cross sections measured by Straub *et al.* (1996) for  $\text{H}_2$ , Bandyopadhyay *et al.* (1995) for H, and Stephan *et al.* (1980) for He.

Rovibrational excitation by H<sub>2</sub> is a very efficient cooling process for low energy electrons. The cross section for vibrational excitation of H<sub>2</sub> used is in agreement with Buckman *et al.* (1990) and Miles *et al.* (1972) and the rotational excitation cross section of H<sub>2</sub> has been fitted to the measurements of Linder-Schmidt (1971). The analytical excitation cross sections described by Ajello *et al.* (1995) are adopted to account for doubly excited states of H<sub>2</sub>. These states are responsible for the dissociation of H<sub>2</sub> in fast H(2p) and H(2s) fragments which are involved in the neutral heating process.

#### VI.4.1 Total inelastic cross-section

The total differential inelastic collision cross section  $\sigma^k(E,E')$  is constructed from the differential cross sections of the individual processes involving the k<sup>th</sup> neutral species. Collisions of suprathemal electrons with the ambient electrons are not included in this cross section and are treated separately during the degradation process. The total differential cross section is of major importance in the energy degradation problem since it is used to calculate the "production" of electrons at energy E' (degraded primaries or secondaries) due to electrons of energy E colliding with neutral species (q<sup>±</sup> in the formulation of Nagy and Banks).

Figure 35 is a plot of  $\sigma_a(E) = \int_0^E \sigma(E,E') dE'$  for inelastic collisions of electrons with

H<sub>2</sub>, which is the dominant neutral species in the upper stratosphere.

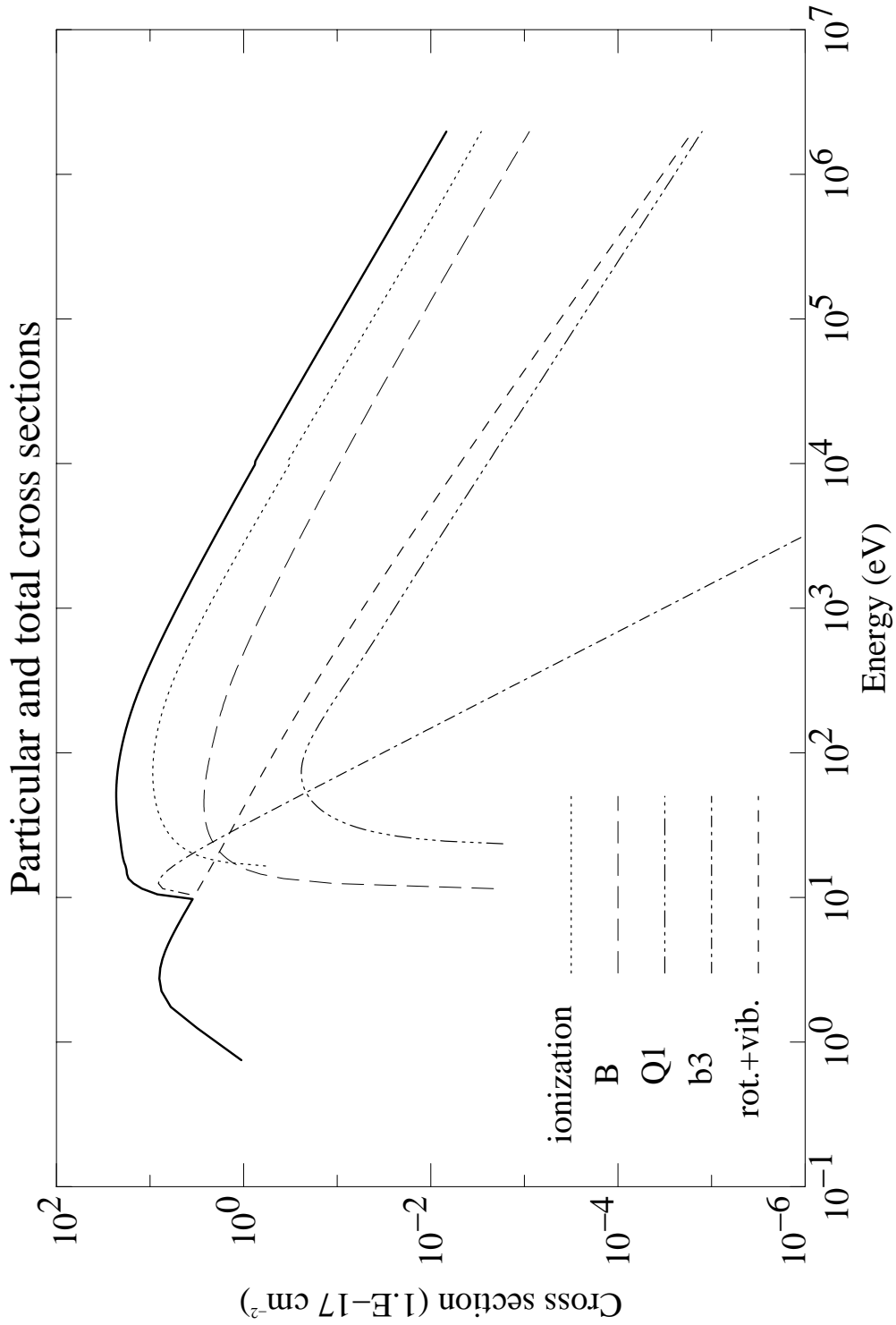
This cross section gives the probability that an electron of energy E undergoing an inelastic collision with H<sub>2</sub> will loose enough energy to end up in a lower energy bin.

For energies less than 10 eV,  $\sigma_a(E)$  is essentially due to the energy loss by excitation of vibrational and rotational levels of the H<sub>2</sub> ground state.

Between 10 and 20 eV excitation of triplet states of H<sub>2</sub> ( $a^3 \Sigma_g^+, b^3 \Sigma_u^+, c^3 \Pi_g$ ) becomes the major loss process. The energy separation between these two kinds of processes gives rise to an important cross section gap around 10 eV.

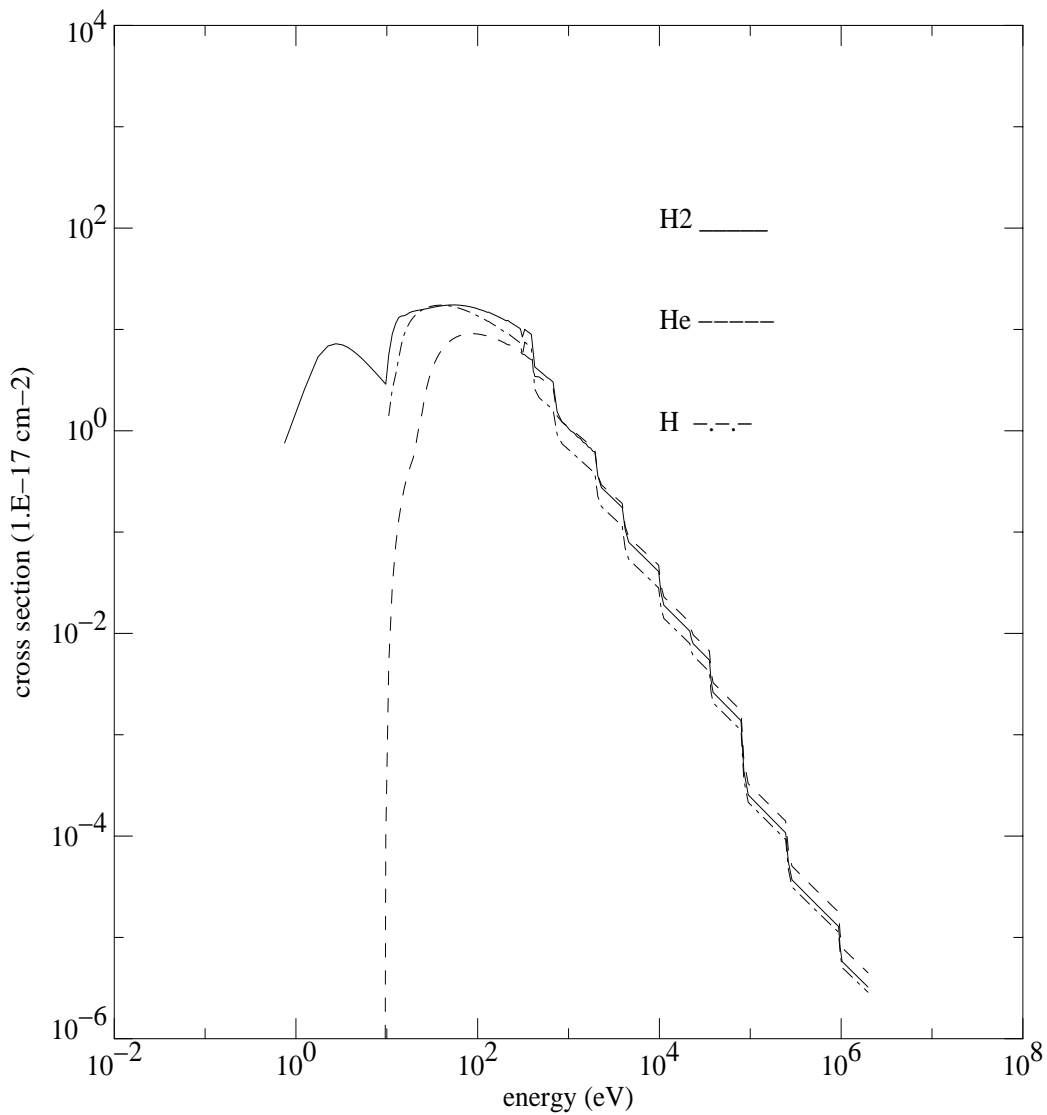
From 15 eV, the most efficient loss processes rapidly increase. They are ionization and excitation of the Lyman ( $B' \Sigma_u^+$ ) and Werner ( $C' \Pi_u$ ) singly excited states of H<sub>2</sub>. Other processes involving higher energy levels of H<sub>2</sub>, such as the Rydberg states and

doubly excited states (Q1), have much smaller cross sections but cannot be neglected since they give rise to important energy losses.



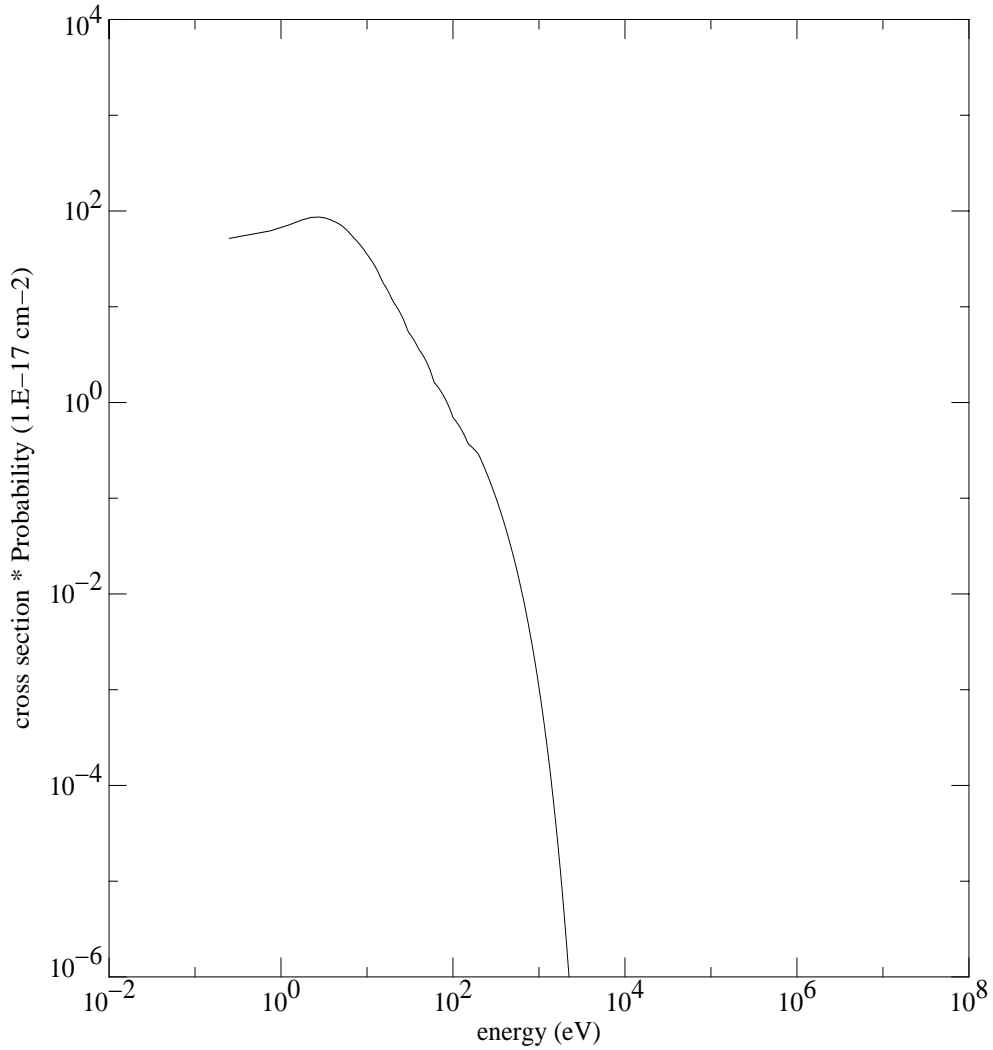
**Figure 35** : Energy dependence of the cross sections. "B" refers to the excitation from the ground level to the B state of H<sub>2</sub>, "Q1" accounts for the doubly excited states of H<sub>2</sub>. "b3" refers to the excitation to the b<sub>3</sub> triplet state of H<sub>2</sub> and "rot.+vib." represent the rotational and vibrational excitation cross section of H<sub>2</sub>.

Figure 36 compares the total cross sections for inelastic collision with H<sub>2</sub>, He and H. The major difference obviously stems from the absence of vibrational and rotational excitation for the He and H atoms; they are transparent to low energy electrons. For energies higher than 10 eV, excitation of the electronic states of He and H rapidly takes place and finally leads to ionization. The high energy tail of the cross sections is almost equal for the three species. This means that the energy degradation of high energy electrons will not depend on the distribution among the neutral densities.



**Figure 36** : Energy dependence of the total cross sections for inelastic collisions with H<sub>2</sub>, He, and H. The stairs shape of the curves is due to the method of "energy reapportionement".

The cross sections are plotted after processing by the "energy reapportionment" (described in a further section) which is used to ensure energy conservation. This method gives the stairs shape to the cross section at energies  $> 100$  eV. Each "step" corresponds to a change in the size of the energy bin.



**Figure 37** : Product of the elastic collision cross section with the backscattering probability for elastic collision as a function of the electron energy.

## VI.4.2 Backscattering

Figure 37 represents the product of the elastic collision cross section with the backscattering probability for elastic collision as a function of the electron energy. This process, which only changes the direction of the electron, is more efficient than the inelastic collisions in the 0-100 eV energy range, with a peak at 10 eV, and rapidly vanishes with increasing energy. Backscattering can also occur during inelastic collision. Its probability as a function of energy is on the same order than that of elastic collision.

The major effect of backscattering is to balance the energy distributions between the upward and downward electron streams. However, this balance is mostly efficient at low to medium energies and departures in the energy distributions of the beams appear at high energies. As a result, the upward stream carries very few high energy electrons compared to the downward stream. Another effect of the negligible backscattering efficiency at high energy is that energetic primary electrons ( $E > 1$  keV) injected at the top of the atmosphere have a chance to reach the lower region of the atmosphere where they will deposit most of their energy. On the other hand, injected soft primary electrons with energy less than 10 eV have a non-negligible probability to be backscattered to space and thus to be definitely lost for the beam. For other energies, the exact path followed by a primary electron after injection and prior to thermalization is unpredictable. We can however take the example of a 100 eV primary electron. After downward injection, backscattering probability is relatively weak and the first few collisions (elastic or inelastic) with a neutral will probably not modify its direction. As it loses energy and reaches denser regions, the backscattering probability progressively increases. At some altitude, the direction of the electron is reversed. After further collisions the electron is again backscattered downward and so on. As the frequency of direction change increases, the altitude of the electron tends toward a limiting value proportional to the initial energy. After a series of rapid bounces back and forth, the electron is finally thermalized and as far as this electron is concerned, the degradation process is over.

The different cross sections that are used in the energy degradation model are summarized in tables 11 to 14. They correspond to electron-H<sub>2</sub>, electron-He, electron-H and electron-electron collisions, respectively. In each table, the first column characterizes the energy loss process, the second column gives the reference for an analytical fit to the observed cross section, and the third column eventually gives reference for recent observations still matched by the analytical representation given in the reference of the second column. In the case of H<sub>2</sub>, He, and H ionization, the analytical fits were scaled to the new references.

### electron-H<sub>2</sub> impact cross-sections

elastic collision	Shyn and Sharp (1980, 1981)	
elastic backscatter probability	"	
inelastic backscatter probability	"	
$B' \Sigma_u^+ \quad C' \Pi_u$	Liu <i>et al.</i> (1998)	
$B'' \Sigma_u^+ \quad B''' \Sigma_u^+ \quad D' \Pi_u$ $D'' \Pi_u \quad E, F \Sigma_g^+$	Shemansky <i>et al.</i> (1985)	
$a^3 \Sigma_g^+$	Garvey <i>et al.</i> (1977)	Khakoo <i>et al.</i> (1994)
$b^3 \Sigma_u^+$	"	Rescigno <i>et al.</i> (1993)
$c^3 \Pi_g$	"	Khakoo <i>et al.</i> (1980)
d, e, f, g, h, i, j, k, p, r, s, v triplet states	"	
Ly $\alpha$ (dissociation)	Ajello <i>et al.</i> (1995)	
ionization	Garvey <i>et al.</i> (1977)	Straub <i>et al.</i> (1996)
vibrational excitation	Miles <i>et al.</i> (1972)	
rotational excitation	Linder-Schmidt (1971)	
doubly excited states (Q1)	Ajello <i>et al.</i> (1985)	

**Table 11**

**electron-He impact cross-sections**

elastic collision	Moisewitsch <i>et al.</i> (1962)	
elastic backscatter probability	assumed to be 0.5	
inelastic backscatter probability	assumed to be 0.5	
inelastic collision : ns <sup>1</sup> S, n=2, 3, 4, 5, >5 np <sup>1</sup> P, np <sup>3</sup> P, ns <sup>3</sup> S, nd <sup>1</sup> D, n=2, 3, 4, >4 nd <sup>1</sup> D, n=3, 4, 5, >5	Jackman <i>et al.</i> (1977)	
ionization	"	Stephan <i>et al.</i> (1980)

**Table 12**

**electron-H impact cross-sections**

elastic collision	Moisewitsch (1962)	Callaway <i>et al.</i> (1993)
elastic backscatter probability	assumed to be 0.5	
inelastic backscatter probability	assumed to be 0.5	
inelastic collision : electronic level n=2 ,3 ,4 ,5, >5	Olivero <i>et al.</i> (1973)	
ionization	"	Bandyopadhyay <i>et al.</i> (1995)
Ly $\alpha$	James <i>et al.</i> (1997)	
Ly $\beta$	Ajello <i>et al.</i> (1996)	

**Table 13**

**electron-electron impact cross-section**

electron-electron collision	Swartz <i>et al.</i> (1971)	
-----------------------------	-----------------------------	--

**Table 14**

## VI.5 Numerical treatment of the electron energy loss

The discrete energy degradation procedure used in the electron transport code rests on the "energy reapportionment" method described by Swartz (1985). This method allows us to use an optimized variable energy bin structure, with small 0.5 eV energy bins below 10 eV gradually increasing to 25 keV wide bins near 1 MeV. With such a variable energy grid, it is possible to account for a wide range of energies while introducing a minimum of numerical discontinuities and using a reasonably small number of energy bins.

### VI.5.1 Energy reapportionment

The term "energy reapportionment" refers to the redistribution of electron energy to the various neutral, ion, and electron species as a result of collisions. Individual inelastic collisions with the neutrals cause discrete step losses of energy from the electrons that vary from a fraction of eV to many tens of electron volts, while interactions with the ambient electrons result in a continuous loss. Ionizing collisions result in a step plus a continuum energy loss from the incident electron due to the variable energy of the secondary electron. The present method provides a practical means for achieving the best energy conservation and the most accurate repartition of energy to secondaries and the various excited states, with the smallest number of energy cells and therefore minimize computing costs.

The optimized scheme described here uses the same discrete formalism at all energies, and guarantees numerical energy conservation independently of the energy grid size or configuration. The cells of the energy grid rapidly increase in width with increasing energy, and the cells can even be larger than the excitation thresholds.

### VI.5.2 Energy reapportionment following inelastic collisions

With any discrete energy grid, there will always be incompatibilities between the true electron energies, the mean cell energies, and the discrete losses, as shown in Figure 38. In this figure the mean energies of the cell are labeled by  $E_i$  and the cell boundaries

appear at equal distances on either side. We would like to use large energy cells to minimize the number of cells required, however, if the grid is too coarse (as in the upper portion of the figure), excitation of a state whose threshold is much less than the width of the energy cell may not actually provide a loss from that cell in just one collision. (figure 38 refers to a case where three collisions were required for full

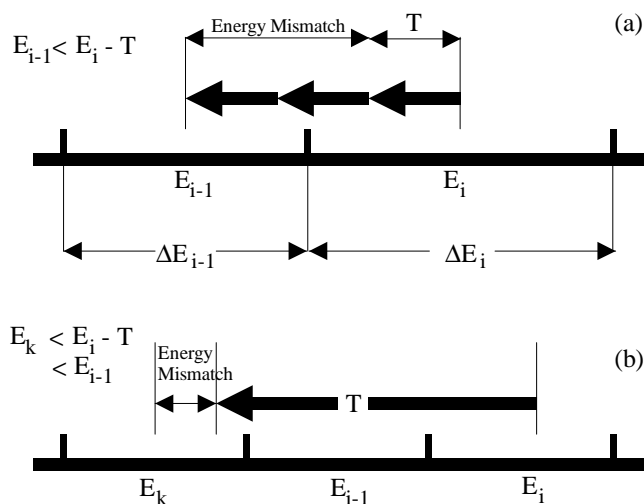


**Figure 38**

degradation from one cell to the next). Even when the cell width is less than the excitation energy (i.e., the discrete loss), there can still be energy mismatches of the order of  $\frac{1}{2}\Delta E$  like that shown in the bottom portion of figure 38. Of course, it should again be emphasized that such energy mismatches can be made arbitrarily small using a sufficiently fine energy grid with any of the basic codes used in the past, but there is a better way.

For perfect matching of the initial and degraded energies, effective cross sections ( $\sigma_a'$ ) for each excitation should be generated as products of the actual cross section ( $\sigma_a$ ) times the ratio of the threshold (T) divided by the difference between the original energy ( $E_i$ ) and the grid cell energy nearest to  $E_i - T$ . Designating this nearest cell energy as  $E_k$ , we have

$$\sigma_a' = \sigma_a \frac{T}{E_i - E_k}$$

where  $E_k$  must always be strictly less than  $E$ . For example, if three inelastic collisions (that excite a given state) are required to degrade an electron from the mean energy of one cell to the next lower cell (as in figure 38a), then the cross section is reduced by a factor of three to make such a total degradation just one-third less probable.

If the electrons of a large energy cell are entirely degraded into a smaller cell, the shape of the spectral distribution will be distorted even though energy is conserved. This situation is diagrammed in figure 39a. Assume for the moment that the cell sizes are less than the excitation energy. A simple discrete calculation would take all the electrons in cell  $E_i$  and dump them into cell  $E_k$ . In fact, the electrons would have some energy distribution over the source cell  $E_i$ , so that some being degraded (by the given process with threshold  $T$ ) near the lower cell boundary of  $E_i$  should be placed into cell  $E_{k-1}$ , while those near the upper cell boundary of  $E_i$  should go into  $E_{k+1}$ , as shown in figure 39b. Hence, if all of these electrons were degraded into cell  $E_k$  only, the distribution at  $E_k$  would be artificially enhanced in relation to the adjacent energy cells. The use of rapidly increasing energy cell sizes is contingent on means for eliminating this effect, and the key is to simply spread the electrons from the large cell over a group of smaller cells having the same total width, so long as  $T$  is greater than the cell widths. This assumes that the true spectral distribution varies slowly over any given cell.

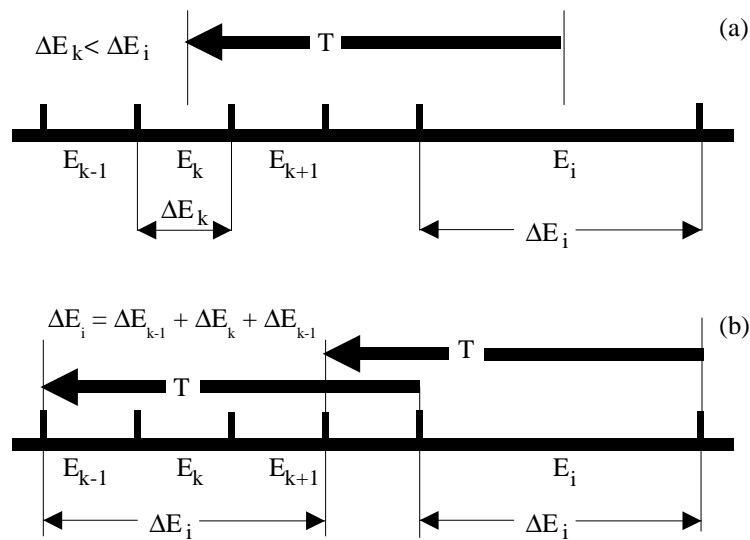


**Figure 39**

### VI.5.3 Energy reapportionment following ionizing collisions

Implementing the scheme to guarantee energy conservation for ionizing collisions is only slightly more involved than for simple inelastic collisions. Since the energy of the secondary electron is a random quantity, we must deal with functions describing distributions of secondary energies, i.e. the partial ionization cross sections. All the above arguments can then be applied to the emergent primary electrons produced by the partial ionization cross sections applied to each secondary energy. If a given secondary has an energy  $E_s$ , then the actual primary energy is

$$E_p = E_i - T_i - E_s$$

where  $E_i$  is the initial primary energy and  $T_i$ , is the ionization threshold. To compute the rates by which emergent primaries of this energy are deposited in the cell nearest to  $E_p$ , the partial ionization cross section is modified in a manner similar to that used before, giving

$$\sigma_i'(E_k) = \sigma_i(E_s) \frac{T_i + E_s}{E_i - E_k}$$

where  $\sigma(E_s)$  is the true partial ionization cross section corresponding to the given secondary energy ( $E_s$ ) and the incident primary energy ( $E_i$ ). The modified cross sections are summed to yield the total ionization cross section, which will be used to compute the loss rate from the initial primary energy cell. However, the reapportionment of secondaries is determined from the unmodified partial cross section, while the reapportionment of primaries follows the modified form. Hence the use of small energy cells at low energies will imply that the primaries cascading into a large high energy cell correspond to secondaries going into several adjacent cells of approximately the same combined width in energy.

## VI.6 Calculation of the neutral temperature profile

To investigate the effect of the auroral electron precipitation on the thermal structure of the upper atmosphere, we consider the balance between heating, cooling and transport of energy by thermal conduction. The neutral temperature profile is calculated according to the heat conduction equation

### VI.6.1 The heat conduction equation

The temperature in the thermosphere of Jupiter reflects primarily a balance between energy input from the auroral heating (and marginally from the absorption of solar EUV energy) and energy loss by conduction of the lower parts of the the atmosphere where radiative cooling at infrared wavelengths becomes important. The equation that governs the globally averaged vertical thermal structure in the thermosphere of a planet is

$$\rho C_p \frac{\partial T}{\partial t} = \frac{\partial}{\partial z} \left( \Gamma \frac{\partial T}{\partial z} \right) + H(z) - C(z)$$

where :

- T is the temperature (K),
- $\rho$  is the density of the ambient gas ( $\text{cm}^{-3}$ ),
- $C_p$  is the specific heat at constant pressure ( $\text{erg K}^{-1}$ ),
- $\Gamma$  is the thermal conductivity ( $\text{erg cm}^{-1} \text{s}^{-1} \text{K}^{-1}$ ),
- $H(z)$  is the local heating rate ( $\text{erg cm}^{-3} \text{s}^{-1}$ ),
- and  $C(z)$  is the local cooling rate ( $\text{erg cm}^{-3} \text{s}^{-1}$ ).

The thermal conductivity may be parametrized by

$$\Gamma = AT^s$$

where  $s=0.75$ ,  $A=252. \text{ ergs cm}^{-1} \text{ K}^{s+1}$  for an  $\text{H}_2$  atmosphere (Hanley *et al.*, 1970).

The time constant is sufficiently long that we can drop the time-dependent term. With this simplifying assumption we can use the following heat conduction equation to calculate the neutral temperature profile from the altitude dependent heating and cooling rates :

$$\frac{d}{dz} F(z) = H(z) - C(z)$$

where  $F(z) = \left( -\Gamma \frac{dT}{dz} \right)$  is the local heat flux in  $\text{erg cm}^{-2} \text{s}^{-1}$ .

## VI.6.2 Numerical resolution

Integrating the equation from altitude  $z$  to infinity gives the heat flux  $F(z)$  in  $\text{erg cm}^{-2} \text{s}^{-1}$  at altitude  $z$  (cm)

$$\begin{aligned} F(z) &= \int_z^{\infty} H(z') - C(z') dz' = -A T^s(z) \left( \frac{dT}{dz} \right)_z \\ &= \frac{-A}{s+1} \left( \frac{d}{dz} T^{s+1} \right)_z \end{aligned}$$

Integration between two altitude steps  $z_1$  and  $z_2$  gives

$$(s+1) \int_{z_1}^{z_2} F(z) dz = T^{s+1}(z_1) - T^{s+1}(z_2)$$

Letting  $\Theta = (s+1) \int_{z_1}^{z_2} F(z) dz$  we finally get  $T(z_2) = (T(z_1)^{s+1} + \Theta)^{\frac{1}{s+1}}$

which leads to the recurrence relation

$$T_{n+1} = (T_n^{s+1} + \Theta)^{\frac{1}{s+1}} \quad n=1, \dots, \text{NZ}-1$$

used to build a temperature profile, knowing the heating and cooling rates.

The estimation of  $\Theta$  requires two successive numerical integrations of  $F(z)$  that are achieved using a *shifted two-point Gauss-Legendre method*, which has been previously described.

### VI.6.3 Boundary conditions

The temperature profile is uniquely determined by two boundary conditions. The first condition is applied at the top of the model atmosphere where it imposes the net heat flux to be 0 (no heat exchange with the interplanetary medium).

$$\frac{d}{dz} \left( -\Gamma \frac{dT}{dz} \right)_{\text{TOP}} = H(\text{TOP}) - C(\text{TOP}) = 0$$

that is, developing the derivative  $S T_{\text{TOP}}^{S-1} \left( \frac{dT}{dz} \right)_{\text{TOP}} + \frac{d}{dz} \left( \frac{dT}{dz} \right)_{\text{TOP}} = 0$

Since the temperature at the top (the exospheric temperature) and  $S$  are different from 0, this is equivalent to apply the Neumann boundary condition :

$$\left( \frac{dT}{dz} \right)_{\text{TOP}} = 0 ,$$

that is, as expected, the temperature profile must be isothermal at the top of the model.

The second boundary condition is a Dirichlet condition which sets the tropospheric temperature at the bottom of the atmospheric model. We usually consider the temperature given by the *Galileo* profile at the pressure corresponding to the bottom of our model.

## VI.6.4 Heat sources

The major electron heating mechanisms that we considered are :

- electron impact dissociation of  $H_2$
- thermal electron cooling of the energetic electrons, and subsequent  $H_2$  vibrational and rotational cooling of the thermal electrons
- vibrational excitation of the ground electronic state of  $H_2$  following Lyman and Werner band transitions
- chemical heating due to the formation of  $H_2^+$  and H and subsequent reactions resulting in dissociative recombination of  $H_3^+$  to produce  $H_2$  and H
- excess kinetic energy from the dissociation of  $H_2$ .

The energy stored into  $H^+$  is not available for heating, since  $H^+$  recombines radiatively unless charge exchange with  $H_2$  ( $v \geq 4$ ) occurs.

### VI.6.4.1 $H_2$ dissociation

The average fractions of the transitions from the B state, including cascade from EF and from the C state terminating into the vibrational continuum of the ground state  $X^1\Sigma_g^+$ , are calculated from Dalgarno and Stephens (1970), and Stephens and Dalgarno (1972). The average kinetic energy of the fragments is determined from Stephens and Dalgarno (1973) and is consistent within 5% with the temperature sensitive values given by Abgrall *et al.* (1997). For the B'', D and D' excited states, we used the branching ratios determined by Ajello *et al.* (1984) at 100 eV to discriminate the direct transitions to the ground state from the predissociation to the B' state. These branching ratios to the ground state are 3.3%, 70.2% and 42.1%, respectively. The fraction of the transitions from the D excited state to the vibrational continuum of the ground state is from Glass-Maujean *et al.* (1984). For the B' excited state we use Kwok *et al.* (1985) which is in agreement with Liu *et al.* (1996). According to Liu *et al.* (1996), B'' the and staD' tes have approximately the same equilibrium separation as the B' and D states respectively. We thus consider the same fractions of transitions ending

in the  $X^1\Sigma_g^+$  continuum. Predissociation to B' and direct dissociation of singly excited states are considered in a global cross section determined by Ajello *et al.* (1995), giving rise to two "slow" H fragments carrying 0.3 eV each. The production of "fast" H(2p) fragments from dissociative excitation of a series of doubly excited states is also considered in the same reference. It is computed by combining two analytical cross sections giving mean fragments energies of 6.5eV+4eV(40%) and 2 times 4eV(60%), respectively. In order to account for the energy carried by the H(2s) fragments, we have considered that the singly excited states give rise to 40% of H(2s) and 60% of H(2p), while the doubly excited states are responsible for 50% of H(2p) and 50% of H(2s) (Ajello *et al.*, 1991).

Another important electron impact heat source is associated with vibrational excitation of the ground electronic state of H<sub>2</sub> following Lyman and Werner band transitions. We estimate the population of these excited states with a simple H<sub>2</sub> spectrum generator (described in part 3) for a temperature of 500 K and deduce an average vibrational energy of 2.8 eV per Lyman emission and 2.2 eV per Werner emission. Heat is produced since the time constant for vibrational relaxation is shorter than the radiative time constant for the vibrationally excited electronic ground state.

#### VI.6.4.2 Thermal electron heating

Collisions of suprathermal precipitating auroral electrons with thermal electrons is a source of heat for the thermal electron gas. The complete expression for the energetic electron-thermal electron energy loss rate (in eV cm<sup>-3</sup> s<sup>-1</sup>) was approximated by Swartz *et al.* (1971) :

$$\frac{dE}{dt} = \frac{-2 \times 10^{-12} n_e^{0.97}}{E^{0.94}} \left( \frac{E - E_e}{E - 0.35 E_e} \right)^{2.36}$$

where  $E_e = 8.6167 \times 10^{-5} T_e$  is the electron thermal energy (eV)

E is the energy loss (eV)

$n_e$  is the electron density (cm<sup>-3</sup>)

Since the ambient electrons transfer their energy to the neutral gas, all this energy is eventually transformed into neutral heat through efficient coupling of the electron thermal gas to H<sub>2</sub> rotational and vibrational excitation.

### VI.6.4.3 Chemical heating

Considerable amounts of heat are released from exothermic chemical reactions involving production and loss of atomic hydrogen (table 15). Indeed, once formed, H<sub>2</sub><sup>+</sup> ions react with H<sub>2</sub> to produce H<sub>3</sub><sup>+</sup> and H, thus breaking an H<sub>2</sub> bond. The H<sub>3</sub><sup>+</sup> ions recombine with electrons to yield either H<sub>2</sub> + H or H + H + H, along with excess kinetic energy. The H atoms ultimately recombine through three-body association with H<sub>2</sub>.

Reaction #	Reaction	Rate coefficient (cm <sup>3</sup> s <sup>-1</sup> )	Reference
1	H <sub>2</sub> <sup>+</sup> + H <sub>2</sub> → H <sub>3</sub> <sup>+</sup> + H + 1.6 eV	2.0×10 <sup>-9</sup>	Theard <i>et al.</i> (1974)
2	H <sub>3</sub> <sup>+</sup> + e <sup>-</sup> → H + H + H + 4.8 eV	1.15×10 <sup>-7</sup> $\left(\frac{300}{T}\right)^{0.65}$	Datz <i>et al.</i> (1995), Sundström <i>et al.</i> (1994)
3	→ H <sub>2</sub> + H + 9.3 eV		
4	H + H + H <sub>2</sub> → H <sub>2</sub> + H <sub>2</sub> + 4.48 eV	8×10 <sup>-33</sup> $\left(\frac{300}{T}\right)^{0.6}$	Ham <i>et al.</i> (1970)
5	H <sub>2</sub> <sup>+</sup> + e <sup>-</sup> → H + H + 10.95 eV	1×10 <sup>-8</sup>	Auerbach <i>et al.</i> (1977)

**Table 15** : list of chemical reactions, exothermicities and reaction coefficients involved in chemical heating sources.

The branching ratio of the two possible channels was measured by Datz *et al.* (1995). They show that 75% of the H<sub>3</sub><sup>+</sup> ions follow the H + H + H pathway and 25% lead to H<sub>2</sub> + H. The temperature dependence of the H<sub>3</sub><sup>+</sup> recombination coefficient was measured by Sundström *et al.* (1994) (table 15, reactions 2 and 3). Note that the H<sub>2</sub> + H pathway releases 9.3eV, almost twice as much energy as the H + H + H pathway. The very efficient H<sub>2</sub><sup>+</sup> + H<sub>2</sub> reaction (table 15, reaction 1) rapidly converts H<sub>2</sub><sup>+</sup> ions into H<sub>3</sub><sup>+</sup> ions with an energy release of 1.6eV. The three-body recombination of H atoms with

$\text{H}_2$  (table 15, reaction 4) provides 4.48eV of kinetic energy. These very large auroral heat sources will certainly generate strong thermospheric winds that will globally redistribute both heat and neutral constituents like H, however, we have considered that this reaction chain occurs in the same layer and that heat is produced at the same level. The  $\text{H}_2^+ + e \rightarrow \text{H} + \text{H}$  dissociative recombination (table 15, reaction 5) is also considered. It is less efficient than reaction (1) but provides 10.95 eV to the ambient gas.

#### VI.6.4.4 Unspecified heat sources

So far, we have considered heat sources resulting from auroral particle precipitation in the atmosphere, other non-auroral heat sources might play an important role in the temperature budget but have not been directly taken into account in this study. Joule heating generated by the presence of a perpendicular electric field in the presence of Pedersen conductivity is an important heating process in the auroral ionosphere (in the Earth atmosphere, it represents almost 50% of the heating). It is difficult to quantify since the jovian ionospheric electric field is largely unknown. Therefore, it was neglected in this study.

Solar EUV heating has been neglected as well which restricts the validity of the model to night time conditions or to daytime aurora where the particle flux exceeds the solar EUV input of  $0.1 \text{ erg cm}^{-2} \text{ s}^{-1}$ .

The exothermic hydrocarbon chemistry might as well play an important role in the stratosphere but has not been addressed in the code.

#### VI.6.4.5 Breaking gravity waves

Young *et al.* (1997) showed that the energy viscously dissipated by breaking gravity waves is comparable to that needed to heat the equatorial atmosphere. However, this conclusion was recently challenged (Matcheva *et al.*, 1999). For reasons described below, this potentially produced heat is not included in our model.

Heating of Jupiter's thermosphere by viscous dissipation of upward propagating

gravity waves due to molecular heat conduction and viscosity has been recently evaluated by Matcheva and Stobel (1999). According to Schroeberl *et al.* (1983) the large sensible heat flux associated with dissipating gravity waves and induced turbulence lead to a redistribution of sensible heat so that cooling predominates in the upper part of the wave breaking region, whereas net heating occurs in the lowest, highest pressure levels of wave breaking. By accounting for these heating and cooling regions Matcheva and Stobel found that gravity waves with amplitudes and properties consistent with those inferred from temperature variations in the *Galileo* probe temperature profile by Young *et al.* (1997) are incapable of heating Jupiter's thermosphere sufficiently to account for the large temperature gradients and high temperatures derived from probe data. The total wave energy flux at the homopause level is  $0.39 \text{ erg cm}^2 \text{ s}^{-1}$ , which produces a maximum temperature gradient of  $2.8 \text{ K km}^{-1}$  at 355 km and maximum thermospheric temperature of 380 K at 552 km above the 1-bar pressure level. The resulting thermal profile is compared to the *Galileo* profile in figure 40.

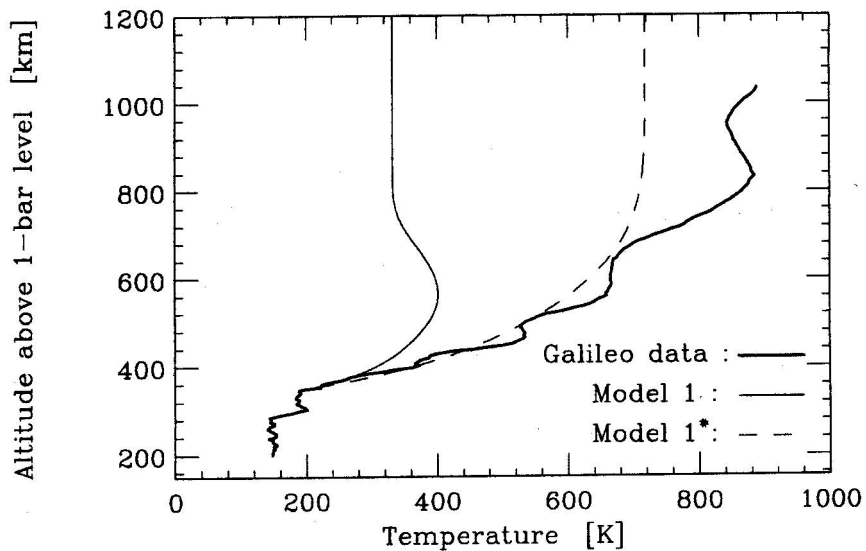


**Figure 40** : Comparison of temperature profiles generated by model 1 (thin continuous line) with the thermospheric temperature profile of Jupiter inferred from *Galileo* probe data (thick line). Taken from Matcheva and Stobel (1999)

They also demonstrated that gravity waves which attain near saturation amplitudes above 1000 km can transport and deposit sufficient power to overcome  $H_3^+$  near-IR radiation cooling and maintain large temperature gradients and high temperatures in Jupiter's thermosphere. However, no evidence for the required wave amplitudes and vertical wavelengths has been derived from Galileo probe data to date. They finally concluded that gravity waves may not be solely responsible for the observed steep temperature gradient just above the homopause.

The heating and cooling rates due to wave dissipation in model 1 of Matcheva and Strobel are shown in figure 41. Unfortunately, the authors could not conduct their calculation below approximately 380-400 km since hydrocarbon thermal IR emission is becoming important and a complete description would have required inclusion of this radiative transfer. Accordingly, it is impossible for us to account for this heating source in the stratospheric region (below the homopause) where we expected that breaking gravity waves would bring enough energy to, at least partly, balance the strong hydrocarbon cooling. Instead, (as we did) they imposed a lower boundary condition ( $z_0 = 355$  km) which fixes the temperature at  $T(z_0) = 214$  K to agree with the *Galileo* probe temperature profile.

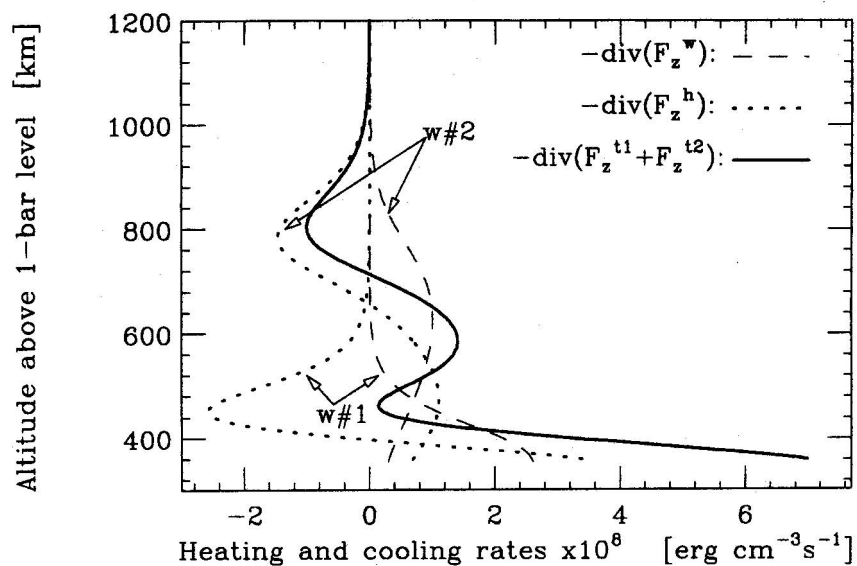


**Figure 41** : Heating and cooling rates due to wave dissipation in model 1, the net effect is plotted with a solid line. Taken from Matcheva and Strobel (1999)

Another consequence of this limitation is that the origin for the stratospheric temperature remains unexplained, although breaking gravity waves might be a good candidate.

As will be illustrated in the next sections, these non-auroral heat sources are required to balance the hydrocarbon cooling in the polar regions and to sustain the thermal profile observed in the equatorial regions. Their effect is, at least partly, mimicked by preventing the temperature, deeper than a critical pressure, to drop below the initial temperature profile.

## VI.6.5 Heat sinks

Altitude-dependent radiative cooling by thermal infrared band emissions from  $\text{H}_3^+$ ,  $\text{CH}_4$  and  $\text{C}_2\text{H}_2$  is considered following the method described by Drossart *et al.* (1993).

### VI.6.5.1 Estimation of the radiative cooling

To obtain the cooling term used in the heat conduction equation, we calculate altitude dependent rates for radiative cooling by thermal infrared band emissions from  $\text{CH}_4$ ,  $\text{C}_2\text{H}_2$  and  $\text{H}_3^+$ .

For the hydrocarbon species, we assume an optically thin regime and calculate thermal emission rates as a function of altitude for the  $\nu_4$  band of  $\text{CH}_4$  and the  $\nu_5$  band of  $\text{C}_2\text{H}_2$ . Infrared emissions from these bands play a dominant role in radiative cooling just above the homopause. The method used to calculate the hydrocarbon cooling is based on Drossart *et al.* (1993). Non-local thermodynamic equilibrium (non-LTE) effects were accounted for through the use of the cool-to-space approximation (Appleby, 1990) which neglects radiative exchange between layers compared with energy that escapes directly to space. To calculate the  $\text{H}_3^+$  cooling, we employed a method similar to that used for methane and acetylene for the  $\nu_2$  fundamental band of  $\text{H}_3^+$ . In most cases  $\text{H}_3^+$  is found to be optically thin (Lam *et al.*, 1997).

### VI.6.5.2 The local thermodynamic equilibrium (LTE)

In the local thermodynamic equilibrium (LTE) approximation, the infrared emission of  $\text{H}_3^+$ ,  $\text{CH}_4$  and  $\text{C}_2\text{H}_2$  is proportional to the number of molecules in the first vibrational level, which is an increasing function of temperature. The non-LTE correction depends on the quenching rate for each molecule. It does not significantly modify this temperature dependence and therefore, the radiative cooling efficiencies remain proportional to the gas temperature.

The internal energy of a gas in local thermodynamic equilibrium (LTE) is characterized by a single temperature, applicable to all degrees of freedom. This temperature specifies the populations of states according to a Boltzmann distribution which, within many atmospheric levels of interest, is maintained by collisions. At relatively low pressures, however, radiative processes usually control the populations of states, departures from a Boltzmann distribution occur, and the corresponding atmospheric temperatures can significantly differ from values that would hold in LTE. If  $a$  is the collisional deexcitation rate for the transition, we define

$$\xi = a/A ,$$

where  $A$  is the Einstein coefficient for spontaneous emission. In general,  $\xi$  is the parameter of importance concerning transfer of energy between the radiation field and matter.

In LTE, collisional deexcitation predominates, i.e.,  $\xi \gg 1$ , and the radiation field is coupled to the kinetic temperature of the gas. Conversely, non-LTE means that radiative decay is dominant, i.e.,  $\xi \ll 1$ , which implies, in an optically thick atmosphere, complete scattering (true absorption, followed by emission). If, as is the case for  $\text{H}_3^+$ , the atmosphere is assumed to be optically thin, then complete departure from LTE will lead to almost no excitation and therefore no emission.

Since the value of  $a$  depends on pressure and temperature,  $\xi$  provides an estimate of the

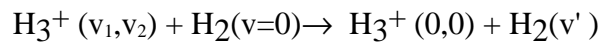
importance of non-LTE processes.

### VI.6.5.3 $\text{H}_3^+$ density and radiative cooling

We can now address the question : how does quenching of  $\text{H}_3^+$  by  $\text{H}_2$  influence the  $\text{H}_3^+$  radiative cooling ?

We only consider quenching by  $\text{H}_2$  which is dominant in the upper stratosphere and lower thermosphere.  $\text{H}_3^+$  has two vibrational modes, a symmetric breathing mode with quantum number  $\nu_1$ , and a doubly degenerate asymmetric bending mode with quantum number  $\nu_2$ .

Quenching (deactivation) of excited  $\text{H}_3^+$  by  $\text{H}_2$  may be described as



with a rate coefficient  $k_d = 2.7 \pm 0.6 \cdot 10^{-10} \text{ cm}^3 \text{ s}^{-1}$  (Kim *et al.*, 1974) (we consider complete deactivation of  $\text{H}_3^+$  to its vibrational ground state).

At thermodynamical equilibrium, the concentration of vibrationally excited  $\text{H}_3^+$  is given by

$$[\text{H}_3^+ (\nu_1, \nu_2)] = N \frac{g_\nu}{Q} \exp\left(\frac{-E\{\text{H}_3^+ (\nu_1, \nu_2)\}}{kT}\right)$$

where  $E\{\text{H}_3^+ (\nu_1, \nu_2)\}$  is the energy associated with the vibrational level  $(\nu_1, \nu_2)$

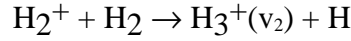
$g_\nu$  is the degeneracy of this level

$Q$  is the vibrational partition function

$N$  is the total number of  $\text{H}_3^+$  molecules

According to Drossart *et al.* (1989), the  $\text{H}_3^+$  infrared emission observed in the polar

regions of Jupiter does not arise from  $\text{H}_3^+(\nu_2)$  produced directly in the reaction



but from collisional excitation of  $\text{H}_3^+(\nu_1=0, \nu_2=0)$  by  $\text{H}_2$  with a rate coefficient  $k'_d$ .

Therefore, under steady-state conditions, the production of  $\text{H}_3^+$  excited by  $\text{H}_2$  collision equals the loss of excited  $\text{H}_3^+$  by quenching, i.e.

$$k'_d[\text{H}_2][\text{H}_3^+] = k_d[\text{H}_2][\text{H}_3^+(\nu_1, \nu_2)]$$

where  $[\text{H}_3^+]$  represents the concentration of  $\text{H}_3^+$  molecules in the  $(\nu_1=0, \nu_2=0)$  vibrational ground state, and  $[\text{H}_2]$  is the molecular hydrogen concentration in the ground state.

Since in the optically thin approximation, production by optical excitation can be neglected compared to collisional excitation, and since  $N \approx [\text{H}_3^+(\nu_1=0, \nu_2=0)]$ , the rate coefficient  $k'_d$  for the excitation reaction is related to  $k_d$  by

$$k'_d = k_d \frac{g_v}{Q} \exp\left(\frac{-E\{\text{H}_3^+(\nu_1, \nu_2)\}}{kT}\right)$$

The non-LTE correction may be brought into the production-loss balance by including a radiative loss term of  $\text{H}_3^+$  so that the production by collisional excitation is balanced by quenching **and** radiative losses. We only consider the fundamental transition  $\nu_1=0, \nu_2=1 \rightarrow \nu_1=0, \nu_2=0$  which is dominant in the infrared spectrum of  $\text{H}_3^+$ . The production-loss balance may be written as

$$k_d[\text{H}_2][\text{H}_3^+] \frac{g_v}{Q} \exp\left(\frac{-E\{\text{H}_3^+(\nu_2)\}}{kT}\right) = k_d[\text{H}_2][\text{H}_3^+(\nu_2)] + A[\text{H}_3^+(\nu_2)]$$

where  $H_3^+(v_2)$  refers to  $H_3^+$  excited in the  $v_1=0, v_2=1$  vibrational level, and  $A$  is the Einstein coefficient (in  $s^{-1}$ ) for the radiative deexcitation



at the central wavelength  $2521.31 \text{ cm}^{-1}$  ( $3.97 \text{ }\mu\text{m}$ ). An optically thick regime would have implied an additional production term (left side) due to the radiative excitation.

$$\text{By letting } \xi = \frac{k_d [H_2]}{A_{v_2}} \text{ (previously introduced)}$$

where the product  $k_d [H_2]$  represents the collisional deexcitation rate ( $a$ ) for the transition, we can estimate the number of  $H_3^+$  molecules in the vibrationally excited state with

$$[H_3^+(v_2)] = [H_3^+] \frac{g_v}{Q} \exp\left(\frac{-E\{H_3^+(v_2)\}}{kT}\right) f_{\text{LTE}}$$

where  $f_{\text{LTE}} = \frac{\xi}{1+\xi}$  is the correction factor due to non-LTE effects, and depends on the quenching rate for  $H_2$ . It is such that

if  $\xi \gg 1$ , collisions are dominant (atmosphere in LTE) and  $f_{\text{LTE}} \rightarrow 1$ , while

if  $\xi \ll 1$ , radiation is dominant (non-LTE atmosphere) and  $f_{\text{LTE}} \rightarrow 0$ .

Finally, the local emission within  $2\pi$  steradians  $I(H_3^+)$  radiated by a volume element of  $H_3^+$  (in other words, the local  $H_3^+$  cooling rate) is given by the relation

$$I(H_3^+) = [H_3^+(v_2)] A_{v_2} hc\sigma(H_3^+) \text{ in erg cm}^{-3}\text{s}^{-1},$$

where  $hc\sigma(H_3^+)$  is the energy of the transition ( $0.31 \text{ eV}$ ), so that

**$I(H_3^+)$  is proportional to  $f_{\text{LTE}}$**

Since fLTE can be rewritten in the form  $f\text{LTE} = \frac{k_d[\text{H}_2]}{k_d[\text{H}_2] + A_{v_2}}$  it is directly seen that

if  $k_d \gg \frac{A_{1,0}}{[\text{H}_2]}$ ,  $f\text{LTE} \rightarrow 1$  (LTE) and  $I(\text{H}_3^+)$  tends toward its maximum

value, while

if  $k_d \ll \frac{A_{1,0}}{[\text{H}_2]}$ ,  $f\text{LTE} \rightarrow 0$  (non-LTE) and  $I(\text{H}_3^+)$  vanishes.

From this discussion it appears that the effect of the quenching rate is solely due to the non-LTE correction factor.

This relation also shows that the  $\text{H}_3^+$  radiative cooling efficiency is temperature dependent. Indeed,  $I(\text{H}_3^+)$  is proportional to the excited population  $[\text{H}_3^+(v_2)]$  which has just been shown to be proportional to the exponential term

$$\exp\left(\frac{-E\{\text{H}_3^+(v_2)\}}{kT}\right)$$

A plot of this exponential as a function of temperature is presented in figure 42 in arbitrary units. It clearly shows that the cooling efficiency increases as the temperature increases. This temperature effect is extremely pronounced in the 100-1000 K region (that is the range of temperatures observed in the Jovian atmosphere) as the exponential spans 13 orders of magnitude in that range.

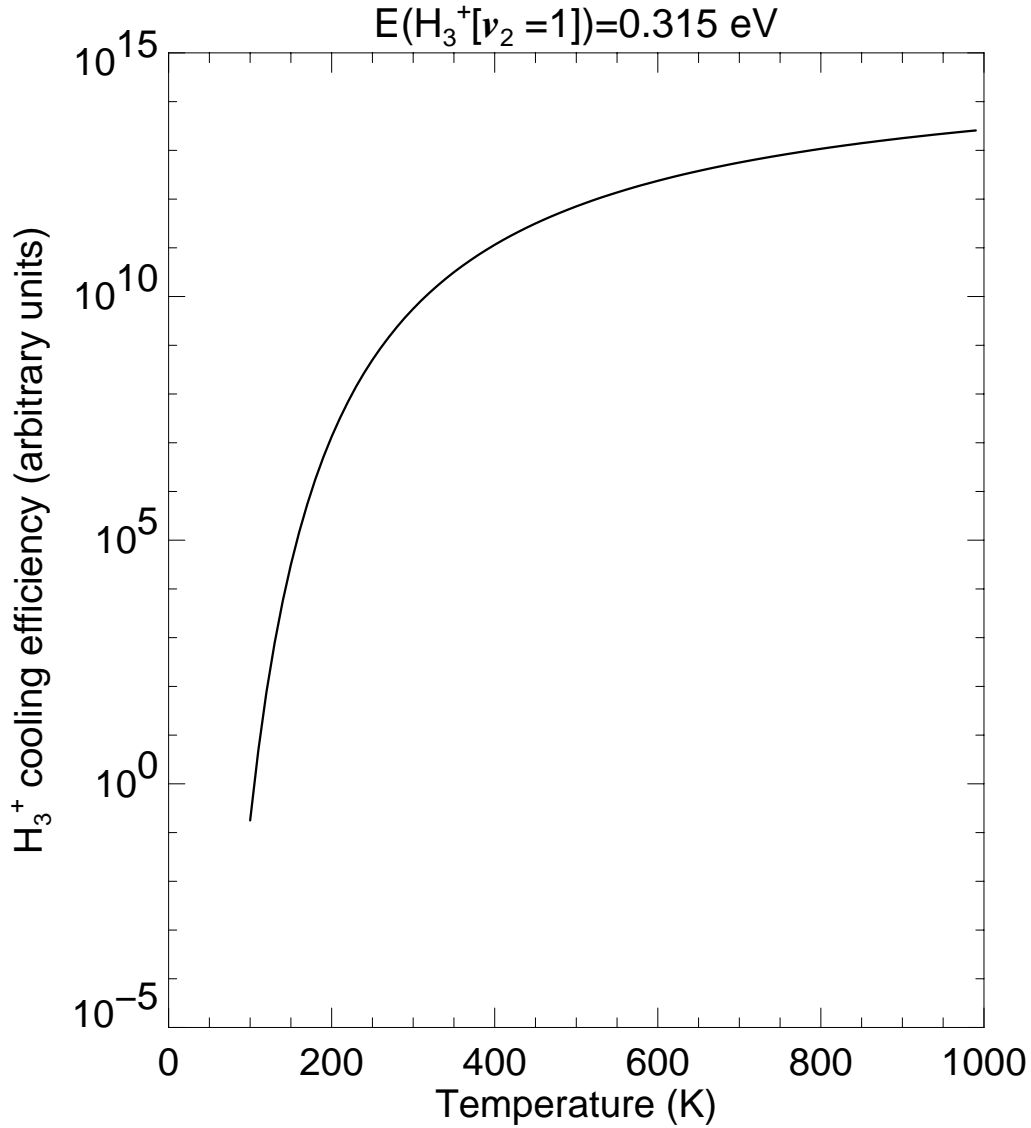
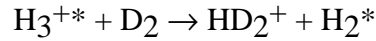


**Figure 42** : Temperature dependence of the  $\text{H}_3^+$  cooling efficiency.

Quenching of  $\text{H}_3^+$  by  $\text{H}_2$  can occur either by vibrational transfer without atom transfer or by chemical reaction such as proton transfer. Kim *et al.* (1974) measured a "phenomenological" rate coefficient of  $2.7 \pm 0.6 \times 10^{-10} \text{ cm}^3 \text{ s}^{-1}$  for the deactivation of  $\text{H}_3^+$  with vibrational energies of 0.5-2.5 eV by  $\text{H}_2$ . It is to be compared with the experimental vibration-to-translation (VT) quenching rate of  $\text{H}_3^+$  by  $\text{H}_2$  which is on the order of  $10^{-12} \text{ cm}^3 \text{ s}^{-1}$  (Blakley *et al.*, 1977), and to the rate constant for resonant

proton transfer between  $\text{H}_3^+$  and  $\text{H}_2$ , i.e.



for which the Langevin gas kinetic rate constant is  $3 \times 10^{-10} \text{ cm}^3 \text{ s}^{-1}$ .

Comparison between the rate coefficients of these processes show that resonant proton transfer may in fact be the mechanism for energy transfer in the collisions.

#### VI.6.5.4 Collisional deexcitation for hydrocarbons and radiative cooling

Two collision relaxation rates are identified for methane and acetylene,  $a^{\text{VV}}$  and  $a^{\text{VT}}$ .

"VT" (vibration-to-translation) refers to the collisional deexcitation from a molecule's lowest energy vibrational mode to the ground vibrational state. In other words, all vibrational energy in the molecule is transferred to translational degrees of freedom. For  $\text{CH}_4$  in Jupiter, the VT transition is  $\nu_4 \rightarrow \text{ground}$ .

"VV" relaxation refers to the faster vibration-to-vibration transitions between the sublevels of each band group. These mechanisms result in LTE distributions within each group, if pressure and temperature are high enough. A molecule excited to a given level will generally undergo multiple VV transitions prior to a VT relaxation. Much smaller energies are exchanged in VV, as compared with VT processes. In general,  $a^{\text{VV}} \gg a^{\text{VT}}$ , which means all rate-determining steps involve VT transitions. We therefore only considered  $a^{\text{VT}}$  as the collisional deexcitation rate for the transition ( $a \approx a^{\text{VT}}$ ).

For non-LTE "nominal" models considering a mixture of  $\text{CH}_4$  and  $\text{H}_2$ , the following  $\text{CH}_4$  VT collisional relaxation time  $t^{\text{VT}} (= a^{\text{VT}-1})$  was employed :

$$t^{\text{VT}} = t_0^{\text{VT}} / P(\text{H}_2) \quad (P(\text{H}_2) \text{ is the } \text{H}_2 \text{ pressure}),$$

and  $t_0^{\text{VT}}$  is temperature dependent and is given by

$$\ln(t_0^{\text{VT}}) = 35.6 T^{-1/3} - 6.838$$

This collisional relation time can be used to define the non-LTE correction factor fLTE (equivalent to the correction factor defined for H<sub>3</sub><sup>+</sup>) giving the fraction of v<sub>4</sub> vibrational energy which is converted to kinetic energy at the atmospheric level in question.

$$\xi = a/Av_4 \quad (\text{or } \xi = (t^{\text{VT}} Av_4)^{-1})$$

and,

$$f\text{LTE} \equiv (1 + \xi^{-1})^{-1}$$

where Av<sub>4</sub> is the Einstein coefficient (in s<sup>-1</sup>) for radiative deexcitation



and the central wavelength is 1306 cm<sup>-1</sup> (7.7 μm).

As already mentioned, fLTE is bounded by 0 (non-LTE ; ξ= 0) and 1 (LTE ; ξ≫ 1).

Using the same considerations as with H<sub>3</sub><sup>+</sup>, we can estimate the local emission within 2π steradians I(CH<sub>4</sub>) radiated by a volume element of CH<sub>4</sub> (in other words, the local CH<sub>4</sub> cooling rate) with the relation

$$I(\text{CH}_4) = [\text{CH}_4(v_4)] Av_4 hc\sigma(\text{CH}_4) \quad \text{in erg cm}^{-3}\text{s}^{-1},$$

where hcσ(CH<sub>4</sub>) is the energy of the v<sub>4</sub> → ground transition, and the concentration of excited methane is given by

$$[\text{CH}_4(v_4)] = [\text{CH}_4(0)] \frac{g_v}{Q} \exp\left(\frac{-E[\text{CH}_4(v_4)]}{kT}\right) f\text{LTE}$$

The case of acetylene is treated in exactly the same way. Following Appleby (1990), the CH<sub>4</sub> VT collisional relaxation time t<sup>VT</sup> can be applied directly to C<sub>2</sub>H<sub>2</sub> v<sub>5</sub> without modification. Accordingly, we can estimate the local emission within 2π steradians

$I(\text{C}_2\text{H}_2)$  radiated by a volume element of  $\text{C}_2\text{H}_2$  (the local  $\text{C}_2\text{H}_2$  cooling rate) with the relation

$$I(\text{C}_2\text{H}_2) = [\text{C}_2\text{H}_2(v_5)] A_{v_5} hc\sigma(\text{C}_2\text{H}_2) \quad \text{in erg cm}^{-3}\text{s}^{-1},$$

where  $hc\sigma(\text{C}_2\text{H}_2)$  is the energy of the  $v_5 \rightarrow$  ground transition, and

$$[\text{C}_2\text{H}_2(v_5)] = [\text{C}_2\text{H}_2(0)] \frac{g_v}{Q} \exp\left(\frac{-E[\text{C}_2\text{H}_2(v_5)]}{kT}\right) \text{fLTE}$$

with  $\text{fLTE} \equiv (1 + \xi^{-1})^{-1}$ , and  $\xi = (t^{\text{VT}} A_{v_5})^{-1}$

where  $A_{v_5}$  is the Einstein coefficient for the radiative deexcitation



and the  $v_5$  central wavelength is  $729 \text{ cm}^{-1}$  ( $1.4 \mu\text{m}$ ).

#### VI.6.5.5 Departure from the optically thin approximation

The optically thin condition can be viewed as the probability that a photon, emitted at an altitude  $z$ , will be reabsorbed in the atmosphere is smaller than 0.5. This implies (Drossart *et al.*, 1993) that the pressure level  $P \leq 40 \mu\text{bars}$  for  $\text{C}_2\text{H}_2$ , and  $P \leq 50 \mu\text{bars}$  for  $\text{CH}_4$ . Below this level, the observed infrared emission does not remain a reliable indicator of the atmospheric cooling due to methane and acetylene. However, the cooling efficiency should not be reduced in the optically thick regime. Indeed, since the excited population can always be neglected compared to the ground state population, the optical excitation of  $\text{CH}_4$  and  $\text{C}_2\text{H}_2$  will not reduce the (cooling) collisional excitation process but increase the (trapped) infrared emission.

## VI.7 Response of the atmospheric structure to auroral electron precipitation

### VI.7.1 The initial model atmosphere

The initial model atmosphere is based on an analytical fit using a Bates function fitted to the thermal profile determined by Seiff *et al.* (1998) from the *Galileo* probe data (Figure 43). This thermal profile was calculated from the atmospheric density deduced from the deceleration measurement of the probe during its entry and descent in the Jovian atmosphere. It assumes an exospheric temperature of 900 K.

### VI.7.2 Effects of electron precipitation

As a consequence of the heating processes previously described, precipitating auroral electrons modify the thermal profile of the jovian thermosphere. In order to self-consistently account for the adjustment of the densities to the resulting temperature profile, the code iteratively solves a diffusion equation for the major constituents.

#### VI.7.2.1 Diffusion of the neutral species

The neutral atmosphere of Jupiter is mainly composed of  $\text{H}_2$ . Other important neutral gases considered in this model are He, H,  $\text{CH}_4$ , and  $\text{C}_2\text{H}_2$ .

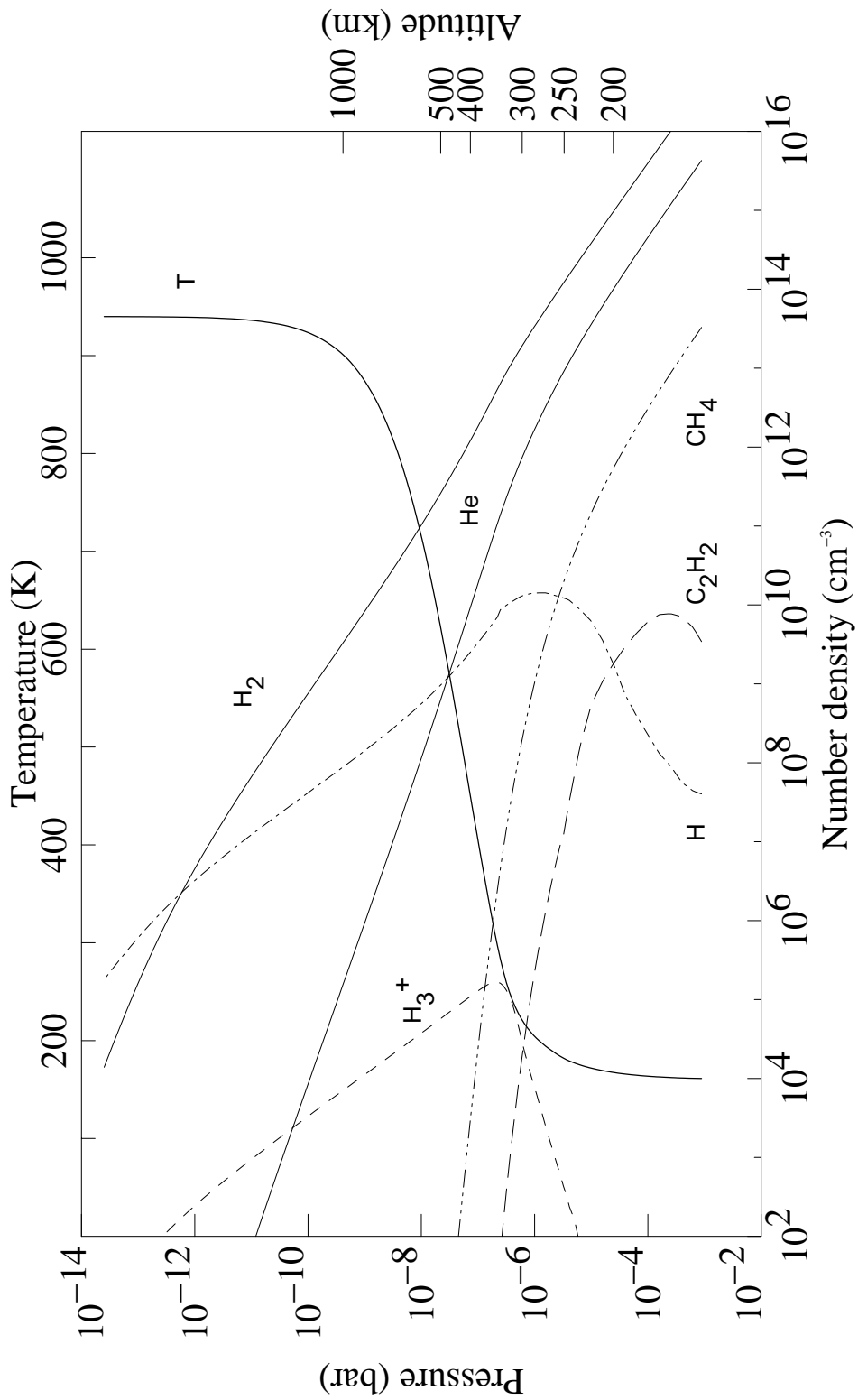


**Figure 43** : Initial model atmosphere : the temperature profile is an analytical fit to the equatorial thermal profile determined from the *Galileo* probe data adapted to the larger acceleration of gravity at 60° N and thermospheric altitudes. The density profiles are calculated as discussed in the text. The energy distribution of case A determines the ionization rate from which the  $H_3^+$  density is estimated.

### VI.7.2.1.1 The diffusion equation

For a binary mixture the general diffusion equation giving the relative diffusion velocity  $\mathbf{v} = \mathbf{v}_1 - \mathbf{v}_2$  of gas 1 with respect to gas 2, can be written as (Chapman and Cowling, 1970)

$$\mathbf{v} = -D_{12} \left[ \frac{n^2}{n_1 n_2} \nabla \left( \frac{n_1}{n} \right) + \frac{m_2 - m_1}{m} \nabla (\ln p) + \alpha_T \nabla (\ln T) - \frac{m_1 m_2}{mkT} (\mathbf{F}_1 - \mathbf{F}_2) \right].$$

In this equation,  $n_1, n_2$  are the respective concentrations of particles 1 and 2,  $n = n_1 + n_2$  is the total concentration of the binary mixture,  $T$  is the absolute neutral gas temperature,  $p = p_1 + p_2$  is the total pressure,  $k$  is the Boltzmann constant,  $m_1, m_2$  are the masses of particles 1 and 2,  $m = (n_1 m_1 + n_2 m_2) / (n_1 + n_2)$  is the mean molecular mass,  $\mathbf{F}_1, \mathbf{F}_2$  are the acceleration vectors of particles 1 and 2 due to external forces,  $D_{12}$  is the molecular diffusion coefficient of gas 1 in gas 2, and  $\alpha_T$  is the thermal diffusion factor. According to gas kinetic theory, the molecular diffusion coefficient may be written

$$D_{12} = \frac{3kT(m_1 + m_2)}{16n m_1 m_2 \Omega_{12}},$$

with

$$\Omega_{12} = \frac{\sigma_{12} \bar{v}}{2} = \frac{f \pi r_{12}^2}{2} \sqrt{\frac{2kT(m_1 + m_2)}{\pi m_1 m_2}}.$$

Here  $\Omega_{12}$  is the collision integral between particles 1 and 2, with a collision cross section  $\sigma_{12}$ ,  $f$  is a correction factor to the collision cross section for rigid elastic spheres and  $\bar{v}$  is the average relative velocity.

When neutral gases diffuse in a gravitational field and no other external force is applied on the gas, the term  $\mathbf{F}_1 - \mathbf{F}_2$  is zero. Taking the vertical component of the equation and assuming that there is no net flow through an elementary surface at height  $z$ , i.e., if  $n_1 v_1 + n_2 v_2 = 0$  (with  $v$  being the vertical component of  $\mathbf{v}$ ), the equation can be transformed into

$$v_1 = -D_{12} \left[ \frac{1}{n_1} \frac{dn_1}{dz} + \frac{1}{H_1} + (1 + \alpha_T) \frac{1}{T} \frac{dT}{dz} \right] \quad \text{with} \quad H_1 = \frac{kT}{m_1 g}$$

where we have used the hydrostatic equation and the perfect gas law. It was further assumed that gas 1 is a minor constituent ( $n_1 \ll n_2$ , and therefore  $m_2 \approx m$ ).

This equation shows that diffusion is caused by concentration gradients, pressure gradients, and temperature gradients. However, there are other possibilities giving rise to a vertical transport as well. Molecular diffusion tends to separate the atmospheric constituents according to their masses. Turbulence tends to mix them preventing their separation by molecular diffusion.

The vertical eddy diffusion velocity  $v_E$  for the constituent  $n_1$  can be defined by analogy with molecular diffusion velocity

$$v_E = \frac{-K [d(n_1/n)/dz]}{(n_1/n)}$$

where  $K$  is the vertical **eddy diffusion coefficient**. Using the hydrostatic equation and the perfect gas law, the total transport velocity,  $v = v_1 + v_E$ , can be written as

$$v = -D_{12} \left[ \frac{1}{n_1} \frac{dn_1}{dz} + \frac{1}{H_1} + (1 + \alpha_T) \frac{1}{T} \frac{dT}{dz} \right] - K \left[ \frac{1}{n_1} \frac{dn_1}{dz} + \frac{1}{H_a} + \frac{1}{T} \frac{dT}{dz} \right]$$

If we assume that  $H_2$  is the dominant atmospheric component and that all other species can be considered as minor constituents, this equation can be used for each, with the index 1 replaced by  $i$ .

Remembering that the flux of neutral species  $i$  is  $\Phi_i = n_i v_i$ , we may rearrange the previous equation as

$$\Phi_i = -(K + D_i) \frac{dn_i}{dz} + n_i \left( \frac{D_i}{H_i} + \frac{K}{H_a} \right) - n_i [K + D_i (1 + \alpha_i)] \frac{1}{T} \frac{dT}{dz}$$

where  $\Phi_i$  = flux of neutral species  $i$   
 $n_i$  = number density of species  $i$   
 $z$  = altitude

$K$  = eddy diffusion coefficient

$D_i$  = molecular diffusion coefficient of species  $i$  in  $H_2$

$H_i$  = scale height of species  $i$

$H_a$  = atmospheric scale height

$\alpha_i$  = thermal diffusivity of species  $i$

$T$  = atmospheric temperature

Assuming that an equilibrium distribution exists between the mixing and the diffusive equilibria, (i.e.  $\Phi_i = 0$ ) we can write:

$$(K+D_i)\frac{dn_i}{dz}+n_i\left(\frac{D_i}{H_i}+\frac{K}{H_a}\right)-n_i[K+D_i(1+\alpha_i)]\frac{1}{T}\frac{dT}{dz}=0.$$

With  $\frac{K}{D_i} = \Lambda_i$ , this equation becomes

$$\frac{dn_i}{dz}\frac{1}{n_i}=-\left(\frac{\frac{1}{H_i}+\frac{\Lambda}{H_a}}{1+\Lambda}\right)\left\{\left(1+\frac{\alpha}{1+\Lambda}\right)\frac{1}{T}\frac{dT}{dz}\right\}$$

For time-independent conditions, the partial derivatives can be turned into total derivatives. The integration of the previous equation between altitudes  $z_0$  and  $z$  yields the following distribution of the number density of species  $i$ , as a function of altitude, in a situation of diffusive equilibrium,

$$n_i(z)=n_i(z_0)\frac{T(z_0)}{T(z)}\exp\left\{-\int_{z_0}^z\left(\frac{1}{H_i}+\frac{\Lambda}{H_a}\right)(1+\Lambda)^{-1}dz'-\int_{z_0}^z\frac{\alpha}{1+\Lambda}\frac{dT}{T}\right\}$$

This relationship can only be used for the minor constituents ( $H$ ,  $He$ ,  $CH_4$ ,  $C_2H_2$ ) diffusing in the major constituent, i.e.  $H_2$ . In the atmospheric regions where  $H_2$  is the major constituent, the atmospheric scale height  $H_a$  is approximately equal to the  $H_2$  scale height  $H_a \sim H(H_2)$ . At high altitude above the homopause, where  $H_2$  is no longer

the major constituent, molecular diffusion is the dominant process,  $\Lambda_{H_2} \rightarrow 0$  and the  $\Lambda_{H_2}/H_a$  term vanishes. After simplification, the diffusion terms disappear and the diffusion equation becomes :

$$n_{H_2} = n_{H_2}(z_0) \frac{T(z_0)}{T(z)} \exp - \int_{z_0}^z \frac{dz'}{H_{H_2}}$$

which is equivalent to the hydrostatic equilibrium, or diffusive equilibrium since in both cases  $H_a$  is the molecular hydrogen scale height. In fact  $H_2$  remains in diffusive equilibrium at all altitudes. Its vertical distribution is thus determined solely by the neutral temperature profile.

The Fickian diffusion coefficients for He and H diffusing in  $H_2$ , and for He in H were taken from the compilation of Mason and Marrero (1970). The thermal diffusion coefficients for He in  $H_2$  has a value of 0.145 (Chapman and Cowling, 1970). All other thermal diffusion coefficients were assumed to be zero.

#### VI.7.2.1.2 Hydrocarbon species

In the case of methane and acetylene, the resolution method can be simplified by assuming that the temperature gradient is negligible in one thin layer, in the lower atmosphere (where the altitude grid is dense) so that  $dT \rightarrow 0$  and  $(\frac{1}{H_i} + \frac{\Lambda}{H_a})(1 + \Lambda)^{-1}$  is approximately constant over a given layer. The diffusion equation for  $CH_4$  takes the form

$$n_{CH_4}(z) = n_{CH_4}(z_0) \frac{T(z_0)}{T(z)} \exp \left\{ - \left( \frac{1}{H_{CH_4}} + \frac{\Lambda}{H_a} \right) (1 + \Lambda)^{-1} (z - z_0) \right\} .$$

A similar equation is deduced for  $C_2H_2$ .

### VI.7.2.1.3 Boundary conditions

It should be stressed \*that chemical processes are not accounted for in the calculation of the number densities of H, CH<sub>4</sub>, and C<sub>2</sub>H<sub>2</sub>. Chemical reactions will be confined in the lower stratosphere and we thus assumed constant mixing ratios for H below the 10<sup>-5.5</sup> bar pressure level, and for C<sub>2</sub>H<sub>2</sub> below 10<sup>-6.6</sup> bar (the mixing ratios are taken from Drossart *et al.* [1993]). We used only one value of the CH<sub>4</sub> mixing ratio (also from Drossart *et al.* [1993]) at the bottom of our model. This method implicitly sets the boundary conditions for the number densities of these species. For H<sub>2</sub> and He, (boundary) mixing ratios at the bottom of the model atmosphere were set to 0.88 and 0.12, respectively (Atreya, 1986). The diffusion equations are then numerically solved with a shifted 2-point Gauss-Legendre rule.

### VI.7.2.1.4 Characteristic times for diffusion

By defining the characteristic times for molecular and eddy diffusion, we can determine under which conditions one type of diffusion process will prevail on the other.

The molecular diffusion time is defined by  $\tau_m = \frac{H_1}{v_1}$

and the eddy diffusion time by  $\tau_E = \frac{H_a}{v_E}$

Generally speaking, terms involving temperature gradients can be neglected compared to others. Terms in  $\frac{1}{n_i} \frac{dn_i}{dz}$  are of the order of  $\frac{1}{H_i}$ , so that the characteristic times for molecular and eddy diffusion can be approximated as follows:

$$\tau_m \approx \frac{H_1^2}{D_{12}}$$
$$\tau_E = \frac{H_a^2}{\kappa}$$

The dominating diffusion process will be the one with the shortest characteristic time.

## VI.7.2.2 Molecular and eddy diffusion profiles

Three coefficients are used in the diffusion equation presented in the previous section: the molecular diffusion coefficient  $D$ , the thermal diffusion coefficient  $\alpha_T$ , and the eddy diffusion coefficient  $K$ . While  $D$  and  $\alpha_T$  can be estimated by calling upon the gas kinetic theory, the eddy diffusion coefficient is a much more speculative parameter. The eddy diffusion coefficient in photochemical models of planetary atmospheres other than Earth's is essentially a free parameter. It is actually related to the hydrodynamical regime atmosphere and represents, to a certain extent, the degree of turbulence. Apart from a value for  $K_H$  (the eddy coefficient at the homopause) at low latitudes derived by Voyager UVS measurements and a stellar occultation, and various measures of mixing in the lower stratosphere utilizing *Voyager* IRIS data, the eddy diffusion profile on Jupiter is completely unconstrained. Methane and acetylene density profiles are strongly affected by the choice of the eddy diffusion profile.

### VI.7.2.2.1 The eddy diffusion coefficient

The basic form for the eddy diffusion profile in our model is taken from Gladstone *et al.* (1996)

$$K(z) = K_H \left( \frac{n_H}{n(z)} \right)^\gamma$$

where  $K_H$  is the eddy diffusion coefficient at the homopause ( $\text{cm}^2 \text{s}^{-1}$ ),

$n(z)$  is the total density at altitude  $z$  ( $\text{cm}^{-3}$ ),

$$\gamma = 0.45$$

We will see that the molecular diffusion coefficient as a function of altitude can be derived from the general expression

$$D(z) = \frac{\alpha}{n(z)} T(z)^s.$$

At the homopause,  $D(z) = K_H$ ,  $n(z) = n_H$  and  $T(z) = T_H$ . Hence, the constant  $\alpha$  is given by

$$\alpha = \frac{K_H n_H}{T_H^\beta}.$$

The relationship giving the density at the homopause can then be written as

$$n_H = \frac{n(z) T(z)^{-\beta} D(z) T_H^\beta}{K_H}$$

If, at a given pressure  $p_o$ , the temperature  $T_o$  and the molecular diffusion coefficient  $D_o$  are known, then we obtain the relationship from Gladstone *et al.* (1996) :

$$n_H = \frac{A T_H^{s-1} n_o T_o}{K_H} \text{ in (cm}^{-3}\text{)}.$$

Here, we use their numerical values :

$$A = T_o^{-s} D_o = 3.64 \cdot 10^{-5} \text{ cm}^2 \text{ s}^{-1} \text{ K}^{-s}$$

$$s = \beta + 1 = 1.75$$

$$n_o T_o = p_o / k = 7.3439 \cdot 10^{21} \text{ cm}^{-3} \text{ K} \quad (p_o = 1 \text{ b})$$

$$T_H = 200 \text{ K}$$

For our sensitivity study we examined the effect of varying the eddy diffusion coefficient at the homopause on the profiles of  $\text{CH}_4$ ,  $\text{C}_2\text{H}_2$  and H. The  $K_H$  value for He was kept fixed at  $1.4 \cdot 10^6 \text{ cm}^2 \text{ s}^{-1}$ .

#### VI.7.2.2.2 The molecular diffusion coefficient

The molecular diffusion coefficient can be estimated from the gas kinetic theory. The following general expression for  $D_{12}$ , the coefficient for the diffusion of gas 1 in gas 2, is obtained (Chapman and Cowling, 1970) :

$$D_{12} = \frac{3\pi}{32\bar{Q}_D n} v_{12},$$

where  $\bar{Q}_D$  is the mean momentum transfer cross-section,  $n = n_1 + n_2$  is the total gas concentration,  $v_{12}$  is the velocity of gas 1 relative to gas 2, given by

$$v_{12} = (8kT/\pi\mu)^{1/2},$$

where,

$$\mu = (1/m_1 + 1/m_2)^{-1}$$

is the reduced mass.

For a minor constituent diffusing through the background atmosphere,  $n$  becomes the atmospheric density ( $n \approx n_2$ ), and the mean molecular weight is close to  $m_2$ . The diffusion coefficient  $D$  then becomes

$$D = \frac{B}{n\bar{Q}_D} T^{1/2}.$$

The mean momentum transfer cross-section  $\bar{Q}_D$  also depends on  $T$ . The molecular diffusion coefficient can thus be written in the general form

$$D = \frac{\alpha}{n} T^s$$

where  $1/2 \leq s \leq 1$ . The value  $s = 1$  corresponds to Maxwellian molecules and the value  $s = 1/2$  corresponds to elastic spheres.

The molecular diffusion profile of CH<sub>4</sub> (and C<sub>2</sub>H<sub>2</sub>) in H<sub>2</sub> is given by (Gladstone, 1982)

$$D(z) = 2.3 \times 10^{17} \frac{T(z)^{0.765}}{n(z)} \sqrt{\frac{16.04}{m} \frac{m + 2.016}{18.059}}$$

where m is the molecular mass of the hydrocarbon constituent diffusing in H<sub>2</sub> (amu), n(z) is the total density (cm<sup>-3</sup>), and T(z) is the temperature (K). D(z) is in cm<sup>2</sup> s<sup>-1</sup>

The molecular diffusion profile for He in H<sub>2</sub> may be given by (Gladstone, 1982)

$$D(z) = 1.98 \times 10^{20} \frac{T(z)^{0.51}}{(\ln(5.34 \times 10^6 / T(z)))^2 n(z)}$$

and the molecular diffusion profile for H in H<sub>2</sub> by

$$D(z) = 8.19 \times 10^{17} \frac{T(z)^{0.728}}{n(z)}$$

Since the homopause is defined as the level where K(z)=D(z) and since each of the previous species is characterized by a different molecular diffusion profile, a different homopause should be defined for each of these species. **For convenience we adopt the homopause as the main methane homopause.**

#### VI.7.2.2.3 The thermal diffusion factor

The final parameter involved in the diffusion equation is the thermal diffusion factor  $\alpha_T$ . It is associated with the temperature gradient and is significantly different from 0 for H, H<sub>2</sub> and He.

The thermal diffusion coefficient for He in H<sub>2</sub> has a value of 0.145. All other thermal diffusion coefficients were assumed to be zero.

#### VI.7.2.2.4 Relationship between molecular and eddy diffusion

So far, we have presented the eddy and the molecular diffusion coefficients independently. However, they are indirectly linked. It can be seen from the general form of the molecular coefficient that this parameter is proportional to the atmospheric temperature and inversely proportional to the total atmospheric density.

One could be surprised that the eddy coefficient could significantly influence the molecular coefficient since eddy diffusion mainly affects the density profiles of the minor species, and has no relevant effect on the major species, i.e. molecular hydrogen. Therefore, it should leave the bulk atmospheric density almost unaffected. However this argumentation is incomplete because methane, a minor species strongly affected by eddy diffusion, is an important radiative cooler in the lower stratosphere. Any density variation of CH<sub>4</sub> will, in turn, have an important feedback on the thermal profile (which controls diffusion processes to a large extent) and thus the density profiles of the major species. The situation becomes very complex because the eddy coefficient itself is inversely proportional to the total atmospheric density. The iterative processing of our code allows to account for the multiple interconnections between these parameters. The indirect link between  $K(z)$  and  $D(z)$  may be illustrated with cases B, E and F which only differ by the value adopted for the eddy diffusion coefficient at the homopause ( $K_H=1.4 \times 10^6 \text{ cm}^2 \text{ s}^{-1}$ ,  $1.4 \times 10^5 \text{ cm}^2 \text{ s}^{-1}$ , and  $1.4 \times 10^7 \text{ cm}^2 \text{ s}^{-1}$ , respectively).

The three plots of figure 44 show that the main effect of  $K_H$  on the eddy coefficient is a shift of the profile toward higher values of  $K(z)$  as  $K_H$  increases. In the region above  $\sim 300$  km, modifying  $K_H$  by one order of magnitude corresponds to a shift characterized by a multiplicative factor of the order of 5. Below this altitude the multiplicative factor is of the order of 3. As we shall see below, the variation of this multiplicative factor is due to the feedback effect of the temperature profile below  $\sim 300$  km (1  $\mu$ bar).

A similar shift (by a factor 3.2) for the molecular diffusion coefficient profiles  $D(z)$  is observed above  $\sim 300$  km. Below this altitude,  $D(z)$  is unaffected by  $K_H$ . This is partly due to a restriction that we have to apply to the lower part of the thermal profile (below the 1  $\mu$ bar level). In order to prevent an excessive (and unobserved) cooling of this region by the hydrocarbons, the lower part of the thermal profile is artificially fixed and is therefore unaffected by  $K_H$ .

The distributions of  $K(z)$  and  $D(z)$  directly control the altitude of the homopause, which is defined as the level where  $K(z) = D(z)$ .

case	$K_H$ ( $\text{cm}^2 \text{ s}^{-1}$ )	homopause altitude (km)
E	$1.4 \times 10^5$	252
B	$1.4 \times 10^6$	312
F	$1.4 \times 10^7$	381

**Table 16** : effect of  $K_H$  on the altitude of the homopause

Table 16 and figure 44 clearly show that increasing  $K_H$  means increasing the mixing effect of the eddy diffusion. The maximum altitude below which eddy diffusion efficiency exceeds molecular diffusion, i.e. the homopause, raises accordingly. As a consequence, the density of heavier molecules, such as methane, which normally rapidly decreases with increasing altitude under the action of molecular diffusion, can reach appreciable values in the upper stratosphere.

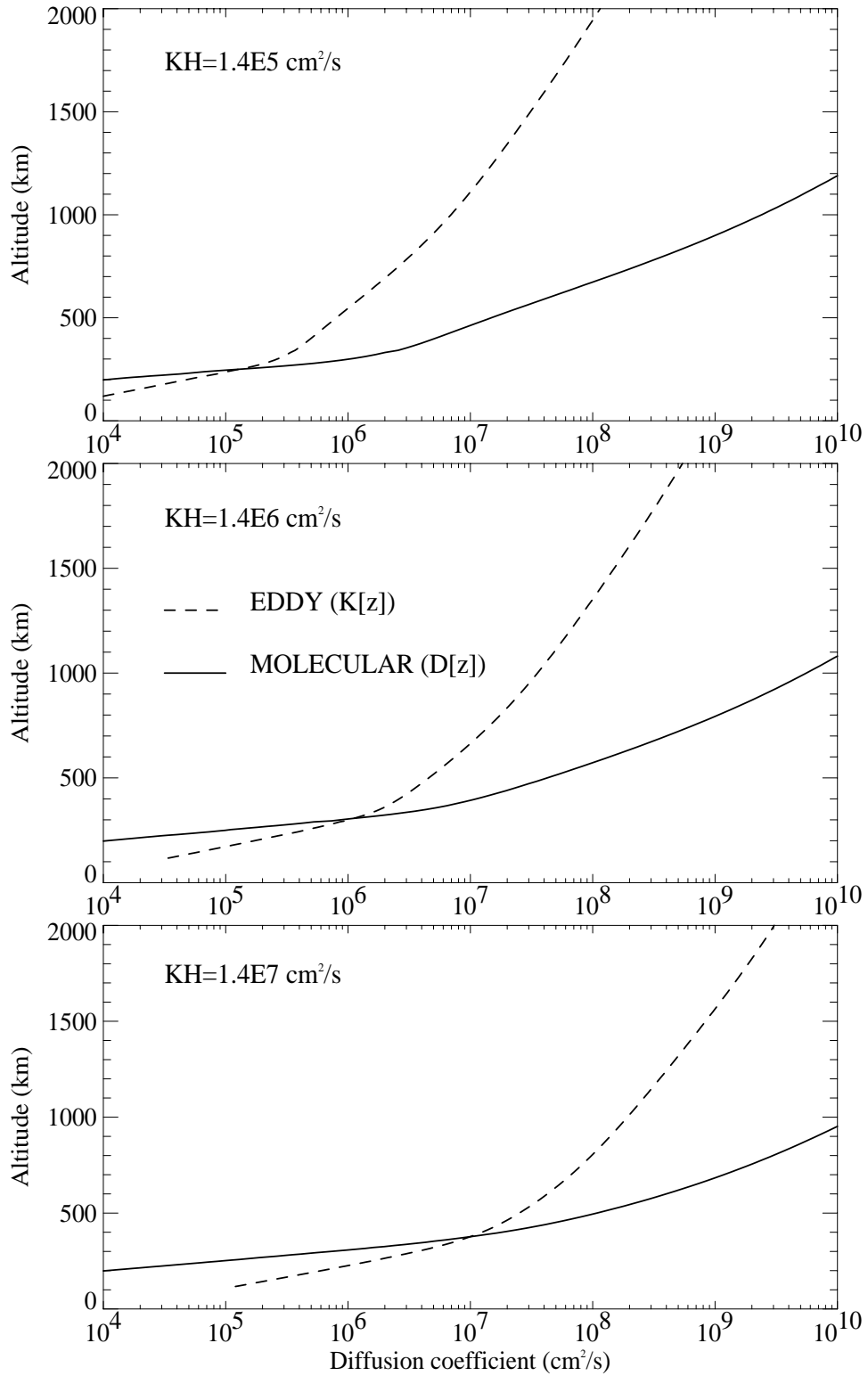


**Figure 44** : Effect of the eddy coefficient at the homopause ( $K_H$ ) on the molecular diffusion  $D(z)$  and eddy diffusion  $K(z)$  coefficients.

## VI.7.3 Chemical reactions

### VI.7.3.1 Atomic hydrogen chemistry

We already mentioned in the section describing the diffusion equation that, as far as the minor constituents are concerned, the composition of the atmospheric gas is not solely controlled by diffusion processes. In the case of atomic hydrogen, the distribution is also controlled by the balance between the thermospheric sources of H (i.e., H<sub>2</sub> dissociation and ionization) and the sinks that exist in the lower atmospheric hydrocarbon layer. The main sink in the hydrocarbon layer is the catalytic recombination of H by C<sub>2</sub>H<sub>2</sub>. Other sinks include three-body reactions of H with CH<sub>3</sub> and with itself. In order to indirectly account for these atomic hydrogen production and loss processes, we adopt the auroral H mixing ratio profile derived by Drossart *et al.* (1993) from the bottom of the model (1 mbar) to a pressure level of 10<sup>-6.6</sup> bar. From this level we assume that H concentration is determined by diffusion alone, and not affected by chemical reactions.

### VI.7.3.2 Hydrocarbon photochemistry

The hydrocarbon photochemistry is not included in the present model. A comprehensive study on this complex chemistry for the solar-driven low and mid-latitude Jovian atmosphere can be found in Gladstone *et al.* (1996). It should be noted however that the photochemistry of methane and other hydrocarbons in the upper atmosphere of Jupiter is important in a number of ways. Photochemistry represents the major source of disequilibrium species in the upper atmosphere, although the aurora also represents an important source. Many of the long-lived photochemical products are optically active and contribute to the opacity of the atmosphere at wavelengths shorter than 2000 Å. Although the circulation patterns of the upper atmosphere are currently unknown, it is likely that many species of photochemical origin are important sources and/or sinks of heat, and thus contribute to the upper atmospheric dynamics. Hydrocarbon photochemistry may also be an important source for aerosol formation through the production of long-chain polymers.

We indirectly account for acetylene photochemistry in the same way as for atomic hydrogen: for pressures greater than  $10^{-5.5}$  bar, we adopt the mixing ratio profile derived by Drossart *et al.* (1993). Above this level, the diffusion equation is solved. Above the 1 mbar level, the methane concentration is almost independent of chemical reactions (Gladstone, pers. com., 1999). The diffusion equation is therefore solved to determine the density profile of CH<sub>4</sub>. The mixing ratio at the lower boundary is also taken from Drossart *et al.* (1993).

### VI.7.3.3 The H<sub>3</sub><sup>+</sup> density profile

In order to calculate a H<sub>3</sub><sup>+</sup> density profile that is consistent with the neutral model atmosphere, three reasonable hypotheses are made:

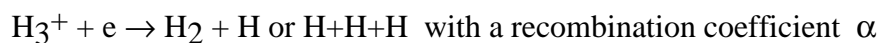
1. the atmosphere is at the photochemical equilibrium so that the production of H<sub>3</sub><sup>+</sup> is balanced by loss H<sub>3</sub><sup>+</sup>;
2. as the H<sub>2</sub><sup>+</sup> ion is rapidly converted to H<sub>3</sub><sup>+</sup> via ion exchange reaction  $H_2^+ + H_2 \rightarrow H_3^+ + H$ , we assume that the H<sub>3</sub><sup>+</sup> and H<sub>2</sub><sup>+</sup> production are comparable;
3. there is a local charge neutrality, i.e. the electron concentration is approximately equal to the H<sub>3</sub><sup>+</sup> concentration ( $[e] \approx [H_3^+]$ ), in the region where  $[H_3^+]$  is important.

According to hypotheses 1 and 2, the H<sub>2</sub><sup>+</sup> production is approximately balanced by the H<sub>3</sub><sup>+</sup> loss i.e. :

$$P(H_2^+) \approx [H_3^+] [e] \alpha + [H_3^+][CH_4]\beta + [H_3^+][C_2H_2]\gamma$$

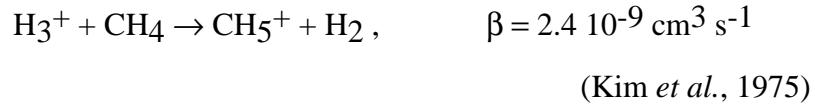
The three loss terms on the right-hand side of this relationship respectively take into account

- electron recombination of H<sub>3</sub><sup>+</sup>:

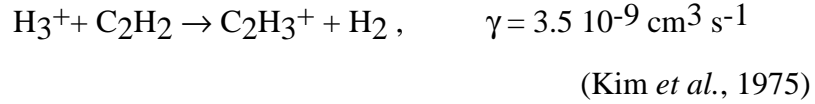


$$\alpha(T) = 1.15 \times 10^{-7} \left( \frac{300}{T} \right)^{0.65} \quad (\text{Datz } et al., 1995)$$

- destruction by methane:



- destruction by acetylene:



The third hypothesis allows to write a second-order linear equation in  $[\text{H}_3^+]$  :

$$\alpha [\text{H}_3^+]^2 + ([\text{CH}_4]\beta + [\text{C}_2\text{H}_2]\gamma) [\text{H}_3^+] - P(\text{H}_2^+) \approx 0$$

which obviously admits only one positive solution (the negative one is physically meaningless)

$$[\text{H}_3^+] = \{ -([\text{CH}_4]\beta + [\text{C}_2\text{H}_2]\gamma) + [([\text{CH}_4]\beta + [\text{C}_2\text{H}_2]\gamma)^2 + 4\alpha P(\text{H}_2^+)]^{1/2} \} / 2\alpha$$

It should be stressed that this concentration is an approximation which is only valid in atmospheric regions where  $[e] \approx [\text{H}_3^+]$ . Departures from the actual  $\text{H}_3^+$  concentration will take place at high altitude (above  $\sim 2000$  km) where the  $\text{H}^+$  concentration cannot be neglected compared to  $[\text{H}_3^+]$ . Fortunately, at these high altitudes,  $[\text{H}_3^+]$  is relatively small and the error introduced by this approximation has only minor consequences on the calculated  $\text{H}_3^+$  cooling.

The resulting density profiles calculated on the basis of the *Galileo* thermal profile, are shown in figure 43. In this case, the  $\text{H}_3^+$  density is estimated from the ionization produced in case A (described in a later section) with the atmospheric structure appropriate to the *Galileo* thermal profile.

Since the temperature profile, the atmospheric composition, and the heating and cooling efficiencies are intimately related, an iterative approach has to be adopted to calculate the steady-state composition of the atmosphere under auroral precipitation. The heating and cooling vertical profiles are calculated at each time step. The energy balance equation resulting from the energetic electron energy deposition is then iterated with the new temperature and density profiles until stable steady-state temperature and density profiles are achieved.

Little is known about non-auroral heating processes below the homopause. Neglecting these additional heating sources would cause radiative cooling by  $\text{CH}_4$  and  $\text{C}_2\text{H}_2$  not to be balanced and the stratospheric temperature would drop below its observed value. In order to maintain an appropriate stratospheric temperature without arbitrary assumptions regarding unspecified heating processes, we define a critical (threshold) pressure such that for pressures exceeding this value, a) only net heating is allowed, and b) if heating is insufficient, the temperature is not allowed to decrease below its initial value. This critical pressure will obviously influence the thermospheric thermal structure, but it is set in such a manner that it does not substitute for auroral heating where it is sufficient to dominate cooling.

## VI.8 Iteration process

As discussed before, the heat conduction equation, the diffusion equation (including the equations for eddy and molecular diffusion), and the electron transport differential equation system are tightly coupled.

The diffusion equation, which provides the density profiles of the different atmospheric constituents, depends upon the thermal structure of the atmosphere which is calculated from the heat conduction equation. The heat conduction uses the heating and cooling rates which are derived from the electron transport. Since electron transport deals with energy degradation of electrons colliding with neutral species, it is directly linked to the atmospheric composition calculated with the diffusion equation.

The easiest way to handle this kind of problem is to assume a set of realistic starting values, compatible with the boundary conditions, and to iteratively solve the equations until a steady state is reached. The *Galileo* equatorial thermal profile (corrected for the higher acceleration of gravity at the pole) is taken as the starting thermal profile. An initial atmospheric composition is then established by solving the diffusion equation using that thermal profile.

As illustrated in figure 45, the resulting initial atmospheric structure ( $n_i(z)$ ,  $T(z)$ ) and the auroral electron energy distribution at the top of the atmosphere ( $\Phi^\infty(E)$ ) are then introduced into the equations. Then, an iterative process is started, where the equations for electron transport (the energy degradation), heat conduction, and diffusion are solved in turn. The process is iterated until a steady-state thermal profile is reached. The final atmospheric structure, the upward and downward profiles of the energy flux of electrons obtained with this method are consistent with the energy distribution of the precipitating electrons. They can be used as inputs for other codes such as the H<sub>2</sub> UV spectral generator (described in part 3). We have seen in a previous section that other outputs, such as the cooling rate profile, can further be used, for example, to calculate the hydrocarbons and H<sub>3</sub><sup>+</sup> infrared emission profiles. These optical signatures, consistent with the atmospheric structure, can in turn be used to constrain the energy distribution of the auroral electrons.

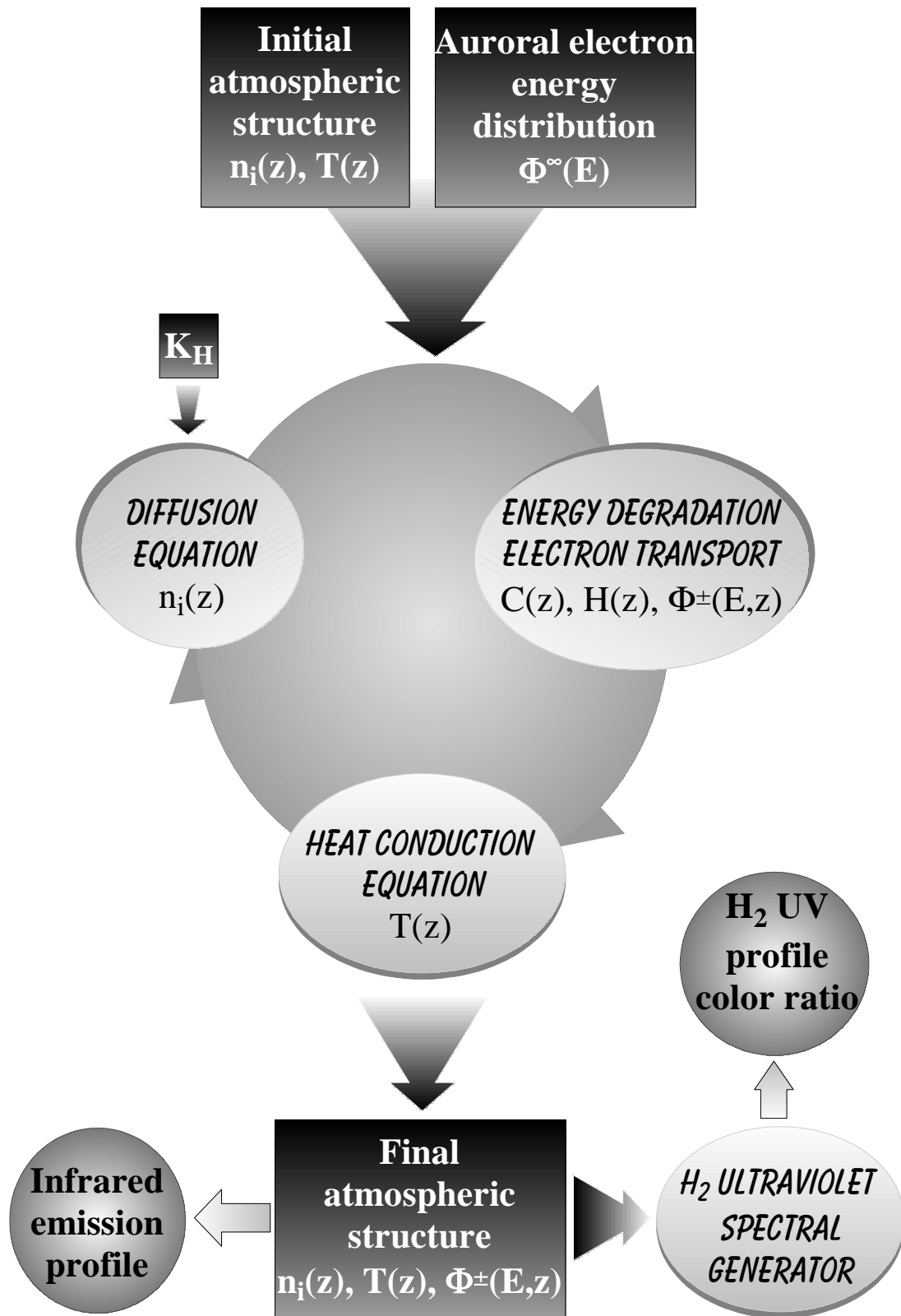


**Figure 45** : Iteration process used in the two-stream model

## VI.8.1 Convergence strategy

Since we calculate a steady-state auroral atmosphere, convergence cannot be reached with one single iteration for which any temperature variation would be allowed. Indeed, during the first step the energy degradation of the auroral electrons gives rise to heating and cooling rate profiles. These profiles are used in the heat conduction equation to build a new thermal profile. The diffusion equation makes use of this temperature profile to calculate improved densities. The process cannot be stopped here because at steady state, the auroral electrons are not interacting with the initial -auroral free- atmosphere but with an atmosphere that was already acted on by auroral precipitation. A second step is therefore necessary to calculate the interaction of the auroral electrons with the new atmospheric structure obtained at the end of the first step. One could think that a few iterations would then be sufficient to reach a steady-state atmospheric structure. However, the temperature dependency of the heating and cooling processes and the impossibility to cool down the region below the critical pressure level makes the convergence path more complex. As illustrated in figure 46 this method leads to discontinuities and overshoots, especially about the homopause where the heating is highest and where  $\text{CH}_4$  cooling combines with  $\text{H}_3^+$  cooling.

The thermal profile plotted in figure 46 was obtained after 16 iterations. The input parameters were exactly the same as in case B, but the temperature increment was not limited above the critical pressure level (set to  $0.1 \mu\text{b}$ ). In order to avoid local overshoot phenomena in the temperature profile, the convergence of the thermal profile is slowed down by allowing only small temperature increments. A variable temperature step (on the order of 5 K) is adopted above the critical pressure level, and a fixed temperature step of 0.1 K is imposed below (when heating is sufficient to increase temperature in the lower stratosphere).

Convergence is assumed to be reached once the thermal profile starts oscillating around an equilibrium profile with an amplitude lower than the local maximum temperature increment.

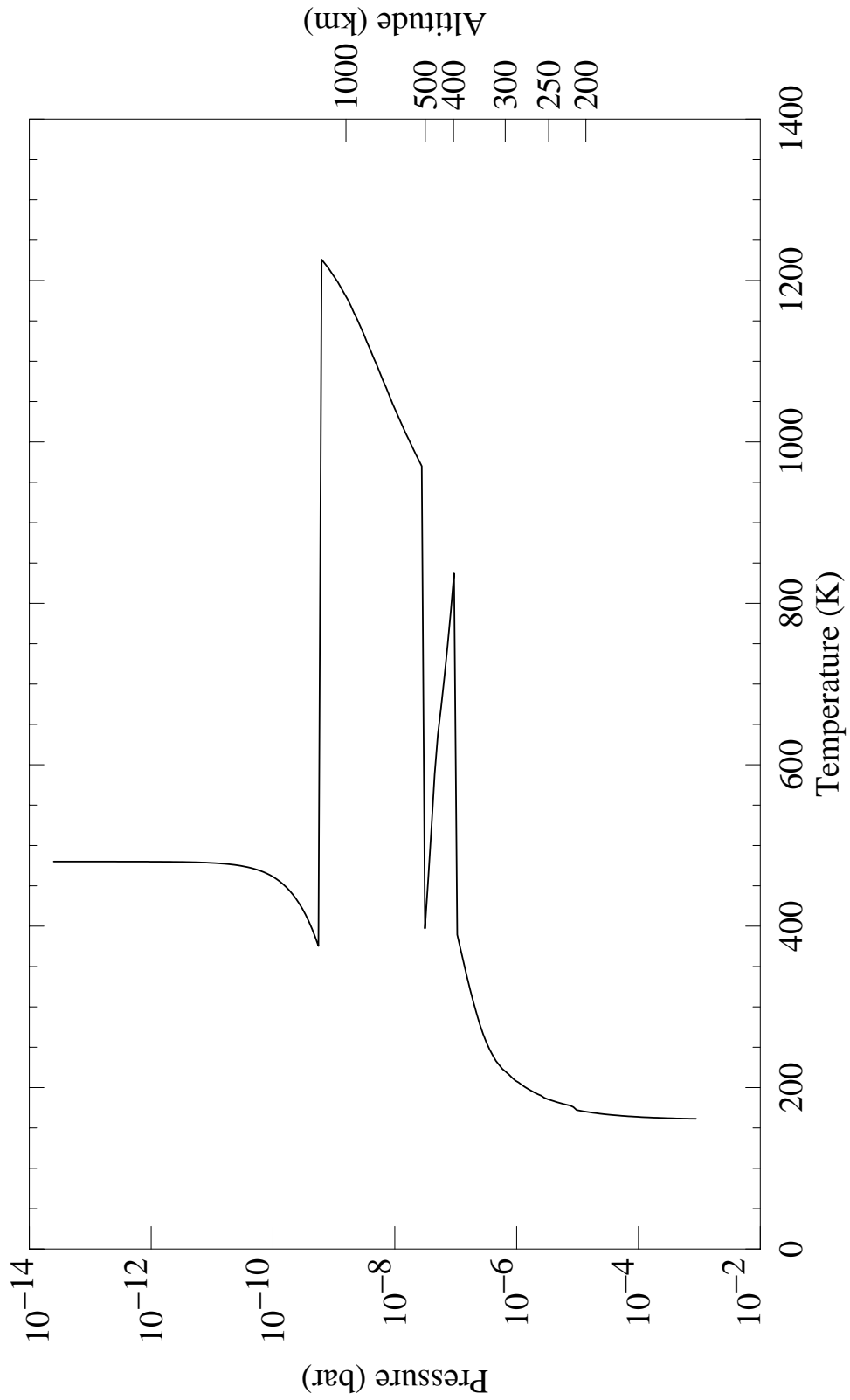


**Figure 46** : Thermal profile obtained after 16 iterations without slowing down the convergence. A huge temperature overshoot appears above 300 km.

## VII Model application

The present chapter was taken and adapted from a paper written by Denis Grodent, J. Hunter Waite, Jr. and Jean-Claude Gérard that was submitted to *J. Geophys. Res. (Space Physics)* in August, 1999.

### VII.1 Abstract

A one-dimensional (1D) model coupling a two-stream electron transport model of energy deposition with a 1D thermal conduction model has been described in the theoretical part. It is used to investigate the links between the auroral heat input and the atmospheric temperature and composition structures of Jupiter. Different energy distributions are used to evaluate the importance of the energy spectrum of the incident electrons for the thermal balance of Jupiter's auroral thermosphere. The values of observable quantities such as the altitude of the  $\text{H}_2$  emission peak, infrared (IR) and ultraviolet (UV) emissions and temperatures associated with various optical signatures are used to constrain the parameters of these distributions. From these simulations, it appears that the  $\text{H}_3^+$  and exospheric temperatures are mainly due to the level of soft electron influx and that they are almost independent on the  $\text{H}_2$  UV and hydrocarbon IR emissions and temperatures which are controlled by the high-energy component of the energy distribution. In order to meet the  $\text{H}_2$  integrated brightness constraint, a trade-off is necessary between the far-UV color ratio and the  $\text{H}_2$  rovibrational temperature.  $\text{H}_3^+$  plays an important thermostatic role and a similar trade-off exists between the  $\text{H}_3^+$  temperature and the observed  $\text{H}_3^+$  IR emission intensity which also increases with the low-energy component of the energy distribution. The precipitated auroral energy is not able to directly provide the necessary heat to balance the hydrocarbon cooling below the homopause but it is suggested that the auroral upper stratosphere is probably warmer than the equatorial upper stratospheric temperature deduced from *Galileo* data.

A kappa energy distribution, fitted on *in-situ Galileo* measurements at the distance of Ganymede's orbit, does not produce results in agreement with observations. Such an energy distribution does probably not reflect acceleration processes undergone by the auroral electron during their travel along the magnetic field lines. A Maxwellian energy distribution with a total flux of  $20 \text{ ergs cm}^{-2} \text{ s}^{-1}$  and a characteristic energy of 22 keV added to a soft Maxwellian component of  $1 \text{ erg cm}^{-2} \text{ s}^{-1}$  and a characteristic energy of 350 eV produces results in good agreement with thermospheric observations.

## VII.2 Energy distribution of auroral electrons

Three energy distributions of the precipitating particles are selected from theoretical considerations and *in-situ* measurements ; case A: a Maxwellian energy distribution, case B : a double Maxwellian distribution, mixing case A with a soft electron Maxwellian component, case C : a kappa distribution fitting the observations from the Energetic Particle Detector (EPD) experiment onboard *Galileo*. In the following section, we will first concentrate on case A: a single Maxwellian distribution with a characteristic energy of 22 keV and a total energy flux of  $20 \text{ ergs cm}^{-2} \text{ s}^{-1}$ .

The detailed parameters of these distributions are listed in table 19 and will be discussed below. It should be pointed out that the distributions A and B produce an H<sub>2</sub> FUV emission that peaks at an altitude close to 245 km. Recent visible-wavelength images obtained by the Galileo Solid State Imaging (SSI) system (Ingersoll *et al.*, 1998) have determined the altitude of this auroral night side emission to be  $245 \pm 30$  km above the 1 bar level (Vasavada *et al.*, 1999). James *et al.* (1998) have shown that these visible-wavelength emissions could be ascribed to the H<sub>2</sub> (a3  $\rightarrow$  b3) continuum, together with strong lines assigned to the radiative decay of the gerade singlet states of H<sub>2</sub>, and to members of the H Balmer series resulting from dissociative excitation of H<sub>2</sub>. Since these emissions are presumably excited by auroral electron impact on H<sub>2</sub>, it is assumed that the H<sub>2</sub> FUV and the visible emissions peak at the same altitude.

Figure 47 illustrates the dependence of the energy spectrum of the auroral electron flux on altitude for case A. As the primary electron beam reaches deeper pressure levels, the electrons degrade their energy, partly backscatter and produce secondary electrons. Four altitude levels are illustrated: 1) initial energy distribution at the top of the atmosphere, 2) degraded energy distribution above the H<sub>2</sub> emission peak (600 km), 3) at the emission peak (242 km), and 4) below the emission peak (200 km).

The flux profiles result from the balance between production and loss into the different energy bins. Since all degrading processes occur simultaneously, it is impossible to discriminate their individual action. The degradation rate of the electron flux along its path is mainly controlled by the H<sub>2</sub> density profile.

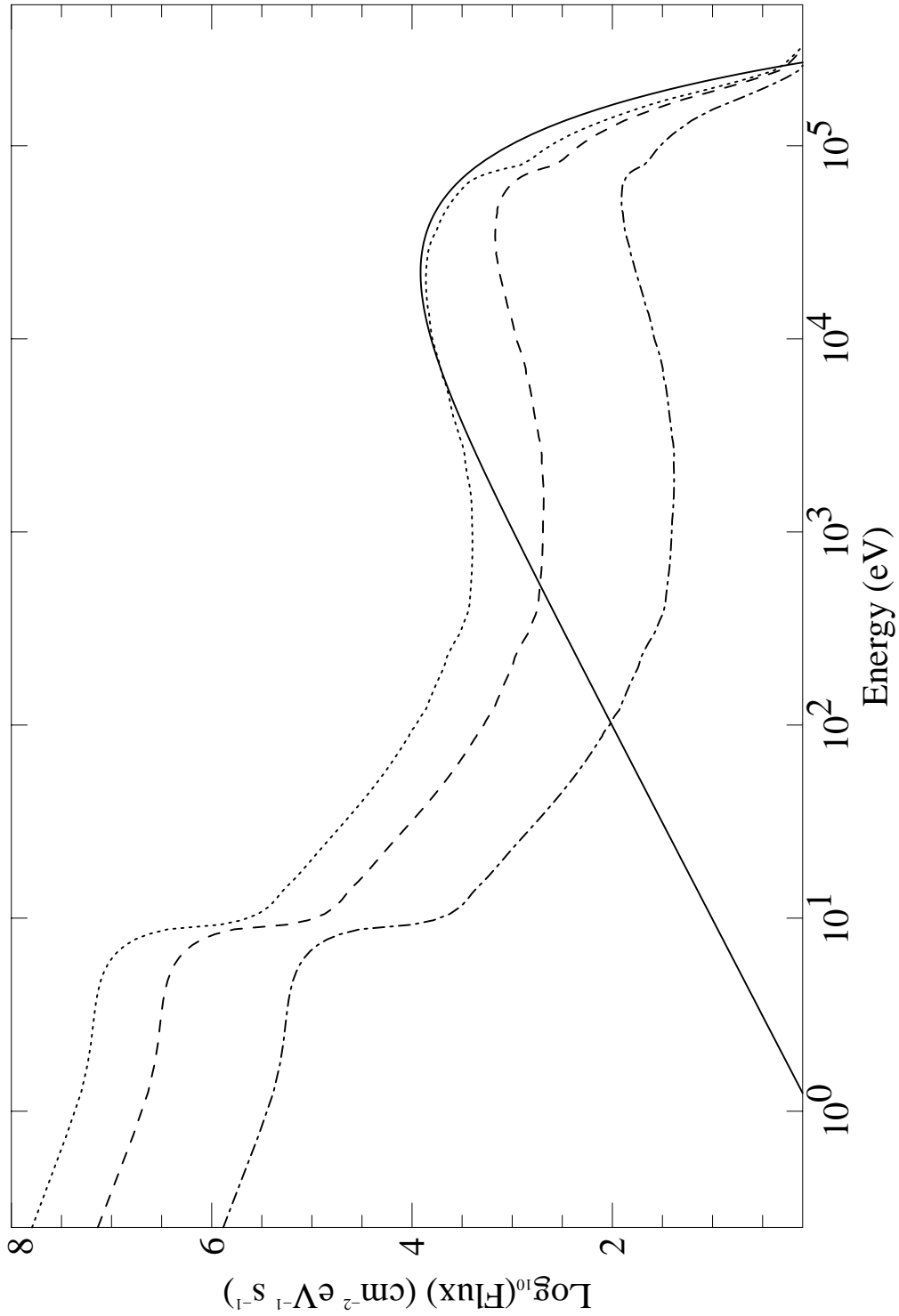


**Figure 47** : Evolution of the Maxwellian energy flux distribution of case A ( $E_0=22$  keV) as the electron beam penetrates into the atmosphere. Four altitude levels are considered: 1) initial energy distribution at the top of the atmosphere (—), 2) degraded energy distribution above the  $\text{H}_2$  emission peak (600 km) (.....), 3) at the emission peak (242 km) (-----), and 4) below the emission peak (200 km) (-.-.-).

Below the level of the peak  $\text{H}_2$  emission, where energy deposition is highest, the electron flux rapidly vanishes. This level is determined by the shape of the initial energy distribution of the electrons; in the case of a monoenergetic electron beam, the pressure level of the peak is proportional to the energy, and for more complex distributions, such as the Maxwellian distribution used in case A, the altitude mainly depends on the mean energy which is twice the characteristic energy  $E_0$  of the Maxwellian distribution.

The shape of the electron flux distributions in figure 47 can be explained with simple physical considerations. For energies higher than 20 eV, the total electron interaction cross section rapidly decreases, thus leading to a slower degradation of high energy electrons. An efficient depopulation of the low energy bins occurs at all altitudes. With a mean energy per ion pair of 40 eV, one single 40 keV electron is able to produce about 1000 secondary electrons which will rapidly populate these low energy bins. At the top of the atmosphere, the population processes of the low energy bins are relatively efficient compared to loss processes. As the electron beam penetrates into the atmosphere, this tendency is reversed and the flux drops at all energies. The abrupt rise of the electron flux below 10 eV corresponds to a minimum in the total inelastic cross section between rotational and vibrational excitation and other processes having a threshold energy of the order of 10 eV. In order to avoid numerical problems, we assume that all cascading energy which populates the lowest energy bin under consideration here (0.25 eV) is ultimately converted into electron heating.

### VII.2.1 $\text{H}_2^+$ and $\text{H}^+$ production rate profiles

The ionization produced by the electron energy spectrum of case A is illustrated in figure 48. The integrated ion production rates of the various processes are listed in table 17.

$\text{H}_2^+$  presents the largest ion production rate in the jovian ionosphere, about 1 order of magnitude higher than the dissociative ionization rate of  $\text{H}_2$ . However, the efficient reactions described in table 15 rapidly convert  $\text{H}_2^+$  into  $\text{H}_3^+$ , which is dominant in the jovian ionosphere.

ion produced	integrated production
	rate (cm <sup>-2</sup> s <sup>-1</sup> )
H <sub>2</sub> <sup>+</sup>	2.7×10 <sup>11</sup>
H <sup>+</sup> (H <sub>2</sub> ) diss. ion.	2.2×10 <sup>10</sup>
H <sup>+</sup> (H) direct	8.1×10 <sup>7</sup>
He <sup>+</sup>	9.8×10 <sup>9</sup>
<b>total</b>	3.0×10 <sup>11</sup>

**Table 17** : Integrated production rates of major ions

The H<sup>+</sup> production rate from dissociative ionization of H<sub>2</sub>, hereafter denoted H<sup>+</sup>(H<sub>2</sub>), is about 2 orders of magnitude higher than the H<sup>+</sup> production rate from direct ionization of H, hereafter H<sup>+</sup>(H). The corresponding ion production rate profiles do not peak at the same level : 240 km for H<sup>+</sup>(H<sub>2</sub>) and 300 km for H<sup>+</sup>(H). This can be explained by the large difference between the H and H<sub>2</sub> density profiles leading to a large fractional abundance of H at high altitude. The He<sup>+</sup> production rate is about half the H<sup>+</sup>(H<sub>2</sub>) production rate, the difference in the shape of the profiles also stems from the changing chemical composition as altitude increases in the thermosphere (heterosphere). The average energy to create an ion pair is 40 eV, slightly higher than the 37 eV derived from laboratory measurements. This difference stems from low energy electrons which do not have enough energy to ionize the gas while they contribute to the total energy of the beam.

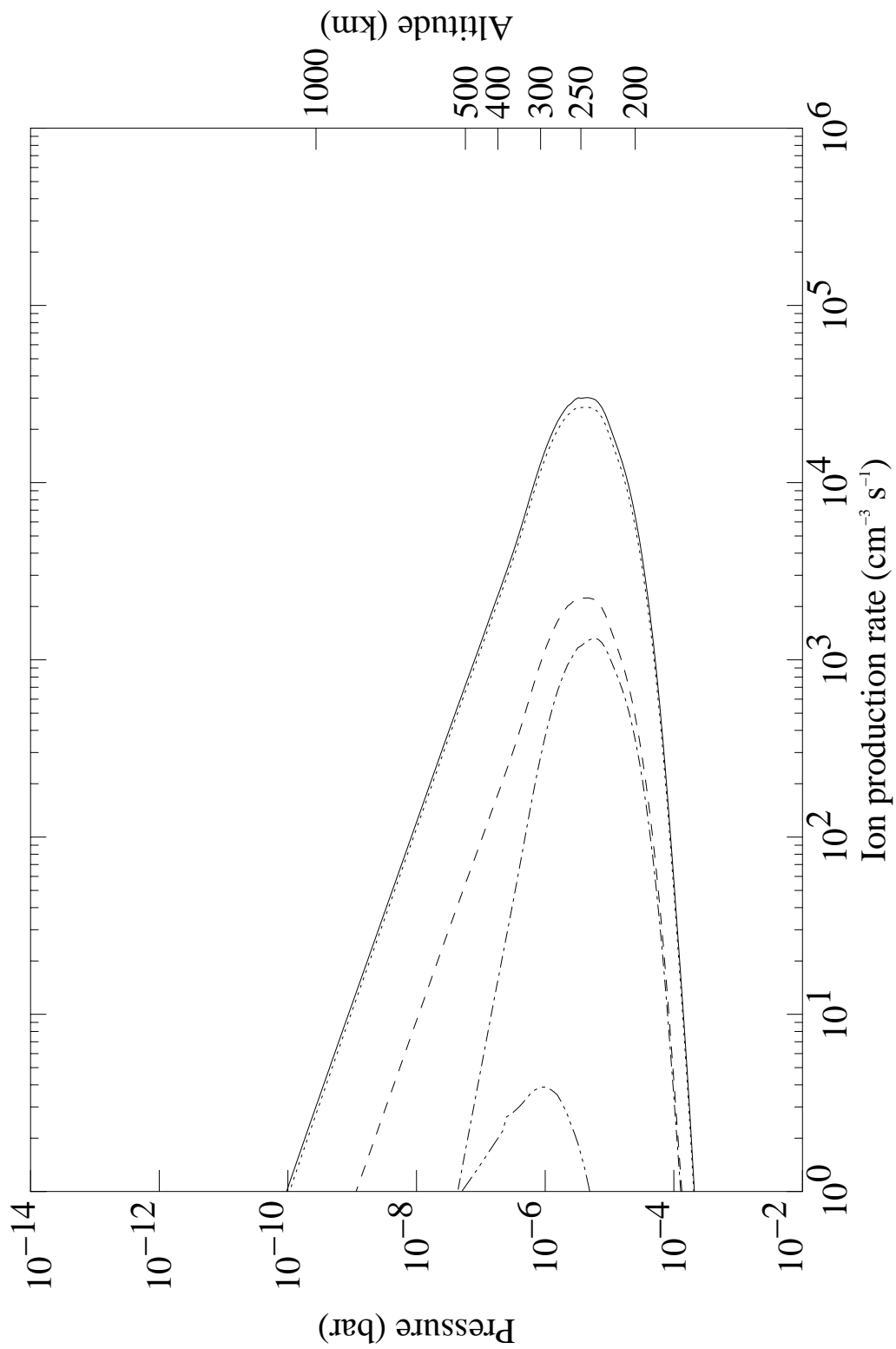


**Figure 48** : Ion production rates as a function of altitude and pressure for the Maxwellian energy distribution of case A. The plot shows the total ion production (—), the  $\text{H}_2^+$  production (.....), the  $\text{He}^+$  production (-----) and the  $\text{H}^+$  production resulting from direct ionization of atomic hydrogen (-·-·-·-) and from dissociative ionization of  $\text{H}_2$  (- - - -).

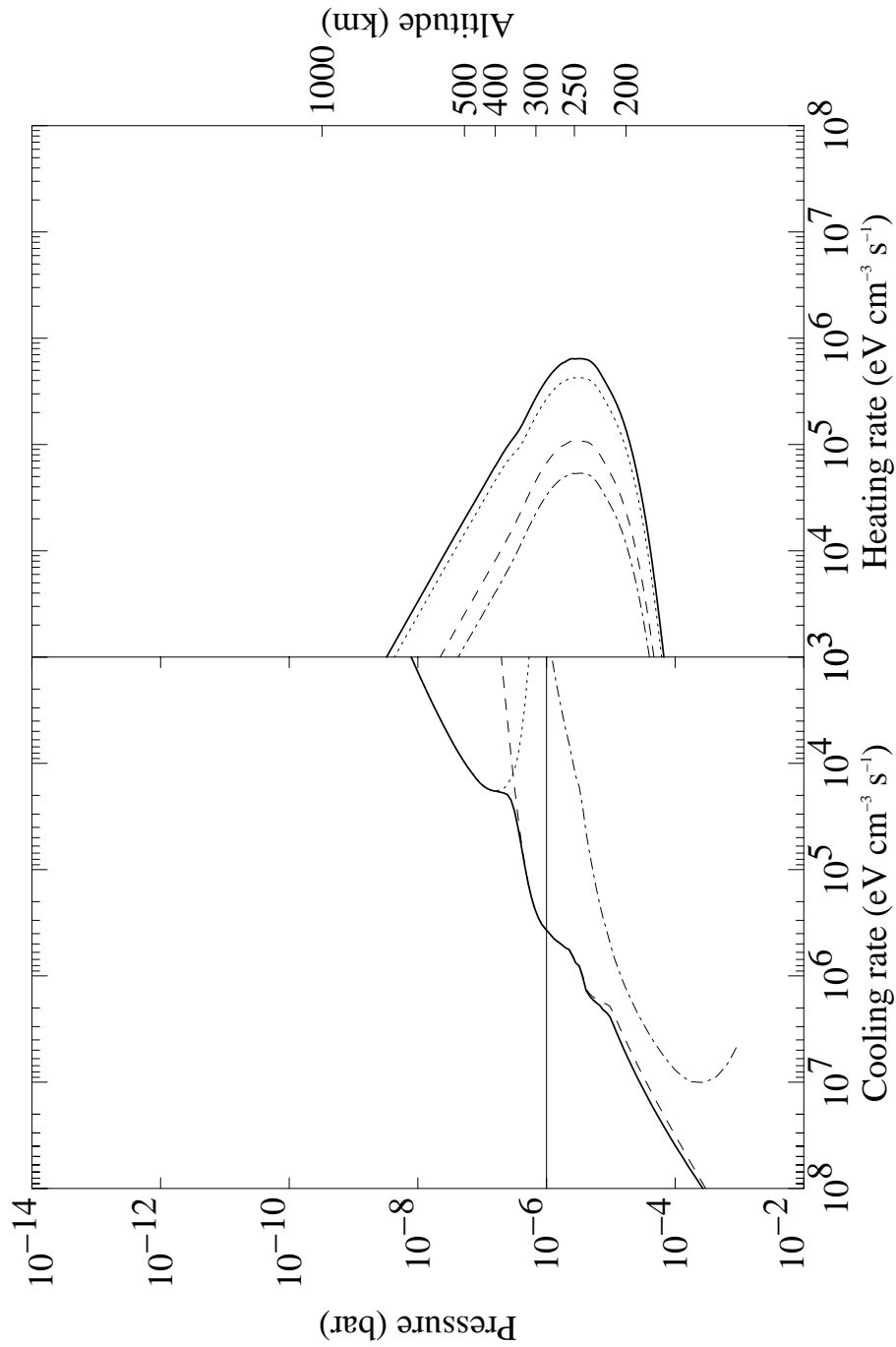
## VII.2.2 Heating and cooling profiles

Figure 49 shows the cooling and heating rate profiles for case A (single Maxwellian distribution). As mentioned before, we consider here the cooling associated with thermal IR radiations from  $\text{H}_3^+$ ,  $\text{CH}_4$  and  $\text{C}_2\text{H}_2$ . These molecules cool different regions of the atmosphere because the heavier hydrocarbon molecules are mostly confined below the homopause (312 km) while the  $\text{H}_3^+$  ion, which is destroyed by hydrocarbons below the homopause, has a density profile peaking  $\sim 40$  km above the homopause.

Turbulent transport controls the  $\text{CH}_4$  density and therefore plays an important role on the cooling rate in the vicinity of the homopause, i.e. in the region that includes the level of maximum energy deposition. The effect of change of the eddy diffusion coefficient on the thermal profile and on the absorption of  $\text{H}_2$  UV emission by  $\text{CH}_4$  will be considered later. The abundance of  $\text{H}_3^+$ , on the other hand, mainly controls the ionospheric region of the temperature profile and directly regulates the exospheric temperature.

The different heat sources have been described previously. Their individual and total heating rate profiles for case A are shown in figure 49. Table 18 lists their contribution to the total heating. For the Maxwellian energy distribution of case A, the heating efficiency of the atmosphere represents exactly 50% of the total auroral energy. For the electron energy distribution of case A, more than half of the auroral heat is produced below the homopause where it is efficiently lost to the hydrocarbon cooling. The main contribution of the auroral particles on the thermal profile is associated with the heat produced above the homopause, in a region where cooling is controlled by  $\text{H}_3^+$  infrared radiation.

Heating of the jovian atmosphere is largely dominated by chemical heating which results from the reaction chain initiated by the ionization of  $\text{H}_2$ . The excitation of the vibrational and rotational levels of the ground state of  $\text{H}_2$  molecules is the second most important heat source. Its importance reflects the large excitation cross sections of these processes occurring at low energies for which energy bins are highly populated.



**Figure 49** : Cooling (left plot) and heating rate (right plot) profiles resulting from the energy degradation of the Maxwellian energy distribution considered in case A ( $E_0=22$  keV). The cooling rates profiles for  $H_3^+$  (.....),  $CH_4$  (-----) and  $C_2H_2$  (-·-·-) are shown together with the total cooling rate profile (—) on the lefthand side. The horizontal line at  $10^{-6}$  bar indicates the critical pressure below which only heating of the atmosphere is allowed (see text). The right side of the plot shows the total heating rate profile (—), the chemical (.....) and rovibrational (-----) heating rate profiles, along with the heating rate profile resulting from  $H_2$  excitation (-·-·-).

The heat produced by the dissociation of excited H<sub>2</sub> singlet states and by excitation of the H<sub>2</sub> ground level following radiative transition from the B and C electronic states are comparable. These two processes are linked as they both result from deexcitation of excited singlet states. The heat released by H<sub>2</sub> dissociation from doubly excited states represents only a marginal contribution to the total heat produced because of the high threshold energies of these processes and their low cross sections. All heating rate profiles have similar shapes. The imbalance between heat sources and heat sinks is accounted for by downward heat conduction equation and gives rise to the thermal profile presented in figure 50 for case A.

Above the homopause, heating exceeds cooling and the difference is sufficient to sustain an exospheric temperature of 599 K. As will be discussed in the next section, this temperature is too low to match the observation and the initial electron energy distribution must be modified to raise the temperature. Below the homopause, the heating processes we consider cannot compensate the efficient hydrocarbon cooling. A critical pressure of 1  $\mu$ bar, corresponding roughly to the level of the homopause, is therefore imposed (horizontal bar in figure 49) which defines the level below which unspecified heating sources will prevent the thermal profile from cooling down. If heating is sufficient to increase temperature at some level below this critical level, any temperature increase will be allowed.

heating sources	contribution to total
chemical heating	66.8 %
vibrations + rotations	16.5 %
H <sub>2</sub> dissociation from singly excited states	7.4 %
Lyman and Werner bands heating	6.2 %
electron heating	2.3 %
H <sub>2</sub> dissociation from doubly excited states	0.8 %

**Table 18** : Contribution of the different heat sources to the total heating for case A

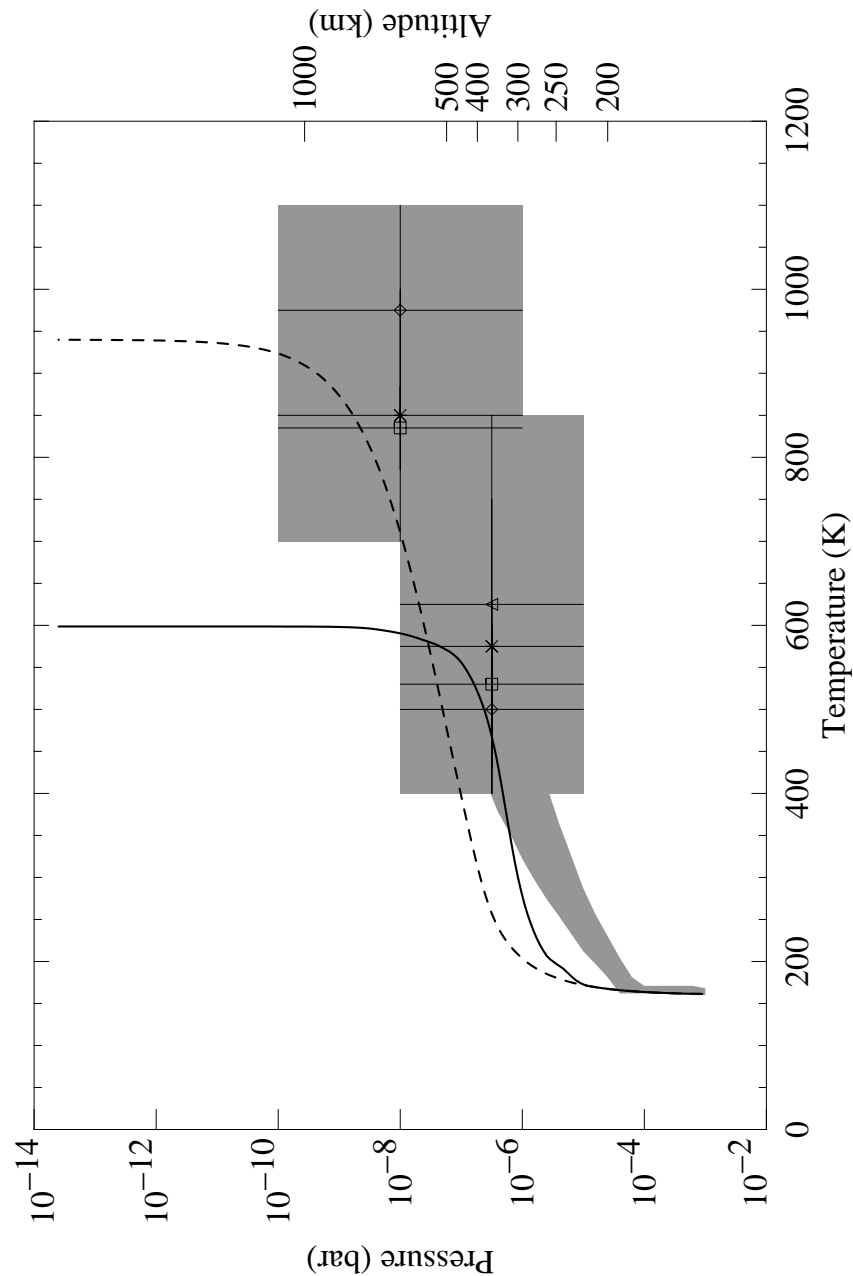


**Figure 50** : Observational constraints on the auroral temperature profile. The first shaded region (between 160 and 400 K) is derived from hydrocarbon (mainly  $\text{CH}_4$  and  $\text{C}_2\text{H}_2$ ) IR thermal emissions in the auroral hot spot (Drossart *et al.*, 1993). The second shaded region (between 400 and 850 K) is defined from  $\text{H}_2$  FUV auroral spectra ( $\diamond$  : Liu *et al.*, 1996;  $\square$  : Trafton *et al.*, 1994, 1998;  $\times$  : Clarke *et al.*, 1994;  $\Delta$  : Kim *et al.*, 1997). The third region (between 700 and 1100 K) is inferred from  $\text{H}_3^+$  near-IR emissions in the aurora ( $\square$  : Maillard *et al.*, 1990;  $\times$  : Lam *et al.*, 1997;  $\diamond$  : Drossart *et al.*, 1989). The solid line is the temperature profile calculated for case A. The dashed line represents the equatorial temperature profile deduced from the *in-situ* Galileo measurements. The altitude scale is calculated from the initial model atmosphere (Galileo).

## VII.3 Observational constraints

The values of various observable quantities such as the altitude of the H<sub>2</sub> emission peak, IR and UV emissions and temperatures associated with various optical signatures are used to constrain the parameters of the energy distribution of the precipitating electrons.

- A domain of observational constraints on the auroral temperature profile is constructed on the basis of multispectral analysis of the auroral region emissions.
- A general FUV emission rate deduced from spectra and images is used to provide an order of magnitude for the total precipitated energy, while the emission profile (including H<sub>2</sub> visible emission) gives important clues regarding the distribution of the auroral particle energy deposition with altitude and more specifically regarding the altitude of the H<sub>2</sub> emission peak.
- The FUV color ratio and the associated CH<sub>4</sub> column density are used to estimate the penetration depth of the degraded beam below the methane homopause.
- IR emission processes are diagnostic of the cooling processes in the mesosphere from CH<sub>4</sub> and C<sub>2</sub>H<sub>2</sub> at wavelengths between 7 and 14 μm and also an important diagnostic of the upper thermosphere and ionosphere from H<sub>3</sub><sup>+</sup> emission near 3.5 microns.

It should be noticed that all these observations are not simultaneous in time and space, and do not necessarily stem from the same processes. Knowing the temporal and spatial variability of the jovian aurora, one needs to be careful when comparing quantities resulting from different mechanisms and appearing at different times and locations.

### VII.3.1 Thermal profile

A range of observational constraints on the auroral temperature profile can be constructed from observations spanning three different overlapping pressure level regions (shaded regions in figure 50).

The first region (between 160-400 K) is constrained by the hydrocarbon (mainly CH<sub>4</sub> and C<sub>2</sub>H<sub>2</sub>) thermal infrared emissions observed with the Voyager IRIS and reanalyzed

by Drossart *et al.* (1993). They derived two temperature profiles based on different CH<sub>4</sub> density profiles :

- a. a warm upper boundary corresponding to the best fit for hydrocarbon emission for the hydrocarbon distribution derived from Voyager UVS observations (Atreya *et al.*, 1981),
- b. a cold boundary inferred from the thermal profile derived from the hydrocarbon distribution of Gladstone *et al.* (1982).

The second region constraining the temperature profile (400-850 K) is defined by the temperature values derived from H<sub>2</sub> FUV auroral emission. Different H<sub>2</sub> rovibrational temperature ranges were derived by fitting synthetic spectra to various spectral ranges observed with GHRS (Trafton *et al.*, 1994, 1998; Clarke *et al.*, 1994; Liu *et al.*, 1996; Kim *et al.*, 1997). These measurements define an H<sub>2</sub> temperature range of 400-850 K corresponding to emissions occurring between the 10<sup>-5</sup> and 10<sup>-8</sup> bar pressure levels.

The third region (700-1100 K) is defined on the basis of the temperatures inferred from the H<sub>3</sub><sup>+</sup> near-IR emission (Drossart *et al.*, 1989; Maillard *et al.*, 1990; Lam *et al.*, 1997). They define an ionospheric temperature range of 700-1100 K for the region where the H<sub>3</sub><sup>+</sup> emission originates, that is approximately between the 10<sup>-6</sup> and 10<sup>-10</sup> bar levels.

The equatorial temperature profile deduced from the *in-situ Galileo* measurements, which is used as the initial thermal distribution of the atmosphere, was shown in figure 43. It is imposed as the coldest permitted limit to the calculated temperature profile.

The effective H<sub>2</sub> temperature has been deduced from the H<sub>2</sub> UV rovibrational spectra and from the IR line of H<sub>2</sub> quadrupole emission. It can be roughly estimated in the model by weighting the temperature profile with the calculated H<sub>2</sub> UV emission rate profile. A similar method is applied to estimate the H<sub>3</sub><sup>+</sup> temperature from the calculated H<sub>3</sub><sup>+</sup> emission profile. This method does not make use of the detailed calculated thermal structure, however, it allows a direct comparison of the converged thermal profile with the observational constraints, without making any assumption on the altitude range of the emitting regions.

The thermal profile derived from case A is presented in figure 50. As already stated in the previous section, the profile clearly demonstrates that the energy distribution of auroral electrons considered in case A does not produce the temperature required above the homopause. This is especially true in the upper thermosphere, where the temperature is about 340 K colder than in the *Galileo* equatorial temperature profile (940 K). The temperatures reached in the upper stratosphere ( $10^{-4}$ - $10^{-6}$  bar) are considerably lower than the cold auroral hydrocarbon-IR boundary. They are, however, significantly higher than the initial *Galileo* equatorial profile. At  $10^{-7}$  bar, the calculated profile reaches its isothermal limit at a colder value than the one observed at the equator.

A first conclusion can be drawn from test case A. Since the calculated profile is too cold above the homopause and reasonably warm below the homopause, more heat deposition is required above the homopause, i.e. above the  $10^{-6}$  bar level. However, the Maxwellian energy distribution of case A sets the maximum energy deposition at about  $10^{-5}$  bar, approximately 70 km below the methane homopause. This implies that more than half of the released auroral heat is used to balance the efficient hydrocarbon cooling. The *Galileo* equatorial profile suggests that this role can, at least partly, be attributed to non-auroral processes, the corresponding auroral energy being more efficiently used above the homopause.

In the next sections, we will examine how the electron energy distribution of case A can be reasonably modified in order to produce a thermal profile in better agreement with the observations. However, before testing other distributions, it is important to consider other observational constraints such as the UV and IR auroral emissions which will reduce the range of possible energy distributions.

### VII.3.2 UV emission

Total Lyman band emission rates of 20-270 kR were measured by Kim *et al.* (1997) with the Large Science Aperture (LSA) of the GHRS spectrometer. The estimated total Lyman band intensity depends on the filling factor of the auroral emission in the LSA. The authors have assumed that the LSA aperture is completely

filled with the auroral emission, however recent UV images have show thin bright auroral structures which only partially fill the LSA. Their emission rates should therefore be regarded as lower limits to the actual UV auroral emission intensities corresponding to a viewing angle of approximately  $60^\circ$ . Trafton *et al.* (1998) obtained similar GHRS spectra with total integrated intensity (Lyman and Werner bands) averaged over the aperture varying from 54 to 228 kR. These derived apparent emission rates are attenuated by hydrocarbon absorption and also assume that the aperture is fully filled with auroral emission. They therefore also represent a lower limit to the emission. Morrissey *et al.* (1997) measured a mean  $H_2$  brightness of 106 kR with HUT however these measurements suffer from large uncertainties on the auroral area integrated in the aperture.

The recent study of HST WFPC2 images obtained close in time with *Galileo* UVS spectra and *in situ* particles, fields, and plasma wave measurements (Clarke *et al.*, 1998) show that a more typical emission brightness of 300 to 400 kR is to be considered along the main auroral oval.

To synthesize these results, a vertically integrated excitation rate of the  $B^1\Sigma_u^+$ , including cascade, and  $C^1\Pi_u$  states of 200 kR (unattenuated), approximately corresponding to 400 kR for a viewing angle of  $60^\circ$  is adopted.

Little information on the FUV vertical emission profile has been deduced so far from images taken by the FOC and the WFPC2 on board HST. The emission profile can only be determined at the limb where the apparent brightness distribution is biased by the viewing geometry, the spatial limitations of HST, and the instrument's point spread function (PSF) (Grodent *et al.*, 1997; Gérard *et al.*, 1998). However, *Galileo* images taken during orbit G7 show that the  $H_2$  visible emission profile is characterized by a vertical full width at half maximum of  $120 \pm 30$  km (Vasavada *et al.*, 1999) and drops below the detection limit at a full width of  $350 \pm 70$  km. The UV emission profile can also be crudely constrained by the  $H_2$  - FUV color ratio. As explained below, this constraint gives some indication on the distribution of the emission profile above and below the homopause.

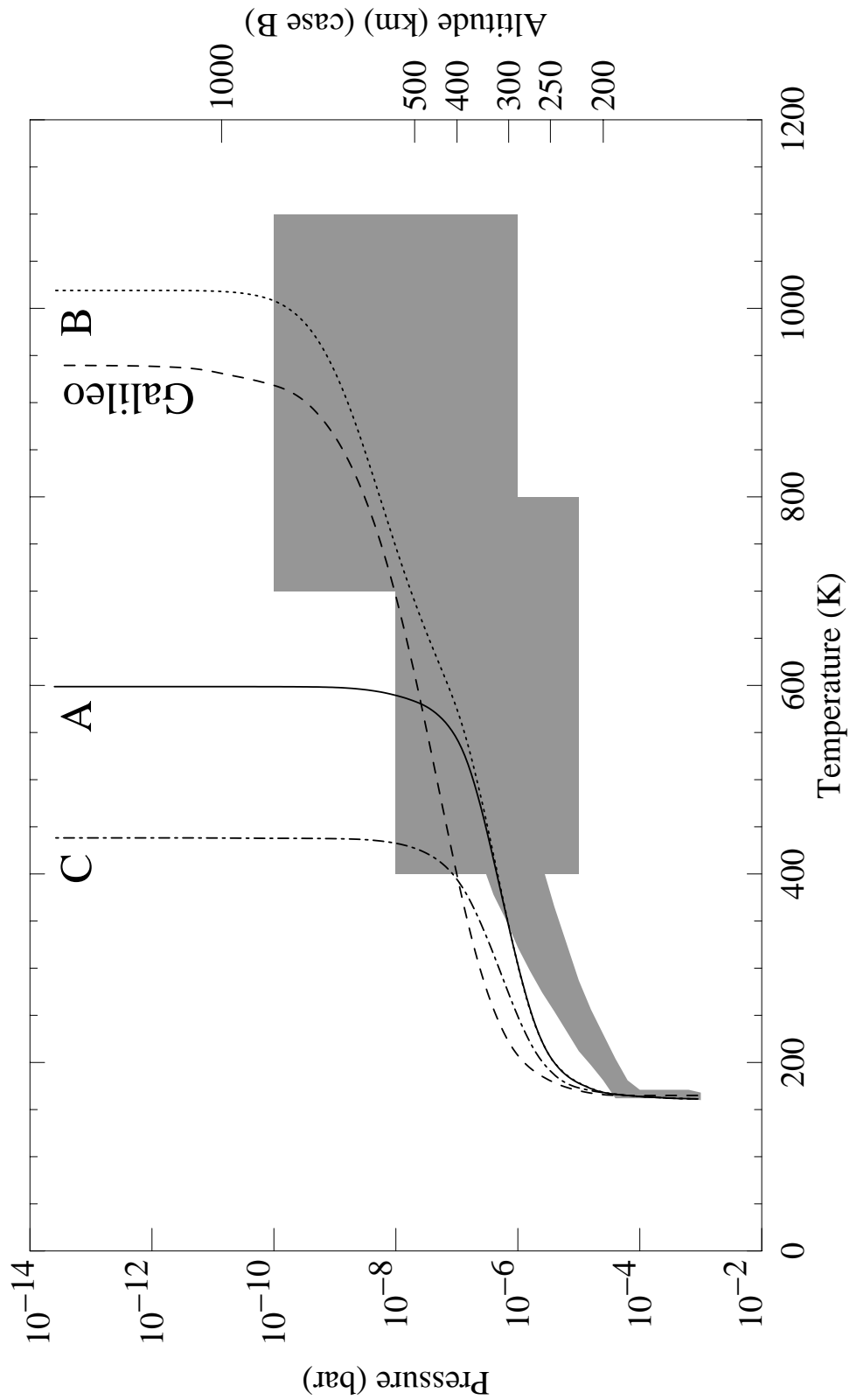


**Figure 51** : Temperature profiles calculated for cases A (—), B (.....), C (-·-·-·-). The *Galileo* equatorial temperature profile is shown for comparison (----). The altitude scale refers to case B. The shaded areas are the regions of observational constraints defined in text.

### VII.3.3 Color ratio and CH<sub>4</sub> column density

The H<sub>2</sub> -FUV color ratio  $C = \frac{I(1550-1620)}{I(1230-1300)}$  is related to the considerable drop in the CH<sub>4</sub> absorption cross section at wavelengths above 1350 Å (Yung *et al.*, 1982; Harris *et al.*, 1996; Gérard *et al.*, 1998). It leaves the bulk of the longer wavelength H<sub>2</sub> Lyman band emissions unattenuated, while the Werner and Lyman band emissions at wavelengths less than 1350 Å are substantially absorbed by methane. The color ratio  $C$  is calibrated to give a value of 1.13 for an unattenuated H<sub>2</sub> spectrum, compatible with the value derived from the laboratory H<sub>2</sub> spectrum for 100 eV electrons obtained by Liu *et al.* (1995). The color ratio is linked to the ratio of emission above and below the homopause and is therefore a proxy for the penetration depth of the electron beam below the homopause.

In order to evaluate the color ratio associated with the energy distribution of the precipitating electrons, a synthetic spectral generator is used to calculate the UV emission intensity in a prescribed spectral band for each atmospheric layer. The spectral model will be fully described in the next part.

At the temperature of the jovian atmosphere, the H<sub>2</sub> molecules in the ground state are mostly in the ground vibrational level ( $v''=0$ ). The population of the vibrational levels ( $v'$ ) of the B, C and E,F states, excited by the electron impact, are calculated with the analytical energy-dependent excitation cross sections from Shemansky *et al.* (1987), updated by Liu *et al.* (1998). The transition probabilities from these excited states to the ground level are taken from Allison and Dalgarno (1970). The corresponding wavelengths of these transitions are deduced from the calculated energy levels from Dabrowsky *et al.* (1984). At each altitude step, a spectrum is generated, depending on the local electron energy distribution calculated with the energy degradation model and H<sub>2</sub> density. In order to account for the continuum emission, the spectra are normalized to the column excitation rate of the B, E,F and C levels from the ground levels. The synthetic spectra generated at each altitude step are attenuated by absorption from the overlying methane column and integrated along a line of sight, assuming a slant path

angle of  $60^\circ$ . A wavelength-dependent  $\text{CH}_4$  absorption cross section (Mount and Moos, 1978) is used along with the methane density profile calculated by the model.

Based on eleven years of IUE spectral observations, Harris *et al.* (1996) deduced an average C color ratio of 2.5 in the north corresponding to the best linear fit to auroral  $\text{H}_2$  archival bandpass intensities. Galileo FUV observations in the northern hemisphere provide a similar mean value (W.R. Pryor, private communication). The color ratio is often expressed in terms of a corresponding vertically integrated  $\text{CH}_4$  column density above the emission peak. This integrated column only depends on the  $\text{CH}_4$  density profile and can be directly used to attenuate any bandpass of the  $\text{H}_2$  UV spectrum. However, it should be noted that such an expression assumes that all of the emission is concentrated at the emission peak and it does not account for the decreasing attenuation of the emission above the peak. Kim *et al.* (1997) observed high-resolution GHRS spectra of the aurora in the two wavelength ranges 1257-1293 Å and 1587-1621 Å and estimated methane column densities in the range  $(1.5-6.5) \times 10^{16} \text{ cm}^{-2}$ , corresponding to an altitude variation of about one scale height.

The value of the C color ratio (at  $60^\circ$ ) and the associated vertically integrated  $\text{CH}_4$  column density are listed in table 13 for cases A to C. For case A, they are 1.8 and  $2.8 \times 10^{16} \text{ cm}^{-2}$ , respectively. These values, although somewhat low, are bracketed by the observations. Higher values could be obtained by increasing the characteristic energy of the Maxwellian distribution (deeper aurora) or by raising the  $\text{CH}_4$  homopause altitude (higher absorption). These options will be discussed in later.

### VII.3.4 IR emission

Drossart *et al.* (1993) estimated the hydrocarbon IR excess emission from IRIS *Voyager* observations in the northern auroral hot spot. These emissions were viewed at about  $60^\circ$  emission angle and the IRIS projected field of view was 23,000 km in latitude and 11,500 km in longitude, which is larger than the auroral hot spot. They deduced  $\text{CH}_4$  and  $\text{C}_2\text{H}_2$  IR emissions, integrated over  $2\pi$  and averaged over the global IRIS field of view, of  $93 \pm 9 \text{ ergs cm}^{-2} \text{ s}^{-1}$  and  $26 \pm 13 \text{ ergs cm}^{-2} \text{ s}^{-1}$ , respectively. They

correspond to a filling factor of the aperture by the auroral emission on the order of 0.4. Therefore, these values could easily be doubled. The assumption of an optically thin hydrocarbon emission layer restricts the range of pressure to which their model can be applied. It is roughly defined by the pressure levels corresponding to a CH<sub>4</sub> integrated column of  $5.3 \times 10^{17} \text{ cm}^{-2}$  and a C<sub>2</sub>H<sub>2</sub> integrated column of  $7 \times 10^{15} \text{ cm}^{-2}$ , respectively. We use these column densities to determine the altitude at which the thermal IR radiation is able to leave the hydrocarbon layer. We also assume that half of the emission produced above this level finally escapes the atmosphere while the remaining half is directed downward and is ultimately lost to the optically thick layers. For case A, the altitudes of the top of the layers of unit optical depths are 206 km ( $1.9 \times 10^{-5}$  bar) and 183 km ( $5. \times 10^{-5}$  bar), for CH<sub>4</sub> and C<sub>2</sub>H<sub>2</sub> layers respectively.

Lam *et al.* (1997) observed the H<sub>3</sub><sup>+</sup> infrared auroral emission with the United Kingdom Infrared Telescope (UKIRT) high spectral resolution instrument. They found a total emission power (integrated over  $4\pi$  and corrected for line of sight effects) of the order of  $1.5 \text{ erg cm}^{-2} \text{ s}^{-1}$  at 60°, corresponding to a H<sub>3</sub><sup>+</sup> column density  $2.5\text{-}12.5 \times 10^{12} \text{ cm}^{-2}$ . These values were averaged over a 3" x 3" pixel, which covered an area on Jupiter of approximately  $9800 \times 9800 \text{ km}^2$  at the time of the observations. The total H<sub>3</sub><sup>+</sup> emission and column density should therefore be taken as lower limits to the actual auroral values. It should also be emphasized that since this thermal emission is dependent on both temperature and column density, a single emission spectrum can be fitted by different temperature/column density pairs. It is therefore impossible to determine the temperature and the column density independently from an observed spectrum. Lam *et al.* (1997) observed confined auroral zones showing a strong anticorrelation between temperature and column density. A strong H<sub>3</sub><sup>+</sup> IR emission is therefore not necessarily related to a high temperature.

It should be emphasized again that no simultaneous H<sub>3</sub><sup>+</sup> or hydrocarbon IR and H<sub>2</sub>-FUV auroral emission data sets are currently available. The relationship between these emissions, probing different altitude regions and excited by different mechanisms, has therefore never been directly observed. The spatial-temporal variability of the H<sub>2</sub>-FUV

emission is not necessarily directly linked to the variability of the hydrocarbon and  $H_3^+$  IR thermal emissions. Nevertheless, the simultaneous use of the UV and IR average emissions is still of considerable interest to constrain the radiative signature of a general energy distribution, compatible with the thermal profile.

## VII.4 Model results

### VII.4.1 Energy distribution

We now describe electron energy distributions different from case A and compare the outputs of the model to the observational constraints that were just described. All the results are listed along with the observational summary in table 13.

#### VII.4.1.1 Effect of a soft electron component : double Maxwellian energy distribution (case B)

We have already shown that the energy distribution of case A could be modified to increase the temperature above the homopause. One straightforward way to do so would be to increase the total integrated flux of the precipitated electrons. However, calculations performed with case A show that (table 13) with a  $20 \text{ ergs cm}^{-2} \text{ s}^{-1}$  aurora, a vertically integrated  $\text{H}_2$  emission excitation of 200 kR (400 kR at  $60^\circ$ ) is reached, while the integrated  $\text{H}_3^+$  emission and the exospheric temperature are below their observed values. This suggests that only the upper part of the atmosphere needs additional energy input. This result may be achieved by adding a weak soft electron contribution to the energy distribution. In case B, this soft electron component is specified by a Maxwellian distribution of  $1 \text{ erg cm}^{-2} \text{ s}^{-1}$  and a characteristic energy of 350 eV. The energy of this second component is totally degraded above the homopause, between  $10^{-8}$  and  $10^{-10}$  bar and raises the exospheric temperature to 1005 K, higher than the equatorial *Galileo* value. The integrated  $\text{H}_3^+$  emission increases to a larger value of  $2 \text{ ergs cm}^{-2} \text{ s}^{-1}$  and the estimated  $\text{H}_3^+$  rovibrational temperature increases from 542 K to 648 K, very close to the lower limit of the observed  $\text{H}_3^+$  temperature (700 K). The FUV color ratio of case A (1.83) is lower than the average IUE value of 2.5. It is slightly reduced by the soft electron component in case B (1.8) which generates unattenuated emission between the  $10^{-8}$ - $10^{-10}$  bar levels. The corresponding

vertically integrated CH<sub>4</sub> columns are 2.8x10<sup>16</sup> cm<sup>-2</sup> for case A and 2.7x10<sup>16</sup> cm<sup>-2</sup> for case B, in agreement with the observational range.

As expected, the soft electron component does not perturb the lower part of the atmosphere and the CH<sub>4</sub> integrated emission remains at 21 ergs cm<sup>-2</sup> s<sup>-1</sup>, about 0.2 times the magnitude of the observed value. The C<sub>2</sub>H<sub>2</sub> integrated emission remains at 12 ergs cm<sup>-2</sup> s<sup>-1</sup>, almost one order of magnitude below its observed value. The large discrepancy with the observation might be explained by the difference between the warm stratospheric temperature profile used by Drossart *et al.* (1993) and the stratospheric part of the temperature profile deduced from *Galileo* observations which is used in this model. The approximation made on the limit of the optically thin emission region is another source of difference.

case	energy distribution	formal equation	$\Phi_0$ (erg cm <sup>-2</sup> s <sup>-1</sup> )	$E_0$ (keV)
A	Single Maxwellian	$\Phi = \alpha \Phi_0 \frac{E}{E_0} \exp\left(-\frac{E}{E_0}\right)$	20	22
B	Double Maxwellian	$\Phi = \Phi_1 + \Phi_2$	$\Phi_{0,1}=20$ $\Phi_{0,2}=1$	$E_{0,1}=22$ $E_{0,2}=0.35$
C	Kappa Distribution	$\Phi = \alpha \Phi_0 \frac{E}{E_0} \left(1 + \frac{E}{kE_0}\right)^{-k-1}$	20	15    k=2.1

**Table 19** : characteristics of the energy distributions considered in cases A, B and C

As a consequence of the confinement of the soft electron contribution above the homopause, the calculated H<sub>2</sub> rovibrational temperature does not appreciably increase and, with 296 K, is still below the lower limit of the observational constraint (400 K). In conclusion, the inclusion of the soft electron component raises the temperature of the upper thermosphere but does not significantly increase the H<sub>2</sub> temperature.

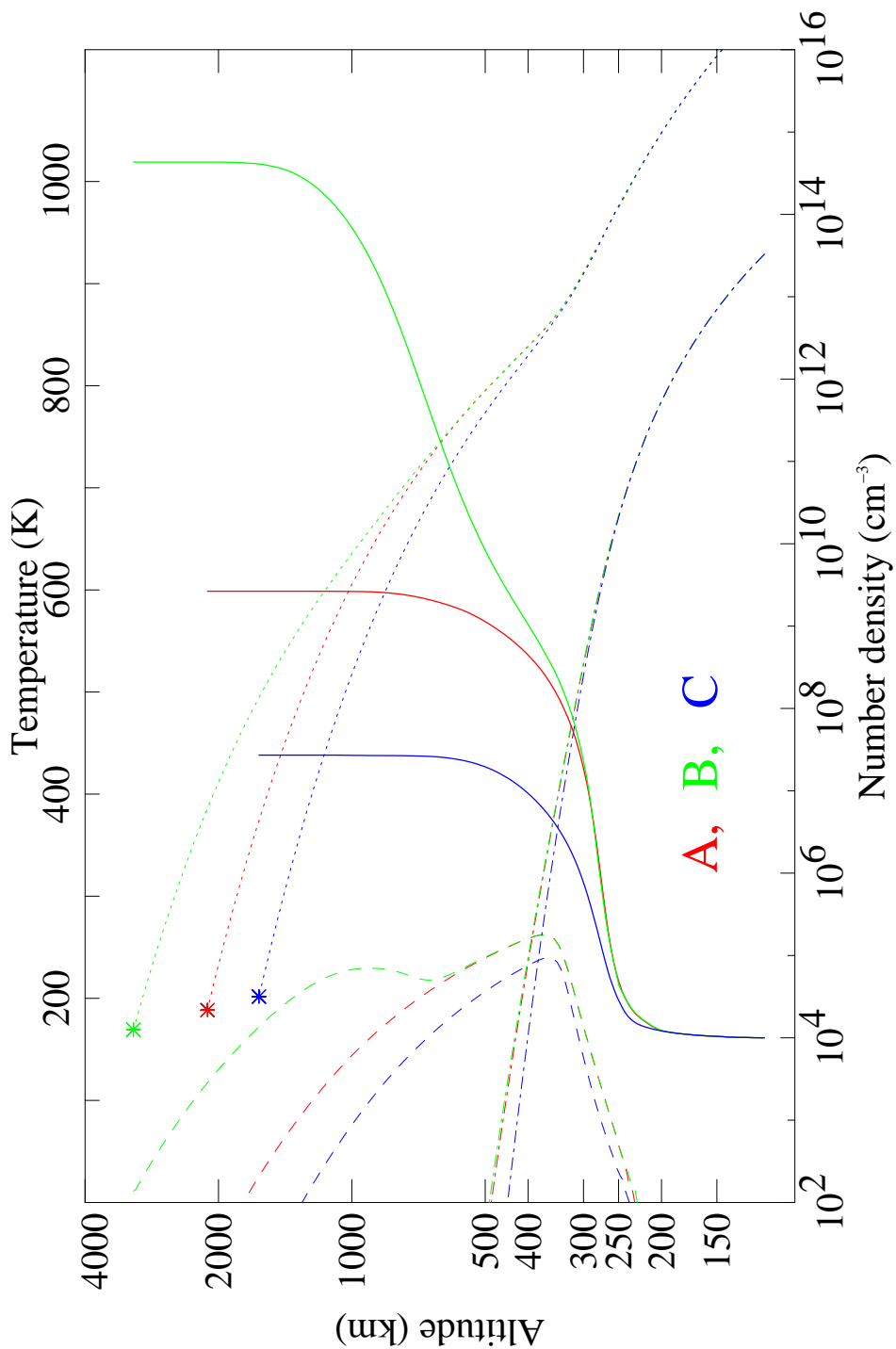


**Figure 52** : Effect of the auroral precipitation on the atmospheric composition. Each color is associated with a different case: A, dark grey; B, light grey; C, black. Four different profiles are shown for each case : temperature (—),  $H_2$  density (·····),  $H_3^+$  density (-----),  $CH_4$  density (-·-·-). The star symbol at the upper end of each  $H_2$  density profile corresponds to a pressure of  $2.5 \times 10^{-14}$  bar. The shaded areas are the regions of observational constraints defined in text.

### VII.4.1.2 Kappa energy distribution (case C)

Case C is derived by fitting measured *Galileo* Energetic Particle Detector (EPD, Williams *et al.*, 1992) near-isotropic distributions with a kappa function (Bhattacharya *et al.*, 1998). The near-isotropic distribution in the equatorial magnetosphere implies a loss cone that is filled as a result of plasma wave scattering of energetic particles, which subsequently precipitate into the atmosphere. The kappa distribution combines a power law distribution for high energy electrons and a linear distribution for the low energy electrons. The fit parameters used (table 19) are derived from multiple fits to the EPD energetic electron distribution measured between 10 and 20 R<sub>J</sub>. It should be noted that at this distance from the jovian atmosphere, the observed energy distribution may not represent the accelerated electron component of the auroral electron precipitation. Also, the EPD is designed to measure the spectra and angular distributions of electrons with energy >15 keV and therefore does not include the low energy electrons responsible for heating the upper atmosphere. The low energy part of the distribution is extrapolated with the linear part of the kappa distribution.

The integrated energy flux of the kappa distribution was set to 20.0 ergs cm<sup>-2</sup> s<sup>-1</sup> to meet the 200 kR of H<sub>2</sub> UV excitation constraint. This emission sharply peaks at 180 km, that is 134 km below the methane homopause (314 km). With this emission profile, the color ratio is equal to 5.7, a very high value which can be explained by the confinement of about 95% of the emission below the methane homopause. The corresponding overlying CH<sub>4</sub> column densities is 9.1x10<sup>16</sup> cm<sup>-2</sup>, above the GHRS range.

The integrated H<sub>3</sub><sup>+</sup> emission (0.04 erg cm<sup>-2</sup> s<sup>-1</sup>) is two orders of magnitude below the average observed emission. It corresponds to an H<sub>3</sub><sup>+</sup> column of 1.7x10<sup>12</sup> cm<sup>-2</sup>, smaller than the observed range. The resulting thermal profile (figure 51) is much colder than the *Galileo* equatorial profile (except in the lower stratosphere where the temperature is not allowed to be lower than the equatorial one). The H<sub>2</sub> temperature is only 185 K, that is 215 K below the observed H<sub>2</sub> cold limit. The H<sub>3</sub><sup>+</sup> logically follows the same trend and is 403 K, that is 300 K colder than the lower limit of the observed range. Finally, the temperature profile reaches an isothermal value 500 K colder than

the equatorial exospheric temperature. The hydrocarbon IR emissions ( $14 \text{ ergs cm}^{-2} \text{ s}^{-1}$  for  $\text{CH}_4$  and  $12 \text{ ergs cm}^{-2} \text{ s}^{-1}$  for  $\text{C}_2\text{H}_2$ ) are not enhanced compared to cases A and B. Indeed, even though most of the energy is deposited below the methane homopause, less than 50% of the resulting hydrocarbon IR emission appears above the optically thick layers. The unsuitability of the results obtained with the kappa energy distribution used in case C and the observational constraints suggests that this distribution is modified by acceleration processes undergone by the auroral electron as they travel along the magnetic field lines.

#### VII.4.1.3 Effect of the auroral precipitation on the atmospheric composition

Figure 52 illustrates the effect of the different energy distributions (A, B, C) on the composition of the atmosphere. The major effect comes from the expansion or contraction of the atmosphere following a temperature variation. Dramatic differences are observed at the top of the model atmosphere where the altitude corresponding to a pressure of  $2.5 \times 10^{-14}$  bar varies from 1620 km (case C) to 3111 km (case B). The expansion effect is not as pronounced near the homopause but it is sufficient to modify the pressure corresponding to the altitude of the  $\text{H}_2$  emission peak (245 km) which varies from  $1.35 \times 10^{-7}$  bar, for case A, to  $4.1 \times 10^{-6}$  bar, for case B. The pressure-altitude relationship is of great importance for the intercomparison of images and spectra. Indeed, some quantities are measured relative to a pressure vertical scale while others such as the *Galileo* SSI data refer to an altitude scale above the cloud deck. The atmospheric composition is also affected by the ionization produced by the auroral electrons. This effect is well illustrated by case B for which the soft electron component significantly raises the  $\text{H}_3^+$  density above 600 km.

## VII.4.2 Thermostatic role of $\text{H}_3^+$

We have checked the thermostatic role of  $\text{H}_3^+$  by canceling its cooling effect in two different cases. The first case uses the double Maxwellian energy distribution of case B while for the second case we multiplied by 10 the soft electron component of case B.

We have seen previously that the soft electrons of case B release most of their energy in the upper atmosphere. Therefore, they have a strong influence on the exospheric temperature. Cooling by  $\text{H}_3^+$  has been shown to be efficient at high altitudes, i.e. around 400 km where the  $\text{H}_3^+$  density is peaking. In case B the competition between soft electron heating and  $\text{H}_3^+$  cooling leads to an exospheric temperature of 1020 K. If cooling by  $\text{H}_3^+$  is turned off, the heat released by the soft electrons is no longer balanced at high altitude and an exospheric temperature of 2040 K is reached. Neglecting  $\text{H}_3^+$  cooling does, with the electron energy distribution of case B, double the exospheric temperature. In such a case, this limited effect also shows the importance of the downward heat conduction. Indeed, even though  $\text{H}_3^+$  substantially prevents a large increase of the exospheric temperature, its suppression does not lead to an "explosion" of the thermosphere characterized by extremely high temperatures. This means that considerable amounts of heat are conducted downward in colder regions.

However, downward heat conduction has limited effects and the situation becomes critical if the soft electron component of case B is raised to  $10 \text{ ergs cm}^{-2} \text{ s}^{-1}$  (instead of 1). Without  $\text{H}_3^+$  cooling, the exospheric temperature reaches a (never observed) value of 18400 K, to be compared to 2040 K obtained with case B without  $\text{H}_3^+$  cooling.

Accounting for the  $\text{H}_3^+$  cooling with this electron energy distribution decreases the exospheric temperature to a more reasonable value of 3920 K, that is, a temperature 5 times colder. All these temperatures are summarized in table 20.

	Energy distribution	
	case B	case B + increased soft electron component
with H <sub>3</sub> <sup>+</sup> cooling	1020 K	3920 K
no H <sub>3</sub> <sup>+</sup> cooling	2040 K	18400 K

**Table 20** : Exospheric temperatures obtained with two different soft electron components, with and without H<sub>3</sub><sup>+</sup> cooling.

From this table it is seen that increasing by 10 the soft electron component of the energy distribution of case B increases the exospheric temperature :

- by a factor 9, if H<sub>3</sub><sup>+</sup> cooling is turned off
- by a factor 4, else.

This non-linearity clearly shows the temperature dependence of the H<sub>3</sub><sup>+</sup> cooling efficiency : the higher the temperature, the more efficient the cooling (this temperature dependence was already illustrated in figure 42). It also demonstrates the thermostatic role of H<sub>3</sub><sup>+</sup> which prevents an overheating of the thermosphere, especially when downward heat conduction is not sufficient to evacuate heat toward colder regions.

### VII.4.3 Sensitivity study

We now consider the sensitivity of the outputs of case B (giving the best results) to four important parameters: 1) the altitude of the H<sub>2</sub> emission peak, 2) the H<sub>3</sub><sup>+</sup> quenching rate for the translation-vibration reaction, 3) the eddy diffusion coefficient, and 4) the temperature of the stratosphere. The altitude of the H<sub>2</sub> emission peak is mainly controlled by the characteristic energy of the electrons. This altitude also determines the region of the atmosphere which is heated by the precipitating electrons. It also constrains the region where ionization occurs and therefore controls the H<sub>3</sub><sup>+</sup> density profile and the associated cooling efficiency. Consequently, the altitude of the H<sub>2</sub> emission peak can be considered as a major parameter for the control of the thermal profile.

The H<sub>3</sub><sup>+</sup> cooling efficiency is also dependent on the quenching rate of H<sub>3</sub><sup>+</sup> by H<sub>2</sub>. This parameter modifies the upper part of the thermal profile, especially the exospheric temperature.

We have shown that methane and acetylene are important heat sinks in the stratosphere which control the thermal profile in this region. The CH<sub>4</sub> cooling rate profile depends on the CH<sub>4</sub> density profile which in turn is determined by the eddy coefficient near the homopause. The relative altitudes of the H<sub>2</sub> emission and the hydrocarbon homopause determine the value of the H<sub>2</sub> FUV color ratio. The stratospheric part of the thermal profile has direct effect on the efficiency of the hydrocarbon radiative cooling. Results of the following sensitivity tests are summarized in table 12.

#### VII.4.3.1 Sensitivity to the altitude of the emission peak (case D)

So far we have considered that the peak of the H<sub>2</sub> emission is located at an altitude of 245 km, determined from the H<sub>2</sub> visible emission profile observed with *Galileo*. However, this altitude is uncertain within a range of  $\pm 30$  km. Moreover, Pryor *et al.* (1999) used the FUV/MUV/violet ratios on a *Galileo* spectrum acquired along orbit G7 to deduce a peak altitude between 275 and 295 km for a Chapman

function representing the auroral excitation in the Gladstone *et al.* (1998) atmospheric model. These results suggest that an emission altitude peak of 275 km, corresponding to the upper limit set by the visible *Galileo* images, might be reasonable.

	Observation	case A	case B	case C
		Maxwellian	double Maxwellian	Kappa
exospheric temperature (K)	940 (equat.)	599	1019	438
H <sub>2</sub> temperature (K)	400-800	265	296	185
H <sub>3</sub> <sup>+</sup> temperature (K)	700-1200	542	648	403
vertically integrated H <sub>2</sub> excitation (kR)	200	200	200	200
H <sub>2</sub> emission peak altitude (km)	245 (± 30)	242	246	179
CH <sub>4</sub> homopause altitude (km)		312	312	314
H <sub>2</sub> FUV color ratio (60°)	2.5	1.83	1.8	5.7
integrated CH <sub>4</sub> column (10 <sup>16</sup> cm <sup>-2</sup> )	1.5-6.5	2.8	2.7	9.1
integrated H <sub>3</sub> <sup>+</sup> emission (60°) (erg cm <sup>-2</sup> s <sup>-1</sup> )	1.5	1.	2.	0.04
H <sub>3</sub> <sup>+</sup> column (10 <sup>12</sup> cm <sup>-2</sup> )	2.5-12.5	4.2	8.6	1.7
integrated CH <sub>4</sub> emission (60°) (erg cm <sup>-2</sup> s <sup>-1</sup> )	93 (± 9)	20.5	21	14
integrated C <sub>2</sub> H <sub>2</sub> emission (60°) (erg cm <sup>-2</sup> s <sup>-1</sup> )	86 (± 5)	12	12	12

**Table 21** : Main outputs resulting from the energy degradation of cases A, B and C compared with the observation.

Such an altitude is reached with the double Maxwellian energy distribution of case B if the characteristic energy of the fast electron component is set to 13 keV. This energy distribution is considered in case D, the major results are presented in table 12 and should be compared with those of case B in table 13. As expected, the thermal profile is mainly modified in the region of the H<sub>2</sub> emission peak, i.e. in the 10<sup>-5</sup>-10<sup>-7</sup> bar pressure region. This results into a higher H<sub>2</sub> temperature which increases from 296 K to 410 K. It should be pointed out that in this case the hydrocarbon cooling must be balanced by unspecified heat sources. Since a non negligible part of the CH<sub>4</sub> density profile lies in a

warmer region, the integrated CH<sub>4</sub> infrared radiative cooling emission is increased by 15%. The C<sub>2</sub>H<sub>2</sub> emission remains unchanged.

The exospheric temperature increases by 40 K and the H<sub>3</sub><sup>+</sup> (emission weighted) temperature increases by 15 K. The lower H<sub>3</sub><sup>+</sup> temperature increase can be explained by the higher H<sub>3</sub><sup>+</sup> production between 250 km and 800 km. The H<sub>3</sub><sup>+</sup> temperature is indeed estimated from the H<sub>3</sub><sup>+</sup> emission profile which, in case D, puts more weight on a colder region. Another consequence of the higher H<sub>3</sub><sup>+</sup> production is the enhanced integrated H<sub>3</sub><sup>+</sup> IR emission which is about 2.5 that of case B. This clearly illustrates the hydrostatic role played by the H<sub>3</sub><sup>+</sup> ions: a temperature increase raises the H<sub>3</sub><sup>+</sup> radiative cooling efficiency and prevents any dramatic increase of temperature in the thermosphere. Moreover, if the thermospheric temperature increase is due to the injection of soft electrons then the cooling efficiency is also strengthened by the production of H<sub>3</sub><sup>+</sup> resulting from the ionization parallel to heat deposition.

The FUV color ratio (1.2) is very close to the unattenuated ratio (1.1) since most of the H<sub>2</sub> FUV emission originates from above the CH<sub>4</sub> absorbing layer. This very low attenuation is in disagreement with the observation. A (double) Maxwellian energy distribution resulting in a H<sub>2</sub> emission peak at 275 km might therefore not be compatible with the average observed FUV-color ratio. Either the emission profile is not correctly shaped and requires more emission below the peak, as would be obtained with another energy distribution including more high energy electrons, or the methane column is too low resulting in too little attenuation of the H<sub>2</sub> emission. The dependence of the outputs on the methane column is illustrated in the following section.

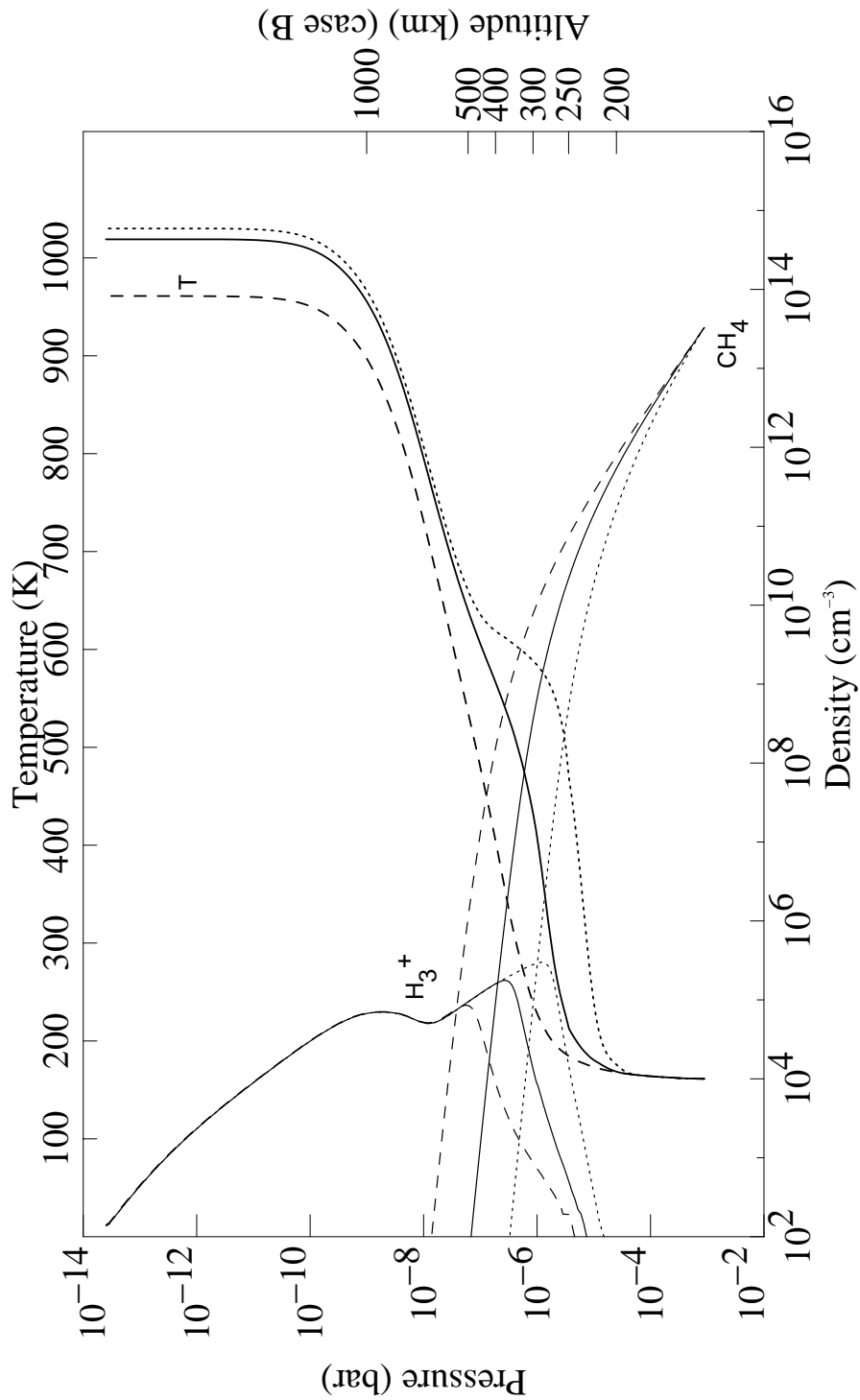


**Figure 53** : Destruction of  $\text{H}_3^+$  by methane and acetylene for different values of the eddy coefficient. Three cases are illustrated: case B (—), case E (⋯⋯), case F (----), corresponding to homopause altitudes of 312 km ( $K_H=1.4 \times 10^6 \text{ cm}^2 \text{ s}^{-1}$ ), 251 km ( $K_H=1.4 \times 10^5 \text{ cm}^2 \text{ s}^{-1}$ ), and 381 km ( $K_H=1.4 \times 10^7 \text{ cm}^2 \text{ s}^{-1}$ ), respectively. The altitude scale is calculated for case B. For the sake of clarity, only the density profiles of  $\text{H}_3^+$  and  $\text{CH}_4$  are shown with the temperature profile.

### VII.4.3.2 Sensitivity to the altitude of the homopause (cases E and F)

The eddy coefficient at the homopause ( $K_H$ ) plays a key role in the establishment of the methane density profile, especially in the region of the  $H_2$  emission peak since it defines the altitude of the homopause. Two cases are simulated, E and F, for which  $K_H$  differs from case B by 1 order of magnitude.

In case E,  $K_H=1.4 \times 10^5 \text{ cm}^2 \text{ s}^{-1}$  and the altitude of the homopause is 251 km, significantly lower than in case B where the altitude of the homopause was 312 km.

The lower  $CH_4$  density has direct effects on the temperature profile: the  $H_2$  rovibrational temperature increases by 40% as a result of the lower  $CH_4$  (and  $C_2H_2$ ) cooling, while the  $H_3^+$  temperature decreases by 4% due to the higher  $H_3^+$  density resulting from a lower destruction by  $CH_4$ . This higher  $H_3^+$  cooling efficiency translates to an increase of the  $H_3^+$  IR emission by a factor 3.3. The modification of the  $H_3^+$  density profile resulting from the lower destruction by methane and acetylene is compared with the density profile of case B in figure 53. The strong temperature increase at 300 km and the raise of the  $H_3^+$  density between 250 and 400 km are clearly related to the drop the homopause altitude.

Since the temperature profile is substantially modified in the region of the emission peak, the altitude-pressure relationship is modified accordingly and the energy distribution, similar to that of case B, leads to a peak of  $H_2$  emission at 238 km (compared to 246 km in case B). As expected, the lower eddy coefficient decreases the FUV color ratio to 1.2, close to the unattenuated value. The integrated  $CH_4$  column density ( $0.4 \times 10^{16} \text{ cm}^{-2}$ ) is much below the observational range.

An interesting conclusion might be drawn from the similarities between cases D and E. In both cases the  $H_2$  emission peaks about 20 km below the homopause. As far as methane attenuation of the  $H_2$  FUV spectrum is concerned, cases D and E are therefore almost equivalent. There is indeed no net difference between the color ratios ( $\sim 1.2$ ) and between the integrated  $CH_4$  columns above the emission peak ( $\sim 0.5 \times 10^{16} \text{ cm}^{-2}$ ). The

color ratio and the CH<sub>4</sub> column may be considered as proxies for the altitude difference between the H<sub>2</sub> emission peak and the homopause. The absolute altitude of the emission peak, and consequently the characteristic energy of the auroral electron energy distribution cannot be deduced from these parameters if the model neutral atmosphere is not fully determined or if other observables are not taken into account. Another important point is the difficulty to get both the H<sub>2</sub> temperature and the H<sub>2</sub> FUV color ratio right with the same total energy influx. In case D the altitude of the emission peak is raised by shifting the energy distribution towards lower energies. This leads to the expected increase of H<sub>2</sub> temperature but also implies an inappropriate decrease of the H<sub>2</sub> FUV color ratio. The energy distribution used in case E is similar to that of case B where the H<sub>2</sub> temperature increase is achieved by reducing the hydrocarbon cooling through decreases in the eddy coefficient. The resulting lowering of the altitude of the methane homopause leads again to a drop of the color ratio.

	case D	case E	case F	case G	case H
	$E_0=12.6$ keV	$K_H=1.4 \times 10^5$ $\text{cm}^2 \text{s}^{-1}$	$K_H=1.4 \times 10^7$ $\text{cm}^2 \text{s}^{-1}$	halved quench. rate	warm stratosphere
exospheric temperature (K)	1059	1030	961	1130	1018
H <sub>2</sub> temperature (K)	410	418	240	304	342
H <sub>3</sub> <sup>+</sup> temperature (K)	663	624	699	682	645
vertically integrated H <sub>2</sub> excitation (kR)	200	200	200	200	200
H <sub>2</sub> emission peak altitude (km)	273	238	245	242	251
CH <sub>4</sub> homopause altitude (km)	309	251	381	312	325
H <sub>2</sub> FUV color ratio (60°)	1.24	1.19	3.13	1.78	1.69
integrated CH <sub>4</sub> column ( $10^{16} \text{ cm}^{-2}$ )	0.7	0.4	5.8	2.7	2.4
integrated H <sub>3</sub> <sup>+</sup> emission (60°) ( $\text{erg cm}^{-2} \text{ s}^{-1}$ )	5.	6.5	0.5	1.8	2.3
H <sub>3</sub> <sup>+</sup> column ( $10^{12} \text{ cm}^{-2}$ )	11.7	12.6	5.9	9.1	9.0
integrated CH <sub>4</sub> emission (60°) ( $\text{erg cm}^{-2} \text{ s}^{-1}$ )	25.	14.5	16.	20.5	139.
integrated C <sub>2</sub> H <sub>2</sub> emission (60°) ( $\text{erg cm}^{-2} \text{ s}^{-1}$ )	12.	12.	12.	12.	23.

**Table 22:** Main outputs resulting from the energy degradation of cases D, E, F, G, H.

In case F, the eddy coefficient  $K_H$  is set to the large value of  $1.4 \times 10^7 \text{ cm}^2 \text{ s}^{-1}$ . This leads to a homopause altitude of 381 km, 70 km higher than in case B. The

corresponding higher CH<sub>4</sub> density is responsible for the drop (20%) of the H<sub>2</sub> temperature as CH<sub>4</sub> cools down the region where most of the auroral energy is converted into heat. As a result of the smaller H<sub>3</sub><sup>+</sup> column, which is destroyed by the CH<sub>4</sub> excess (figure 53), the H<sub>3</sub><sup>+</sup> temperature increases by 50 K. The decrease of the H<sub>3</sub><sup>+</sup> column also implies a decrease of the H<sub>3</sub><sup>+</sup> IR emission by a factor 4. The integrated CH<sub>4</sub> column above the H<sub>2</sub> emission peak ( $5.8 \times 10^{16} \text{ cm}^{-2}$ ) and the FUV color ratio (3.13) are almost twice as large as the values in case B. Upwelling of methane due to the large amount of auroral energy deposited near the homopause may indeed cause redistribution of the CH<sub>4</sub> mixing ratio above the homopause similar to the O<sub>2</sub>/N enrichment observed in the Earth auroral thermosphere.

#### VII.4.3.3 Sensitivity to the H<sub>3</sub><sup>+</sup> quenching rate coefficient (case G)

The quenching rate of H<sub>3</sub><sup>+</sup> by H<sub>2</sub> is an important parameter which determines the H<sub>3</sub><sup>+</sup> cooling efficiency directly acting on the upper thermospheric thermal profile. To date, there are no direct measurements of rate coefficients of elementary processes occurring during quenching of H<sub>3</sub><sup>+</sup> by H<sub>2</sub> and we considered the "phenomenological" rate coefficient  $(2.7 \pm 0.6) \times 10^{-10} \text{ cm}^3 \text{ s}^{-1}$  determined by Kim *et al.* (1974). It is based on a simplified reaction rate which does not account for the distribution of excited states of H<sub>3</sub><sup>+</sup>. Also, it is not known whether deactivation occurs directly from each vibrational state to the ground state or by sequential deactivation in a number of collisions. This quenching coefficient therefore represents only an average or overall value.

Case G uses the same set of parameters as case B, but in order to test the effect of a different quenching rate, this parameter has been arbitrarily halved ( $1.35 \times 10^{-10} \text{ cm}^3 \text{ s}^{-1}$ ). The resulting reduced H<sub>3</sub><sup>+</sup> radiative cooling increases the H<sub>3</sub><sup>+</sup> temperature by 34 K while the H<sub>2</sub> temperature remains almost unchanged, mainly because the two

regions are spatially separated. Indeed, the thermal profile departs from the profile of case B at an altitude of 400 km. The  $\text{H}_3^+$  column is higher than in case B. This might be explained by the lower efficiency of the  $\text{H}_3^+$  loss term (reactions 1 and 2 in table 15) which is inversely proportional to the temperature. The exospheric temperature slightly increases by 10 K. A lower quenching rate might therefore be an alternative to the soft electron component to increase the thermospheric temperature and especially the  $\text{H}_3^+$  temperature.

#### VII.4.3.4 Sensitivity to the stratospheric temperature profile (case H)

Cases A to G, described in tables 13 and 12, illustrate the difficulty to increase the  $\text{CH}_4$  and  $\text{C}_2\text{H}_2$  IR emissions. One straightforward solution is to raise the stratospheric temperature. However, we showed that the degradation of the auroral energy could not increase that temperature and we therefore assumed that non-auroral processes, such as breaking gravity waves, could sustain the stratospheric part of the equatorial thermal profile deduced from *Galileo* observations. In case H, we assume that these non-auroral processes and probably exothermic processes triggered by the aurora (such as the hydrocarbon chemistry) produce a stratospheric temperature profile similar to the auroral (hot spot) IRIS cold boundary previously described. The upper part of the thermal profile is approximated by shifting the *Galileo* profile downward until a continuous profile is obtained. This new thermal structure is used as an initial profile and the energy flux of case B is iteratively degraded until a steady state thermal profile is reached. As expected, the IR methane emission is multiplied by 7 and reaches a value ( $139 \text{ ergs cm}^{-2} \text{ s}^{-1}$ ), in better agreement with the observation. The  $\text{C}_2\text{H}_2$  emission increase (factor two) is limited by the lower temperature increase in the lower stratospheric region (below 200 km). The resulting temperature profile is shown in figure 54. It is compared to the equatorial *Galileo* profile and to the domain of observational constraints previously defined. Below the  $10^{-7}$  bar pressure level the converged temperature profile is somewhat warmer than that of case B. Above this level, the two profiles are equivalent. As a result, the  $\text{H}_2$  temperature increases by 46 K

while the  $\text{H}_3^+$  temperature remains the same.

The IRIS warm upper boundary has been tested similarly. In these conditions the energy flux of case B is unable to sustain the thermal profile. The thermal energy radiated by methane ( $1270 \text{ ergs cm}^{-2} \text{ s}^{-1}$ ) is so important that this deep heat sink drives most of the auroral heat and prevents any further heating of the atmosphere. This unlikely situation might be explained by an incompatibility between the IRIS warm upper boundary and the methane density profile calculated by the degradation model. Indeed, as was already the case for  $\text{H}_3^+$ , methane IR emission is intimately linked to the temperature-density pair.

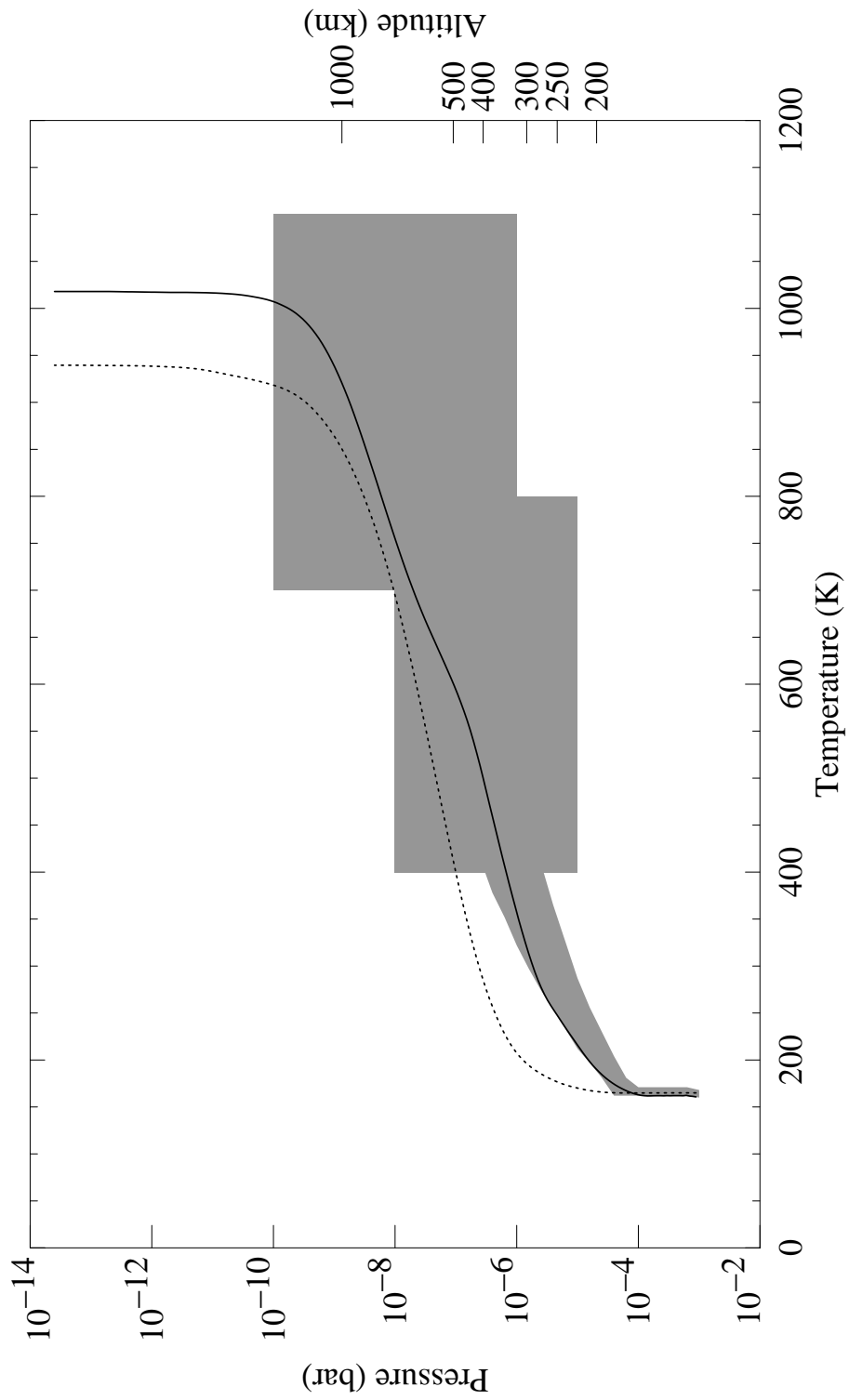


**Figure 54** : Temperature profile calculated for case H (—). The equatorial Galileo profile (---) is shown for comparison. The shaded areas are the regions of observational constraints defined in text.

## VII.5 Conclusion

A one-dimensional model has been developed which couples a two-stream electron transport model of energy deposition with a 1-D thermal conduction model including particle heating,  $\text{CH}_4$ ,  $\text{C}_2\text{H}_2$  and  $\text{H}_3^+$  cooling. The initial atmospheric structure is defined by a thermal profile deduced from *Galileo* observations. The code allows us to monitor the energy degradation of an electron beam as it penetrates into this atmosphere which self-consistently adapts to the auroral conditions. The resulting thermal profile, UV and IR emissions profiles, FUV color ratio, and densities generated by various choices of the precipitating electron energy distribution are constrained by data derived from spectra and images taken in different bandpasses. Sensitivity tests are performed to evaluate the importance of the energy spectrum of the incident electrons for the thermal balance of Jupiter's auroral thermosphere and to show the limitations of the degradation code.

Different conclusions can be drawn from the eight test cases considered. In order to meet the  $\text{H}_2$  integrated brightness constraint, a trade-off is necessary between the FUV color ratio and the  $\text{H}_2$  rovibrational temperature. Indeed, case D shows that the easiest way to get a sufficiently high  $\text{H}_2$  temperature is to shift the  $\text{H}_2$  emission profile towards higher altitudes. However, this shift places most of the  $\text{H}_2$  emission above the methane homopause and the FUV color ratio almost equal to its unattenuated value. A second way to increase the  $\text{H}_2$  temperature is to reduce the hydrocarbon cooling by assuming a lower eddy coefficient. However, this also lowers the altitude of the homopause which in turn reduces the FUV color ratio. Similarities between the results of cases D and E demonstrate that the FUV color ratio deduced from spectral observations cannot be used to determine the absolute altitude of  $\text{H}_2$  emission but rather the altitude of  $\text{H}_2$  emission relative to the altitude of the methane homopause.

The  $\text{H}_3^+$  and exospheric temperatures are mainly due to the level of soft electron influx and are almost independent from the  $\text{H}_2$  UV and hydrocarbon IR emissions and temperatures (which are partly controlled by the high energy component of the energy distribution). The  $\text{H}_3^+$  temperature can be raised independently from the  $\text{H}_2$  and

hydrocarbon observables by increasing the soft electron component, but it must be traded off with the observed  $\text{H}_3^+$  IR emission intensity, which also increases with the low energy component of the distribution. It was shown in case G that reducing the  $\text{H}_3^+$  quenching rate leads to a higher  $\text{H}_3^+$  temperature and a lower integrated  $\text{H}_3^+$  brightness. These cases illustrate the essential thermostatic role played by  $\text{H}_3^+$  which regulates the heating in the thermosphere and thus the atmosphere expansion.

Case H suggests that the auroral upper stratosphere is probably warmer than the equatorial upper stratosphere measured by *Galileo*. With case C, it also shows that the auroral energy precipitated is not able to provide the necessary heat to balance the hydrocarbon cooling. Non-auroral processes, such as Joule heating or breaking gravity waves, and indirect auroral processes, like exothermic hydrocarbon chemistry, need to be specified as well.

The kappa energy distribution used in case C produces outputs that do not match the observational constraints. This might be explained by the fact that this distribution which fits *Galileo* EPD measurements between 10 and 20 R<sub>J</sub> may not reflect the accelerating processes undergone by the auroral electron as they travel along the magnetic field lines.

The different cases show that the IR  $\text{H}_3^+$  emission probes a region sensitive to the soft electron component of the energy distribution, while the  $\text{H}_2$  FUV emission is sensitive to energetic electrons. The IR hydrocarbon emissions give information on the non-auroral and indirect auroral processes controlling the temperature in the lower stratosphere.

The  $\text{H}_2$  extreme ultraviolet emission (EUV) could be used to probe the region sensitive to the soft electrons. Indeed, the EUV photons produced by electron impact on  $\text{H}_2$  are subject to self-absorption. They will therefore escape the optically thick region at an altitude higher than the level where the initial electron impact occurred. EUV *Galileo* and HUT (Wolven *et al.* 1998) observations already exist and observations spanning the 900-1200 Å range will soon be available with the Far Ultraviolet Spectroscopic Explorer (FUSE) satellite. However before these data can be used, an important effort is required (in progress) to include the self-absorption of  $\text{H}_2$  Lyman and Werner emission below 1000 Å in synthetic spectra.

It has been stressed that the multispectral observational constraints have been established from measurements that are not simultaneous in time and space. Moreover since these observations probe different altitude regions of the atmosphere, they do not necessarily stem from the same processes. A campaign of simultaneous multispectral observations of Jupiter's aurora would allow a more reliable determination of the complete energy budget of the precipitating electrons and would give some clues on the possible link between the different auroral signatures.

# Part 3

## VIII The spectral generator

### VIII.1 H<sub>2</sub> far ultraviolet spectroscopy

A detailed study of molecular spectroscopy is largely out of the scope of the present work. We restrict ourselves to an overview of the main processes that are taken into account by the generator synthesizing high resolution H<sub>2</sub> spectra within the UV range 900-1700 Å.

These processes include :

1. electron impact excitation of the H<sub>2</sub> X<sup>1</sup>Σ<sub>g</sub><sup>+</sup> ground state to the different rovibrational states of the B<sup>1</sup>Σ<sub>u</sub><sup>+</sup>, C<sup>1</sup>Π<sub>u</sub> and E,F<sup>1</sup>Σ<sub>g</sub><sup>+</sup> excited electronic states
2. radiative deexcitation from the B<sup>1</sup>Σ<sub>u</sub><sup>+</sup>, C<sup>1</sup>Π<sub>u</sub> states to the X<sup>1</sup>Σ<sub>g</sub><sup>+</sup> ground state.

The effect of the B'<sup>1</sup>Σ<sub>u</sub><sup>+</sup>, B''<sup>1</sup>Σ<sub>u</sub><sup>+</sup>, D<sup>1</sup>Π<sub>u</sub> and D'<sup>1</sup>Π<sub>u</sub> Rydberg states are not included in the present model as their contribution to the jovian spectrum is very small above 1200 Å (*Ajello et al.*, 1984).

In the following section, useful notations and conventions applying to H<sub>2</sub> are reviewed. They are used to introduce the quantum numbers that are relevant to characterize the rovibrational levels of the H<sub>2</sub> molecule. The principal selection rules applying to dipole transitions are then summarized. Finally we give the formulae that are used to calculate the line intensity for the radiative deexcitation from the B<sup>1</sup>Σ<sub>u</sub><sup>+</sup> and

$C^1\Pi_u$  electronic states to the  $X^1\Sigma_g^+$  ground state of  $H_2$ .

## VIII.1.1 Conventions

Selection rules for radiative deexcitation involve quantum numbers and symmetry properties of the various energy levels of a molecule. These characteristics are conventionally summarized by symbols in the spectroscopic term of the molecule. For the H<sub>2</sub> molecule, the following notation is used :

$$X \quad 2S+1 \quad \mathbf{A}_{g,u}^{+,-}$$

### VIII.1.1.1 X, $\mathbf{A}$

The letter in front of the term symbol (X) designates different electronic states which may be of the same type. This letter may be X, A, B, C, ..., a, b, c, ... (states represented by a lower-case letter do not have the same multiplicity than those represented by an upper-case letter) and X is usually used for the ground state of the molecule.

$\mathbf{A}$  is a symbol related to  $\Lambda$  : the quantum number associated to the  $\mathbf{\Lambda}$  vector which is the component of the electronic orbital angular momentum  $\mathbf{L}$  along the internuclear axis (*vectors are represented with bold characters*).

Following the international nomenclature,

$$\Lambda = |M_L|$$

and  $M_L$  can take only the values

$$M_L = L, L-1, L-2, \dots, -L$$

where L is the quantum number characterizing the magnitude of  $\mathbf{L}$ .

For a given value of L, the quantum number  $\Lambda$  can take the values

$$\Lambda = 0, 1, 2, \dots, L.$$

Thus in the molecule for each value of L there are L+1 distinct states with different energies (in diatomic molecules, states differing only in the sign of  $M_L$  have the same energy). According as  $\Lambda = 0, 1, 2, 3, \dots$ , the corresponding molecular state is designated as  $\Sigma, \Pi, \Delta, \dots$  state, analogous to the mode of designation for atoms.

$\Pi, \Delta, \dots$  states are doubly degenerate since  $M_L$  can have the two values  $+\Lambda$  and  $-\Lambda$ ;  $\Sigma$

states are non-degenerate since  $M_L$  can only have one value (zero).

### VIII.1.1.2 $2S+1$

The left superscript  $2S+1$  is called the *multiplicity of the state* and is due to the electron spin. Under the action of electrostatic forces the spins of the individual electrons form a resultant vector  $\mathbf{S}$ , the corresponding quantum number  $S$  being integral or half integral according as the total number of electrons in the molecule is even or odd. For the  $H_2$  molecule,  $S=0$  or  $S=1$  (antiparallel or parallel spins) and give rise to singlet or triplet states, respectively. In  $\Sigma$  states ( $\Lambda = 0$ ), the resultant spin  $\mathbf{S}$ , since it is unaffected by an electric field, is fixed in space as long as the molecule does not rotate and if there is no external magnetic field. Consequently, these states remain single. On the other hand, if  $\Lambda \neq 0$ , ( $\Pi$ ,  $\Delta$ , ... states), there is an internal magnetic field in the direction of the internuclear axis resulting from the orbital motion of the electrons. This field causes a precession of  $\mathbf{S}$  about the internuclear axis and the electronic term splits into a multiplet of  $2S+1$  components. Each component is characterized by the quantum number  $M_S$  which can take the values  $M_S = S, S-1, \dots, -S$ .

### VIII.1.1.3 (+,-)

The right superscript (+,-) refers to the symmetry properties of the electronic eigenfunctions of  $\Sigma$  states. These properties depend on the symmetry properties of the field in which the electrons move. In a diatomic molecule any plane through the internuclear axis is a plane of symmetry. Therefore the electronic eigenfunctions of a non-degenerate state ( $\Sigma$  state) either remains unchanged or changes sign when reflected at any plane passing through both nuclei. In the first case, the state is called a  $\Sigma^+$  state, and in the second case it is called a  $\Sigma^-$  state.

#### VIII.1.1.4 (g,u)

The right subscript (g,u) refers to the symmetry properties of the electronic eigenfunctions. These properties apply to diatomic molecules for which the two nuclei have the same charge. In this case, the field in which the electrons move has, in addition to the symmetry axis, a center of symmetry at the midpoint of the internuclear axis. The field remains unaltered by a reflection of the nuclei at this center of symmetry. As a consequence, the electronic eigenfunctions remain either unchanged or only change sign when reflected at the center (that is, when the coordinates of all the electrons  $x_i, y_i, z_i$ , are replaced by their negative  $-x_i, -y_i, -z_i$ ). In the first case, the state to which the eigenfunction belongs is called an *even state* ("gerade" *g state*), in the second case an *odd state* ("ungerade" *u state*). Thus for molecules with like nuclei we have  $\Sigma_g, \Sigma_u, \Pi_g, \Pi_u, \dots$  states.

#### VIII.1.1.5 Other symmetry properties

The symmetry properties of the rotational levels are not represented in the spectroscopic term but they are taken into consideration in the selection rules. We have seen above that the electronic eigenfunctions of an atomic system may remain unchanged or just change sign when reflection at the origin (replacement of all  $x_k, y_k, z_k$  by  $-x_k, -y_k, -z_k$ ) is applied. A closer investigation of the rotator functions ( $\Psi_r$ ) shows that for such a reflection they remain unchanged for even values of J (the rotational quantum number) but change to  $-\Psi_r$  for odd values of J. Therefore, a *rotational level is called positive or negative* depending on whether the total eigenfunction remains unchanged or changes sign for such a reflection. This property is also called the *parity*.

The complete eigenfunction of a molecule, in the Born-Oppenheimer approximation, is a product of an electronic, a vibrational, and a rotational contribution

$$\Psi = \Psi_e \frac{1}{r} \Psi_v \Psi_r .$$

Since, as we saw above,  $\Psi_e$  may itself change sign by reflection at the origin (as is the case for  $\Sigma$  states), the total eigenfunction remains unaltered for odd  $J$  and changes sign for even  $J$ . In this case the + and - have to be changed for the rotational levels.

In homonuclear molecules like  $H_2$ , it can be shown that for an exchange of the two nuclei the total eigenfunction either remains unchanged or changes its sign. According as the former or the latter is the case, the state under consideration is said to be *symmetric* ( $s$ ) or *antisymmetric* ( $a$ ) in the nuclei. Again, for electronic states whose  $\Psi_e$  change sign upon such a reflection,  $s$  and  $a$  have to be reversed.

In the actual molecule rotation and vibration take place simultaneously with the electronic motions. We must find out by what quantum numbers we can describe the rotational levels in the different types of electronic states, how their energy depend on these quantum numbers, and what symmetry properties the corresponding eigenfunctions possess. All this is essential for the determination of the selection rules.

## VIII.1.2 $\Lambda$ -type doubling

In most diatomic molecules the interaction between the rotation of the nuclei and  $\mathbf{L}$  is neglected. However, for light molecules like  $\text{H}_2$ , the speed of nuclear rotation is larger and this interaction must be taken into account. For  $\text{H}_2$  states with  $\Lambda \neq 0$  it is found to produce a splitting into two components, with their own symmetry properties, for each  $J$  value which are doubly degenerate ( $M_L$  can have the two values  $+\Lambda$  and  $-\Lambda$ ). This splitting is called  $\Lambda$ -type doubling. We will see its effects on the electric dipole transitions from the  $\text{C}^1\Pi_u$  state to the  $\text{X}^1\Sigma_g^+$  ground state of  $\text{H}_2$ .

## VIII.1.3 Selection rules for electronic transitions

The quantum numbers and symmetry properties that we just introduced affect the spectra of diatomic molecules through the selection rules that hold for them.

The selection rules are obtained by evaluating the matrix element  $\mathbf{R}^{nm}$  of the electric dipole moment. Indeed, the interaction of an electromagnetic wave having an electric vector  $\mathbf{E}$ , with a molecular system is in first approximation the interaction with the (variable) electric dipole moment  $\mathbf{M}$ .

If the interaction energy  $\mathbf{M}\cdot\mathbf{E}$  is introduced into the wave equation it is found that the probability of a transition between two states  $n$  and  $m$  produced by the interaction is proportional to the square of the magnitude of certain vector quantities  $\mathbf{R}^{nm}$  -the matrix elements of the dipole moment- whose components depend in the following manner on the eigenfunctions  $\Psi_n$  and  $\Psi_m$  of the two states:

$$\mathbf{R}_x^{nm} = \int \Psi_n^* \mathbf{M}_x \Psi_m d\tau$$
$$\begin{matrix} y \\ z \end{matrix}$$
$$\begin{matrix} y \\ z \end{matrix}$$

If the matrix element  $\mathbf{R}^{nm}$  differs from zero for two states  $n$  and  $m$ , the two states combine with each other with a certain probability with emission or absorption of radiation; if it is zero the transition under consideration is forbidden as a dipole transition. A non-zero transition probability may also be produced by the interaction of

an electromagnetic wave with the magnetic dipole moment, the quadrupole moment, or higher moments of the molecular system.

For reasons of symmetry the H<sub>2</sub> molecule has no permanent electric dipole, in other words the diagonal elements of the  $\mathbf{R}^{nm}$  matrix are all zero. As a result, (dipole) transitions between rovibrational levels of a single electronic state are forbidden. We therefore only consider transitions involving two different electronic states ( $m \neq n$ ).

### VIII.1.4 General selection rules

For any atomic system the selection rule for the quantum number  $J$  of the total angular momentum is

$$\Delta J = J' - J'' = 0, \pm 1, \text{ with the restriction } J = 0 \nrightarrow J = 0$$

where  $J'$  refers to the upper state and  $J''$  refers to the final state.

This rule holds rigorously for electric dipole radiation. Thus, from this selection rule one expects three or two branches. These are known as the P, Q and R branches. They are related to the value of  $J$  jump :

$$\text{P branch, } \Delta J = J' - J'' = -1$$

$$\text{Q branch, } \Delta J = 0$$

$$\text{R branch, } \Delta J = +1$$

Positive terms combine only with negative, and vice versa, or symbolically

$$+ \leftrightarrow -, \quad + \langle \uparrow \rangle +, \quad - \langle \uparrow \rangle -$$

It should be noted that, in the case of a  $\Sigma$  state, the sign (+ or -) refers to the complete eigenfunction of the molecule and not only to the electronic eigenfunction (right superscript of the spectroscopic term).

H<sub>2</sub> having identical nuclei symmetric terms combine only with symmetric and

antisymmetric only with antisymmetric, or

$$\mathbf{s} \leftrightarrow \mathbf{s}, \mathbf{a} \leftrightarrow \mathbf{a}, \mathbf{s} \leftrightarrow \mathbf{a}$$

Finally, in the case of a molecule with nuclei of equal charge (again H<sub>2</sub>) even electronic states combine only with odd; that is,

$$\mathbf{g} \leftrightarrow \mathbf{u}, \mathbf{g} \leftrightarrow \mathbf{g}, \mathbf{u} \leftrightarrow \mathbf{u}.$$

### VIII.1.5 Influence of the nuclear spin

The nuclear spin vector has a strong influence on the population of the symmetric and antisymmetric levels. The spin vectors  $\mathbf{I}$  of the two nuclei of a diatomic molecule form a resultant  $\mathbf{T}$ , *the total nuclear spin of the molecule*. According to the rules of addition of the angular momentum vectors, for two identical nuclei the quantum number of the total nuclear spin is given by

$$T = 2I, 2I-1, \dots, 0$$

In the case of H<sub>2</sub>,  $I=1/2$  and the possible values of  $T$  are  $T=1$  (parallel nuclear spins,  $\uparrow\uparrow$ ) and  $T=0$  (antiparallel spins,  $\uparrow\downarrow$ ). The first value is associated with the antisymmetric levels and the second with the symmetric levels. It is shown that the statistical weights are 3 and 1, respectively (Fermi statistics). In the case of H<sub>2</sub>, the antisymmetric rotational levels occur three times as frequently as the symmetric; that is, the total statistical weights are  $3 \times (2J + 1)$  and  $1 \times (J + 1)$ , respectively. Since the configuration having the greater statistical weight is usually called the *ortho modification*, an ortho-H<sub>2</sub> corresponds to parallel nuclear spins and a para-H<sub>2</sub> corresponds to antiparallel nuclear spins.

## VIII.1.6 Emission intensity

The intensity of an electronic transition from an upper state  $n$  to a lower state  $m$  is determined by the transition probability  $A_{nm}$  in emission. The transition probability  $A_{nm}$  is determined by the matrix element  $\mathbf{R}^{nm}$  of the dipole moment according to

$$A_{nm} = \frac{64\pi^4 \nu_{nm}^3}{3h} |\mathbf{R}^{nm}|^2 .$$

Frequently the experimental data are expressed in terms of the **oscillator strength**  $f_{nm}$  which is related to  $|\mathbf{R}^{nm}|^2$  by

$$f_{nm} = \frac{8\pi^2 \mu c \nu_{nm}}{3h \epsilon^2} |\mathbf{R}^{nm}|^2$$

where  $\mu$  and  $\epsilon$  are mass and charge of the electron and it finally comes

$$f_{nm} = \frac{A_{nm} \mu c}{8\pi^2 \nu_{nm}^2 \epsilon^2} .$$

For electronic transitions

$$\mathbf{R}_e^{nm} = \int \Psi_n^* \mathbf{M}_e \Psi_m d\tau_e$$

where  $m$  and  $n$  are electronic eigenfunctions,  $\mathbf{M}_e$  is the part of the dipole moment depending on the electrons and  $d\tau_e$  is the volume element of the configuration space of the electrons. For non-degenerate electronic states the transition probability  $A_{nm}$  is simply proportional to  $|\mathbf{R}_e^{nm}|^2$ , for degenerate electronic states to

$$\left(\frac{1}{d_n}\right) \sum |\mathbf{R}^{n_i, m_k}|^2$$

where  $d_n$  is the degree of degeneracy of the upper state and where the summation is over all combinations of the sublevels  $n_i$  and  $m_k$ .

The total matrix element for a given rotational and vibrational transition system may be written

$$\mathbf{R} = \mathbf{R}_e^{nm} \mathbf{R}_{\text{vib}}^{v'v''} \mathbf{R}_{\text{rot}}^{J'J''}$$

The transition probability  $A_{nm,v'v'',J'J''}$  is given by

$$A_{nm,v'v'',J'J''} = \frac{64 \pi^4 \nu^3}{3h} |\mathbf{R}_e^{nm}|^2 |\mathbf{R}_{\text{vib}}^{v'v''}|^2 \frac{\sum_{M'M''} |\mathbf{R}_{\text{rot}}^{J'J''}|^2}{2J'' + 1}$$

where summation is over all values of the magnetic quantum numbers  $M', M''$  ( $M = J, J-1, \dots, -J$ ), and where it is assumed that the wave numbers  $\nu$  of the transitions occurring in the summation do not differ too much. For degenerate electronic states with degeneracies  $d_n$  and  $d_m$ , the quantity  $|\mathbf{R}_e^{nm}|^2$  has to be replaced by

$$\left(\frac{1}{d_n}\right) \sum |\mathbf{R}_e^{n_i m_k}|^2$$

where  $i$  and  $k$  number the degenerate sublevels of the upper state level, and the lower state  $m$ ; and where the summation is over all possible combinations of the sublevels of the upper with those of the lower state.

### VIII.1.6.1 Population of the ground level

It is assumed that the molecules in the ground state are in thermal equilibrium. Therefore, we need only consider the distribution of the molecules over the different quantum states in thermal equilibrium.

### VIII.1.6.2 vibrational levels

The relative number of molecules in each of the vibrational levels referred to the number of molecules in the lowest vibrational level is determined by the Boltzmann

factor

$$\exp\left(\frac{-E}{kT}\right) = \exp\left(\frac{-G_0(v)hc}{kT}\right)$$

where  $G_0$  is the energy of the anharmonic oscillator referred to the zero-point energy.

If we wish to refer to the total number of molecules  $N$  we have to consider that  $N$  is proportional to the sum of the Boltzmann factors over all states, that is the so called *partition function*

$$Q_v = 1 + \exp\left(\frac{-G_0(1)hc}{kT}\right) + \exp\left(\frac{-G_0(2)hc}{kT}\right) + \dots$$

Therefore the number of molecules in the vibrational state  $v$  is given by

$$N_v = \frac{N}{Q_v} \exp\left(\frac{-G_0(v)hc}{kT}\right)$$

### VIII.1.6.3 Rotational levels

The population of the rotational levels follows a thermal distribution which is not simply given by the Boltzmann factor  $\exp(-E/kT)$ ; the degeneracy of the rotational level  $(2J+1)$  must be taken into account. The number of molecules  $N_J$  in the rotational level  $J$  of the lowest vibrational state at temperature  $T$  is thus proportional to

$$(2J+1) \exp\left(\frac{-E(J)}{kT}\right)$$

Assuming that the transition probability is the same for all lines of a band, the actual number of molecules in the rotational states may be obtained by multiplying by  $N$  and dividing by the rotational state sum (the rotational partition function  $Q_r$ )

$$N_J = \frac{(3)^J}{4} \frac{N}{Q_r} (2J+1) \exp\left(\frac{-BJ(J+1)hc}{kT}\right)$$

where  $B$  is the rotational constant (prevailing for a particular vibrational level) and  $N$  is the total number of molecules. The factor  $(3)^j/4$  accounts for the degeneracy due to the nuclear spin which, in the case of  $H_2$ , is 3 ( $j=1$ ) for antisymmetric rotational levels and 1 ( $j=0$ ) for symmetric levels. Dividing by 4 preserves the normalization of the total partition function ( $4*Q_r$ ).

### VIII.1.7 Transition wave number

The wave number of a transition is given by

$$\nu_m = \nu_0 + (B' - B'')m + (B' - B'' - D' - D'')m^2 - 2(D' + D'')m^3 - (D' - D'')m^4 \dots$$

where the initial state is, as usual, denoted by a single prime (') and the final state by a double prime (''),  $\nu_0$  is the wave number of the pure vibrational transition without taking account of rotation,  $B$  is the rotational constant of the vibrational state and  $D$  brings a correction due to centrifugal force for that vibrational state, and  $m$  equals  $J'$  (the rotational level of the excited state).

For the  $H_2$  molecule, experimental values for these constants are tabulated in Dabrowski (1984)

## VIII.2 Application to the Lyman and Werner band spectra of H<sub>2</sub>

### VIII.2.1 The B<sup>1</sup>Σ<sub>u</sub><sup>+</sup> state

In this section we study the **H<sub>2</sub> Lyman band** spectrum arising from the radiative deexcitation of the B<sup>1</sup>Σ<sub>u</sub><sup>+</sup> electronic state into the X<sup>1</sup>Σ<sub>g</sub><sup>+</sup> ground state.

In the following sections, we will follow the generally admitted convention for the vibrational and rotational quantum numbers :

v, J refer to the **initial** state,  
v', J' refer to the **excited** state,  
v'', J'' refer to the **final** state.

The volume emission rate  $\eta$  from an upper level (v', J') of the excited H<sub>2</sub> B<sup>1</sup>Σ<sub>u</sub><sup>+</sup> state (hereafter often designated by the letter B) to a lower rovibrational level (v'', J'') of the X<sup>1</sup>Σ<sub>g</sub><sup>+</sup> ground state (hereafter often designated by the letter X) is given by :

$$\eta^{B \rightarrow X}(v', J', v'', J'') = n_{v', J'}^B A_{v', J', v'', J''}$$

where  $n_{v', J'}^B$  is the population of the upper state. This latter population can be estimated from the equilibrium between excitation to and deexcitation from the upper level. It takes the form

$$g^{X \rightarrow B}(v=0, J \rightarrow v', J') = n_{v', J'}^B \sum_{v'', J''} A_{v', J', v'', J''}$$

where  $g^{X \rightarrow B}(v=0, J \rightarrow v', J')$  represents the excitation rate from the ground state X(v=0, J) to the rovibrational level (v', J') of the B state. It is estimated by assuming that

the direct population rate of the B state is governed by direct electron (primary or secondary) impact on ground state H<sub>2</sub> molecules and it is assumed that the same rules apply as for radiative transitions:

$$g^{X \rightarrow B}(v=0, J \rightarrow v', J') = \sum_J N(X, v=0, J) \int \Phi(E) \sigma^{X \rightarrow B}(v, J, v', J', E) dE$$

where  $N(X, 0, J)$  denotes the number density of H<sub>2</sub> molecules in the  $X(v=0, J)$  rovibrational level,  $\Phi(E)$  is the total energetic electron flux at energy  $E$  and  $\sigma^{X \rightarrow B}(v, J, v', J', E)$  is the electron impact excitation cross section from  $X(v, J)$  into the  $B(v', J')$  level. The sum extends over 2 terms corresponding to the P ( $\Delta J = -1$ ) and R ( $\Delta J = +1$ ) branches of the excitation transitions.

According to Shemansky *et al.* (1985), the electron impact cross section may be given by

$$\sigma(v, J, v', J', E) = \frac{\Omega(X)}{E} \quad \text{with} \quad X = \frac{E}{E(v, J, v', J')} \quad \text{and}$$

$$\Omega(X) = ff(X) + C_7 \ln X$$

where  $ff(X)$  is a function (see Shemansky *et al.* [1985] for the detailed relation and coefficients) of  $X$  and  $C_7$  is related to the oscillator strength

$$C_7 = 4 \cdot \frac{f(v, J, v', J')}{E(v, J, v', J')} \quad \text{that is} \quad C_7 = 4 \cdot \frac{A_{nm} \mu c}{8 \pi^2 v_{nm}^2 \epsilon^2} / E(v, J, v', J')$$

Using the equilibrium relation to express the population of the  $B(v', J')$  excited state one can derive a general form for the volume emission rate of the  $B(v', J') \rightarrow X(v'', J'')$  line

$$\eta^{B \rightarrow X}(v', J', v'', J'') = g^{X \rightarrow B}(v=0, J \rightarrow v', J') \frac{A_{v', J', v'', J''}}{\sum_{v'', J''} A_{v', J', v'', J''}}$$

As will be explained in a next section, the transitions from B(v',J') to the continuum of the ground state (B → cont) may be taken into account and the previous relation becomes

$$\eta^{B \rightarrow X}(v', J', v'', J'') = g^{X \rightarrow B}(v=0, J \rightarrow v', J') \frac{A_{v', J', v'', J''}}{\sum_{v'', J''} [A_{v', J', v'', J''} + A_{v', J', c'', J''}^{B \rightarrow \text{cont}}]}$$

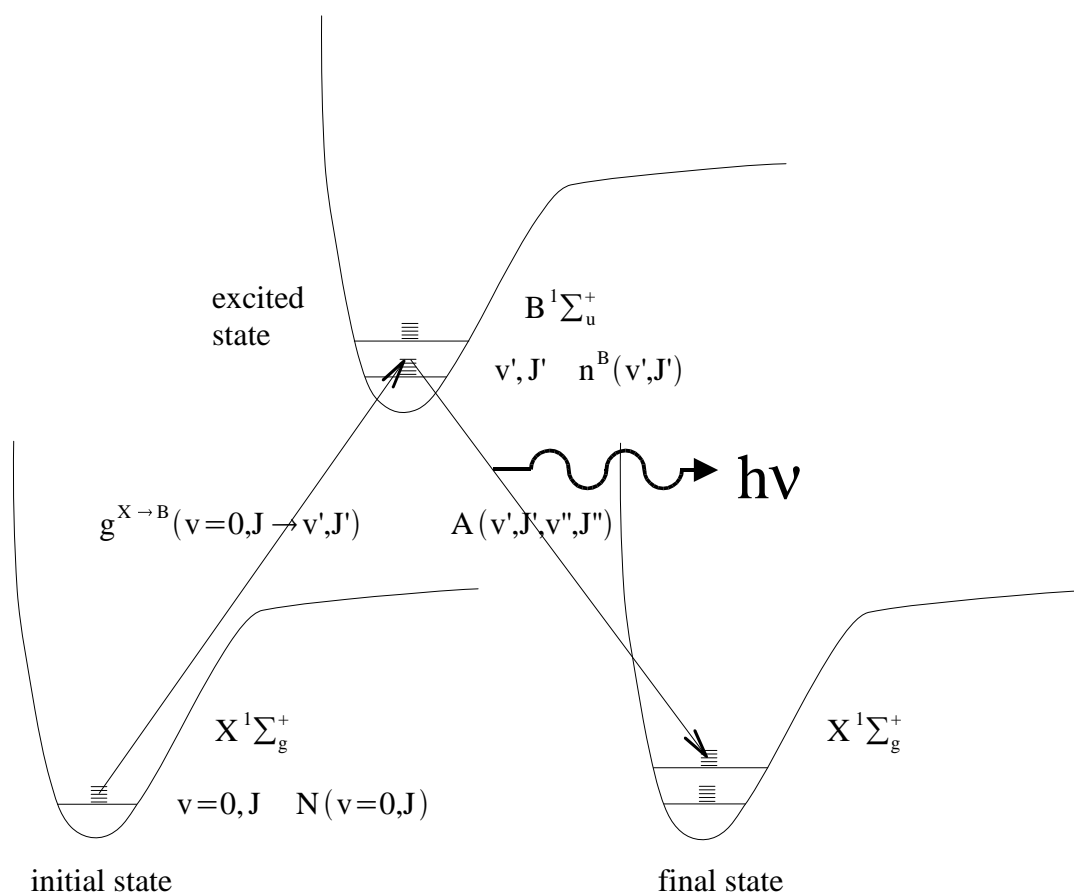


**Figure 55** : Schematic representation of the excitation process from the ground state to the excited B state followed by the radiative deexcitation to the ground state (the potential curves are not to scale).

The electron impact excitation cross sections into individual rovibrational levels of the B state is obtained from the line transition probabilities by Abgrall *et al.* (1993a,b) in

conjunction with the energy dependence formulation by Shemansky *et al.* (1985) upgraded by Liu *et al.* (1998).

In addition to the direct collisional excitation, the population of the  $B^1\Sigma_u^+$  state is enhanced by the cascade process ( $E,F^1\Sigma_g^+ \rightarrow B^1\Sigma_u^+$ ) following direct excitation of the  $E,F^1\Sigma_g^+$  state (hereafter often designated by E,F). It can be written :

$$g(B,v',J') = g_d(B,v',J') + g_c(B,v',J')$$

where the first term corresponds to the direct impact excitation and has the same form as  $g^{X \rightarrow B}(v=0, J \rightarrow v', J')$  ; the second term is a two-step process where electron impact populates the (E,F) state which selectively cascades into the B state. This latter process is explained in the following section.

### VIII.2.1.1 E,F Cascade

The potential-energy curve for the  $E,F^1\Sigma_g^+$  is known (*Davidson*, 1960) to have a double minimum resulting from avoided crossing of the potential-energy curves for the  $1\sigma_g 2s^1\Sigma_g^+$  and  $(1\sigma_u)^2^1\Sigma_g^+$  configurations. The two minima are sometimes referred to as the  $E^1\Sigma_g^+$  and  $F^1\Sigma_g^+$  states, respectively. Both minima are located in roughly the same energy region, but since the equilibrium internuclear distances are considerably different and since the Franck-Condon principle assumes vertical transitions, we only consider the  $E^1\Sigma_g^+$  minimum which has the closest equilibrium internuclear distance to that of the X ground state.

As already mentioned, the B rovibrational levels may be populated by two different processes :

1. electron impact excitation as previously described
2. cascade from the  $E,F^1\Sigma_g^+$  excited state to the rovibrational levels of the B state.

The estimation of the contribution from this second process assumes that excitation from the X ground state to the E,F state is controlled by electron impact. In order to calculate this contribution numerical values for the transition probabilities would be required

$$A_{(v=0,J) \rightarrow (v^{iEF}, J^{iEF})}^{X \rightarrow E,F} \quad \text{and} \quad A_{(v^{iEF}, J^{iEF}) \rightarrow (v^{nB}, J^{nB})}^{E,F \rightarrow B}$$

however these have never been measured.

To date, the only available information are the vibrational transition probabilities

$$A_{v=0 \rightarrow v^{iEF}}^{X \rightarrow E,F}$$

and the Franck-Condon factors calculated by *Lin* (1974)

$$q_{B,EF} = |\langle \Psi_{v_B}^B | \Psi_{v_{EF}}^{EF} \rangle|^2,$$

giving an estimation of the transition probability between the two vibrational states.

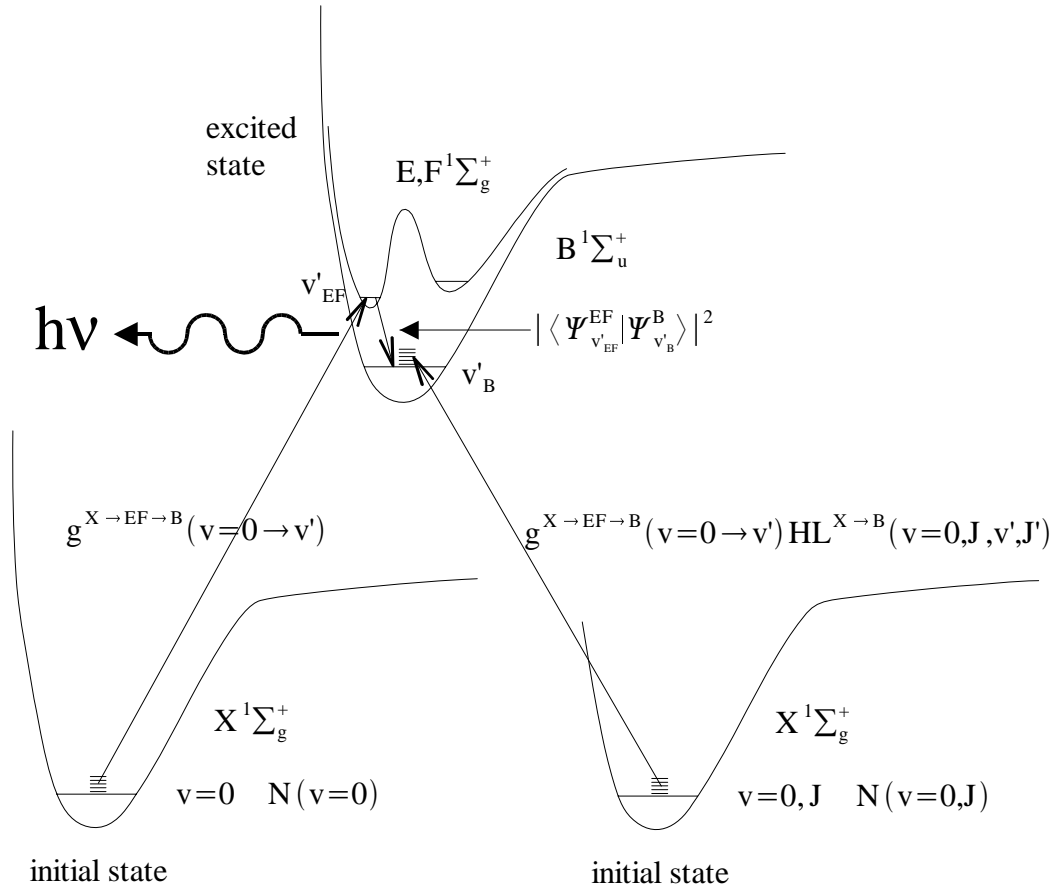


**Figure 56** : Schematic representation of the excitation process from the ground state to the E,F state. The excitation is followed by cascade to the B state then by radiative deexcitation to the ground level. The potential curves are not to scale.

A two-step procedure is therefore used :

1. The transitions sequence  $X \rightarrow EF \rightarrow B$  is treated for the vibrational levels.

This first step implies the estimation of a pseudo-excitation rate

$g^{X \rightarrow E,F \rightarrow B}(v=0 \rightarrow v'_B)$  from the ground system X to the vibrational levels ( $v'$ ) of the B state through the E,F state by direct electron (primary or secondary) impact on ground state  $H_2$  molecules :

$$g^{X \rightarrow E,F \rightarrow B}(v=0 \rightarrow v'_B) = \sum_{v'_{EF}} N(X, v=0) \Phi(E) |\langle \Psi_{v'_B}^B | \Psi_{v'_{EF}}^{EF} \rangle|^2 \sigma^{X \rightarrow E,F}(v=0, v'_{EF}, E)$$

where  $N(X,0)$  denotes the number density of  $H_2$  molecules in the  $X(0)$  vibrational level,  $\Phi(E)$  is the total energetic electron flux at energy E and  $\sigma^{X \rightarrow E,F}(v=0, v'_{EF}, E)$  is the electron

impact excitation cross section from  $X(v=0)$  into the  $E,F(v')$  level.

2. Partitioning of the rotational levels is approximated by using Hönl-London factors. Due to the lack of transition probabilities for individual rovibrational transitions the population of the rotational levels of  $E,F$  state is unknown. Accordingly, the following crude approximation is made. It is assumed that the redistribution over the rotational levels of  $B$  due to cascade from  $E,F$  is similar to that obtained from direct excitation from  $X$  to  $B$ . Therefore the  $E,F$  state is short-circuited and the Hönl-London factors corresponding to the  $X \rightarrow B$  transition are directly applied to the  $X \rightarrow E,F \rightarrow B$  transitions series. The pseudo-excitation rate then becomes

$$g^{X \rightarrow E,F \rightarrow B}(v=0, J \rightarrow v'_B, J'_B) = g^{X \rightarrow E,F \rightarrow B}(v=0 \rightarrow v'_B) HL^{X \rightarrow B}$$

It should be emphasized that the Hönl-London factors were derived under the assumption of negligible interaction of rotation and electronic motion. Such an assumption is reasonable for the  $X$  and  $B$  states of  $H_2$ , but not for the  $E,F$  state. Therefore it would be incorrect to apply the Hönl-London factors of the  $X$  to  $E,F$  and  $E,F$  to  $B$  transitions.

## VIII.2.2 The $C^1\Pi_u$ state

In this section we study the **H<sub>2</sub> Werner band** spectrum arising from the radiative deexcitation of the  $C^1\Pi_u$  state into the  $X^1\Sigma_g^+$  ground state. There are two main differences with the Lyman band system :

1. it can be assumed that electron impact is the sole excitation process from X to C (i.e., no cascade)
2. the  $C^1\Pi_u$  state is characterized by  $\Lambda = 1$  and is therefore doubly degenerate.

For this state, the rotation of the nuclei is large enough to produce  $\Lambda$ -doubling, that is a splitting into two components for each J value corresponding to  $M_L = \pm 1$ . It can be shown that for each J value one component of the rotational level is positive and the other is negative, and that it is alternately the upper and lower that is positive, as illustrated in figure 55. The rules for symmetry with respect to an exchange of the nuclei are the same as for the  $\Sigma$  states, that is in even electronic states the positive levels are symmetric and the negative are antisymmetric, and conversely in odd electronic states (as the  $\Pi$  state).

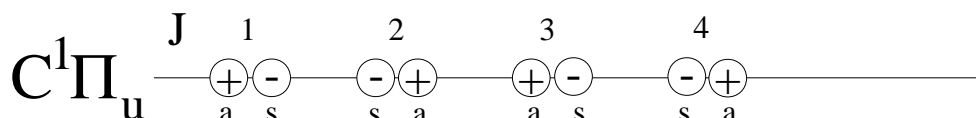


**Figure 57** :  $\Lambda$ -doubling of the C state

It is convenient to separately consider the sub-levels according to their resultant symmetry properties. In the case of the  $C^1\Pi_u$  state the succession of rotational level characteristics ( $[1,-,s]$  ;  $[2,+,a]$  ;  $[3,-,s]$  ;  $[4,+,a]$  ; ... ) is similar to the succession found in a  $\Sigma^+$  state. Accordingly, the corresponding levels are treated as if they belonged to a non degenerate (pseudo) state, called **C<sup>+</sup> state**. The other levels ( $[1,+,a]$  ;  $[2,-,s]$  ; ...) are treated as if they were belonging to a non degenerate  $\Sigma^-$  state, called **C<sup>-</sup> state**. The rotational selection rules are applied accordingly.

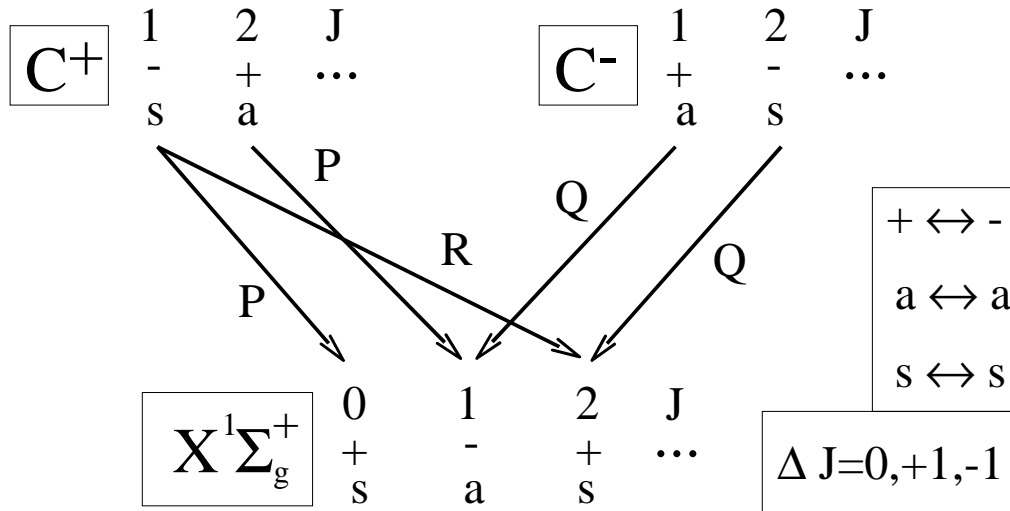


**Figure 58** : Allowed transitions (P, Q and R branches) from the pseudo non degenerate states,  $C^+$  and  $C^-$ , to the ground state. Selection rules are summarized in the right side of the figure

From figure 58, it can be seen that the selection rules applying to transitions between  $C^+$  and X and  $C^-$  and X are such that only P and R branches take place for  $C^+$  to X and only Q branch for  $C^-$  to X.

The volume emission rate  $\eta$  of an upper level ( $v', J'$ ) of the excited  $H_2$  state  $C^1\Pi_u$  to a lower rovibrational level ( $v'', J''$ ) of the  $X^1\Sigma_g^+$  ground state is calculated in the same way as for the Lyman band emission (without the cascade from the E,F state). It is given by

$$\eta^{C^+ \rightarrow X}(v', J', v'', J'') = g^{X \rightarrow C^+}(v=0, J \rightarrow v', J') \frac{A_{v', J', v'', J''}^{C^+}}{\sum_{v'', J''} \left[ A_{v', J', v'', J''}^{C^+} + A_{v', J'}^{C^+ \rightarrow \text{cont}} \right]}$$

$$\eta^{C^- \rightarrow X}(v', J', v'', J'') = g^{X \rightarrow C^-}(v=0, J \rightarrow v', J') \frac{A_{v', J', v'', J''}^{C^-}}{\sum_{v'', J''} \left[ A_{v', J', v'', J''}^{C^-} + A_{v', J'}^{C^- \rightarrow \text{cont}} \right]}$$

where the  $A^{C^+}$  and  $A^{C^-}$  line transition probabilities are given by Abgrall *et al.* (1993 a,b). The electron impact excitation cross sections into individual rovibrational levels of the C state is obtained from the same line transition probabilities in conjunction with the energy dependence formulation by Shemansky *et al.* (1985).

### VIII.2.3 Continuum emission

The continuum emission is the result of a spontaneous radiative dissociation in which the discrete vibrational level of the excited electronic state decays to the vibrational continuum of the ground electronic state with the emission of a photon. We consider in particular the  $B^1\Sigma_u^+$  and  $C^1\Pi_u$  initial states of  $H_2$ . The dissociation products  $H+H$  belong, as a pair, to the vibrational continuum of the ground state  $X^1\Sigma_g^+$ .

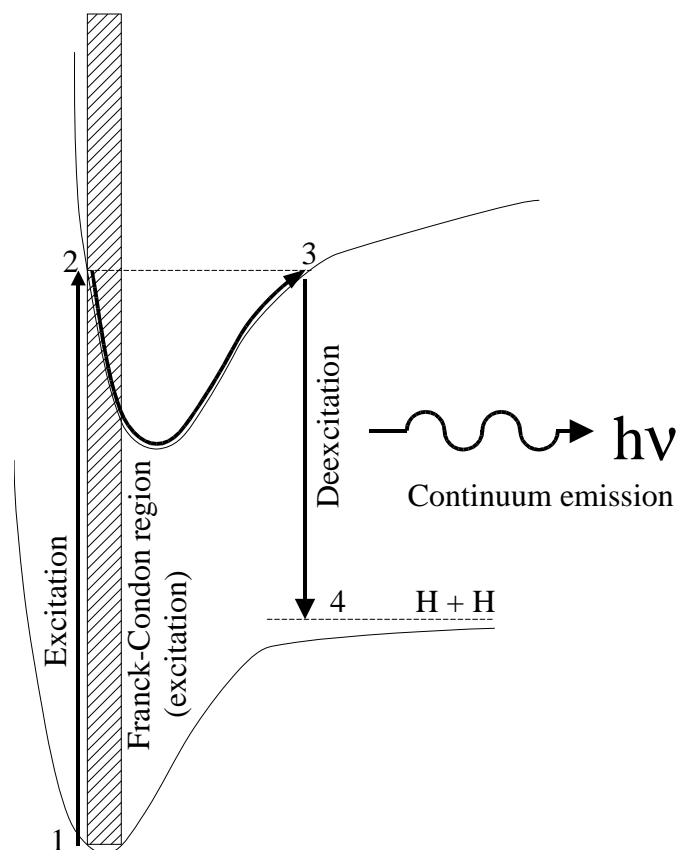


**Figure 59** : Schematic representation of the continuum emission. An  $H_2$  molecule in the ground state (1) is excited to an upper electronic state (2) according to the Franck-Condon principle. If deexcitation occurs when the internuclear distance is maximum (3) a "vertical" transition will give rise to dissociation (4) and emission of a continuum photon. (The deexcitation Franck-Condon region is not represented for clarity).

The principle of continuum emission is illustrated in figure 59. According to the Franck-Condon principle (which states that the internuclear transition does not vary significantly during the transition), a transition from the first vibrational level ( $v=0$ ) of the ground state (position 1 in figure 59) to the B or C electronic state can take place to a point on the upper potential curve which crosses the left side of the Franck-Condon

region (position 2 in figure 59). The transition has therefore a non-negligible probability to excite a high lying vibrational level of the upper state. The Franck-Condon principle also applies to the deexcitation. If the transition occurs when the internuclear distance is maximum (right side of the potential curve depicted by position 3 in figure 59) then the final position on the ground state potential curve has the same internuclear distance (position 4 in figure 59) and may belong to the vibrational continuum. In this case, the emitted photon contributes to the continuum emission.

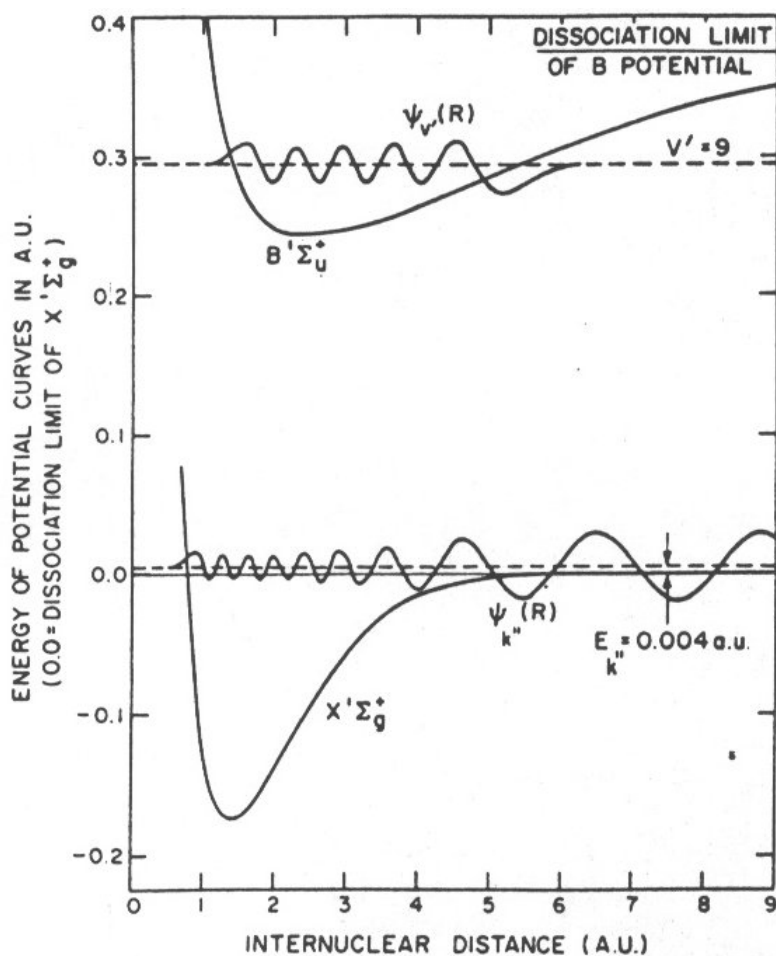


**Figure 60** : Potential energy curves and vibrational wavefunctions of the  $B^1\Sigma_u^+$  and  $X^1\Sigma_g^+$  states of  $H_2$ .

Figure 60 is reproduced from Stephens and Dalgarno (1972). It illustrates the potential energy curves for the B and X states and the  $H_2$  vibrational wave functions  $\Psi_v$  for  $v'=9$  and  $\Psi_{v''}$  for  $E_{k''} = 0.04$  a.u. (i.e. the total kinetic energy of the two fragments). There is a large constructive interference between the two wave-functions in the range  $2.5 \text{ a.u.} \leq R \leq 5.0 \text{ a.u.}$ , which leads to a large transition rate for this particular value of

$E_k$ . According to these authors, the fraction of deexcitation ending in the continuum of the ground state becomes important (>10%) for  $v'=7$  for the B state and for  $v'=10$  for the C state. Radiative deexcitation from lower vibrational levels will mostly result in non-dissociative emissions.

According to Abgrall *et al.* (1997), the differential photon continuum emission rate  $I_\nu$  from electron impact excitation may be given by

$$I_\nu(v', J', c'', J'') = \frac{\sum_{v, J} g(v, J, v', J')}{\sum_{v'', J''} [A(v', J', v'', J'') + A(v', J', J'')] } A_\nu(v', J', c'', J'') d\nu ,$$

where  $A_\nu(v', J', c'', J'')$  is the differential transition probability and  $c''$  refers to transitions to the vibrational continuum of the  $X^1\Sigma_g^+$  ground state. The rate quantity  $\sum_{v, J} g(v, J, v', J')$  represents the sum of the excitation rate from the fine structure levels of the ground state  $X(v, J)$ .

This general relation applies to the  $B \rightarrow X$  (including cascade from E, F),  $C^+ \rightarrow X$  and  $C^- \rightarrow X$  transitions.

## VIII.2.4 Self absorption

The emission lines of  $H_2$  terminating on the ground vibrational level of the ground electronic ( $v''=0$ ) state are optically thick for the  $H_2$  vertical column corresponding to the depth of the bulk of the auroral emission (Wolven *et al.*, 1998). The resonant photons are reabsorbed and converted predominantly into fluorescence photons in transitions terminating at the excited vibrational levels of the ground electronic state. For simplicity, it is assumed that these resonant photons are totally lost and therefore the corresponding lines are absent from the spectra.

## VIII.3 Coupling of the two-stream model with the spectral generator

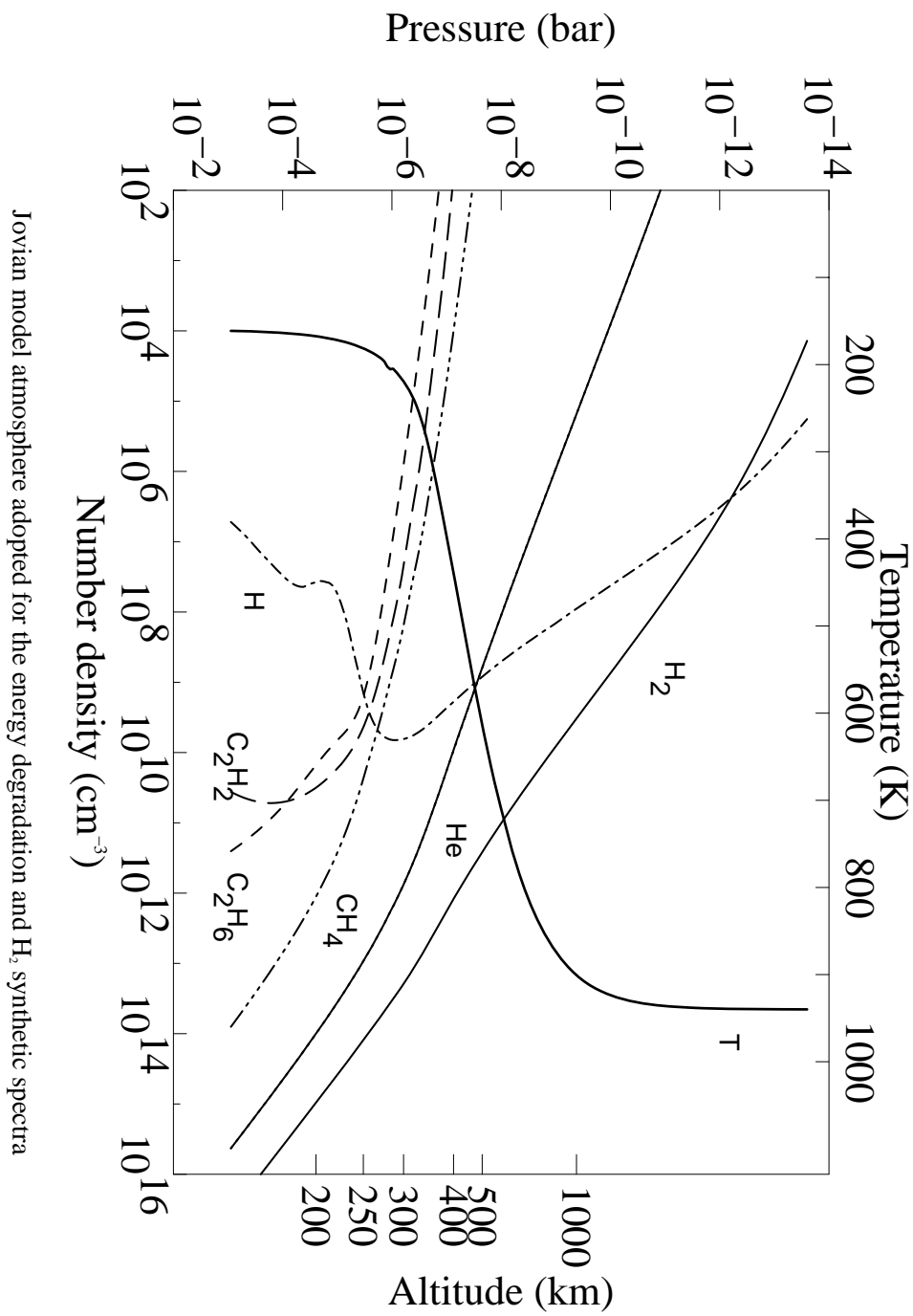
### VIII.3.1 Introduction

In this section we report preliminary results obtained with a model coupling the electron energy degradation code with the detailed synthetic spectral model of the H<sub>2</sub> Lyman and Werner band system previously described. It is used to calculate the emerging auroral ultraviolet spectra from Jupiter's atmosphere excited by electrons with different initial energy distributions. The atmospheric model is adapted from the low latitude vertical P-T profile measured by the *Galileo* probe and mid-latitude hydrocarbon photochemistry. In contrast to earlier studies, the vertical dependence of the auroral emission, H<sub>2</sub> temperature and chemical composition are explicitly considered. Each layer, with its gas temperature, contributes to the emergent spectrum and the absorbers are vertically distributed within the source region. Examples of the calculated spectra are shown to validate the synthetic spectrum and to illustrate the importance of the electron energy distribution and the vertical dimension. The spectral model with a fixed thermal structure has been applied to the analysis of seven GHRS (HST) spectra of the 1200-1700 Å region obtained with a 5 Å resolution at various locations in the north and south Jovian aurora. These results are reported in a paper in press (Dols *et al.*, 2000) and will not be repeated here. Instead, we discuss additional electron energy distribution cases for which synthetic spectra are compared with two echelle spectra that were not satisfactorily fitted in the work of Dols *et al.*

Previous studies of the sensitivity of the electron excited H<sub>2</sub> ultraviolet spectrum to temperature, with the exception of those by Liu and Dalgarno (1996) and Kim and Fox (1997), assumed a monoenergetic electron beam, generally 100 eV, meant to represent the mean energy of the exciting secondary electrons. The effect of the energy of the (primary + secondary) electrons on the line brightness distribution was shown to be small between 100 keV and 1 keV by Liu and Dalgarno (1996). They concluded that the auroral UV spectrum is not a sensitive indicator of the primary electron energy

distribution (we will see that this conclusion only applies for laboratory measurements where the excited gas is confined in a small cell which is not representative of the Jovian atmosphere characterized by complex thermal and chemical vertical structures). Below about 50 eV, the intensity of the Werner band decreases relative to the Lyman band and continuum because the excitation cross section of the  $C^1\Pi_u$  state peaks at higher energies than the  $B^1\Sigma_u^+$  state. Similarly, cascading effects ( $E,F^1\Sigma_g^+ \rightarrow B^1\Sigma_u^+$ ) are enhanced at low energies, near the threshold of the transition. These cascades preferentially populate the low vibrational levels  $v = 0$  to 4 of the  $B^1\Sigma_u^+$  state and originate mostly from excitation of low rotational  $J$  levels of the ground state. Consequently, cascade effects are most conspicuous for excitation of low temperature  $H_2$  by low energy electrons.

A common feature of all previous studies of the  $H_2$  auroral spectrum is that a thin slab approach was adopted. In this schematic view, the aurora is represented by a homogeneous emission layer characterized by a  $H_2$  rovibrational temperature to be determined by the fit to the observed spectrum. A hydrocarbon layer, usually limited to methane, overlies the emission layer and its column density is adjusted to match the color ratio in the observed spectrum. In this work, the vertical dimension, including the temperature, composition and emission rate vertical gradients are explicitly considered. A primary electron beam with a prescribed energy distribution interacts with the high latitude Jovian thermosphere described by a model atmosphere. Each layer, characterized by its own temperature, contributes to the emergent spectrum and the absorbers are vertically distributed within the source region.



Jovian model atmosphere adopted for the energy degradation and  $\text{H}_2$  synthetic spectra

Figure 61

### VIII.3.2 Vertical distribution

As mentioned before, the main new feature of this spectral model is the consideration of the vertical distribution of the atmosphere producing the auroral

emission and absorption. The local electron flux energy distribution ( $\Phi_E$ ) which appears in the excitation rate formula (for example in the first equation of page 228) is calculated with the energy degradation model.

In a first stage we have tested the effect of varying the electron flux energy distribution only. This means that the temperature profile and the atmospheric structure are set to prescribed (unconverged) values. For this purpose, we adopted a neutral model atmosphere based on the NEB model of Gladstone *et al.* (1996) where the densities of H, H<sub>2</sub>, He and CH<sub>4</sub> have been scaled to a double-sided Bates fit to the pressure-temperature profile determined by Seiff *et al.* (1997) from the *Galileo* probe data. The reference altitude corresponds to a pressure of 1 bar and the P-T profile has been adjusted to the larger gravity at 60° N. The hydrocarbon mixing ratios at a given pressure are initially based on the modified NEB profile but their mixing ratios are adjusted with a scaling factor, as described in section 4 of Dols *et al.* (1999). Figure 61 shows the temperature and density profiles adopted. The altitude of the methane homopause in this model is 318 km ( $3.6 \times 10^{-7}$  bar).

A Maxwellian initial energy spectrum is assumed for the auroral electrons at the top of the atmosphere with the characteristic energy left as a free parameter. Recent visible-wavelength images obtained by the *Galileo* solid state imaging (SSI) system indicate that the peak of the visible night side emission is consistently located  $245 \pm 30$  km above the 1-bar level (Vasavada *et al.* 1999). We use this observation as a constraint on the characteristic energy of the incident electron energy spectrum. The atmosphere is vertically divided into 20 layers with equal log-pressure spacing. The energy degradation model divides the same atmosphere into 200 layers but tests have shown that spectra calculated with 20 layers do not significantly differ from the spectra calculated with 200 layers. The detailed H<sub>2</sub> spectrum is generated in each layer based on the local electron flux energy distribution, H<sub>2</sub> density and temperature.

The emerging spectrum for an Earth observer is obtained in physical units for any location and view angle by integrating the volume emission rate of each line or continuum interval along the line of sight, after attenuation by the hydrocarbon absorbers:

$$4\pi I_v = 10^{-6} \int_0^{\infty} \eta_v(z) \exp(-\tau_v) dl$$

where  $4\pi I_v$  is the line brightness expressed in Rayleighs,  $\eta_v$  the local volume emission rate,  $\tau_v$  the total optical thickness of hydrocarbons at the line or continuum wavelength between the emitting volume and the top of the atmosphere, and  $dl$  is the path length along the line of sight. The  $\text{CH}_4$  absorption cross section by Mount *et al.* (1977, 1978) and the  $\text{C}_2\text{H}_2$  values by Smith *et al.* (1991) are adopted.

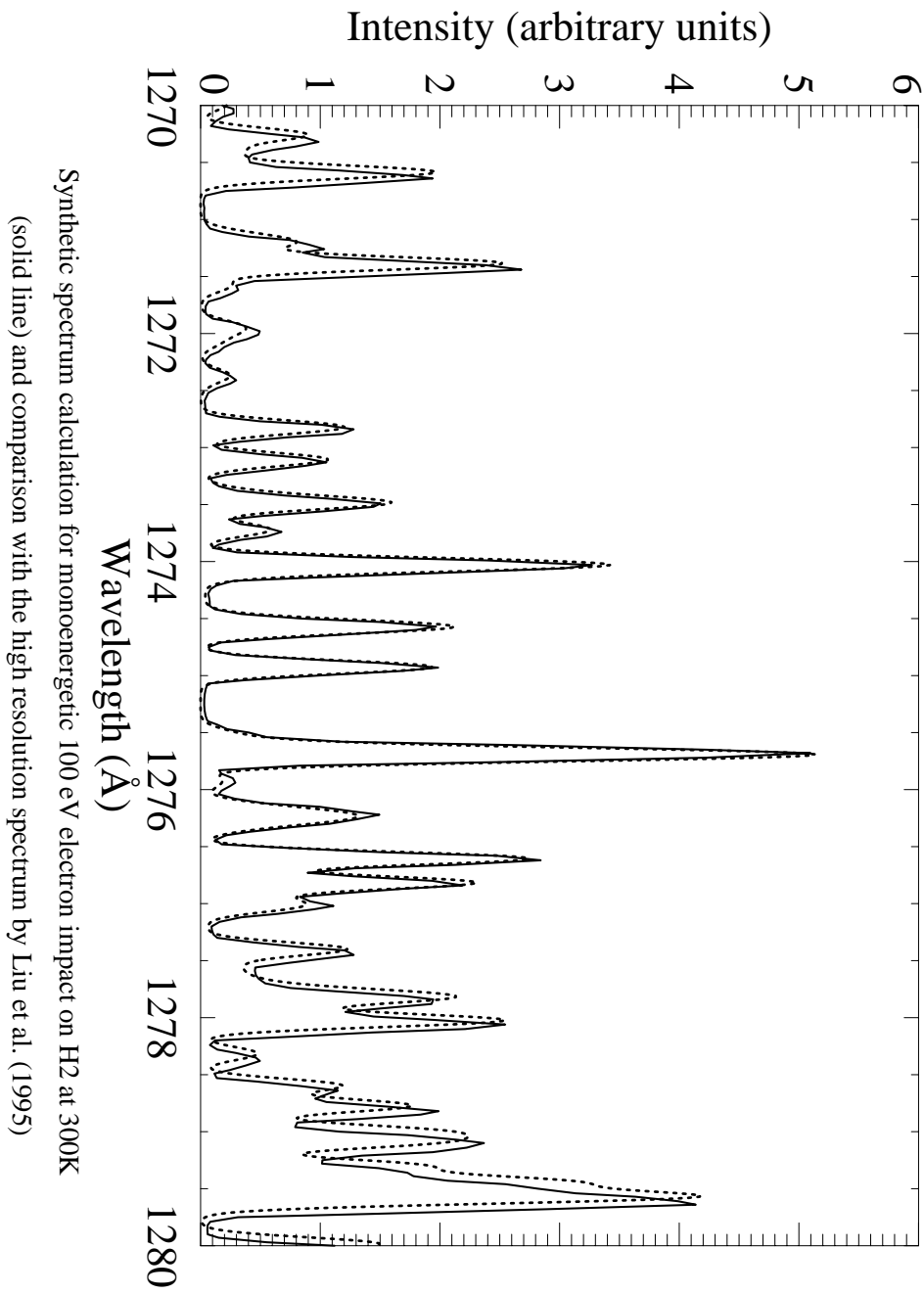


Figure 62

### VIII.3.3 Model validation and sensitivity

Various tests were conducted to assess the validity of the coupled spectral-energy degradation model and to assess the importance of difference factors on the spectral characteristics. The approach adopted may be described as follows :

1. validation of the intensity distribution of the Lyman and Werner lines and continuum by comparison with high-resolution laboratory spectra
2. study of the sensitivity of the vertically integrated H<sub>2</sub> spectrum to the initial electron energy distribution
3. evaluation of the observability of these effects on a mid-resolution (5 Å) spectrum of the UV aurora such as those analyzed in the follow section.

As already mentioned, the third point is out of the scope of the present work and is developed in Dols *et al.* (2000). Instead, additional cases are synthesized using the full capabilities of the energy degradation model.

The synthetic spectrum from 1200 Å to 1700 Å was compared in details to the high-resolution laboratory spectrum obtained at 300 K by Liu *et al.* (1995). An excellent agreement is obtained for virtually all relative line intensities. A comparison is shown in figure 62 for the 1270-1280 Å range as an example. The synthetic spectrum has been smoothed at the resolution of the spectrometer (0.1 Å). The slight shift in wavelength between the observed and calculated spectra is caused by a thermal expansion of the spectrometer during the laboratory measurements. Since this spectral region includes both Lyman and Werner bands, the match of the relative brightness of lines belonging to both transitions also confirms the correct relative magnitude of the B and C state cross sections. It may be concluded from this and comparisons at other wavelengths and for different electron energies that the synthetic spectrum model produces a quasi perfect fit to the best laboratory data available today.

The importance of the vertical distribution of the emission rate, temperature and hydrocarbon absorption is best illustrated by simulating different H<sub>2</sub> UV spectra corresponding to different vertical emission profiles. The emergent spectrum obtained

by integrating the contribution from all layers is then compared to the thin slab approximation. This comparison was performed for 3 initial electron energy distributions :

- **case 1** has a Maxwellian distribution with a characteristic energy  $E_0 = 35$  keV (mean energy = 70 keV) and a  $40 \text{ ergs cm}^{-2} \text{ s}^{-1}$  energy flux. The value of  $E_0$  is selected to produce a peak near 240 km, in agreement with the *Galileo* SSI observations
- **case 2** has the same primary electron component with the addition of a softer Maxwellian electron contribution (0.35 keV) carrying a  $4 \text{ ergs cm}^{-2} \text{ s}^{-1}$  energy flux
- **case 3** is similar to case 2 but the soft component carries  $40 \text{ ergs cm}^{-2} \text{ s}^{-1}$  flux, that is the same amount as the harder component.

The total H<sub>2</sub> volume emission rate is shown for all three cases in figure 63. It may be seen that the soft component has a lower emission efficiency as the result of the increased competition with other processes leading to neutral and electron heating. Figure 64 compares two unconvolved 100 eV synthetic spectra obtained at  $T = 300$  K and  $T = 1000$  K, respectively, in the 1310-1320 Å region dominated by the Lyman band transitions. It clearly shows that all rovibrational lines are more or less affected by a change of temperature.

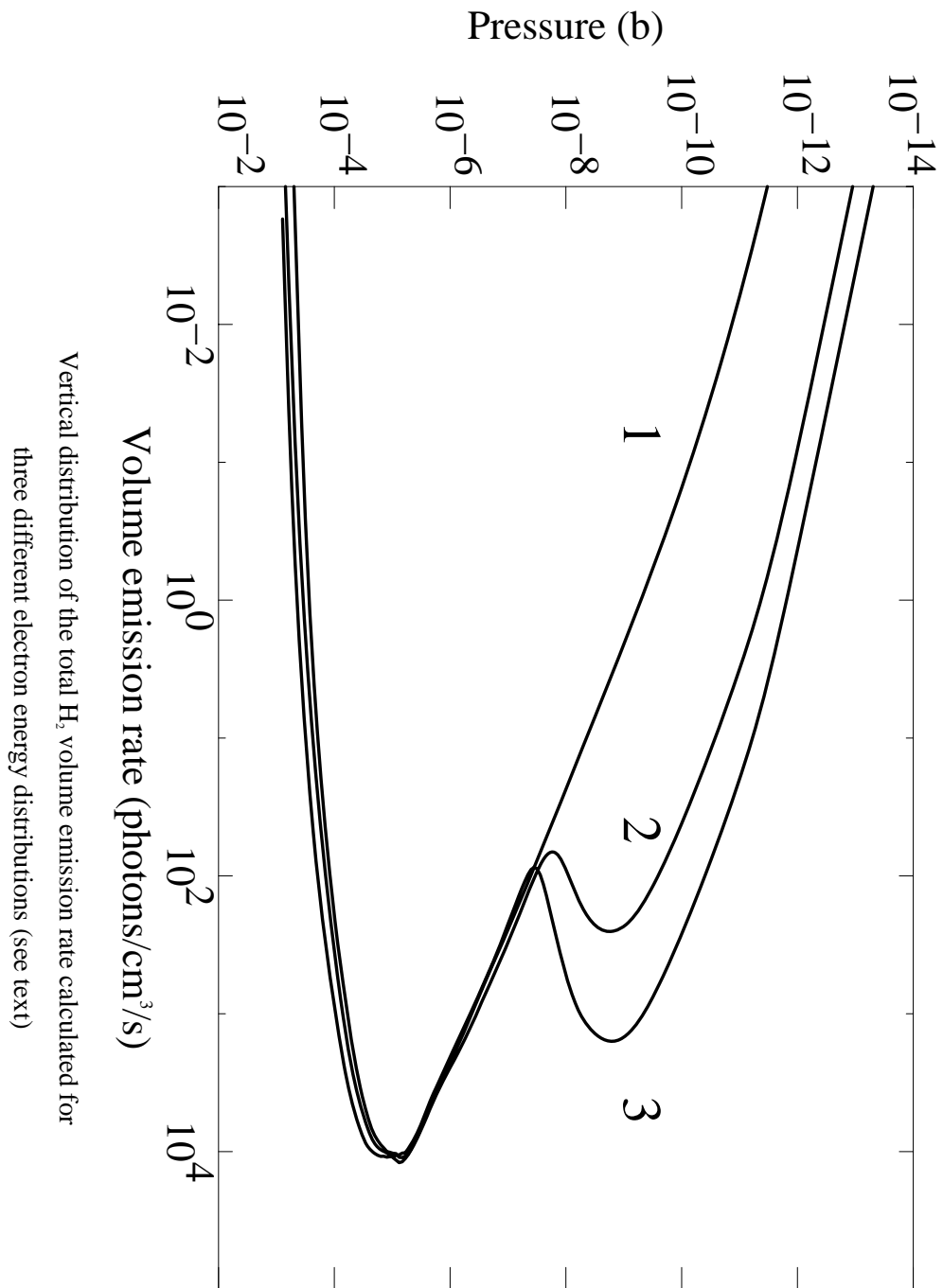


**Figure 63**

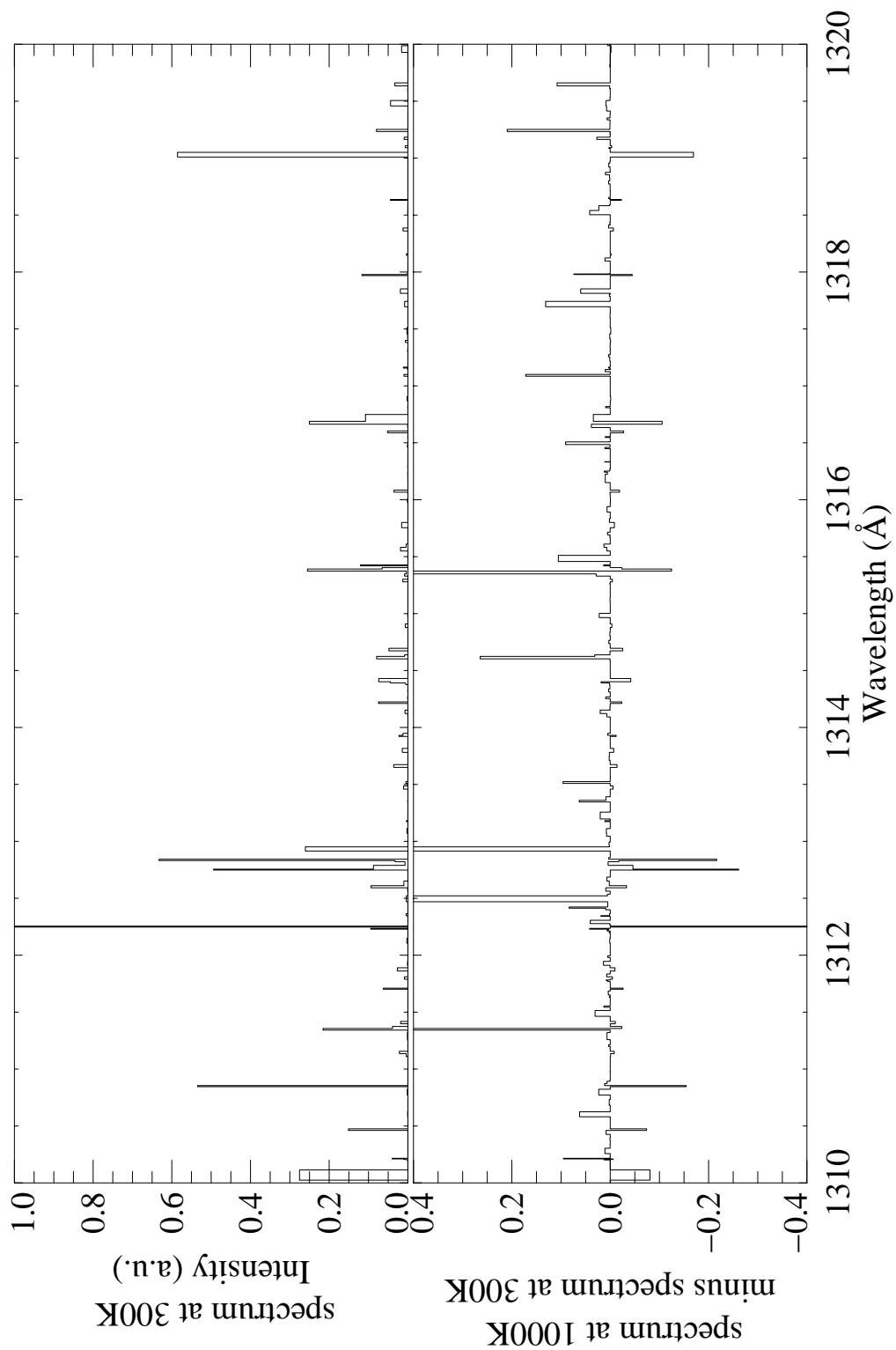


**Figure 64** : Illustration of the temperature effect. Upper plot : unconvolved spectrum at 300 K. Lower plot : difference between the spectrum at 1000 K and the spectrum at 300 K.

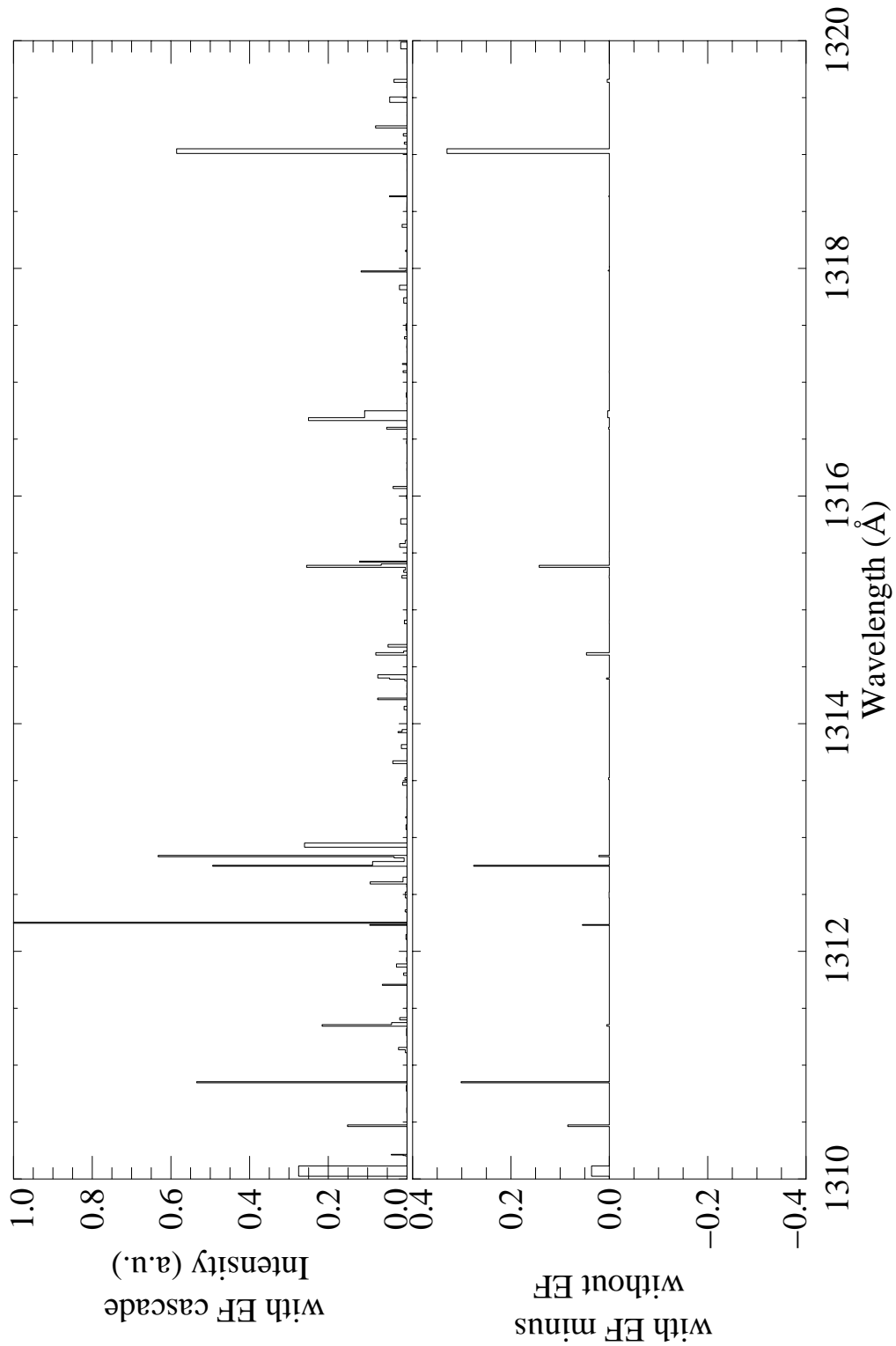


**Figure 65** : Illustration of the E,F cascade effect. Upper plot : unconvolved spectrum with cascade. Lower plot : difference between the spectrum including the E,F cascade and the spectrum without the E,F cascade.

A similar comparison is presented in figure 65 which shows two unconvolved

100 eV spectra at T=300 K with and without E,F cascade, respectively. It is seen that most of the transitions, but not all, are sensitive to the amount of cascade increasing the population of the B state.

The major difference between temperature and cascade effects stems from the fact that the temperature can either increase or decrease the intensity of a line, while cascades can only increase it. Since the two effects are on the same order of magnitude, an interplay of compensation or addition of the two effects is expected to occur when both cascade and temperature are modified. These combined effects are presented in figure 66 and 67 which show a comparison between the three cases (1, 2 and 3) and the monoenergetic (100 eV) – isothermal (300 K) case frequently adopted in previous studies. Panels 1, 2 and 3 illustrate the effect of the vertical integration including the variation of the local electron energy distribution, vertical temperature gradient and vertical differential absorption below 1400 Å. Panel 1 corresponds to a spectral region dominated by the Lyman band system. The 100-eV and the calculated spectra have been normalized for the 3 cases on the 1316.7 Å line which is due to a blend of the L19-11P(7), L16-10P(3) and L9-7P(4) transitions. In this spectroscopic notation, L designates a Lyman transition (W for a Werner transition), the two next numbers are the initial (v') and final (v'') vibrational numbers, P stands for a P branch ( $\Delta J=-1$ ) and the final number is the initial excited rotational quantum number (J'). The distributed electron energy spectrum increases the cascade contribution from the  $E,F^1\Sigma_g^+$  state as shown by both laboratory and synthetic spectra for low electron energies close to the excitation threshold. The temperature effect is due to the increased weight of the upper emission layer at higher temperatures as the contribution of the soft electron increases. Three kinds of effects are present in figure 66 :

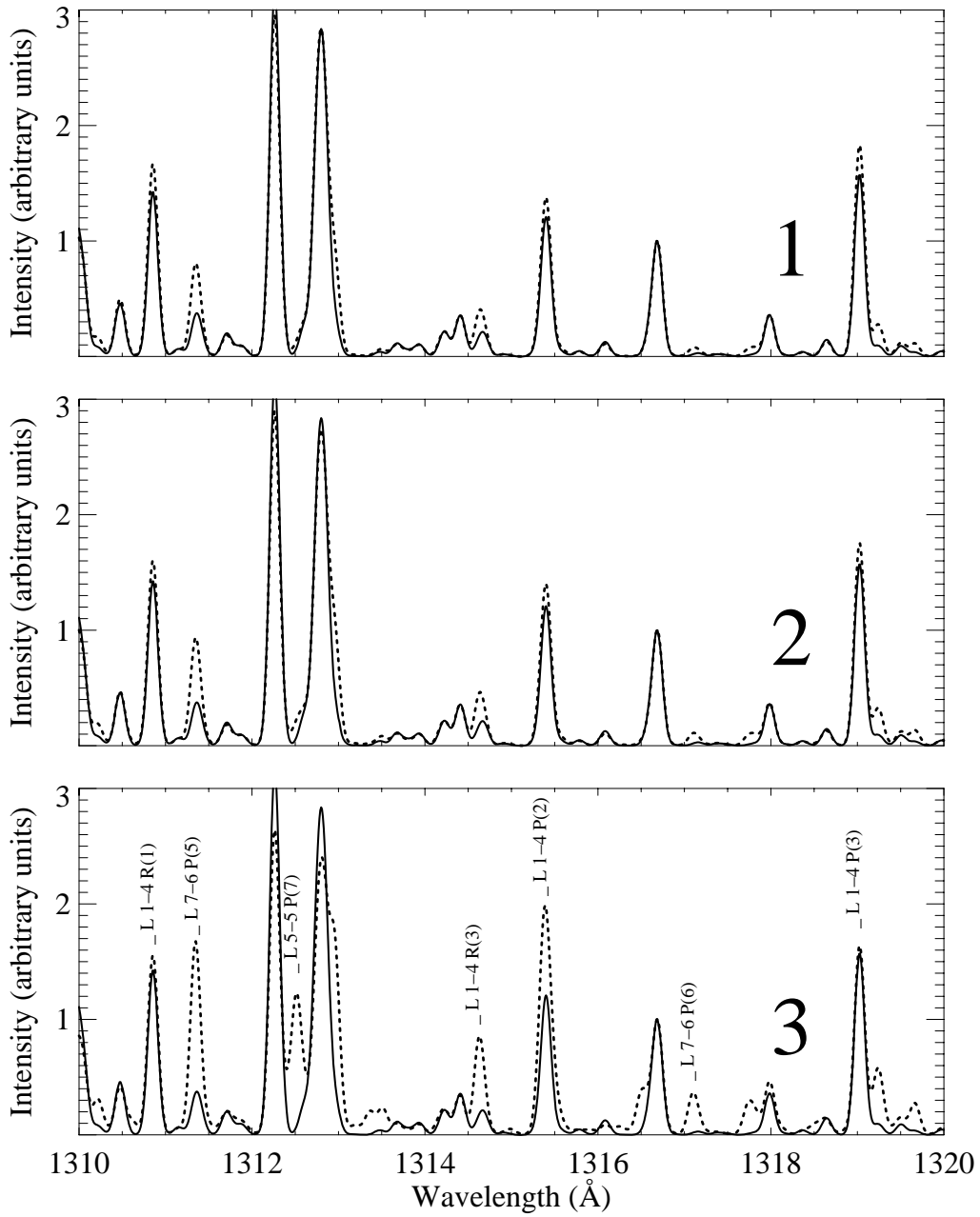
1. a strong enhancement of a line intensity resulting from the addition of a brightness increase due to the higher temperature and from a brightness increase due to the increased E,F cascade. This effect is illustrated by the lines at 1314.6 Å (L1-4R(3)) and at 1315.4 Å (L1-4P(2))
2. persistence of a line intensity stemming from the compensation of the temperature and cascade effects which are decreasing and increasing, respectively, the intensity of the line. It is illustrated by a large number of lines, the brightest being at 1310.85 Å

(L1-4R(1)), 1312.8 Å (L1-4P(1)) and 1319 Å (L1-4P(3)).

3. a strong enhancement or the appearance of a line solely due to the temperature increase. This applies, for example, to the lines at 1311.4 Å (L7-6P(5)), 1312.5 Å (L5-5P(7)), 1317.1 Å (L7-6P(6)).

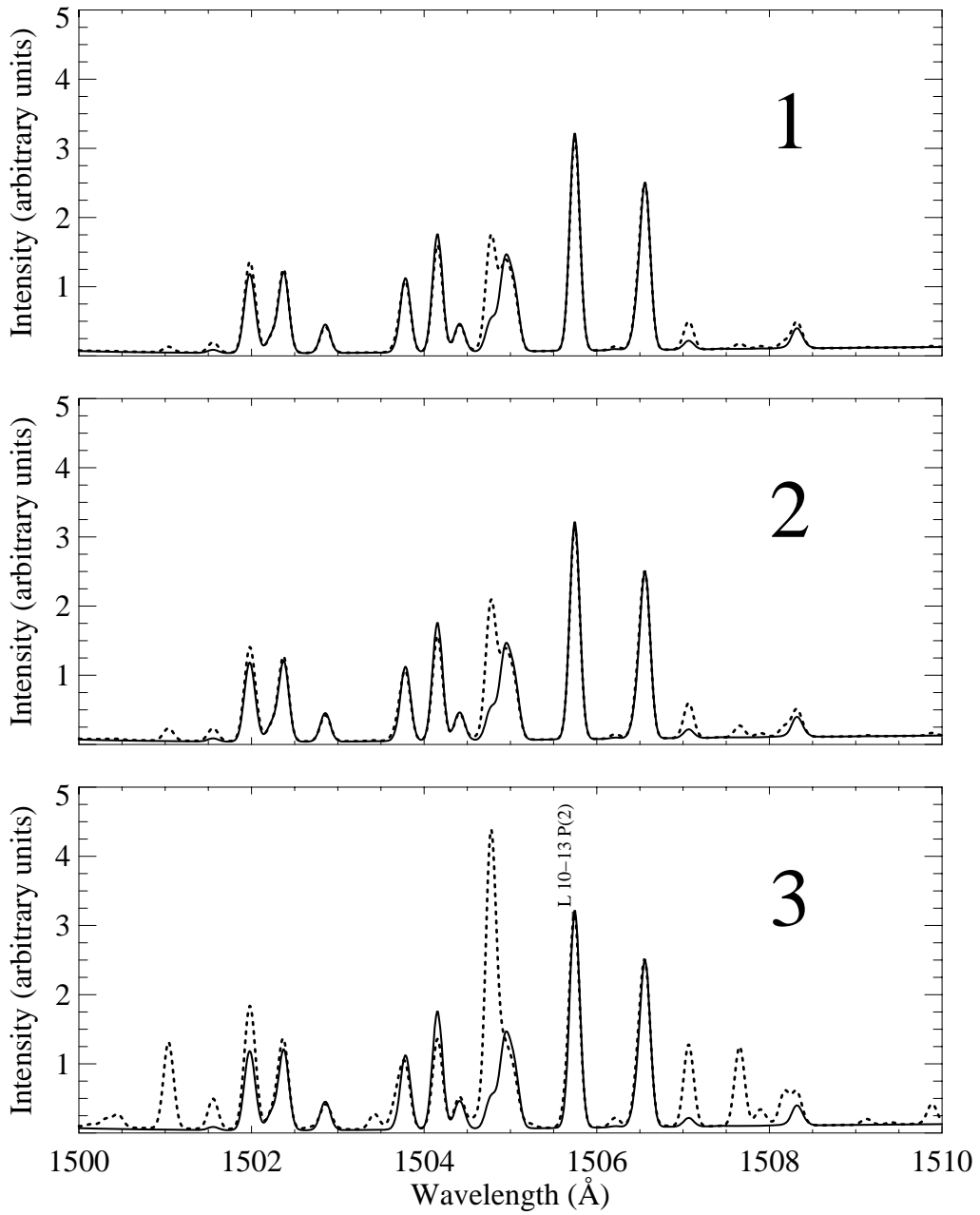
Figure 67 shows a similar comparison for the 1500-1510 Å region where all lines also belong to the Lyman system. All three cases (1, 2 and 3) have been normalized to the (10-13) P(2) transition at 1505.7 Å. Only the (1-7) P(5) line at 1504.76 Å is partly populated by cascade from the  $E,F^1\Sigma_g^+$  state. Panel 1 shows that this line is considerably brighter in the energetically and spatially integrated case 1 than the 100 eV–300 K case. A temperature dependence is also observed at 1507.06 Å, 1507.65 Å and 1508.17-1508.31 Å. Further increases of the line intensity are observed in cases 2 and 3. The latter shows that weak lines in case 1 are enhanced by the presence of the high altitude secondary emission peak.

These examples are illustrative of the changes induced in the H<sub>2</sub> spectrum by the consideration of the vertical dimension of the aurora and the integration along the line of sight of layers with changing temperature and electron energy distribution. Such effects, however, are only unambiguously measured provided that the spectral resolution is high enough to distinguish the line brightness redistribution. At low spectral resolution (~5 Å), the convolution by the instrument line spread function will, to a large extent, smooth and remove the signature of the emission altitude dependence and provides only limited useful temperature information.



Synthetic spectrum calculated from three different electron energy distributions (dashed line) and comparison with the spectrum for a 100-eV impact at 300 K (solid line)

**Figure 66**



Synthetic spectrum calculated from three different electron energy distributions (dashed line) and comparison with the spectrum for a 100-eV impact at 300 K (solid line)

**Figure 67**

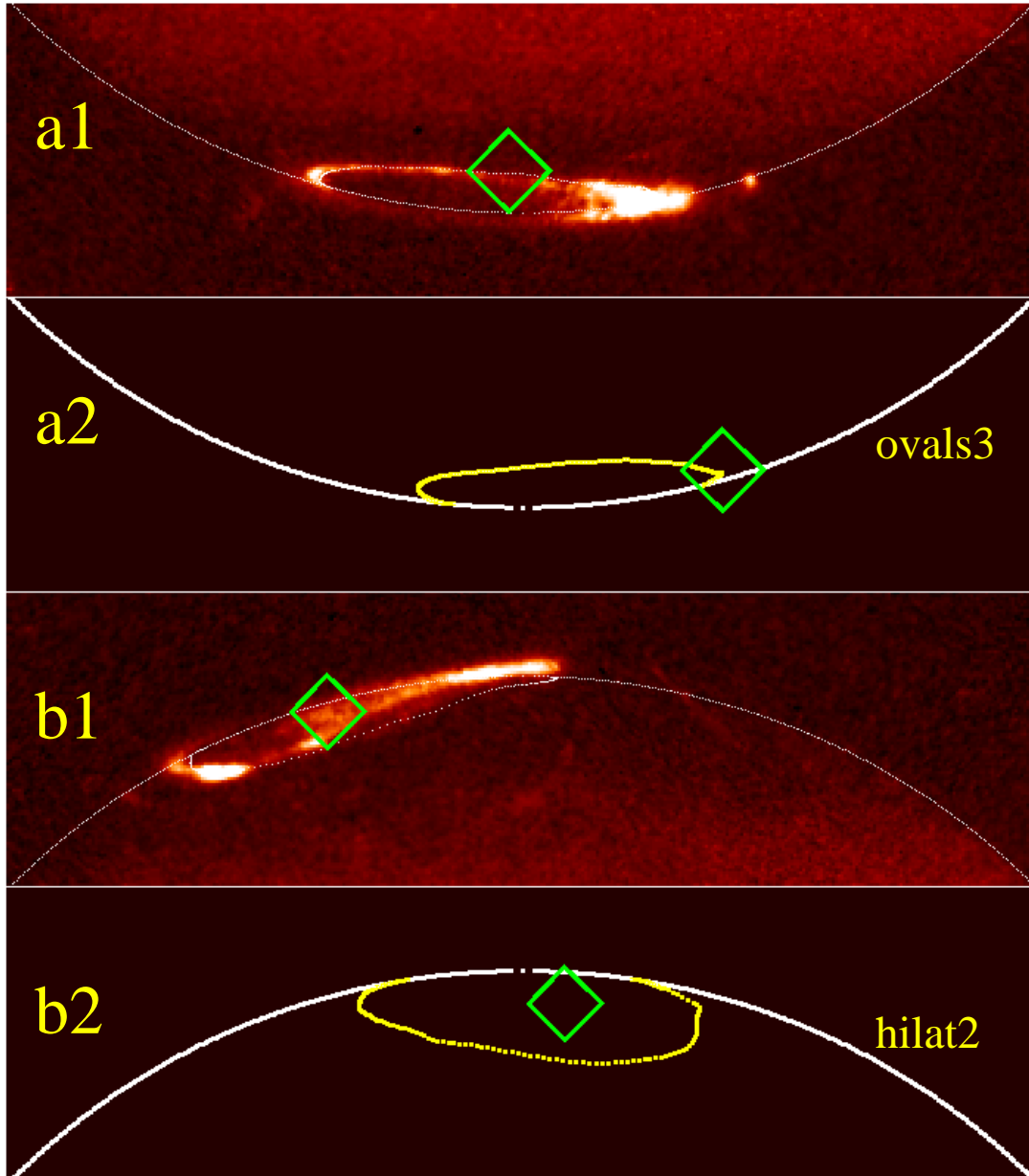


**Figure 68** : Geometry of the observation corresponding to the Ovals3 and Hilat2 GHR spectra modeled in this study. a1), b1) : WFC2 images of Jupiter's aurora observed one HST orbit prior to the spectra. The projection of the GHR aperture (diamond) is shifted to the left to include the same auroral region as will be observed one orbit later. a2), b2) : view of the reference oval (dotted line) as would be seen for the CML of the GHR observations with the projection of the GHR aperture (diamond).

### VIII.3.4 Echelle H<sub>2</sub> spectroscopy

High resolution ultraviolet echelle spectra of H<sub>2</sub> analyzed in conjunction with our auroral model is an indicator of the conditions prevailing in the auroral regions. To illustrate its application to the analysis of the echelle GHRS data (Dols *et al.*, 2000), figure 69 shows synthetic spectra in the 1216-1220 Å region for three temperatures at the echelle resolution (0.07 Å). The electron energy distribution was calculated with the degradation model at the altitude of the peak of case 1. As may be seen, some lines show little brightness dependence on temperature. Others dramatically increase as a result of the redistribution of the population among the rotational levels of the H<sub>2</sub> v=0 ground state.

Among the ten echelle spectra described by Dols *et al.* (2000), only two (Ovals3 and Hilat2) show sufficiently bright H<sub>2</sub> lines to allow a quantitative analysis. The brightest lines belong to the (2,6) Werner band with some additional Lyman and Werner lines. The approach used was to fit the H<sub>2</sub> emissions with the parameters of the best fits to the G140L spectra obtained 25 minutes later on the same HST orbit. This procedure allows to verify whether the effective model temperature, resulting from the vertical distribution emission and hydrocarbon absorption is in agreement with the relative line strengths.

Figure 70 compares the resulting Ovals3 H<sub>2</sub> spectrum (in which the Ly- $\alpha$  contribution was removed) above 1216 Å with the model spectrum calculated from the energy fluxes derived by the two-stream code with a single Maxwellian distribution set to  $E_0 = 17$  keV (panel a). The match is good for several lines but the brightness of the W 1-5 P(5), 2-6 P(2), P(4) and Q(2) lines are clearly underestimated in the model spectrum. By contrast, a good fit is obtained for  $T = 600$  K (panel b), a value reached near 400 km in the neutral model shown in figure 61 but substantially higher than the emission rate weighted temperature associated with the  $E_0 = 17$  keV precipitation which resulted in a mean H<sub>2</sub> temperature of about 228 K. Similar conclusions apply to the Hilat2 spectrum, since the brightness of the temperature-sensitive lines is underestimated and a better fit is obtained using again an effective temperature  $T = 600$  K.

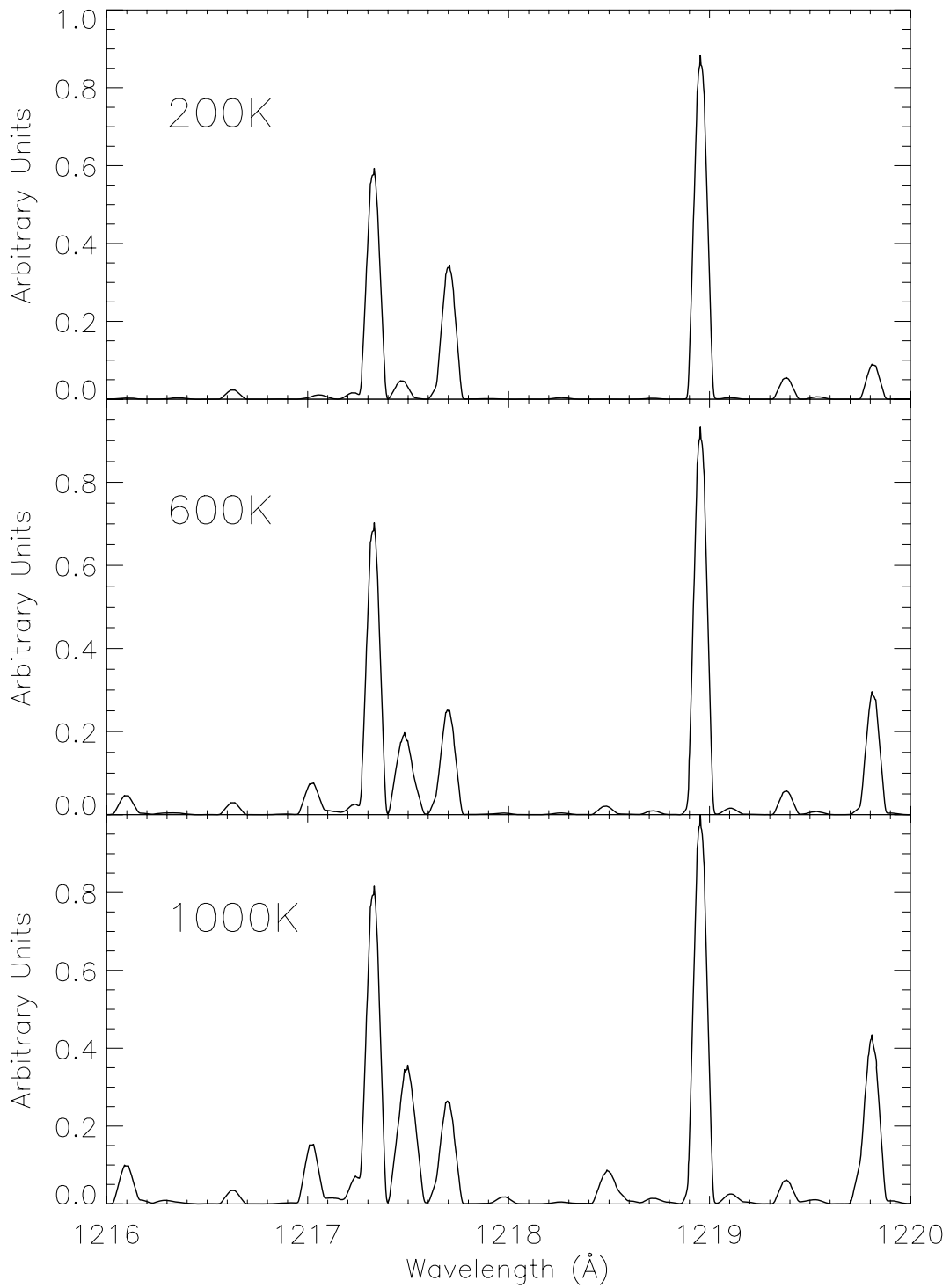


**Figure 69** : Synthetic spectra at three temperatures at the echelle resolution ( $0.07 \text{ \AA}$ ). The electron energy distribution was calculated with the degradation model at the altitude of the peak of case 1.

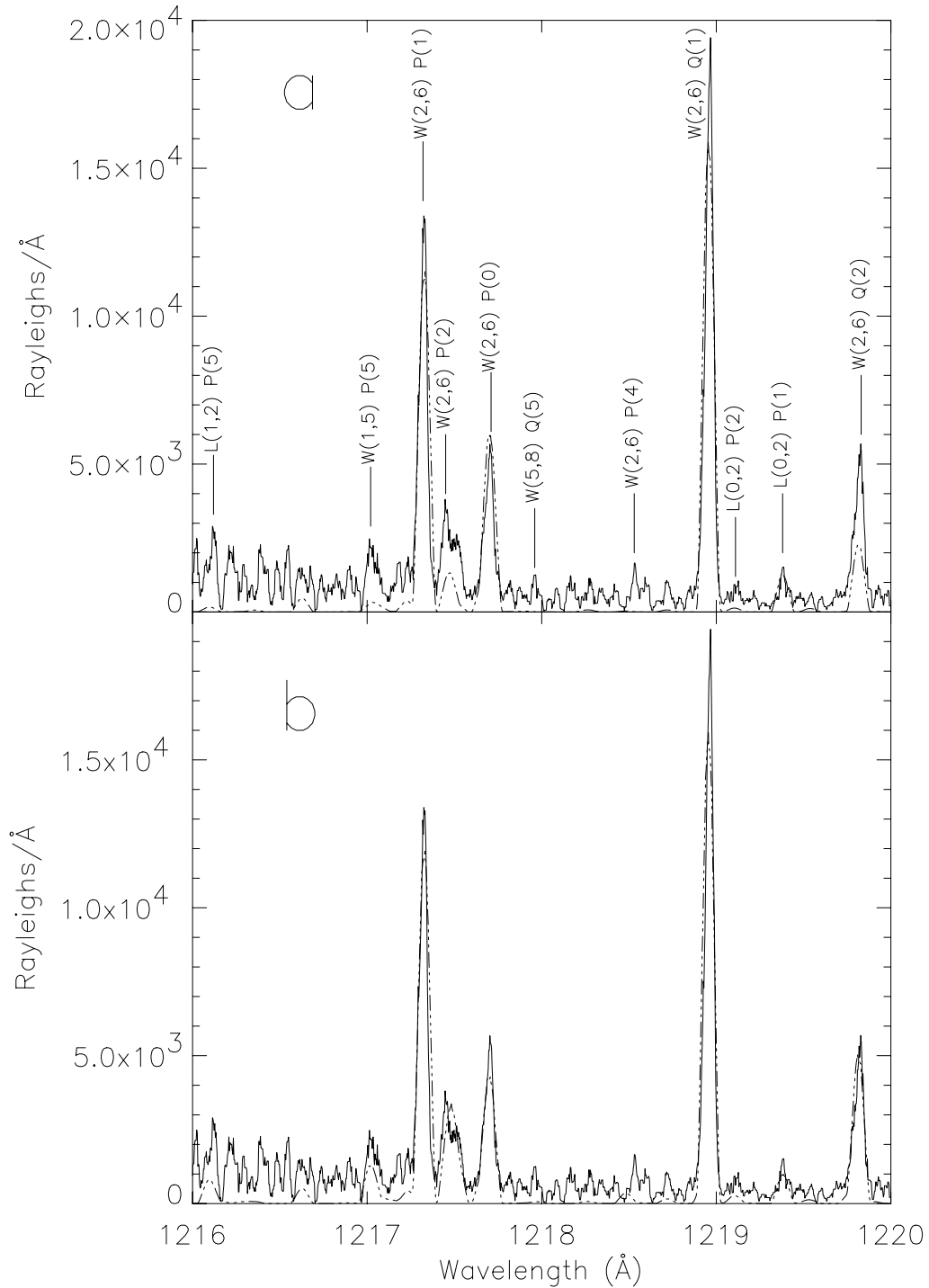


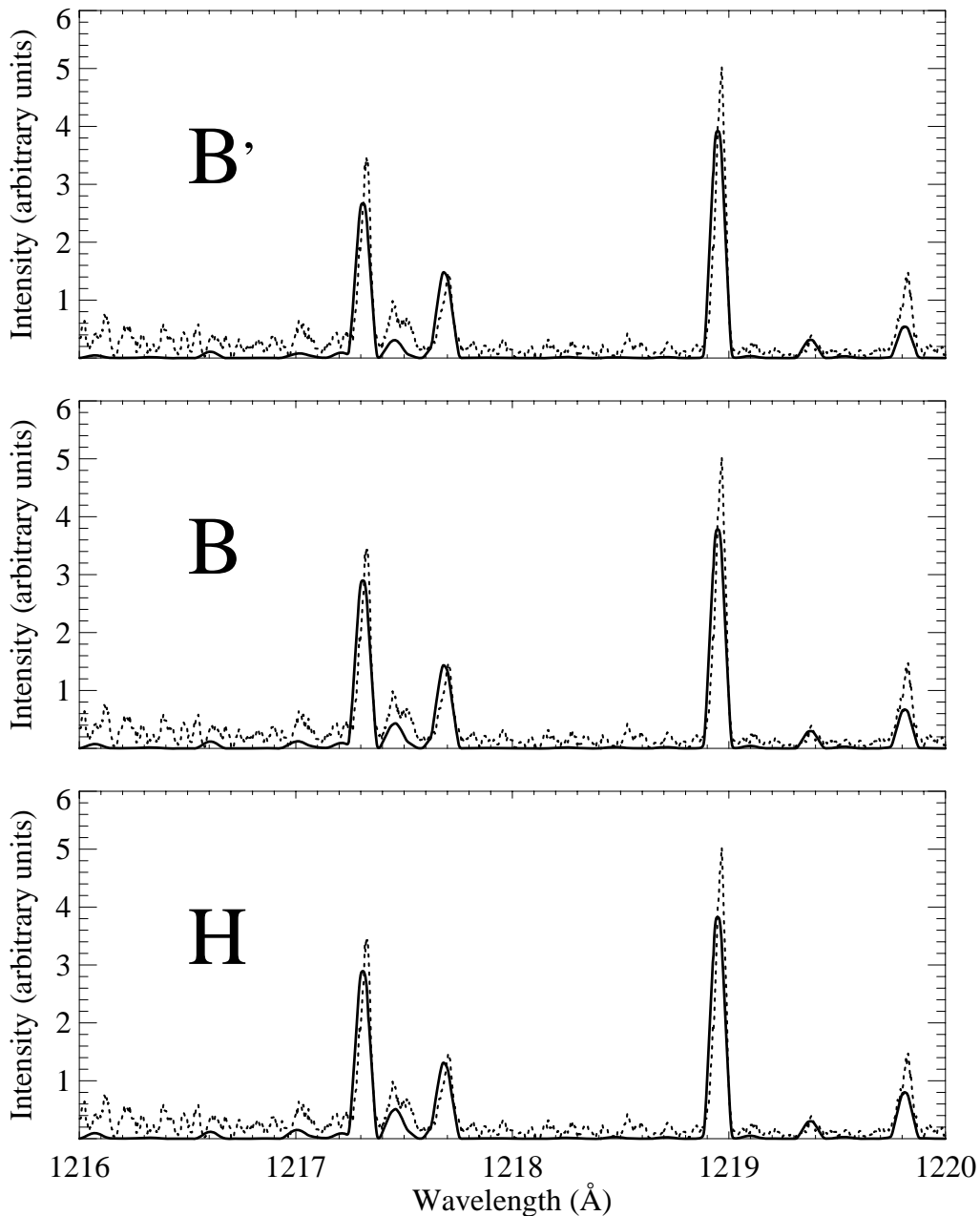
**Figure 70** : comparison between the Ovals3 H<sub>2</sub> spectrum with the model spectrum calculated from the energy fluxes derived by the two-stream code with a single Maxwellian distribution set to  $E_0 = 17$  keV (panel a). The match is good for several lines but the brightness of the W 1-5 P(5), 2-6 P(2), P(4) and Q(2) lines are clearly underestimated in the model spectrum. By contrast, a good fit is obtained for  $T = 600$  K (panel b)

## VIII.4 Use of converged temperature profiles

The model of energy degradation coupled to heat conduction equation which we described was partly developed to address discrepancies of the nature just depicted. It provides, in a consistent way, the local electron flux energy distribution and the temperature and density profiles which result from heating by these electrons.

In order to illustrate the effect of a complex temperature profile compatible with the electron energy distribution on the synthetic spectra, four cases (hereafter referred to cases B, B', B'', and H), two of which are taken from the two-stream section (cases B and H), have been applied to the spectral generator. Cases B, B' and H share the same energy flux distribution (double Maxwellian distribution). The difference arises in the temperature profile : case B' uses a fixed NEB atmospheric structure (temperature, densities) similar to that used in the previous section and is therefore not compatible with the electron flux, cases B and H come with their own converged atmospheric structures as described in the two-stream section. B'' is a single layer case acted on by a monoenergetic electron beam of 100 eV. It assumes a fixed (incompatible) temperature of 600 K.

As already mentioned, cases B and H bear the same energy distribution, but case H has a warmer temperature profile in the stratospheric region (a different boundary condition was applied to the thermal profile in the lower atmosphere). Figure 71 shows the synthetic spectrum obtained with cases B', B, and H in the 1216-1220 Å region and compares them with the observed Ovals3 spectrum. It can be seen that the synthetic spectrum calculated with case B' is not in good agreement with the observed spectrum. The obtained fit is characterized by a chi-squares value of 3.0 (arbitrary units). Using the atmospheric structure compatible with the electron flux, as in case B, significantly improves the fit which is then characterized by a chi-squares value of 2.8. The compatibility of the thermal structure with the electron energy distribution does not by itself explain the improvement of the fit. Instead, the key point is the temperature increase (B has a warmer temperature profile than B').



Synthetic spectrum calculated from three different electron energy distributions  
(solid line) and comparison with the ovals3 spectrum (dashed line)

### Figure 71

This can be verified with the spectrum of case H which implies a warmer profile (in the stratosphere) than case B and for which the fit is again improved. It is now characterized by a chi-squares value of 2.7. It may already be concluded that synthesizing a spectrum with a warm temperature profile, compatible with the energy distribution of the electrons, substantially improves the fit to the observed spectrum.

The spectrum obtained with case B" is an illustration of the former rovibrational

temperature fitting method which assumed a monoenergetic beam (100 eV) interacting with the components of a single layer isothermal atmosphere. This method predicts a best fit temperature of 600 K meant to represent the H<sub>2</sub> temperature. On the other hand, the mean H<sub>2</sub> temperature weighted by the unabsorbed H<sub>2</sub> Lyman and Werner emission for a zenith angle of 60° (we will see in a next section that methane absorption modifies the H<sub>2</sub> temperature) is 342 K for case H and 296 K for case B.

Comparison between the fits obtained with cases B" and H shows that increasing the stratospheric temperature is not the ultimate solution to get a synthetic spectrum fitting the observed spectrum just as well as the monokinetic case at 600 K. It should be pointed out that an H<sub>2</sub> temperature in the auroral region of 296 K is more compatible with the predictions of the energy degradation model. Indeed, it can be shown that an H<sub>2</sub> temperature on the order of 600 K could hardly be obtained by injecting a very large flux of energetic auroral electrons. However such an electron precipitation would be inevitably characterized by very strong H<sub>2</sub> UV and IR emissions that are not observed.

In summary, a source of inconsistency between the temperatures derived by the former and the present methods is that the H<sub>2</sub> temperature is usually represented by a single value. In the next section we show that the H<sub>2</sub> temperature depends on the wavelength and on the geometry of the observation. In fact, the geometry effect is expected to be as important as it was for the color ratio (see part 1). An example applied to case B shows that the maximum difference between the H<sub>2</sub> temperature calculated from the thermal profile and the temperature obtained by accounting for the viewing geometry and wavelength can be greater than 300 K

## IX Coupling of the three models

### IX.1 Introduction

For the first time in this work, we invoke the coupling between the three models presented before :

- the energy degradation model,
- the spectral generator,
- the morphology simulation model.

Preliminary remarks concerning this coupling first need to be formulated. The examples given in this section which estimate the effect of wavelength and observation geometry on the H<sub>2</sub> temperature, obviously represent one of the many possible applications of the coupling. A systematic description of all possible applications represents a natural continuation of this work but is actually out of the scope since we mainly concentrated on the developement of the separate models. Also, the following examples consist in a preliminary application for which a reduced version of the spectral generator and a modified morphology simulation model were used. The reduced version of the spectral generator, which is already used in the energy degradation model to estimate the H<sub>2</sub> color ratio and emission profiles, does not account for the rotational levels but calculates the vibration transitions only. The modified morphology model required more extensive adaptations which are described below.

## IX.2 Modified morphology model

While the original version of the morphology model is a 3-dimensional model (the two spatial dimensions of the detector aperture plus the perpendicular axis along the line of sight), the modified version only accounts for the line of sight (LOS) dimension. It assumes a uniformly emitting region, a spherical planet, and allows to specify either the zenith angle for a line of sight pointing inside the planetary disk or the altitude above the limb for a line of sight pointing off the planet. The most important difference between the original and the modified model lies in the fact that the original model (chapter ...) assumes that the H<sub>2</sub> UV emission is fully described by a Chapman profile independently of the atmospheric structure, while the modified version includes all vertical information provided by the energy degradation model and the spectral generator. That is, it accounts for the methane density profile, the temperature profile, and the wavelength dependent emission profiles. The aim is to calculate an H<sub>2</sub> temperature at each wavelength by weighting the temperature profile by the emission profile at that particular wavelength and for a given viewing angle, or altitude above the limb.

## IX.3 Methane absorption

The reason why the H<sub>2</sub> temperature varies from one wavelength to another in the 1200-1650 Å range essentially stems from the wavelength dependent methane absorption cross section of the H<sub>2</sub> emission. According to the observed color ratio and to the (visible) observed emission peak altitude, a substantial part of the H<sub>2</sub> emission is produced below the homopause where CH<sub>4</sub> density is important. A simple view is that the emission occurring below the level characterized by a wavelength dependent optical depth  $\tau = 1$  is completely absorbed. As a result, the absorbed emission does not contribute to the weighting of the temperature profile and since the region below  $\tau = 1$  is generally confined to the lower stratosphere, where the temperature does not exceed 200 K, the absorption of the emission leads to an increased H<sub>2</sub> temperature.

A similar behavior is expected for the C<sub>2</sub>H<sub>2</sub> absorption, however, due to its lower absorption it has not been accounted for.

## IX.4 Viewing geometry effect

The viewing geometry modifies the H<sub>2</sub> temperature whether or not hydrocarbon absorption occurs. Its effect depends, in a complex way, on the relative shapes of the thermal and emission profiles.

### IX.4.1 Application to case B

We have applied the coupled model to case B for various viewing angles at the central meridian longitude (CML) ranging from 0° (LOS along the local normal, or vertical path) to 90° (LOS perpendicular to the local normal) inside the planetary disk, and for different altitudes above the limb, ranging from 50 km to 1000 km.

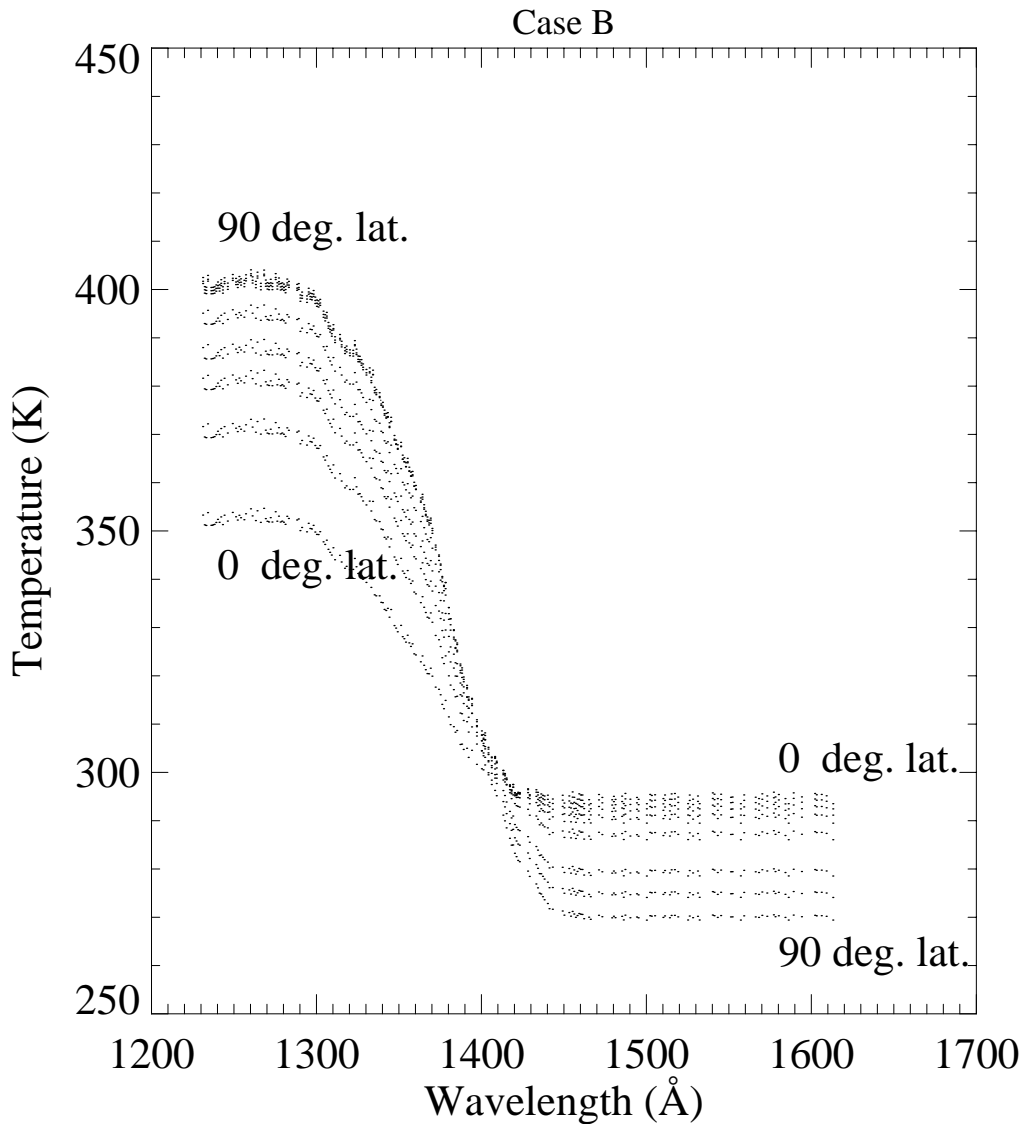
### IX.4.2 Line of sight pointing inside the planetary disk

Since a local temperature  $T(s)$  and a local emission line intensity  $I(s,\lambda)$  are intercepted at each step  $s$  along a given LOS, the H<sub>2</sub> temperature associated to this LOS may be calculated by averaging  $T(s)$  with  $I(s,\lambda)$  weights, i.e.

$$T_{H_2}(\lambda) = \frac{\int T(s) I(s, \lambda) ds}{\int I(s, \lambda) ds}$$

where  $ds$  is the distance step along the LOS.

In this preliminary study we assume that the emission is horizontally uniform over the planet (i.e. unstructured emission only).



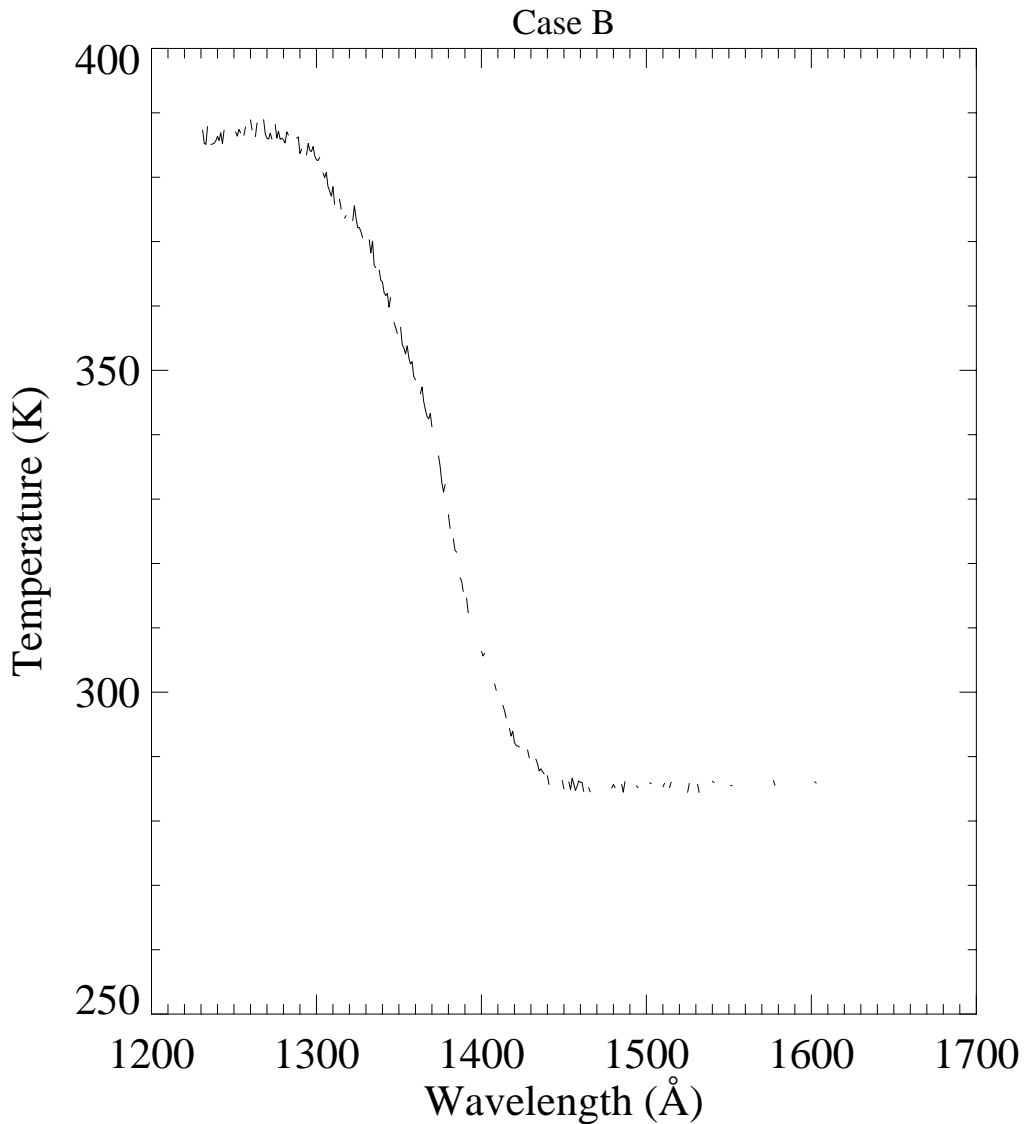
Wavelength dependent temperature as a function of the Jovian latitude intercepted by the line of sight at the CML

**Figure 72**

The resulting wavelength dependent H<sub>2</sub> temperatures are plotted in figure 72. Seven different LOS are considered, they are all pointing at the CML and intercept a latitude on Jupiter (assumed spherical with a radius of 70000 km) of 0°, 60°, 70°, 75°, 80°, 87°, 90°, respectively.

The latitude effect is different according to as methane absorption occurs or not. In the wavelength region where methane absorption is important (below 1400 Å) the temperature increases with latitude. The maximum effect is observed at the shortest

wavelength ( $\sim 1200 \text{ \AA}$ ) for which the temperature increases from 350 K at  $0^\circ$  to 400 K at  $90^\circ$  latitude. The effect decreases as the wavelength increases (as  $\text{CH}_4$  absorption becomes smaller) and finally vanishes around  $1400 \text{ \AA}$ . Beyond this wavelength, methane absorption is negligible and the effect is reversed since temperature decreases as latitude increases (this effect is explained in the appendix).

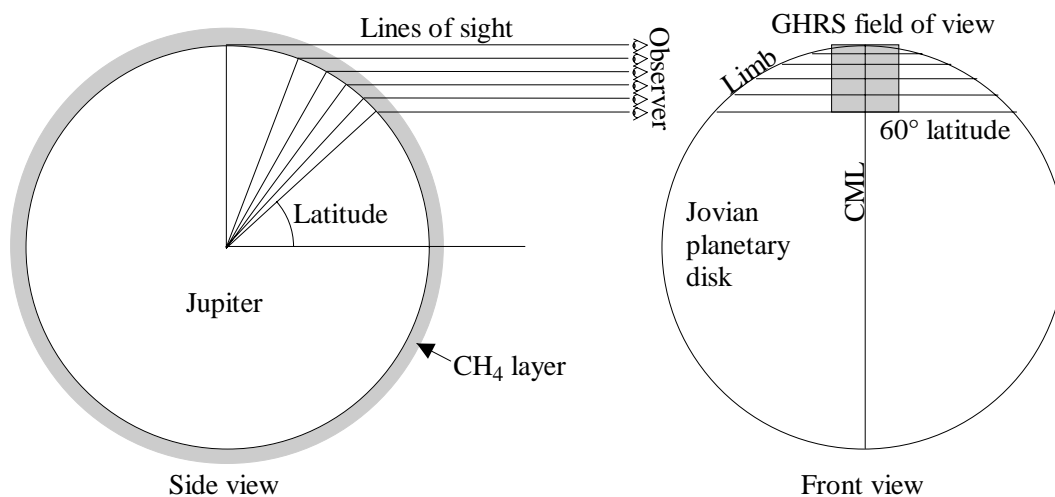


Wavelength dependent temperature averaged over the field of view  
of a GHRS like aperture pointing below the limb

**Figure 73**

Since methane absorption is very small in this region a plateau is rapidly reached and the wavelength dependence disappears. The latitude effect is weak as the temperature

only decreases from 295 K at 0° latitude to 275 K at 90° latitude. It should be reminded that C<sub>2</sub>H<sub>2</sub> absorption is not considered here and similar, but smaller, effects to those observed for CH<sub>4</sub> absorption are expected.



Schematic representation of the field of view of GHRS projected on Jupiter. The side view shows equidistant lines of sight and their relation with the Jovian latitude. The front view shows the portion of the Jovian disk intercepted by a GHRS like aperture positioned as described in the text.

**Figure 74**

The GHRS aperture subtends an angle of  $1.74 \times 1.74 \text{ arcsec}^2$  on the sky. The Jovian latitude range intercepted by this aperture obviously depends on the geometry of the observation. If one imagines that the top edge of the aperture is located at the limb, the bottom edge is located at a latitude of about 60°. An average temperature weighted by the total emission line intensities  $I(\text{LOS}, \lambda)$  integrated along the LOS, as a function of the wavelength, may be obtained from

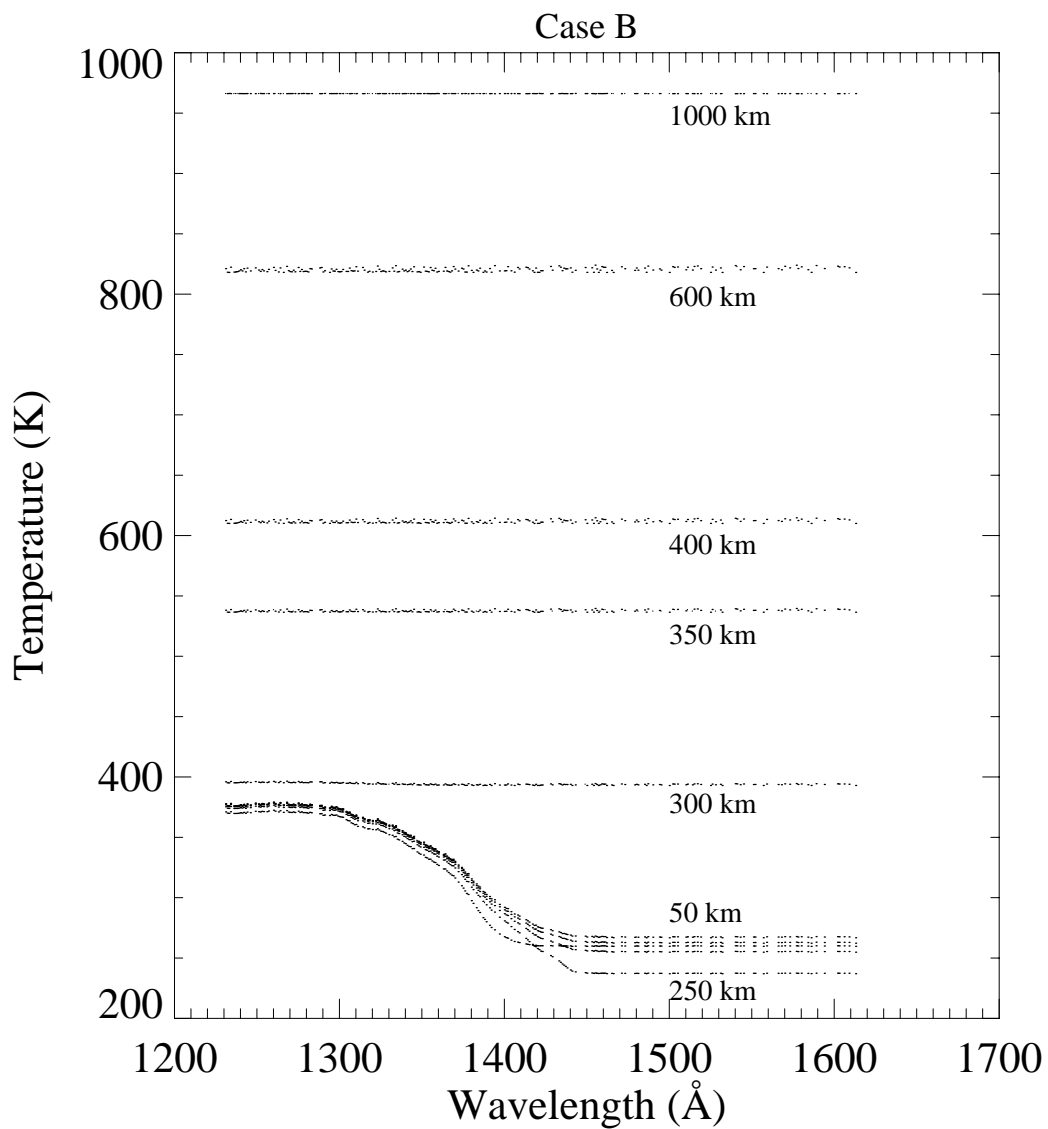
$$T_{\text{H}_2}(\lambda) = \frac{\int_{\text{LOS}} T_{\text{H}_2}(\text{LOS}, \lambda) I(\text{LOS}, \lambda) dz}{\int_{\text{LOS}} I(\text{LOS}, \lambda) dz}$$

where  $dz$  is the distance between two contiguous LOS. It is expected to follow the curve plotted in figure 73 and is essentially similar to the 75° curve plotted in figure 72.

The latitudes used to calculate the average temperature were chosen so that the

corresponding LOS are equally spaced in the aperture ( $dz$  constant).

Even at short wavelengths the average temperature remains below 400 K, that is less than deduced from the Echelle spectra (Ovals3, Hilat2). A further increase of the  $H_2$  temperature arises by considering the fact that for these spectra, as seen on figure 57 (panels a2 and b2), the aperture is centered very close to the limb and therefore a substantial portion of the emission may originate from above the limb and from regions located at high latitudes. It is shown below that emissions observed above the limb give rise to higher temperatures. Since the limb brightening increases the weight of this emission over the emission coming from the planetary disk, it is expected that the emission from above the limb plays a dominant role in the observed  $H_2$  temperature as discussed below.

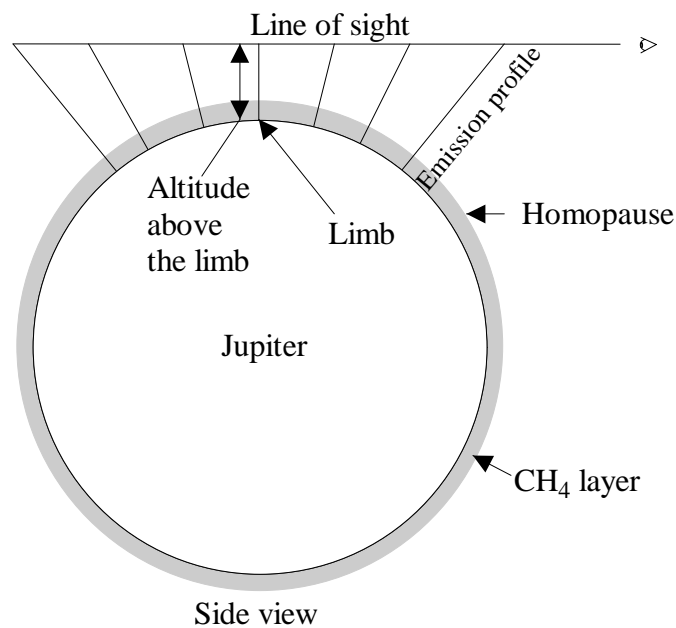


Wavelength dependent temperature as a function of the altitude  
above the limb intercepted by the line of sight

**Figure 75**

### IX.4.3 Line of sight pointing above the limb

The direction of a line of sight pointing off the planet may be specified by its altitude above the limb (figure 76). Ten different altitudes are considered : 50 km, 100, 150, 200, 250, 300, 350, 400, 600 and 1000 km. Above an altitude of 1000 km the H<sub>2</sub> UV emission rapidly vanishes and can therefore be neglected. The wavelength dependent H<sub>2</sub> temperatures associated with the 10 altitudes are plotted on figure 78. It is readily seen that two different regimes apply according to as methane absorption occurs or not. The temperature curves associated to lines of sight passing above the homopause (~300 km) are flat (no absorption and no wavelength effect) since the CH<sub>4</sub> density is negligible compared to that of H<sub>2</sub>. On the other hand, the temperature curves corresponding to LOS below the homopause behave like those obtained with a LOS pointing inside the planetary disk.



Side view of Jupiter showing the relation between a line of sight and its altitude above the limb. The CH<sub>4</sub> layer is represented as a grey shell covering all the planet. The emission profiles intercepted by the line of sight are represented by straight lines. The emission is assumed to be uniform over the planet.

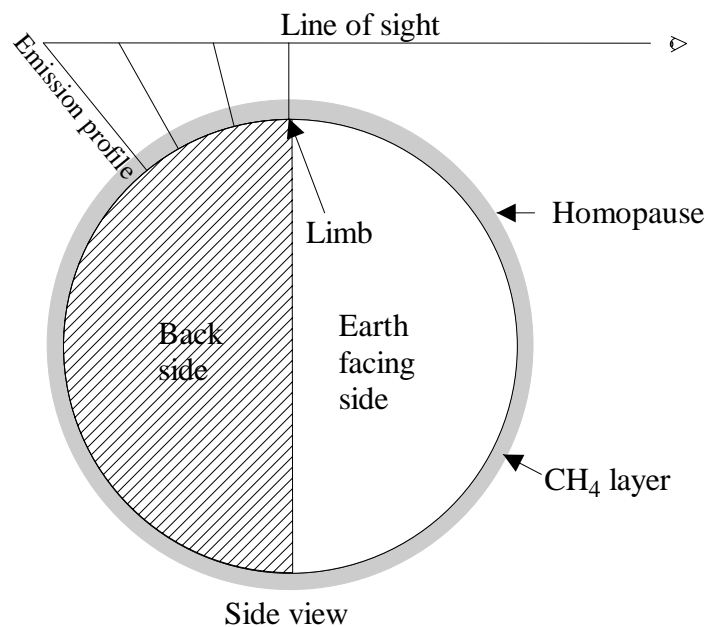
**Figure 76**

Below the homopause, the maximum wavelength-effect is on the order of 250 K (at 50 km) while the maximum altitude-effect does not exceed 30 K (at 1600Å). Above the

homopause the situation is completely different since there is no wavelength effect and the altitude effect is very important. A mean H<sub>2</sub> temperature of 970 K is reached at 1000 km and gradually decreases to 400 K at the homopause.

If one imagines a case where the bottom edge of the GHR aperture is located at the limb, the upper edge may be at about 8000 km above the limb. That is the detector will collect photons emitted at different altitudes and therefore in layers characterized by different temperatures. We can calculate the average H<sub>2</sub> temperature observed through this aperture, as previously, by weighting the ten  $T(\text{LOS},\lambda)$  curves with the corresponding emission brightnesses  $I(\text{LOS},\lambda)$  (integrated over the LOS).

The resulting observed H<sub>2</sub> temperature as a function of wavelength is plotted in figure 82. In this case, a strong wavelength effect is observed which gives rise to temperatures ranging from about 300 K to 500 K.

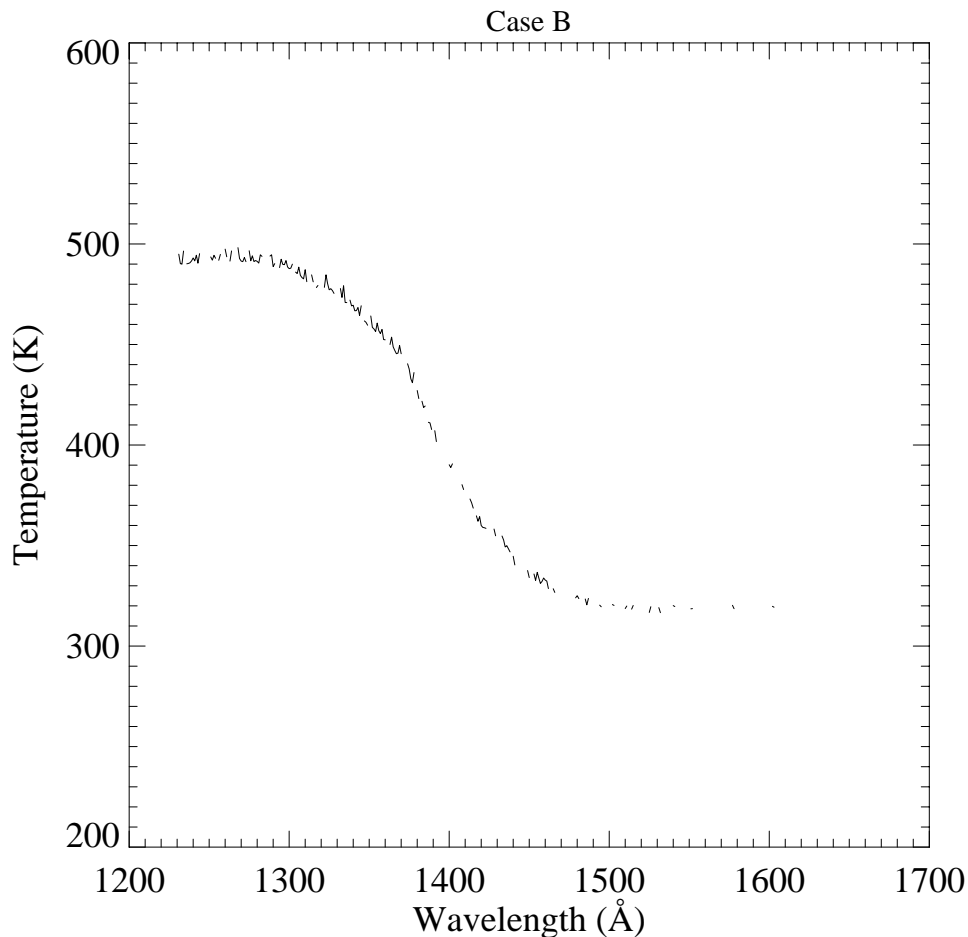


Similar side view of Jupiter than the previous one, but the emission solely comes from the back side of Jupiter.

**Figure 77**

Another point should be taken into account which will increase the temperature. In the previous examples, we considered that the emission is uniform over the planet. The actual auroral morphology is made of complex discrete and diffuse structures which are

not always present on the Earth facing portion of the Jovian disk. In the following example we consider that the emission is originating from the back side of Jupiter so that it only appears above the limb (figure 77). The wavelength dependent temperature as a function of altitude is plotted in figure 68.



Wavelength dependent temperature averaged over the field of view of a GHRS like aperture pointing above the limb

**Figure 78**

Below the homopause the wavelength effect is only partly observed. This can be explained by the complete methane absorption of the emission, especially below 250 km where the temperature does not exceed 250 K. At 200 km a partial wavelength effect changes the temperature from ~150 K to ~250 K. The complete absorption also implies that the emission appearing below the homopause is mostly produced in the Earth facing region of Jupiter. As a consequence, the presence of a gap in the H<sub>2</sub> UV images between the limb and the homopause is a sign that the observed photons mainly come

from the back side of Jupiter.

As was already the case for a uniformly emitting planet, no wavelength-effect is observed above the homopause. A wavelength independent temperature is reached which varies from  $\sim 400$  K at the homopause ( $\sim 300$  km) to  $\sim 970$  K at 1000 km. The mean  $H_2$  temperature characterizing the emitting region observed through a GHRS like aperture with the bottom edge located at the limb (and the top edge at approximately 10000 km above the limb) would lead to a wavelength dependent curve plotted in figure 80. As can be seen a warmer temperature on the order of 600 K is reached in the absorbed region of the spectrum (like Ovals3 and Hilat2). The wavelength effect is on the order of 200 K as the temperature in the unabsorbed region decreases to  $\sim 300$  K.

In conclusion, this example clearly shows that a thermal structure similar to that of case B, that we characterized by a rather low  $H_2$  temperature of 296 K by weighting the temperature profile with the unabsorbed emission seen at  $60^\circ$ , may in some circumstances be compatible with the higher  $H_2$  temperature of 600 K derived by fitting observed high resolution spectra with synthetic spectra. The compatibility rests on the consideration of the wavelength dependence of the measured temperature and on the effect of the viewing geometry.

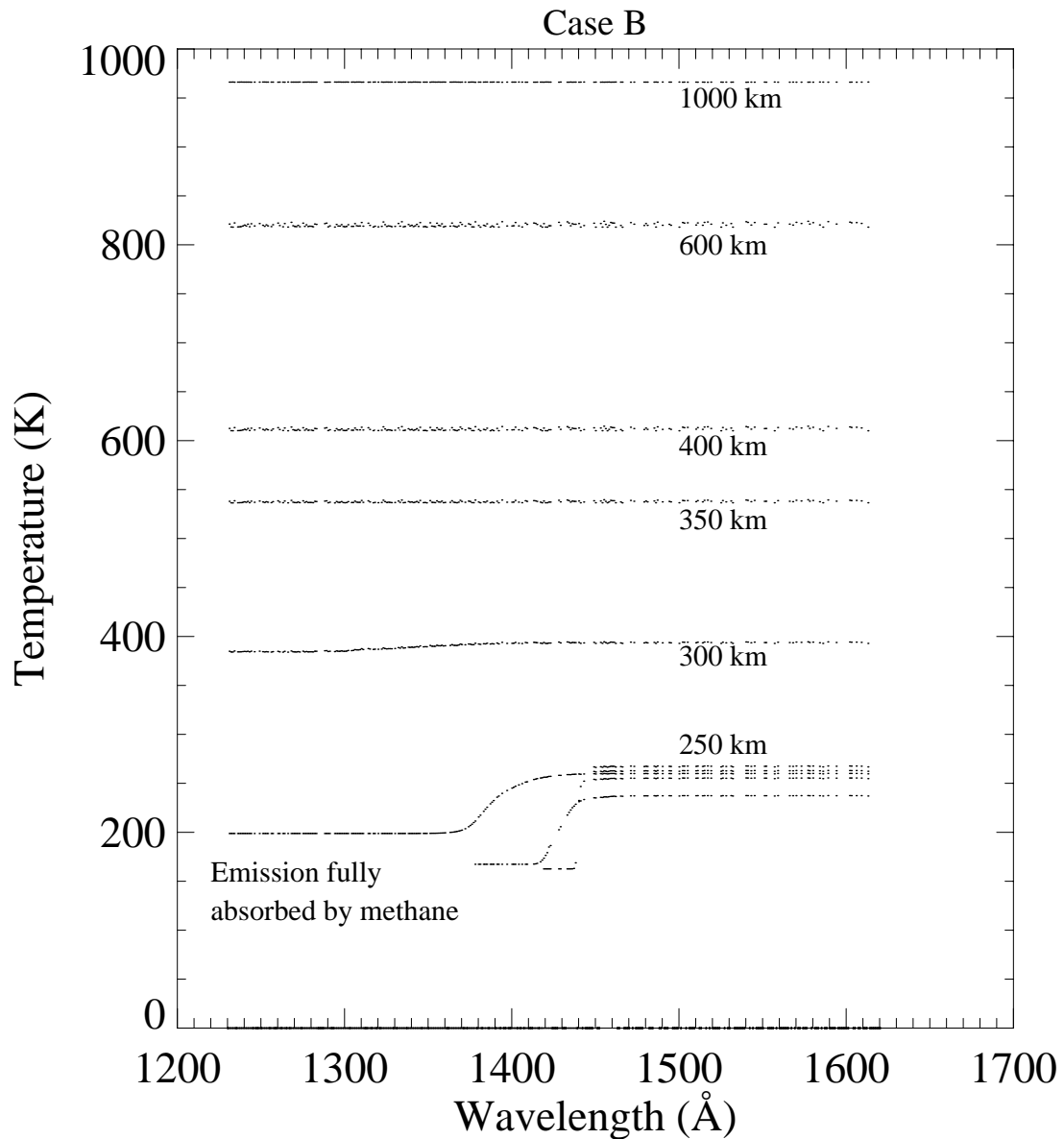
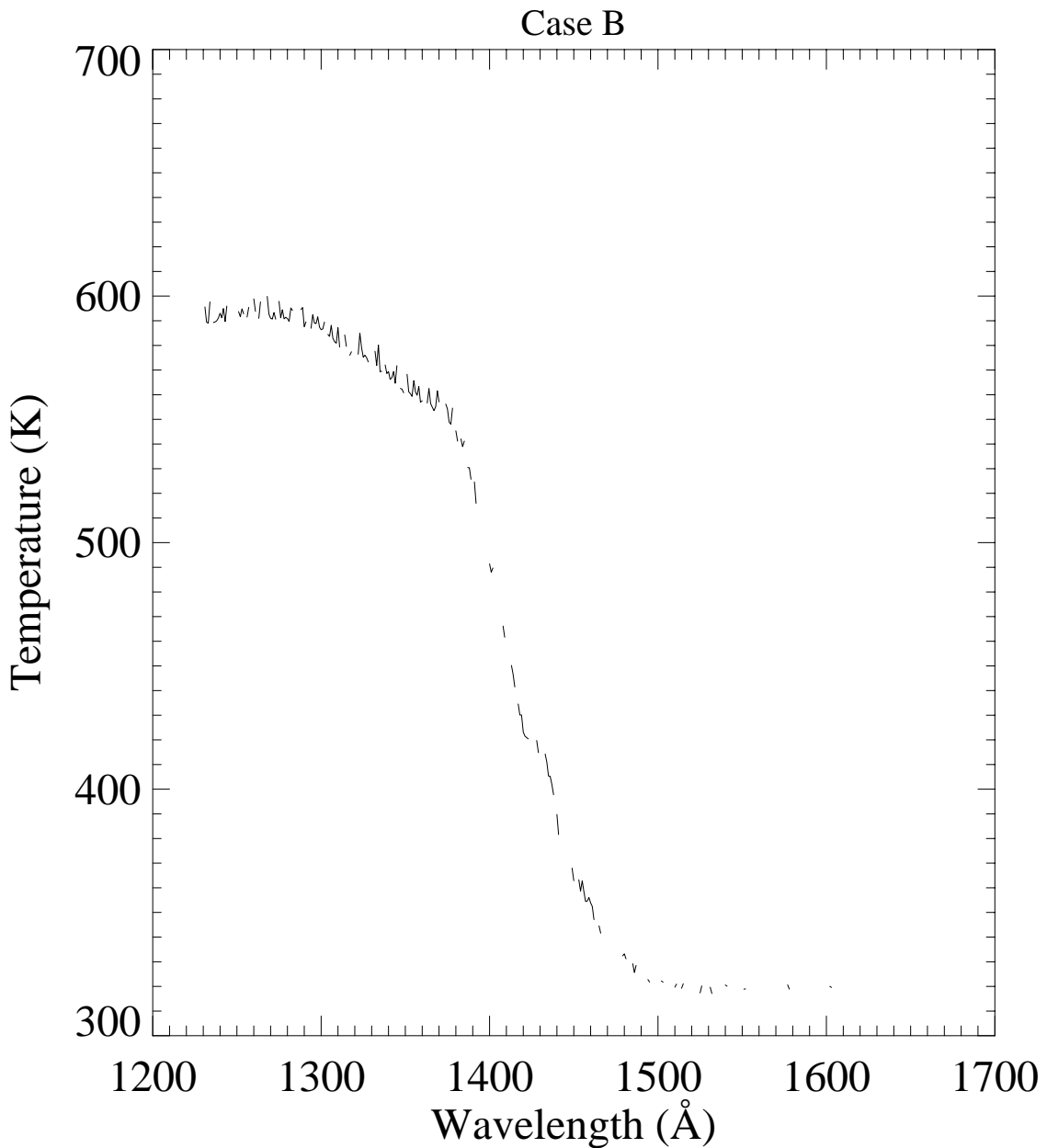


**Figure 79**

An emission characterized by an average  $H_2$  temperature of 600 K observed through a GHRS like aperture is indeed possible if

1. the range of observed wavelengths is included in the part of the spectrum which is absorbed by methane, as is the case for the Hilat2 and Ovals3 echelle spectra
2. the emission originates from a region behind the limb.

The second assumption may not be fully fulfilled by Hilat2 and Ovals3 spectra since at least half of the detector's aperture covers a region inside the Jovian disk and the CML is such that part of the observed emission might come from this Earth facing region. However, according to figure 57, very little emission is expected to come from the disk since the auroral morphology generally favors observed emission at the limb.



Wavelength dependent temperature averaged over the field of view of a GHRS like aperture pointing above the limb. Back side emission only

**Figure 80**

## IX.5 Application to cases D and H

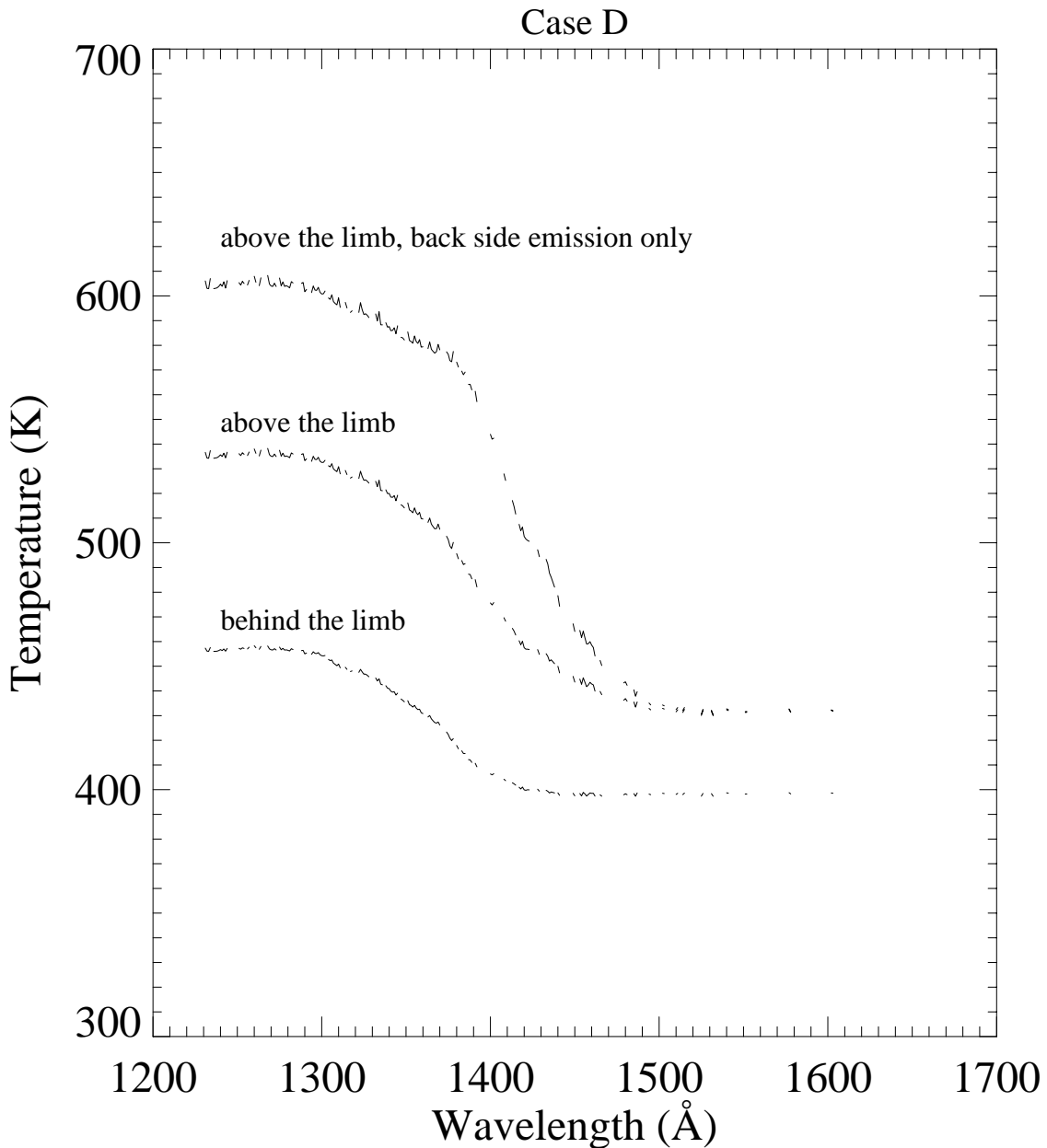
The next two examples illustrate the sensitivity of the average H<sub>2</sub> temperature to the altitude of the peaking emission and to the temperature of the lower stratosphere.

The electron energy flux used in case D leads to an H<sub>2</sub> emission peaking at 273 km, that is 27 km higher than case B. The average wavelength dependent H<sub>2</sub> temperature curves calculated with the same procedures as used for case B are shown in figure 81. The wavelength and viewing geometry effects are similar to those described for case B. The resulting average H<sub>2</sub> temperatures in the absorbed and unabsorbed wavelength regions are presented in table 23. They assume three different configurations : emission originating inside the planetary disk only ("inside disk"), emission above the limb resulting from a uniformly emitting region ("above limb"), emission above the limb exclusively coming from the back side of the planet ("behind disk").

	inside disk		above limb		behind disk	
	absorbed	unabsorbed	absorbed	unabsorbed	absorbed	unabsorbed
case B	390	290	500	320	600	320
case D	460	400	530	430	600	440
case H	420	340	500	360	600	360

**Table 23** : average H<sub>2</sub> temperature (K) observed in a GHRS like aperture for different configurations

A final test performed with case H (warm stratosphere) gives results intermediate to cases B and D (figure 56). The average H<sub>2</sub> temperatures are summarized in table 23. The highest temperatures are reached for case D in all the configurations while the use of case H raises the temperatures obtained in case B by a surprisingly small amount of ~40 K.

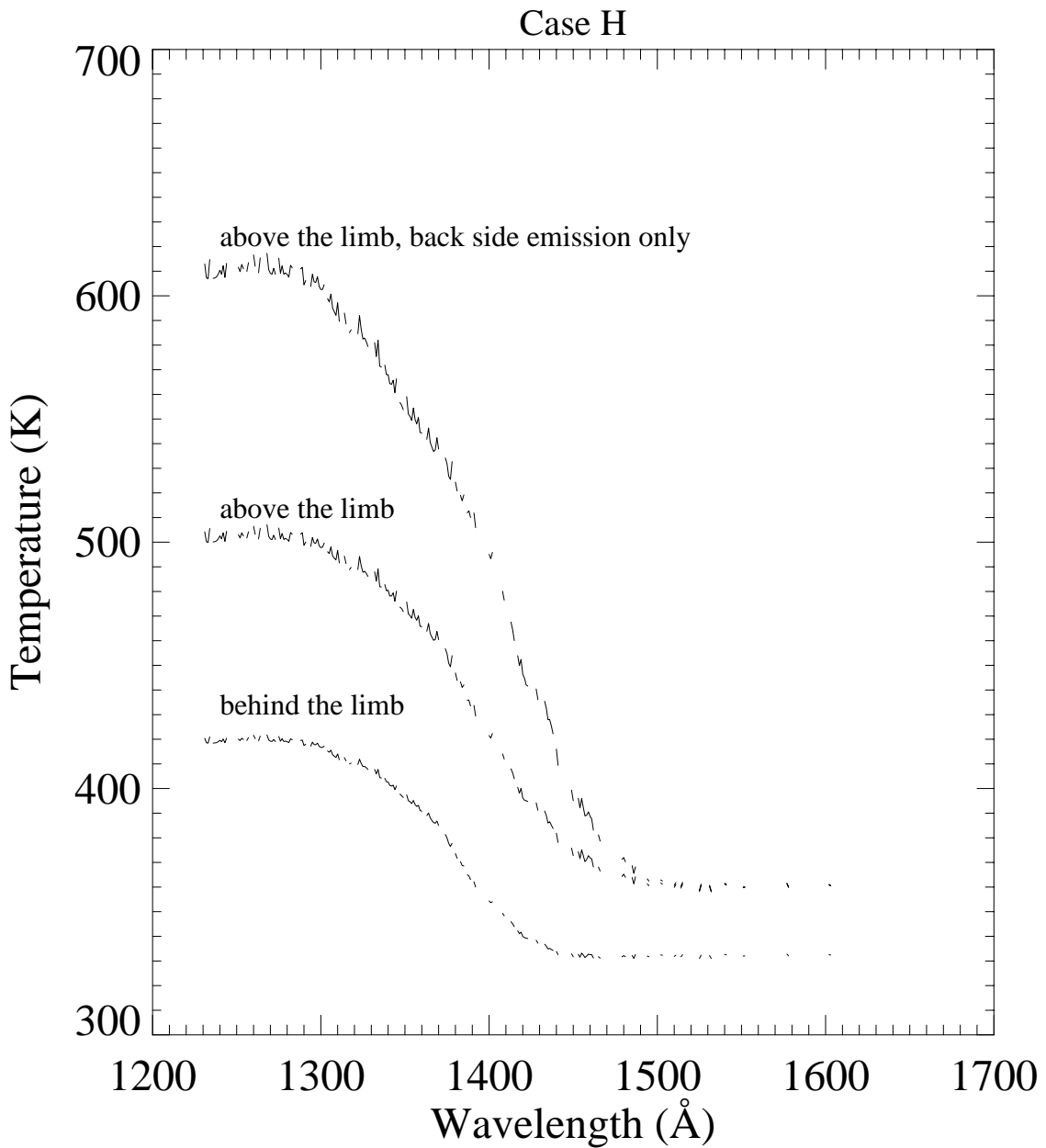


Wavelength dependent temperature averaged over the field of view  
of a GHRS like aperture pointing above and below the limb

**Figure 81**

The use of cases D and H does not significantly increase the temperature that would be determined from observations made through the GHRS aperture. The highest temperature increase is obtained with case D which subtends a raised H<sub>2</sub> peaking emission altitude. This suggests that the emission region that mainly influences the

average H<sub>2</sub> temperature is located above the homopause. The temperature of this region is mainly controlled by the soft electron component of the auroral energy flux.



Wavelength dependent temperature averaged over the field of view  
of a GHRS like aperture pointing above and below the limb

**Figure 82**

In a near future this method will be applied to observations obtained by Kim *et*

*al.* (1997) with GHR in 1995. These observations perfectly suit our purpose since they were made in pairs in the two wavelength ranges 1257-1293 Å and 1587-1621 Å. Spectra in the short wavelength range are mostly due to emission in the H<sub>2</sub> Lyman and Werner band systems. Their intensities are attenuated by hydrocarbon absorption (especially methane). The spectra in the long wavelength range are dominated by unabsorbed emissions of the H<sub>2</sub> Lyman band system. The temperature derived from the latter wavelength region are in the range 400-850 K. Although the authors state a possible tendency toward lower temperatures for higher methane column densities they did not derived temperature from the absorbed spectra. It would be useful to determine the effective temperature from these spectra and see if, as expected from our global model, a systematic difference of the effective temperature is indeed observed between the two spectral windows.

## IX.6 Perspectives : spectroscopic probing of the thermal profile

The examples that we have described illustrate one of the many aspects of the full coupling of the three models that we developed. Following the above considerations, it is possible to elaborate a simple observational strategy based on the wavelength and viewing geometry effects. It would allow us to estimate the atmospheric temperature characterizing different altitude regions. This "spectroscopic probing" of the thermal structure would provide very helpful information to better constrain the thermal profile determined with the energy degradation model.

### IX.6.1 Simple example

In order to illustrate this application, a simple idealized example is now described which allows to estimate the average atmospheric temperature in a region confined between approximately 200 km and 300 km. This region is of major interest since it corresponds to the region of maximum auroral energy deposition. The temperature reached in this region is therefore a good indicator for the total precipitating flux. It also gives important information on the portion of electrons having enough energy to reach these altitudes and therefore constrains the energy distribution of the precipitating electrons.

If one assumes that

1. the auroral emission region is well represented by a uniformly emitting region limited by a realistic auroral oval in corotation with the planet,
2. a GHRS like aperture is used to obtain high resolution spectra with sufficient signal to noise ratio to allow a reliable fit of the spectra,
3. the observed UV and IR emissions are compatible with the electron energy flux distribution of case B,

then :

if the observation is performed while the CML is close to  $0^\circ$  the auroral oval will be

backed out by the planetary disk. This configuration gives rise to an emission that can only be observed above the limb. This case has been described previously and was shown to lead to an average H<sub>2</sub> temperature ranging from 300 K in the unabsorbed region of the spectrum to 600 K in the absorbed region. Ovals3 and Hilat2 indeed give a temperature of 600 K in the absorbed spectral region however no observed spectra are available in the unabsorbed region to confirm that a temperature of 300 K is actually measured. As already discussed, this large temperature difference stems from the complete absorption by methane of the emission below the homopause.

It can be shown from the emission profile derived by the energy degradation model that, for case B, about 4/5 of the integrated unabsorbed emission originates from below the homopause. The temperature derived from the absorbed emission represents the average temperature above the homopause, while the temperature derived from the unabsorbed emission represents the average temperature above the homopause plus the average temperature below the homopause. It can therefore be written that

$$\frac{4}{5}x + \frac{1}{5}y = z$$

where  $x$  = the average temperature below the homopause

$y$  = the absorbed emission temperature, that is 600 K

$z$  = the unabsorbed emission temperature, that is 300 K

and the average temperature below the homopause ( $x$ ) is 225 K. More precisely, within the assumptions made for case B and the emitting morphology, the region represented by this average temperature is located between 200 km and 300 km (the homopause) since the unabsorbed emission profile vanishes below 200 km.

## IX.6.2 Further improvement

Further improvement could be brought by accounting for the complex morphology of the observed auroral zones. It has been shown in part 1 that the morphology of the bright auroral emissions is made of recurrent arcs of oval rather than from uniform zones only. The morphology model would allow to estimate the configuration of these complex auroral structures during the time of the exposure.

Similar effects to those due to methane absorption are expected to arise for acetylene

absorption. They have been neglected because of the lower absorption by C<sub>2</sub>H<sub>2</sub>. The acetylene absorption cross section, however, shows strong peaking values around 1500 Å. Since this region is mostly unaffected by methane absorption, we could take advantage of these peaks to probe the temperature of the lower stratosphere in a manner similar to that previously described (the C<sub>2</sub>H<sub>2</sub> homopause is approximately 50 km deeper than the CH<sub>4</sub> homopause). That is, it is possible to isolate absorbed and unabsorbed spectral regions showing sufficiently different temperatures at the limb (because of the complete absorption of the emission below the C<sub>2</sub>H<sub>2</sub> homopause) so that an estimation of the temperature of the fully absorbed emission is feasible.

Future versions of the spectral generator should include the FUV emission due to the Rydberg states ( B'<sup>1</sup>Σ<sub>u</sub><sup>+</sup>, B''<sup>1</sup>Σ<sub>u</sub><sup>+</sup>, D<sup>1</sup>Π<sub>u</sub> and D'<sup>1</sup>Π<sub>u</sub> ) and should account for self absorption. The Rydberg emission arises below 1200 Å , that is in an optically thick spectral region which deserves a radiative transfer treatment. We could then take advantage of this optically thick emission because it is expected to emerge from the atmosphere at a relatively high altitude (~1000 km). This emission would therefore bear the thermal signature of this high atmospheric region and would constraint the upper part of the thermal profile independently from the IR emissions.

## IX.7 Conclusion

A detailed altitude and energy model of the UV emission resulting from the interaction of an incident electron distribution with the Jovian atmosphere has been constructed. It combines the two-stream electron energy degradation model with a detailed synthetic spectral model of the main three singlet states of H<sub>2</sub> using up-to-date cross sections and molecular constants. In contrast to most earlier studies, the vertical dependence of the auroral emission, H<sub>2</sub> temperature and chemical composition are explicitly considered. Test cases illustrate that the conjunction of the altitude variation of the electron energy spectrum and the atmospheric structure combine to modify the resulting H<sub>2</sub> spectrum integrated along the line of sight. High resolution synthetic spectra fitted to two GHRS echelle spectra of the auroral suggest an H<sub>2</sub> temperature of 600 K. This temperature is in disagreement with the energy degradation model which gives an average temperature (weighted by the emission profile) of 200 K. It is shown that the use of converged (self-consistent) thermal profiles do not remove the discrepancy.

The global coupling of the three models : energy degradation, spectral generator, and morphology is used, as an exploratory application, to estimate the average temperature deduced from the spectrum obtained through a GHRS like aperture. It is shown that the deduced temperature depends both on the wavelength range and on the viewing geometry of the observation. We show how these effects combine to increase an H<sub>2</sub> temperature of 200 K, deduced from the energy degradation model, to an effective H<sub>2</sub> temperature of 600 K (for a particular viewing geometry) that would be deduced by fitting the resulting observed spectrum.

We finally discuss a possible application of the global coupling of the three models that would allow a spectroscopic probing of the jovian thermal vertical profile.

# References

- Abgrall, H., E. Roueff, F. Launay, J.Y. Roncin, and J.L. Subtil, Table of the Lyman band system of molecular hydrogen. *Astron. Astrophys. Suppl.*, **101**, 273-321, 1993a
- Abgrall, H., E. Roueff, F. Launay, J.Y. Roncin, and J.L. Subtil, Table of the Werner band system of molecular hydrogen. *Astron. Astrophys. Suppl.*, **101**, 323-362, 1993b
- Abgrall, H., E. Roueff, X. Liu, and D.E. Shemansky, The emission continuum of electron excited molecular hydrogen. *Astrophys. J.*, **481**, 557-566, 1997
- Ajello, J.M., D.E. Shemansky and G.K. James, Cross sections for production of H(2p, 2s, 1s) by electron collisional dissociation of H<sub>2</sub>, *Astrophys. J.*, **371**, 422-431, 1991
- Ajello, J.M., D. Shemansky, T.L. Kwok and Y.L. Yung, Studies of extreme-ultraviolet emission from Rydberg series of H<sub>2</sub> by electron impact, *Phys. Rev. A*, **29**, 636-653, 1984
- Ajello, J.M., I. Kanik, S.M. Ahmed, Line profile of H Lyman  $\alpha$  from dissociative excitation of H<sub>2</sub> with application to Jupiter, *J. Geophys. Res.*, **100**, 26,411-26,420, 1995
- Ajello, J.M., S.M. Ahmed and X. Liu, Line profile of H Lyman  $\beta$  from dissociative excitation of H<sub>2</sub>, *Phys. Rev.*, **53**, 2302-2308, 1996
- Ajello, J.M. and D.E. Shemansky, Electron excitation of the H<sub>2</sub>( $a^3\Sigma_g^+ \rightarrow b^3\Sigma_u^+$ ) continuum in the vacuum ultraviolet, *Astrophys. J.*, **407**, 820-825, 1993
- Allison, A.C. and A. Dalgarno, Band oscillator strengths and transitions probabilities for the Lyman and Werner systems of H<sub>2</sub>, HD, and D<sub>2</sub>, *at. data*, **1**, 289-304, 1970
- Atreya, S.K., Atmospheres and ionospheres of the outer planets and their satellites, in *Physics and chemistry in space 15*, Edited by L.J. Lanzerotti, M. Hill and D. Stöffler, Springer-Verlag Berlin Heidelberg, 1986
- Auerbach, D., R. Cacak, R. Candano, T.D. Gaily, C.J. Keyser, J.W. McGowan, J.B.A. Mitchell, S.F.J. Wilk, Merged electron-ion beam experiments. I. Methods and measurements of (e-H<sub>2</sub><sup>+</sup>) and (e-H<sub>3</sub><sup>+</sup>) dissociative recombination cross sections, *J. Phys. B*, **10**, 3797-3820, 1977

- Bagenal F., Giant Planet Magnetospheres, *Annu. Rev. Earth Planet. Sci.*, **20**, 289-328, 1992
- Ballester, G. E. and 21 colleagues, Time-Resolved Observations of Jupiter's Far-Ultraviolet Aurora, *Science*, **274**, 409-412, 1996.
- Bandyopadhyay, A., K. Roy, P. Mandal and N.C. Sil, Single-differential total ionization cross sections of hydrogen atom by electron impact, *Phys. Rev. A*, **51**, 2151-2155, 1995
- Banks, P.M., and A.F. Nagy, Concerning the influence of elastic scattering upon photoelectron transport and escape, *J. Geophys. Res.*, **75**, 1902-1910, 1970
- Banks, P.M. and G. Kockarts, *Aeronomy*, Part B, Academic Press, New York and London, 1973
- Bhattacharya, B., R.M. Thorne, S.J. Bolton, D.J. Williams, D. Gurnett, Recirculating Magnetospheric Electrons as a Source for the Jovian Aurora, *Eos Trans. AGU Fall Suppl.*, **79**, P31D-06, F549, 1998
- Broadfoot, A. L., B. R. Sandel, D. E. Shemansky, J. C. McConnell, G. R. Smith, J. B. Holberg, S. K. Atreya, T. M. Donahue, D. F. Strobel, and J. L. Bertaux, Overview of the Voyager ultraviolet spectrometry results through Jupiter encounter, *J. Geophys. Res.*, **86** 8259-8284, 1981
- Broadfoot, A. L., M. J. S. Belton, and P. Z. Takacs, Extreme ultraviolet from Voyager 1 encounter with Jupiter, *Science*, **204**, 979-982, 1979
- Buckman, J.B., M.J. Brunger, D.S. Newman, G. Snitchler, S. Alston, D.W. Norcross, M.A. Morrison, B.C. Saha, G. Dandy, and W.K. Trail, *Phys. Rev. Lett.*, **65**, 3253-3256, 1990
- Burrows, C. J., and 10 colleagues 1995. Wide Field and Planetary Camera 2 Instrument Handbook, pp. 56-61. STScI publication.
- Caldwell, J. A., B. Turgeon, and X. M. Hua, Hubble Space Telescope imaging of the north polar aurora on Jupiter, *Science*, **257**, 1512-1515, 1992
- Callaway, J., K. Unnikrishnan, Electron impact excitation of the  $n=3$  and  $n=2$  states of hydrogen atom at intermediate (14-100 eV) energies, *Phys. Rev. A*, **48**, 4292-4298, 1993
- Clarke, J. T., and 20 colleagues, Hubble Space Telescope Far-Ultraviolet Imaging of Jupiter During the Impacts of Comet Shoemaker-Levy 9, *Science*, **267**, 1302-1306, 1995
- Clarke, J. T., and 20 colleagues, Far-Ultraviolet Imaging of Jupiter's Aurora and the Io "Footprint", *Science*, **274**, 404-409, 1996

- Clarke, J.T., G. Ballester, J. Trauger, J. Ajello, W. Pryor, K. Tobiska, J.E.P. Connerney, G.R. Gladstone, J.H. Waite, Jr., L. Ben Jaffel, J.-C. Gérard, Hubble Space Telescope imaging of Jupiter's UV aurora during the Galileo orbiter mission, *J. Geophys. Res.*, **103**, 20,217-20,236, 1998
- Clarke, J. T., H. W. Moos, S. K. Atreya, and A. L. Lane. Observations from earth and variability of the polar aurora of Jupiter. *Astrophys. J. Lett.*, **241**, 179-18, 1980
- Clarke, J.T., L. Ben Jaffel, A. Vidal-Madjar, G.R. Gladstone, J.H. Waite, Jr., R. Prangé, J.-C. Gérard, J. Ajello, G. James, Hubble Space Telescope Goddard High-Resolution Spectrograph H<sub>2</sub> rotational spectra of Jupiter's aurora, *Astrophys. J.*, **430**, L73-L76, 1994
- Connerney, J. E. P, Jupiter's magnetic field. In Planetary radio emission III (H. Rucker, M. L. Kaiser, S. J. Bauer Eds.), pp. 13-33. Austrian Academy of Sciences Press, Vienna, 1992
- Connerney J.E.P, Magnetic Fields of the Outer Planets, *J. Geophys. Res.*, **98**, 18659-18679, 1993
- Connerney J.E.P., M.H. Acuña, N.F. Ness, T. Satoh, New models of Jupiter's magnetic field constrained by the Io flux tube footprint, *J. Geophys. Res.*, **103**, 11929-11939, 1998
- Coroniti, F. V. and C.F. Kennel, Electron precipitation pulsations, *J. Geophys. Res.*, **75**, 1279, 1970
- Cravens, T.E., G.A. Victor, and A. Dalgarno, The absorption of energetic electrons by molecular hydrogen gas, *Planet. Space Sci.*, **23**, 1059-1070, 1975
- Dabrowski, L., The Lyman and Werner bands of H<sub>2</sub>. *Can. J. Phys.*, **62**, 1639-1664, 1984
- Dalgarno, A., and T.L. Stephens, Discrete absorption and photodissociation of molecular hydrogen, *Astrophys. J.*, **160**, L107-L109, 1970
- Datz, S., G. Sundström, Ch. Biedermann, L. Brodström, H. Danared, S. Mannervik, J.R. Mowar, and L. Larsson, Branching processes in the dissociative recombination of H<sub>3</sub><sup>+</sup>, *Phys. Rev. Lett.*, **74**, 896-899, 1995
- Davidson, G.T. and Y.T. Chiu, An unusual nonlinear system in the magnetosphere: a possible driver for auroral pulsations, *J. Geophys. Res.*, **96**, 19353, 1991
- Dessler, A.J., ed., Physics of the Jovian magnetosphere, Cambridge Univ. Press., 544 pp, 1983
- Dols, V., J. C. Gérard, F. Paresce, R. Prangé, and A. Vidal-Madjar, Ultraviolet imaging of the Jovian aurora with the Hubble Space Telescope, *Geophys. Res. Lett.*, **19**, 1803-1806, 1992

- Dols, V., J.-C. Gérard, J.T. Clarke, J. Gustin and D. Grodent, Diagnostic of the Jovian aurora deduced from ultraviolet spectroscopy : model and GHRM observations, *Icarus*, accepted for publication, 2000 (**see appendix**)
- Dougherty, M.K., D.J. Southwood, A. Balogh and E.J. Smith, Field -aligned currents in the Jovian magnetosphere during the Ulysses flyby, *Planet. Space Sci.*, **41**, 291-300, 1993
- Drossart, P., J.-P. Maillard, J. Caldwell, and J. Rosenqvist, Line-resolved spectroscopy of the jovian H<sub>3</sub><sup>+</sup> auroral emission at 3.5 micrometers, *Astrophys. J.*, **402**, L25-L28, 1993
- Drossart, P., J.-P. Maillard, J. Caldwell, S.J. Kim, J.K.G. Watson, W.A. Majewski, J. Tennyson, S. Miller, S.K. Atreya, J.T. Clarke, J.H. Waite Jr., R. Wagener, Detection of H<sub>3</sub><sup>+</sup> on Jupiter, *Nature*, **340**, 539-541, 1989
- Garvey, R.H., H.S. Porter, and A.E.S. Green, Relativistic yield spectra for H<sub>2</sub>, *J. Appl. Phys.*, **48**, 4353-4359, 1977
- Gérard, J. C., D. Grodent, R. Prangé, J. H. Waite, G. R. Gladstone, V. Dols, F. Paresce, A. Storrs, L. Ben Jaffel and K. A. Franke, A remarkable auroral event on Jupiter observed in ultraviolet with the Hubble Space Telescope, *Science*, **266**, 1675-1677, 1994 (**see appendix**)
- Gérard, J.-C., D. Grodent, V. Dols, J.H. Waite, Jr., The longitudinal variation of the color ratio of the Jovian ultraviolet aurora : a geometric effect ?, *Geophys. Res. Lett.*, **25**, 1601-1604, 1998
- Gérard, J. C., V. Dols, F. Paresce and R. Prangé. Morphology and time variation of the jovian far UV aurora : Hubble Space Telescope observations, *J. Geophys. Res.*, **98**, 18793-18801, 1993
- Gérard, J. C., V. Dols, R. Prangé, and F. Paresce, The morphology of the north Jovian ultraviolet aurora observed with the Hubble Space Telescope: a full longitudinal mapping, *Planet. Space Sci.*, **42**, 905-917, 1994.
- Gérard, J.-C. and V. Singh, A model of energetic electrons and EUV emission in the Jovian and Saturnian Atmospheres and implications, *J. Geophys. Res.*, **87**, 4525, 1982
- Gilmozzi, R., E. Shawn, and E. Kinney, The Geometric Distortion Correction for the WFPC Cameras. In Instrument Science Report, pp. 95-02, STScI Publication, 1995
- Gladstone, G.R., M. Allen, and Y.L. Yung, Hydrocarbon Photochemistry in the upper atmosphere of Jupiter, *Icarus*, **119**, 1-52, 1996.

- Gladstone, G.R. and T.E. Skinner, Spectral analysis of Jovian auroral emissions, *Proceedings of the workshop on time-variable phenomena in the Jovian system*, NASA Spec. Publ. **SP-494**, 221-228, 1989.
- Gladstone, G.R., Radiative transfer and photochemistry in the Upper atmosphere of Jupiter, Ph.D. Thesis, California Institute of Technology, Pasadena, 1982
- Glass-Maujean, M, Transition probabilities for the D and B' vibrational levels to the X vibrational levels and continuum of H<sub>2</sub>, *ADNDT*, **30**, 301-311, 1984
- Gold, T, *Symposium on the exploration of space*, **64**, 1665-1674, 1959
- Green, A. E. S., T. Sawada, Ionization cross sections and secondary electron distributions, *J. Atmos. Terr. Phys.*, **34**, 1719-1728, 1972
- Grodent, D., G.R. Gladstone, J.C. Gérard, V. Dols and J.H. Waite, Simulation of the morphology of the Jovian UV north aurora observed with the Hubble Space Telescope, *Icarus*, **128**, 306-321, 1997.
- Grodent D., V. Dols, J. C. Gérard and D. Rego 1996. The equatorial boundary of the ultraviolet Jovian north aurora observed with multispectral Hubble Space Telescope images. *J. Geophys. Res.* **101** 2163-2168. (see appendix)
- Grodent, D., J.-C. Gérard, and H.J. Waite, Jr., A self-consistent model of the Jovian auroral thermal structure, *J. Geophys. Res.*, accepted for publication, 2000
- Ham, D.O., D.W. Trainor, F. Kaufman, Gas phase kinetics of  $H + H + H_2 \rightarrow 2H_2$ , *J. Chem. Phys.*, **53**, 4395, 1970
- Hanley, H.J.M., R.D. McCarty and H. Inteman, The viscosity and thermal conductivity of dilute gaseous hydrogen from 15 to 5000 K, *J. Res. Natl. Bur. Stand.*, **74A**, 331, 1970
- Harris, W.M., J.T. Clarke, M.A. Mc Grath, and G.E. Ballester, Analysis of Jovian Auroral H Ly- $\alpha$  Emission (1981-1991), *Icarus*, **124**, 350-365, 1996.
- Herbert, F., B. R. Sandel, and A. L. Broadfoot 1987. Observations of the jovian UV aurora by Voyager *J. Geophys. Res.* **92** 3141-3154.
- Herzberg, G., Spectra of diatomic molecules, Van Nostrand Company, New York, 658 pp, 1950
- Holtzman J. A., and 17 colleagues, The Performance and Calibration of the WFPC2 on the Hubble Space Telescope, *Publ. Astron. Soc. Pacific*, **107**, 156-178, 1995
- Ingersoll, A.P., A.R. Vasavada, B. Little, C.D. Anger, S.J. Bolton, C. Alexander, K.P. Klaasen, W.K. Tobiska, Imaging Jupiter's Aurora at Visible Wavelengths, *Icarus*, **135**, 251-264, 1998

- Jackman, C.H., R.H. Garvey, and A.E.S. Green, Electron impact on atmospheric gases, a, Updated cross sections, *J. Geophys. Res.*, **82**, 5081-5090, 1977
- James, G.K., J.A. Slevin, D.E. Shemansky, J.W. McConkey, I. Bray, D. Dziczek, I. Kanik, and J.M. Ajello, Optical excitation function of H(1s-2p) produced by electron impact from threshold to 1.8 keV, *Phys. Rev. A*, **55**, 1069-1087, 1997
- James, G.K., J.M. Ajello, W.R. Pryor, The middle ultraviolet visible spectrum of H<sub>2</sub> excited by electron impact, *J. Geophys. Res.*, **103**, 20,113-20,123, 1998
- Khakoo, M.A., and J. Segura, Differential cross sections for the electron impact excitation of the  $b^3\Sigma_u^+$  continuum of molecular hydrogen, *J. Phys. B*, **27**, 2355-2368, 1994
- Khakoo, M.A., S. Trajmar, Electron-impact of the  $a^3\Sigma_g^+$ ,  $B^1\Sigma_u^+$ ,  $b^3\Sigma_u^+$  and  $C^1\Pi_u$  states of H<sub>2</sub>, *Phys. Rev. A*, **34**, 146-156, 1986
- Kim, J.K., L.P. Theard, W.T. Huntress Jr., Reactions of excited and ground state H<sub>3</sub><sup>+</sup> ions with simple hydrides and hydrocarbons: collisional deactivation of vibrationally excited H<sub>3</sub><sup>+</sup> ions, *Int.J. Mass Spectrom. Ion Phys.*, **15**, 223-244, 1974
- Kim, Y.H., J.L. Fox, H.S. Porter, Densities and Vibrational distribution of H<sub>3</sub><sup>+</sup> in the jovian auroral ionosphere, *J. Geophys. Res.*, **97**, 6093-6101, 1992
- Kim Y.H., J.L. Fox, J.J. Caldwell, Temperatures and altitudes of Jupiter's Ultraviolet Aurora Inferred from GHRs Observations with the Hubble Space Telescope, *Icarus*, **128**, 189-201, 1997
- Kivelson, M.G., C.T. Russell, Introduction to Space Physics, *Cambridge University Press*, 1995
- Kwok, T.L., A. Dalgarno, and A. Posen, Transition probabilities of the  $B^1\Sigma_u^+ \rightarrow X^1\Sigma_g^+$  system of molecular hydrogen, *Phys. Rev. A*, **32**, 646-649, 1985
- Lam, H.A., N. Achilleos, S. Miller, J. Tennyson, L.M. Trafton, T.R. Geballe, and G.E. Ballester, A baseline spectroscopic study of the infrared auroras of Jupiter, *Icarus*, **127**, 379-393, 1997
- Lee, L. C. and C. C. Chiang, Fluorescence yield from photodissociation of CH<sub>4</sub> at 1060-1420 Å, *J. Chem. Phys.*, **78**, 688-691, 1983.
- Lin, C.S., Theoretical analysis of the vibrational structure of the electronic transitions involving a state with double minimum: E,F<sup>1</sup>Σ<sub>g</sub><sup>+</sup> of H<sub>2</sub>. *J. Chem. Phys.*, **60**, 4660, 1974

- Linder, F., and H. Schmidt, Rotational and vibrational excitation of H<sub>2</sub> by slow electron impact, *Zeitschrift für Naturforschung*, **260**, 10, 197
- Liu, W., and A. Dalgarno, The ultraviolet spectrum of the jovian aurora, *Astrophys. J.*, **467**, 446-453, 1996
- Liu, X, S.M. Ahmed, R.A. Multari, G.K. James and J.M. Ajello, High-resolution electron-impact study of far-ultraviolet emission spectrum of molecular hydrogen, *Astrophys. J. Supp.*, **101**, 375-399, 1995.
- Liu, X., D.E. Shemansky, S.M. Ahmed, G.K. James, J.M. Ajello, Electron-impact excitation and emission cross sections of the H<sub>2</sub> Lyman and Werner systems, *J. Geophys. Res.*, **103**, 26,739-26,758, 1998
- Livengood, T. A, and H. W. Moos, Jupiter's north and south polar aurorae with IUE data, *Geophys. Res. Lett.*, **17**, 2265-2268, 1990.
- Livengood, T. A., D. F. Strobel, and H. W. Moos, Long-term study of longitudinal dependence in primary particle precipitation in the north jovian aurora, *J. Geophys. Res.*, **95**, 10,375-10,383, 1990.
- Livengood, T. A., H. W. Moos, G. E. Ballester, and R. Prangé, Jovian ultraviolet auroral activity, 1981-1991. *Icarus*, **97**, 26-45, 1992
- Lyons, L.R., Formation of auroral arcs via magnetospheric-ionosphere coupling, *Rev. Geophys.*, **30**, 93-112, 1992
- Maillard, J.P., P. Drossart, J.K.G. Watson, S.J. Kim, J. Caldwell, H<sub>3</sub><sup>+</sup> fundamental band in Jupiter's auroral zones at high resolution from 2400 to 2900 inverse centimeters, *Astrophys. J.*, **363**, L37-L41, 1990
- Matcheva, K.I., and D.F. Strobel, Heating of Jupiter's Thermosphere by Dissipation of Gravity Waves due to Molecular Viscosity and Heat Conduction, *Icarus*, **140**, 328-340, 1999
- McNutt, R.L., J.W. Belcher, H.S. Bridge, Departure from rigid corotation of plasma in Jupiter's dayside magnetosphere, *Nature*, **280**, 803, 1979
- Miles, W.T., R. Thompson, and A.E.S. Green, Electron impact cross sections and energy deposition in molecular hydrogen, *J. Appl. Phys.*, **43**, 678-686, 1972
- Moiseiwitsch, B.L., Elastic scattering of electrons, *Atmos. Mol. Process.*, 280, 1962
- Morrissey, P.F., P.D. Feldman, J.T. Clarke, B.C. Wolven, D.F. Strobel, S.T. Durrance, J.T. Trauger, Simultaneous spectroscopy and imaging of the jovian aurora with the Hopkins Ultraviolet Telescope and the Hubble Space Telescope, *Astrophys. J.*, **476**, 918-923, 1997

- Mount, G., E.S. Warden, and H.W. Moos, Photoabsorption cross sections of methane and ethane from 11380 to 1600 Å at T = 295 K and T = 200 K. *Astrophys. J.*, **224**, L35-L38, 1978
- Mount, G., E.S. Warden, and H.W. Moos, Photoabsorption cross sections of methane from 1400 to 1850 Å. *Astrophys. J.*, **214**, L47-L49, 1977
- Nagy, A.F., P.M. Banks, Photoelectron fluxes in the ionosphere, *J. Geophys. Res.*, **75**, 6260-6270, 1970
- Neale, L., and J. Tennyson, A high-temperature partition function for H<sub>3</sub><sup>+</sup>, *Astrophys. J.*, **454**, L169-L173, 1995
- Prangé, R., Dougherty, M. and V. Dols, Identification d'une aurore "current-driven" sur Jupiter à l'aide d'observations corélées avec HST et Ulysse, Proc. Séminaire Scientifique du GdR Plasma, 1994
- Prangé, R., S. Maurice, W.M. Harris, D. Rego, and T. Livengood, Comparison of IUE and HST diagnostics of the Jovian aurora, *J. Geophys. Res.*, **102**, 9289-9301, 1997.
- Prangé, R. and M., Elkhamsi, Modeling the precipitation flux in the Jovian auroral zones. 1, The model and its application to the UV auroral emissions, *J. Geophys. Res.*, **96**, 21371-21389, 1998
- Pryor, W.R., A.I.F. Stewart, K.E. Simmons, W.E. McClintock, W. Sweet, J.M. Ajello, G.K. James, W.K. Tobiska, G.R. Gladstone, D.E. Shemansky, A.P. Ingersoll, A.R. Vasavada, J.T. Clarke, Jupiter's UV Aurora on Galileo Orbit G7, Submitted to *Icarus*, 1999
- Rescigno, T.N., B.K. Elza, and B.H. Lengsfeld III, An *ab initio* treatment of near-threshold vibrational excitation of H<sub>2</sub> by electron impact: new perspectives on discrepancies between crossed-beam and swarm data, *J. Phys. B*, **26**, L567-L573, 1993
- Sandel, B. R., and 16 colleagues, Extreme ultraviolet observations from Voyager 2 encounter with Jupiter, *Science*, **206**, 962-966, 1979
- Satoh, T., J. E. P. Connerney and R. L. Baron. Emission source model of Jupiter's H<sub>3</sub><sup>+</sup> aurora : a generalized inverse analysis of images, *Icarus*, **122**, 1-23, 1996
- Seiff, A., D.B. Kirk, T.C.D. Knight, R.E. Young, J.D. Mihalov, L.A. Young, F.S. Milos, G. Schubert, R.C. Blanchard, and D. Atkinson, Thermal structure of Jupiter's atmosphere near the edge of a 5-μm hot spot in the north equatorial belt. *J. Geophys. Res.*, **103**, 22857-22890, 1998
- Seiff, A. and 10 colleagues, Thermal Structure of Jupiter's upper atmosphere derived from the Galileo probe, *Science*, **276**, 102-104, 1997

- Shemansky, D.E., J.M. Ajello, D.T. Hall, Electron impact excitation of H<sub>2</sub> : Rydberg band systems and the benchmark dissociative cross section for H Lyman-alpha, *Astrophys. J.*, **296**, 765-773, 1985
- Shemansky D.E., J.M. Ajello, D.T. Hall, Electron impact excitation of H<sub>2</sub> : Rydberg band systems and the benchmark dissociative cross section for H Lyman-alpha, *Astrophys. J.*, **315**, 408-409, 1987
- Shyn, T.W., and W.E. Sharp, Angular distribution of electrons elastically scattered from H<sub>2</sub>, *Phys. Rev. A*, **24**, 1734-1740, 1981
- Shyn, T.W., and W.E. Sharp, Double differential cross sections of secondary electrons ejected from gases by electron impact: 25-250 eV on H<sub>2</sub> (abstract), *Eos. Trans. AGU*, **61**, 285, 1980
- Skinner, T.E., S.T. Durrance, P.D. Feldman and H.W. Moos, IUE observations of longitudinal and temporal variations in the Jovian auroral emission, *Astrophys. J.*, **278**, 441-448, 1984.
- Smith P.L., K. Ito, and G. Stark, High-resolution, VUV (147-201 nm) photoabsorption cross sections for C<sub>2</sub>H<sub>2</sub> at 195 and 295 K. *J. Geophys. Res.* **96**, 17529-17533, 1991
- Stephan, K., H. Helm, and T.D. Märk, Mass spectrometric determination of partial electron impact ionization cross sections of He, Ne, Ar and Kr from threshold up to 180 eV, *J. Chem. Phys.*, **73**, 3763-3778, 1980
- Stephens, T.L., and A. Dalgarno, Kinetic energy in the spontaneous radiative dissociation of molecular hydrogen, *Astrophys. J.*, **186**, 165-167, 1973
- Stephens, T.L., and A. Dalgarno, Spontaneous radiative dissociation in molecular hydrogen, *J. Quant. Spectrosc. Radiat. Transf.*, **12**, 569-586, 1972
- Stern, D.P., Large-Scale Electric Fields in the Earth's Magnetosphere, *Rev. Geophys. Space Phys.*, **15**, 156-194, 1977
- Straub, H.C., P. Renault, B.G. Lindsay, K.A. Smith, and R.F. Stebbings, Absolute partial cross sections for electron-impact ionization of H<sub>2</sub>, N<sub>2</sub>, and O<sub>2</sub> from threshold to 1000 eV, *Phys. Rev. A*, **54**, 2146-2153, 1996
- Sundström, G., J.R. Mowat, H. Danared, S. Datz, L. Broström, A. Filevich, A. Källberg, S. Mannervik, K.G. Rensfelt, P. Sigray, M. af Ugglas, M. Larsson, Destruction rate of H<sub>3</sub><sup>+</sup> by low energy electrons measured in a storage-ring experiment, *Science*, **263**, 785, 1994
- Swartz, W.E., J.S. Nisbet, and A.E.S. Green, Analytic expression for the energy transfer rate from photoelectrons to thermal electrons, *J. Geophys. Res.*, **76**, 8425, 1971
- Tascione, T.F., Introduction to the space environment, second edition, Krieger Publishing Company, Malabar, Florida, 1994

- Theard, L.P., and W. T. Huntress, Jr., Ion molecule reactions and vibrational deactivation of  $\text{H}_3^+$  ions in mixtures of hydrogen and helium, *J. Chem. Phys.*, **60**, 2840-1974
- Trafton, L. M., J. C. Gérard, G. Munhoven, and J. H. Waite, High-resolution spectra of Jupiter's northern auroral ultraviolet emission with the Hubble Space Telescope, *Astrophys. J. Lett.*, **421**, 816-827, 1994
- Trafton, L.M., V. Dols, J.-C. Gérard, J.H. Waite, Jr., G.R. Gladstone, G. Munhoven, HST spectra of the jovian ultraviolet aurora: search for heavy ion precipitation, *Astrophys. J.*, **507**, 955-967, 1998
- Vasavada, A.R., A.H. Bouchez, A.P. Ingersoll, B. Little, C. D. Anger and the Galileo SSI Team, Jupiter's visible aurora and Io footprint, *submitted to Science*, 1999
- Vasyliunas, V.M., Plasma distribution and flow, See Dessler, 395-453, 1983
- Waite, J. H., T. E. Cravens, J. Kozyra, A. F. Nagy, S. K. Atreya, R. H. Chen, Electron Precipitation and Related Aeronomy of the Jovian Thermosphere and Ionosphere, *J. Geophys. Res.*, **88**, 6143-6163, 1983
- Waite, J.H., Jr, et al., "*Magnetospheres of the Outer Planets*" (August 1999), 153, 1999
- Waite, J.H., Jr., G.R. Gladstone, W.S. Lewis, P. Drossart, T.E. Cravens, A.N. Maurellis, B.H. Mauk, S. Miller, Equatorial X-ray Emissions: Implications for Jupiter's High Exospheric Temperatures, *Science*, **276**, 104-108, 1997
- Waite J.H., Jr., G.R. Gladstone, P. Robertson, T. Majeed, J.T. Clarke, Rapidly Varying Emissions in Jupiter's Polar Cap: A Signature of Reconnection in the Jovian Magnetotail? *31<sup>st</sup> meeting of the Division of Planetary Science*, Padova (It), 1999
- Williams, D.J., R.W. McEntire, The *Galileo* Energetic Particles Detector, *Space Sci. Rev.*, **60**, 385-412, 1992
- Wolven, B.C. and P. Feldman, Self-absorption by vibrationally excited  $\text{H}_2$  in the Astro-2 Hopkins Ultraviolet Telescope spectrum of the jovian aurora, *Geophys. Res. Lett.*, **25**, 1537-1540, 1998
- Young, L.A., R.V. Yelle, R.E. Young, A. Seiff, D.B. Kirk, Gravity waves in Jupiter's thermosphere, *Science*, **276**, 108-111, 1997
- Yung, Y. L., G. R. Gladstone, K. M., Chang, J. M., Ajello, and S. K. Srivastava,  $\text{H}_2$  fluorescence spectrum from 1200 to 1700Å, by electron impact : Laboratory study and application to Jovian aurora, *Astrophys. J. Lett.*, **254**, L65-L69, 1982.

# Appendix

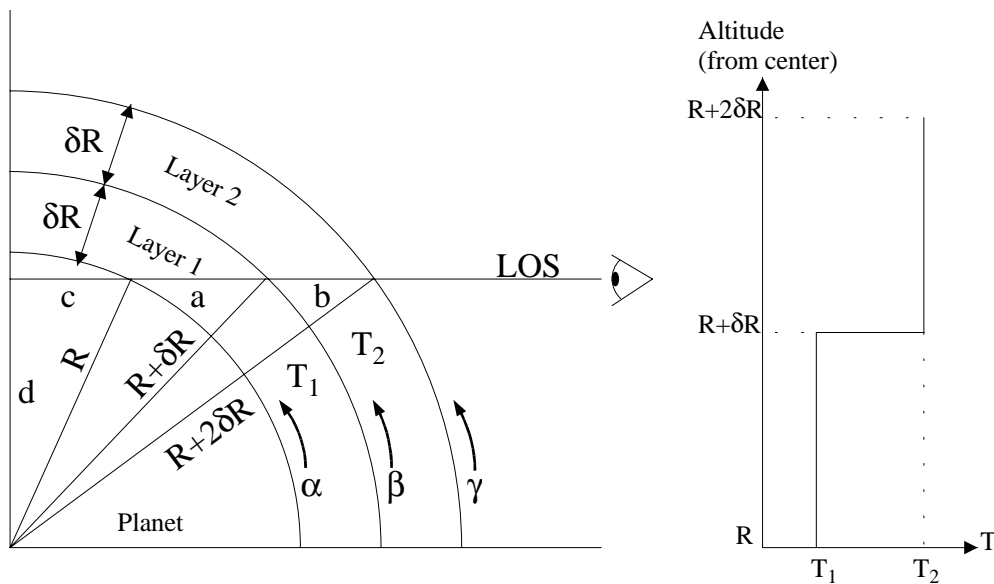
## A. Effect of the geometry of observation on the average temperature

It is possible to estimate the effect of the viewing geometry on the average value of the temperature integrated over a line of sight (LOS) by means of simple trigonometric considerations.

Assuming that Jupiter is a spherical planet with radius  $R$ , and that the thermal profile can be approached by two values (as in figure below) relevant for two atmospheric layers having the same thickness :

- $T_1$  for a lower atmospheric layer located between  $R$  and  $R(1+\delta)$
- $T_2$  for an upper atmospheric layer located between  $R(1+\delta)$  and  $R(1+2\delta)$

where  $\delta R$  is the thickness of each layer and we assume that  $T_1 < T_2$ .



The following relations can be derived from the above drawing :

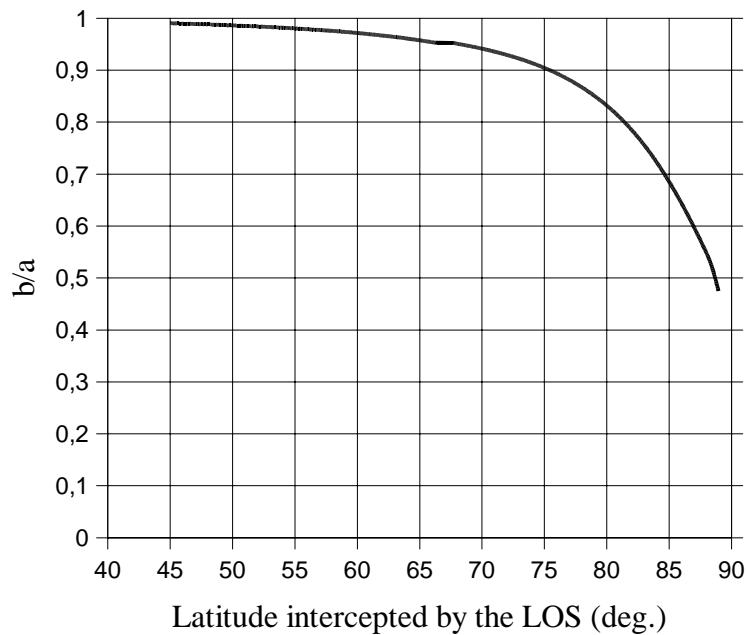
$$d = R \sin \alpha = R(1 + \delta) \sin \beta = R(1 + 2\delta) \sin \gamma$$

$$\begin{aligned}
c &= R \cos \alpha \\
a+c &= R(1+\delta) \cos \beta \\
a+b+c &= R(1+2\delta) \cos \gamma
\end{aligned}$$

from which one can derive the ratio between b and a, that is the ratio between the portion of LOS crossing layer 2 and the portion of LOS crossing layer 1, as a function of the latitude angle ( $\alpha$ ) intercepted by the LOS :

$$\frac{b}{a} = \frac{(1+2\delta) \cos(\operatorname{asin}(\frac{\sin \alpha}{1+2\delta})) - (1+\delta) \cos(\operatorname{asin}(\frac{\sin \alpha}{1+\delta}))}{(1+\delta) \cos(\operatorname{asin}(\frac{\sin \alpha}{1+\delta})) - \cos \alpha}$$

This ratio is plotted in the following figure as a function of the latitude angle intercepted by the LOS for  $\delta = 0.01$  :



It is directly seen that the b/a ratio decreases as latitude increases. From 0 to 45° the portion of LOS passing through layer 1 is approximately equal to the portion crossing layer 2, that is both layers equally weigh the average temperature so that

$$T = \frac{1}{2} T_1 + \frac{1}{2} T_2 .$$

For higher latitudes, the portion of the LOS crossing layer 1 becomes longer than the portion crossing layer 2 and the lower (colder) layer 1 contributes more to the average temperature than layer 2. For example, at 88° the b/a ratio is 0.5 and the average temperature is given by

$$T = \frac{2}{3}T_1 + \frac{1}{3}T_2$$

which is colder than the temperature derived at 0° latitude.

## B. Papers